Selected Optical-to-Radio Observations of the Evolution of Massive Galaxies and Structure Formation in the Early Universe

by

Jeffrey Franklin William Wagg

A thesis submitted to the Instituto Nacional
de Astrofísica, Óptica y Electrónica
for the degree of Doctor of Philosophy
in the department of Astrophysics.

Advisor:

Dr. David H. Hughes

Sta. Maria Tonantzintla, Puebla
December, 2006

Declaration

This thesis is submitted for the degree of Doctor of Philosophy to the Instituto Nacional de Astrofísica, Óptica y Electrónica. I declare that this dissertation is not the same as any that I have submitted for a degree, diploma, or any other qualification in other universities. Some of the work presented here is also presented in the following publications:

1) Gaztañaga, E., **Wagg, J.**, Multamäki, T., Montaña, A., & Hughes, D. H., *Two-point anisotropies in WMAP and the Cosmic Quadrupole*, 2003, MNRAS, 346, 47

2) Gaztañaga, E., & **Wagg, J.**, *Three-point temperature anisotropies in WMAP: Limits on CMB non-Gaussianities and nonlinearities*, 2003, PhysRevD, 68, 021302

3) **Jeff Wagg**, Arif Babul, Romeel Davé, Sara Ellison & Antoinette Songaila, *High-Redshift Lyα forest lines in a Concordance ΛCDM Universe*, poster contribution to *Multi-wavelength AGN Surveys*, Dec. 2003, Cozumel, MX

4) Hughes, D. H., Aretxaga, I., **Wagg, J.**, Olmi, L., & Chapin, E. L., *Resolving the FIR-Submm Background from Dome C, Antarctica*, 2005, EAS Publications Series, 14, 75

5) **J. Wagg**, D.J. Wilner, R. Neri, D. Downes, & T. Wiklind, *HCN J=5-4 Emission in APM08279+5255 at z=3.91*, 2005, ApJ, 634, L13

6) Mortier et al. (**inc. J. Wagg**), *The SCUBA HAlf Degree Extragalactic Survey (SHADES) - I: Survey motivation, design and data processing*, 2005, MNRAS, 363, 563

7) Coppin et al. (**inc. J. Wagg**), *The SCUBA HAlf Degree Extragalactic Survey (SHADES) - II: Submillimetre maps, catalogue and number counts*, 2006, MNRAS, *in press. (astroph/0609039)*

8) D.H. Hughes, **J. Wagg**, I. Aretxaga, et al., *A broadband spectroscopic search for CO line emission in HDF850.1: the brightest submillimetre object in the Hubble Deep Field*, 2006, poster contribution to *From Z-machines to ALMA*, Nov. 2005, Charlottesville, VA, USA

9) **J. Wagg**, D.J. Wilner, R. Neri, D. Downes, & T. Wiklind, *Atomic Carbon in APM 08279+5255 at z=3.91*, 2006a, ApJ, 651, 46

10) Weiss, A. et al. (**inc. J. Wagg**), *Highly Excited CO line Emission in APM 08279+5255 at z=3.9*, 2006, A&A, *submitted*

11) **J. Wagg**, D.H. Hughes, I. Aretxaga, et al., *A broadband spectroscopic search for CO line emission in HDF850.1: the brightest submillimetre object in the Northern Hubble Deep Field*, 2006b, MNRAS, *accepted, astro-ph/0611869*

12) **J. Wagg**, A. Babul, R. Davé, S.L. Ellison, A. Songaila, N. Katz, D.H. Weinberg, & D.H. Hughes, *On Using the QSO Lyα Forest Lines as Probes of the HI Photoionization Rate at 2.5< z <3.5*, 2006c, ApJ, *submitted*

Abstract

This thesis presents a study of the formation and evolution of massive galaxies and large-scale structure in the early Universe, through complementary observations of distinct, but related phenomena over the wavelength range ∼4200 Å to ∼2 cm. I introduce this study by briefly presenting the results of a collaborative analysis of cosmic microwave background fluctuations measured by *WMAP*, where we find that the power on large scales ($\geq 60^o$), although low, is consistent with the ΛCDM model predictions. Meanwhile the quantum fluctuations which initially "seeded" the overdensities in the matter distribution are confirmed to be Gaussian random as predicted by inflationary models. The evolution of large-scale structure following recombination, can be traced by the formation of massive high-redshift galaxies revealed in blank-field sub(mm) wavelength surveys. I present an independent analysis of the 450/850 μm SCUBA Half-Degree Extragalactic Survey (SHADES) survey data, wherein I conclude that a high-redshift tail ($z \gg 3$) of luminous infrared galaxies is missed by current optical redshift surveys of radio-detected (sub)mm galaxy optical/infrared counterparts. In an attempt to address the need for a method of redshift determination for this higher redshift (sub)mm galaxy population, I present a cm-wavelength GBT search for low-J CO line emission in HDF850.1, predicted to have a redshift of z∼4.1. Though this search was unsuccessful due to instrumental limitations, I conclude that future mm wavelength searches for high-J line emission will be more successful due to the gaseous medium in these objects being warm and dense. Once redshifts for these objects are obtained, subsequent studies of the physical conditions responsible for their extreme nature may be carried out through observations of additional diagnostic molecules. I present the first detections of HCN J=5-4 and [CI] J=1-0 in one of the most extreme high-redshift objects currently know, the ultraluminous lensed quasar APM 08279+5255 at z=3.91. Indeed the HCN J=5-4 detection is the first in any extragalactic object. I find that the [CI] line luminosity predicts total molecular gas densities which are consistent with those measured by the CO J=1-0 line luminosity. The HCN J=5-4 line luminosity is a factor of 10 larger than expected, which may be due to radiative excitation by infrared photons from the central AGN. The final study of large-scale structure presented in this thesis uses the Lyα forest of HI absorption lines, in simulated and observed QSO spectra, to explore the impact that extreme high-redshift starburst galaxies and AGN have on the gas in their local environments. I find that 20–40% of the contribution to the HI ionizing radiation field at z∼2.5–3.5, is likely due to UV photons from star-forming galaxies, in addition to that believed to come from QSOs.

These studies of high-redshift galaxies and large-scale structure have made use of current instruments on world-class facilities. I am now preparing to conduct similar studies with the next generation of interferometers and single-dish tele-

scopes that will provide order of magnitude increases in the sensitivities to the continuum and molecular line emission from these tracers of structure formation and evolution.

Resumen

En esta tesis se presenta un estudio sobre la formación y evolución de galaxias masivas, y la estructura a gran escala del universo temprano, mediante observaciones complementarias de diversos fenómenos en un rango de longitudes de onda entre ∼4200 Å y ∼2 cm. Se inicia con una breve descripción de un trabajo colaborativo donde analisamos las fluctuaciones en el fondo cósmico de micro-ondas medidas por *WMAP*, y encontramos que la potencia a grandes escalas ($\geq 60^o$) es consistente con las predicciones del modelo ΛCDM a pesar de tener un valor relativamente bajo. De igual manera, se confirmó que las fluctuaciones cuánticas que inicialmente "sembraron" las sobredensidades en la distribución de materia son Gaussianas, tal y como lo predice el modelo inflacionario.

La evolución de la estructura a gran escala después de la época de recombinación, puede ser trazada por la formación de galaxias masivas a alto corrimiento al rojo (z), reveladas por observaciones milimétricas y sub-milimétricas ((sub)mm). Por esta razón, se presenta un análisis independiente de los datos de SHADES (450/850 μm SCUBA Half-Degree Extragalactic Survey), del cual se concluye que una población de galaxias luminosas en el infrarrojo a $z \gg 3$ está ausente en mapeos ópticos actuales hacia galaxias (sub)mm detectadas en ondas de radio.

Con el fin de abordar la necesidad de un método para determinar corrimientos al rojo de la población de galaxias (sub)mm a alto z, se llevaron a cabo una serie de observaciones con el Telescopio Green Bank (GBT) a longitudes de ondas centimétricas, con el objetivo de detectar lineas de emisión de CO (low-J) en HDF850.1, cuyo corrimiento al rojo se predice es ∼4.1. Aún cuando no se tuvo éxito en dicha búsqueda debido a limitaciones instrumentales, se conluyó que futuras búsquedas de lineas de emisión (high-J) en ondas milimétricas serán más exitosas debido a la densidad y la alta temperatura del medio gaseoso en estos objetos. Una vez que sea posible estimar los corrimientos al rojo de estas galaxias, se podrán llevar a cabo estudios de las condiciones físicas responsables por la naturaleza extrema de éstas mediante observaciones de otras moléculas. En esta tesis también presento la primera detección de HCN J=5-4 y [CI] J=1-0 en un objeto con alto corrimiento al rojo, APM 08279+5255, un quasar ultraluminoso amplificado por lentes gravitacionales a z=3.91. Esta detección de HCN J=5-4 es la primera que se ha hecho en objetos extragalácticos. Se encontró que la luminosidad de la linea [CI] predice densidades de gas molecular consistentes con los valores estimados a partir de la luminosidad de linea del CO J=1-0. La luminosidad de linea de HCN J=5-4 es un factor de 10 mayor que lo esperado, lo cual puede deberse a excitación radiativa producida por fotones infrarrojos provenientes del AGN central. El último estudio de estructura a gran escala presentado en esta tesis utiliza el bosque Lyα de lineas de absorción de HI, en espectros simulados y observados de objetos cuasi- estelares (QSOs), con el objetivo de explorar el impacto

que tiene la presencia de AGNs y galaxias extremadamente luminosas y con alta taza de formación estelar a alto corrimiento al rojo, en el gas de su entorno local. Se encontró que 20–40% de la contribución al campo de radiación ionizante de HI a z$\sim$2.5–3.5, se debe muy probablemente a fotones UV provenientes de galaxias con formación estelar, y no solo a QSOs como se creia hasta hace poco.

En el desarrollo de estos estudios de galaxias a alto corrimiento al rojo y la estructura a gran escala se utilizaron instrumentos en facilidades de nivel mundial. Actualmente estoy preparando estudios similares con la siguiente generación de interfermetros y telescopios, los cuales aumnetarán en un orden de magnitud la sensitividad en la detección del continuo y las lineas de emisión molecular de estos trazadores de la formación de estructura y su evolución.

To those who gave praise when due, but mainly to those who helped push when needed ...

Contents

List of Figures

List of Tables

Acknowledgments

I am grateful for financial support from the Departments of Astrophysics and Docencia at INAOE, and the predoctoral fellowship grant generously awarded by the SAO. Though I accept responsibility for much of the work presented in this thesis, the quality results presented here are due to the guidance of many excellent teachers that I have learned from along the way. These people should all be listed as coauthors on the cover of this thesis.

Without a doubt, the first person I wish to thank is my advisor, David Hughes, for sharing not only his excellent cooking, but moreover his knowledge of astronomy, public presentation, and passion for this branch of science. Despite all of his other obligations, he has never been known to turn away a student in need of help. I also wish to thank my predoctoral fellowship advisor at the Harvard-Smithsonian CfA, David Wilner, for helping me to understand mm-wavelength interferometry and diplomacy. Likewise, in addition to being one of the busiest researchers I have met, he never fails to make time for his students.

Collaborative work with Enrique Gaztañaga has been one of the highlights of my time at INAOE. Along with great discussions on cosmology, knowing that if I sent a result at 1:00 AM he would send comments by 1:10 AM made working with him a real pleasure. Although I thank all of the INAOE professors and staff, I would particularly like to thank Itziar Aretxaga, Guillermo Tenorio-Tagle and Bill Wall for stimulating and imaginative scientific discussions. The students at INAOE have given both friendship and inspiration. I hope, and expect that their kindness will be returned if ever they find themselves visitors to Canada. During the final year of my studies, Alfredo Montaña has been a great friend while providing the support needed to complete this work. Whenever Alfredo was not around, I could equally depend on Juan de Dios. Thank you.

The quality of this thesis has been improved thanks to the constructive comments provided by my examiners, Luc Binnette, Phil Appleton, Laurent Loinard, Vladimir Avila-Reese, Manolis Plionis, Itziar Aretxaga and Guillermo Tenorio-Tagle. Thank you all.

During my time as an undergraduate student at the University of Victoria, I benefited from the imagination and mathematical genius of Arif Babul, and the teachings of Julio Navarro, who first inspired my interest in the formation and evolution of large-scale structure. Russ Rob and Stephenson Yang introduced me to the art of observing. While on Co-op terms at the JAC

in Hawaii, Elese Archibald, Tim Jenness, Ean Robson, Remo Tilanus and Frossie Economou initiated me in both submm-wavelength astronomy and computer programming. I am fortunate to have carried out my undergraduate studies accompanied by a group of brilliant, motivated, and supportive students. In addition to being a close friend, Louis Desroches taught me that greatness can be accompanied by humility. Thank you.

Often our studies are aided indirectly by the words and actions of close friends. To those friends who will always be there, my siblings Will, Lisa, Florent, Faye, Mikey and Carmen, I say thank you for adding so much humour and love to this life. For the incredible experience of living in Mexico, I owe my gratitude to Ed, Leo, Paige, Alfredo, Oscar, Victor, Adi, Yesica, Pablo, Dan, Michael, Megan, Kelly and Pancho.

Of course, none of this would have been possible without the love and support of my family back in Canada. My interest in astronomy was first sparked by the late Donald Wagg, who pointed out constellations and satellites on a moonless night. Through his actions, the late William Ashby taught me that we should not take ourselves too seriously in this life. Dorothy Wagg demonstrated that if one maintains a passion for knowledge, even a 75 year-old can quickly master the internet. Meanwhile, Dorothy Ashby showed me that one can see and understand the politics of the world, without the aid of sight or a PhD in political science. From Gert and Lynn Aikman I have learned that hard work must be balanced by laughter and relaxation, as these are the key to longevity. I thank my aunts and uncles, Carol, Randy, Barry, Kirsty, Rick, Wendy, Ian, Leslie, Dave, Carol, Donna, Danny and Chris, for all of their love and teachings throughout the years.

As for my immediate family, my younger siblings, Ian and Allison, have been a true inspiration for me, and words are not sufficient to express how proud I am of each of them. From the beginning, Barbara Wagg has unselfishly put the desires of her children in front of her own, and should take credit for all of their accomplishments. Finally, I wish to thank Brian Wagg for telling a 5 year-old wanting to know if they could build a robot; “We can do anything we put our minds to.”.

Chapter 1

Introduction

Despite the advances made in recent years toward a coherent and self-consistent model of cosmological structure formation, most of the energy density of the Universe ($\sim$95%) is in an unknown form. Over 2000 years ago, the ancient Greeks believed that all of the matter in the Universe could be composed of some combination of the four elements; "Earth", "Air", "Fire" and "Water". When it became clear that certain phenomena could not be explained using these elements alone, they imagined the existence of a fifth element: "quintessence". Ironically, the model of our Universe that we adhere to today suggests that most of the mass is in the form of some mysterious "dark matter", while the energy density is thought to be dominated by a "dark energy", often referred to as "quintessence".

Given the uncertainties in our knowledge of the contents of the Universe in which we live, it is truly amazing the accuracy with which the predictions of the currently favoured Λ Cold Dark Matter (ΛCDM) are being confirmed through observed characteristics of the large-scale distribution of matter in both nearby and distant structures. Two recent examples of this success stand out prominently:

The first is illustrated by the agreement between theory and observation in the power spectrum of cosmic microwave background (CMB) temperature fluctuations measured over the entire sky by the Wilkinson Microwave Anisotropy Probe (*WMAP*; Bennett et al. 2003; Spergel et al. 2003, 2006). Figure 1.1 illustrates the quality of both the data, and corresponding power

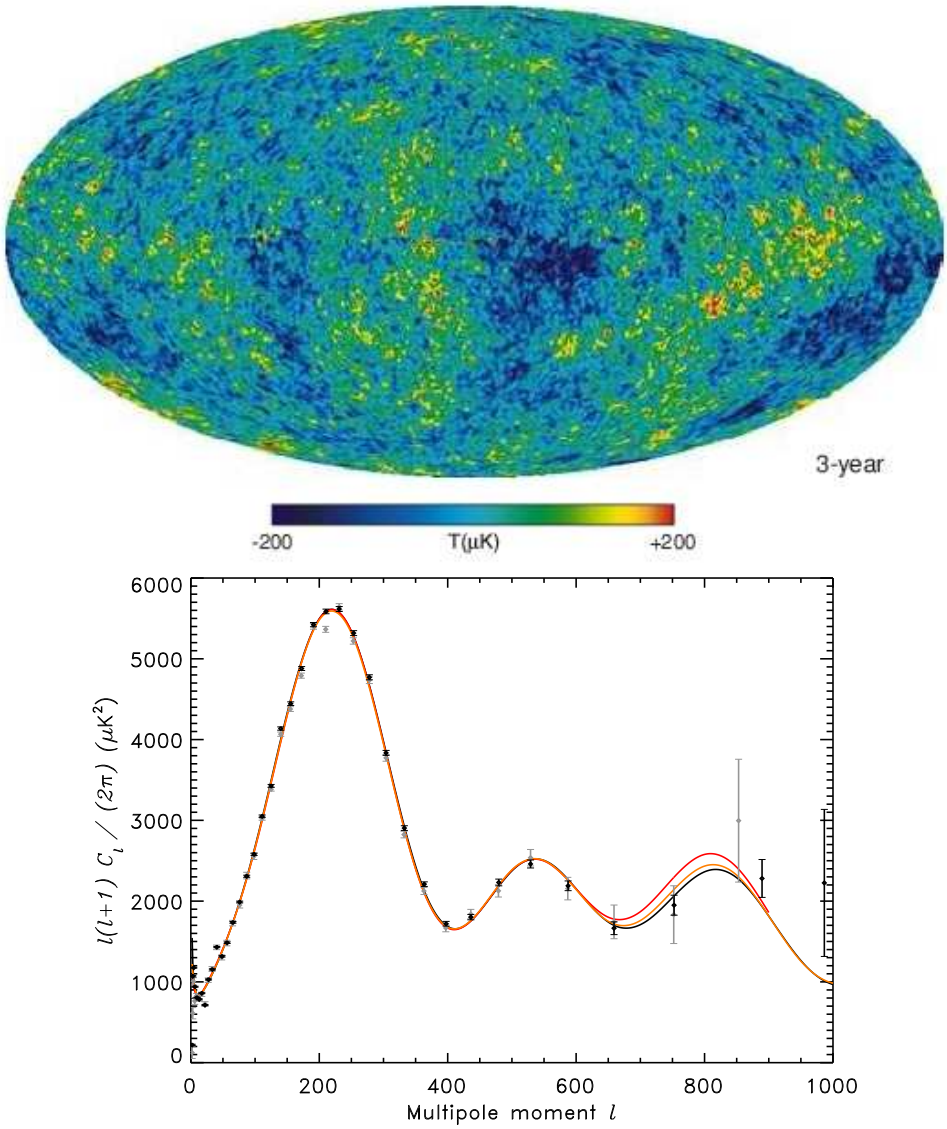

Figure 1.1: *top:* Foreground cleaned map of CMB temperature fluctuations measured in the 3-year WMAP data (Hinshaw et al. 2006). (*bottom:*) The power spectrum of CMB temperature fluctuations calculated from both the 1-year (grey symbols) and 3-year (black symbols) WMAP data (Spergel et al. 2003, 2006). The red line is the bestfit ΛCDM model for the 1-year data while the orange line has been fit to the 1-year data combined with measurements at high multipoles (small angular scales) from the Cosmic Background Imager (CBI; Padin et al. 2002) and Arcminute Cosmology Bolometer Array Receiver (ACBAR; Kuo et al. 2002). The incredible level of agreement between the predictions of the ΛCDM model and the observed data on large angular scales ($\ell < 600$) was well emphasized by Dr. Carlos Frenk during a lecture at the 2006 LENAC advanced summer school in Foz do Iguacu; "If as a student, you are not excited by this result you should quit now and go become a banker, because this is science at its finest!".

spectrum. A second recent success of the ΛCDM model is the detection of an acoustic peak on scales of ∼150 comoving Mpc in the power spectrum of density fluctuations traced by low-redshift ($\bar{z} \sim 0.3$), luminous red galaxies (Eisenstein et al. 2005) in the first 3816 sq. degrees of the SLOAN Digital Sky Survey (SDSS; York et al. 2000). The ΛCDM model predicts that such a peak in the power spectrum of present-day matter density fluctuations (as traced by galaxies) would reflect the evolution of fluctuations on scales of the first acoustic peak ($\ell \sim 220$, or $\sim 1^o$) observed in the CMB temperature power spectrum (e.g. Figure 1.1).

One reason that I have chosen to highlight these two particular observational tests of structure formation models, is that they rely on data acquired over two very different wavelength regimes. The microwave observations which led to the spectacular all-sky CMB maps produced by *WMAP*, could only have been achieved outside the Earth's atmosphere from a balloon-borne, or space-based observatory, as strong thermal emission from atmospheric water-vapour at these wavelengths severely limits sensitivity and accessible frequency range. The atmospheric transparency is much higher at optical wavelengths, meaning that photometric and spectroscopic surveys such as SDSS, can produce wide-area (∼1000 square degrees) maps in only a few years, which are sufficiently sensitive to allow for the detection of the aforementioned peak in the power spectrum of galaxy fluctuations. Hence, without the development of expertise and technological advancement in these two fields of astronomy, a beautiful confirmation of a prediction by the ΛCDM, big-bang model of the Universe would not have been possible.

Another important reason for discussing the *WMAP* results in conjunction with those of the SDSS, is that these experiments measure the spatial characteristics of matter at two very different epochs: *i)* when the Universe was approximately 10^5 years old, and *ii)* when the Universe was closer to 10^{10} years old. Given that such a large cosmic timescale separates these two epochs, alternative multi-wavelength observing methods are needed to measure the growth of structure *on all scales* over this interval in order to test the predictions of ΛCDM structure formation models. As such, the work in this thesis explores some complementary methods of quantifying the growth of large-scale structure over the redshift interval $1 \lesssim z \lesssim 1000$. Although many avenues are not covered here, the aim of this work is to emphasize the complementarity that exists between older, and more recent multi-wavelength observational windows on structure formation at high-redshift.

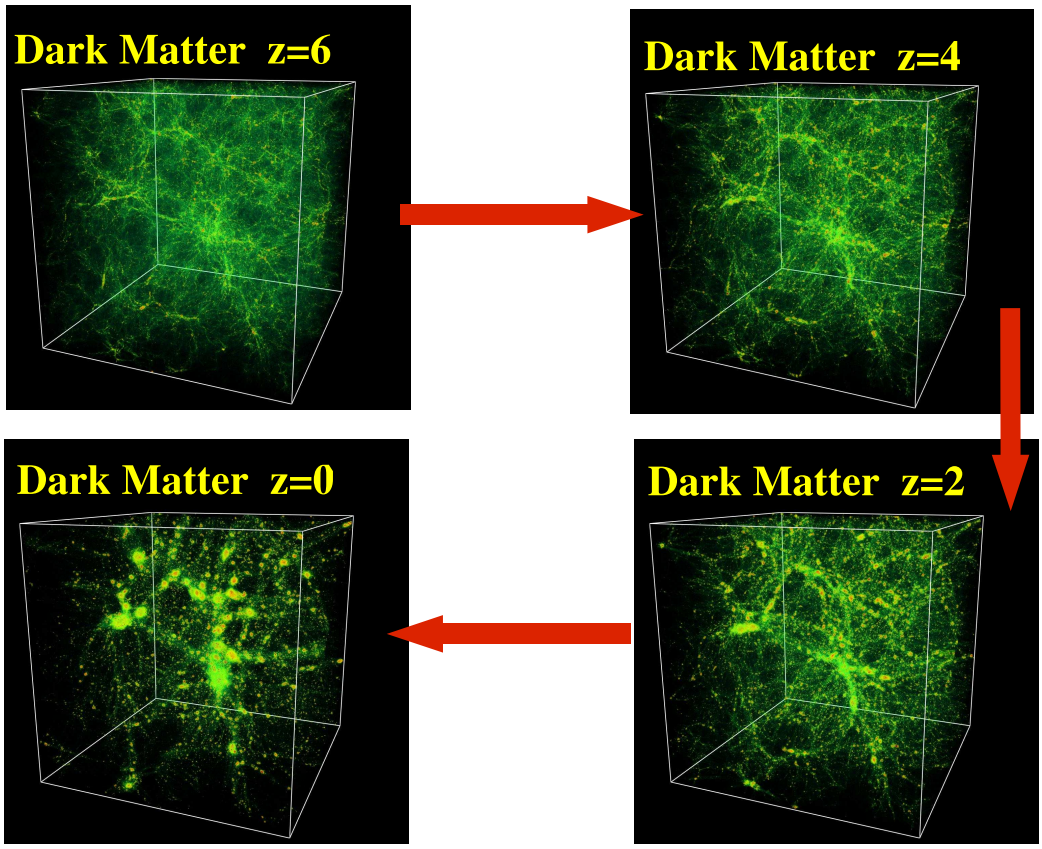

Figure 1.2: The evolution of the dark matter distribution predicted by a simulation of a ΛCDM Universe (simulation by Renyue Cen). These simulations nicely illustrate the sheets and filaments in the mass distribution which are traced by the *luminous* phenomena discussed in this thesis.

1.1 Observational Tracers of Large-scale Structure at High Redshift

Although ∼85% of the mass in the Universe is in the form of some unknown "dark matter" governing the gravitational evolution of large-scale structure (e.g. Figure 1.2), modern-day astronomical instruments are only sensitive to phenomena which interact with radiation. As such, when studying the evolution of structure it is important to fully understand the physical processes which affect the spatial distribution of the observable matter in order to understand the biases which may influence inferred measurements of the underlying mass distribution. For example, "voids" in the high-redshift distribution of neutral Hydrogen gas (on scales of a few Mpc), may be due to true underdensities in the distribution of dark matter traced by the gas, or else the result of material being swept up or ionized by winds from active galaxies (e.g. Babul 1991). In order to determine the probability of the latter, one must study the physical conditions within galaxies and AGN at high-redshift to assess the prevalence and strength of outflows or ionizing radiation.

Before further discussion on the observational windows that may be exploited to study structure at high-redshift, I would like to digress to a brief description of some of the mathematical tools which are often used to quantify the spatial distribution of various forms of matter in the Universe.

1.1.1 Statistical Tools

Before describing a few of the observed multi-wavelength phenomena which may be surveyed to trace large-scale structure at high-redshift, it is helpful to define some common statistical tools and techniques, which are applied directly to an analysis of CMB temperature fluctuations in the next Section.

Within a given survey area, any point on the spherical surface (defined by a unit vector $\hat{k}_i$) may be described by the surface density of a particular class of object:

$$\delta_i(\hat{k}_i) = \frac{n_i}{\bar{n}} - 1, \tag{1.1}$$

where n_i represents the number of these objects at position $\hat{k}_i$, and $\bar{n}$ is the mean number within the area surveyed. The statistical quantity that is then

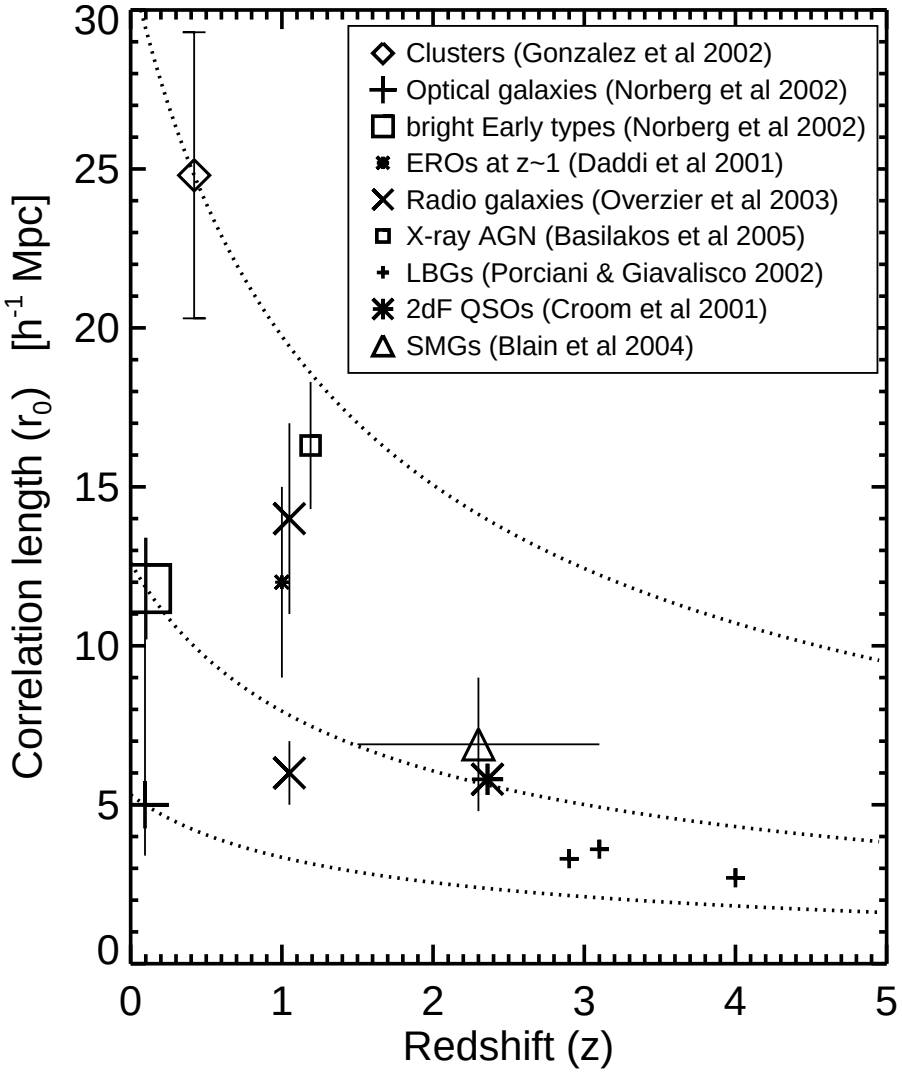

Figure 1.3: The redshift evolution of the characteristic clustering scale length as traced by different populations of objects. The *dotted lines* show the predictions of a stable clustering model from Carlberg et al. (2000) normalized to three different low-redshift samples.

measured was first applied to surveys of extragalactic objects in the 1930s (see review by Peebles 2001), and is commonly referred to as the N-point correlation function:

$$\xi_N(\theta) = \langle \delta_i \; \delta_{i+i} \; ... \; \delta_N \rangle_\theta \, . \tag{1.2}$$

For now, I will only consider the two-point correlation function, ξ_2, which can be translated from a function of angular scale to a function of comoving separation, r, by inclusion of the redshift dimension. For most galaxy samples, the two-point correlation function can be described by a power-law,

$$\xi_2(r) \propto \left(\frac{r}{r_0} \right)^{-\gamma}, \tag{1.3}$$

where r_0 is the correlation length plotted in Figure 1.3. This Figure shows how the growth of structure may be determined through measurement of the correlation function for populations at various redshifts. It is therefore apparent that combining the results of multi-wavelength surveys, sensitive to different populations of objects, can provide a means of measuring the evolution of the distribution of *luminous* matter with redshift.

An important concept that will appear in this thesis is that of *bias*, which effectively quantifies the spatial clustering of some form of *luminous* matter (galaxies or gas) with respect to either another form of luminous matter, or to the underlying *dark* matter. For example, Figure 1.7 illustrates how the distribution of gas (H and He) in the Universe is predicted to exhibit the same filamentary structure as the underlying distribution of dark matter (believed to dominate the mass), due to the lower-mass gas component being biased towards more dense regions. Quantitatively, the bias, b, is defined such that it relates the overdensity of a particular tracer (such as galaxies), to that of the underlying mass distribution,

$$\delta_{\rm tracer} = b \; \delta_{\rm mass}. \tag{1.4}$$

Using the language of the two-point correlation function, the bias also relates the correlation function of a particular class of object (such as galaxies), to the correlation function of dark matter:

$$\langle \delta_G \; \delta_G \rangle = b^2 \, \langle \delta_{DM} \; \delta_{DM} \rangle \, . \tag{1.5}$$

This bias factor will be larger for more massive objects, such as massive cD elliptical galaxies ($\sim 10^{13}$ $M_\odot$), than for lower mass objects such as dwarf

galaxies ($\sim 10^7$ $M_\odot$). A probable reason for this is that within the favoured hierarchical galaxy formation scenario, large galaxies form via mergers of smaller galaxies, and so the most massive galaxies likely exist in higher density environments (such as rich clusters). The existence of such high density environments reflects the presence of massive dark matter haloes, which consequently produce large gravitational potential wells. The most massive galaxies are more likely to be located near the centers of these large gravitational potentials, and therefore will be more highly biased.

1.1.2 Temperature Fluctuations in the CMB

From an observational perspective, structure formation begins with the temperature fluctuations observed in the CMB, reflecting a time when the Universe was cool enough that protons and electrons could recombine to form Hydrogen atoms, leaving the photons free to stream away. These photons carry with them a snapshot of the density enhancements which later grew to define the present-day large-scale distribution of matter.

Prior to the results of the all-sky CMB survey conducted by the *WMAP* satellite (Bennett et al. 2003), there remained a number of outstanding questions related to the statistical nature of these temperature fluctuations. With this statement I do not wish to diminish the incredible achievements of groud-based and balloon-borne experiments such as QMAP (Devlin et al. 1998), BOOMERaNG (de Bernardis et al. 1999) and MAXIMA (Hanany et al. 2000), as these were designed to measure CMB fluctuations on small angular scales and over small survey areas. Unrestricted by observing duration, sky coverage, or the effects of Earth's atmosphere, *WMAP* would measure temperature fluctuations over the entire sky, a feat that no experiment had accomplished since the *COBE* satellite (Bennett et al. 1996). Although many of the outstanding questions centered around constraining a subset of the cosmological parameters defined in Table 1.1 (Spergel et al. 2003, 2006) that define the energy content of our Universe within Einstein's theory of general relativity, two outstanding problems were related to the large-scale density fluctuations that would be measured by *WMAP*.

The first problem had to do with the $l = 2$ mode (the quadrupole) in the power spectrum of CMB temperature fluctuations. The *COBE* measurement had shown that the amplitude of the quadrupole was lower than that predicted by CDM models (Hinshaw et al. 1996a). Whether or not this low amplitude was due to residual foreground contamination (e.g. Galactic fore-

grounds such as synchrotron or dust emission, or extragalactic foregrounds such as distant galaxies), or was truly cosmological in nature, was uncertain. This question could be addressed by the *WMAP* experiment, whose multi-frequency maps would make it easier to model and subtract foregrounds of non-cosmological origin.

The second outstanding question was related to the Gaussianity of the amplitudes of fluctuations on the largest, and the smallest scales. Most models of inflation predict that the quantum fluctuations, which later gave rise to the structure in the Universe *on all scales*, should be Gaussian (see review by Bartolo et al. 2004). However, this prediction had yet to be sufficiently tested on large-scales with *COBE* (Kogut et al. 1996), while the constraints on departures from Gaussianity at small angular scales (e.g. Wu et al. 2001; De Troia et al. 2003) were limited by "Cosmic Variance" due to the small areas surveyed. Non-Gaussian characteristics (such as skewness) should affect the structure and substructure within dark matter haloes (Avila-Reese et al. 2003). Such characteristics could also affect the rate at which the first high-redshift structures grew (e.g. Mathis, Diego, & Silk 2004), and therefore the formation epoch of the first luminous objects in the Universe.

In Gaztañaga et al. (2003) and Gaztañaga & Wagg (2003) we address the aforementioned problems using the *WMAP* data and the correlation functions formally described in the previous Section. In order to compare with the observed V-band (61 GHz) *WMAP* data[1], we generated 2000 mock CMB maps realized from the best-fit temperature power spectrum of Spergel et al. (2003; see Figure 1.1). The theoretical power spectra are generated using the publicly available CMBFAST package (Seljak & Zaldarriaga 1996) where the C_ls are normalised to the COBE spectra and the input parameters are listed in Table 1.1. Along with the cosmological parameters, CMBFAST accepts a reionization optical depth, τ, and the scalar spectral index, η_s. This power spectrum is then used as input to the HEALPix[2] package (Górski, Hivon & Wandelt 1999), which generates all-sky CMB maps.

We estimate both $\xi_2(\theta)$ and $\xi_3(\theta)$ from the observed and simulated pixel maps following:

$$\xi_2(\theta) = \frac{\sum_{i,j} \delta_i \delta_j \; w_i \; w_j}{\sum_{i,j} w_i \; w_j}, \tag{1.6}$$

[1]Both the real V-band map and simulated CMB maps have been filtered according to the KpO mask, which removes pixels believed to contain significant Galactic and extragalactic foreground contamination.

[2]http://www.eso.org/science/healpix/

Table 1.1: CMBFast Cosmological Parameters

Parameter	Value	Definition
H_0	72 km/s/Mpc	Hubble expansion factor
Ω_b	0.046	Baryon density
Ω_c	0.224	Cold dark matter density
Ω_Λ	0.730	Dark energy density
Ω_k	0.0	Spatial curvature
τ	0.17	Optical depth to reionization
η_s	1.0	Scalar spectral index

and

$$\xi_3(\theta_{12}, \theta_{13}, \theta_{23}) = \frac{\sum_{i,j,k} \delta_i \delta_j \delta_k \; w_i \; w_j \; w_k}{\sum_{i,j,k} w_i \; w_j \; w_k}, \tag{1.7}$$

where δ_i, δ_j and δ_k are the temperature differences in the map, and the sum extends to all pairs separated by $\theta \pm \Delta\theta$. The weights w_i can be used to minimise the variance when the pixel noise is not uniform, but this introduces larger cosmic variance. In our analysis we follow the *WMAP* team and use uniform weights (i.e. $w_i = 1$).

Figure 1.4 compares ξ_2 calculated from the V-band *WMAP* data with that calculated from the simulated CMB maps. An individual model is compared with the data using a χ^2 test. A modified version is adopted by employing the covariance matrix which accounts for the bins being correlated:

$$\chi^2 = \sum_{i,j=1}^{N} \Delta_i \; C_{ij}^{-1} \; \Delta_j, \tag{1.8}$$

where $\Delta_i \equiv \xi_2^O(\theta_i) - \xi_2^M(\theta_i)$ is the difference between the "observation" O and model M. The differences are normalised so that $\langle \Delta_i \rangle = 0$. The distribution of χ^2 values is shown in Figure 1.4 and it is apparent that the data are in good agreement with the simulations. This result is used in Gaztañaga et al. (2003) to show that the $\ell = 2$ mode (the quadrupole) measured by *WMAP* has a $\sim$30% probability within the ΛCDM model, compared to a probability $p \sim 10^{-5}$ originally determined by Spergel et al. (2003). A result similar to ours has been found by Efstathiou (2003; 2004).

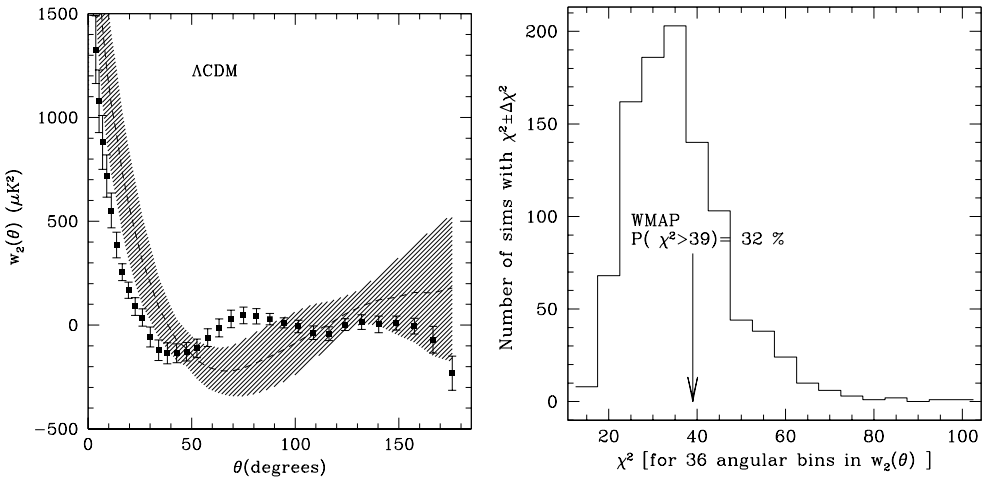

Figure 1.4: *Left:* The two-point angular correlation ξ_2 in the WMAP V-band data compared to the 2000 ΛCDM simulations (shaded region corresponds to 1-σ error dispersion; Gaztañaga et al. 2003). *Right:* Number of ΛCDM simulations with given values of χ^2 in Eq.1.8 using the covariance matrix from the same ΛCDM simulations. The same test for *WMAP* gives: $\chi^2 \simeq 39$ (shown by the arrow), which is below 32% of the simulations.

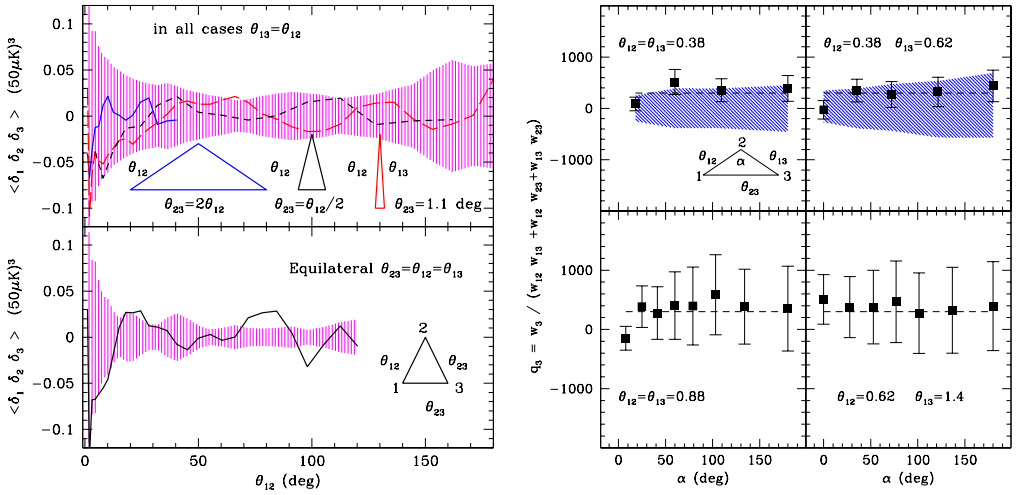

Figure 1.5: three-point function $\xi_3 = w_3 =< \delta_1\delta_2\delta_3 >$ at large angular scales of temperature fluctuations in the *WMAP* CMB maps. *Bottom left* panel shows w_3 for equilateral triangles as a function of side θ_{12}. The *top left* panel shows results for isosceles triangles $\theta_{13} = \theta_{12}$ with $\theta_{23} = 1.1^o$ (long dashed line), $\theta_{23} = \theta_{12}/2$ (short dashed line) and $\theta_{23} = 2\theta_{12}$ (continuous line), in all cases as a function of side θ_{12}. Shaded regions are for the 68% confidence levels estimated using jackknife errors. *Right:* Reduced three-point function q_3 at small angular scales. Different panels show configurations with triangles of fixed sides θ_{12} and θ_{13} (as labeled in each panel) and variable θ_{23} which is given by the interior angle α between θ_{12} and θ_{13} ($\alpha = 0$ corresponds to $\theta_{23} = 0$ and $\alpha = 180$ corresponds to $\theta_{23} = 2\theta_{12}$). Shaded regions are for the 68% confidence levels estimated using low amplitude Quadrupole ΛCDM simulations (see Gaztañaga et al. 2003; Gaztañaga & Wagg 2003).

Gaztañaga & Wagg (2003) test the Gaussianity of the CMB temperature fluctuations on large angular scales using the three-point angular correlation function, ξ_3. The three-point function can be normalized to either a dimensionless amplitude:

$$d_3 \equiv \frac{\xi_3}{(\xi_{12}\ \xi_{23}\ \xi_{13})^{3/2}} \tag{1.9}$$

where $\xi_{ij} = \xi_2(\theta_{ij})$, or a hierarchical amplitude:

$$q_3 \equiv \frac{\xi_3}{\xi_{12}\ \xi_{23} + \xi_{12}\ \xi_{13} + \xi_{23}\ \xi_{13}}. \tag{1.10}$$

The results of calculating these statistics from the V-band *WMAP* data, with uncertainties determined using the simulated maps, are shown in Figure 1.5, implying that the data are indeed consistent with the Gaussian initial condition hypothesis over scales ranging from 180^o to smaller than 1^o. This result is consistent with those first presented by Komatsu et al. (2003), who calculate the bispectrum in Fourier space, which is effectively an average over all triangle configurations.

CMB analyses such as those discussed here are required to constrain the initial conditions, or "seeds" of structure in the Universe. Evolutionary scenarios argue that once these "seeds" were planted, the Universe should have continued to evolve following the dynamics governed by the cosmological parameters, while structure grew on all scales under the influence of gravity. In order to motivate the work presented in this thesis, I now discuss some additional observational phenomena which may be exploited to study this evolutionary process of structure formation in greater detail.

1.1.3 Luminous Galaxies and AGN

While the CMB temperature fluctuations mainly reveal the initial conditions for structure formation, mapping the distribution of *luminous* matter at high-redshift can provide constraints on how the growth of structure evolves with cosmic time. Traditionally, high-redshift galaxies and AGN are detected at optical wavelengths, and in an era of 8 to 10 m diameter optical telescopes, spectroscopic confirmation of $z > 5$ objects is now becoming routine[3]. Op-

[3]The record is tentatively held by a $z \sim 10$ galaxy discovered behind a lensing cluster (Pelló et al. 2004) using colour selection techniques which exploit the 912 Å (rest frame)

tical surveys, such as the SDSS and the 2-degree Field Survey (2dF; Colless 1999), have been very successful at mapping the distribution of luminous matter at low-redshifts ($z \lesssim 0.5$). By cross-correlating the spatial distribution of this matter with the CMB temperature fluctuations (Fosalba & Gaztañaga 2004; Scranton et al. 2003), a detection of the integrated Sachs-Wolfe effect (Sachs & Wolfe 1967) has provided an independant confirmaton of the existence of dark energy. Due to the effects of cosmological dimming, optical surveys become increasingly sensitive to *only* the most luminous, and consequently rarer objects at higher redshifts. This selection effect may be advantageous if using these samples to study structure formation, as the most luminous objects are often biased towards the high-density peaks in the matter density distribution, as in the case of luminous red galaxies (Eisenstein et al. 2005). It is important therefore to explore the potential for multi-wavelength data to reveal new populations that could potentially trace structure over a wide-range of redshifts ($1 \lesssim z \lesssim 1000$).

One alternative method for probing structure at high-redshifts ($z \sim 2-5$) is through multi-wavelength observations of luminous radio galaxies (West 1994). The first 850 μm observations of these objects (Dunlop et al. 1994; Hughes et al. 1997; Ivison et al. 1998, 2000; Archibald et al. 2001) suggested high rates of dust-enshrouded star-formation, while submm imaging of the surrounding regions (Stevens et al. 2003) revealed a significant excess of bright objects relative to that predicted by the number counts of blank-field submm sources, (discussed below). If these serendipitously discovered bright submm sources lie at similar redshifts to the adjacent radio galaxies, and the high far-infrared luminosities are the result of star-formation induced by galaxy mergers being more frequent in the fields, then these regions are likely to represent proto-cluster environments. As such, targeted observations of suspected high-density tracers, such as these powerful radio galaxies (e.g. Hughes et al. 2006 in preparation; see Figure 1.6), provide a means of surveying massive structures at high-redshift.

Along with the luminous high-redshift radio galaxies, a new population of objects discovered in blank-field submm/mm extragalactic surveys (Smail, Ivison & Blain 1997; Hughes et al. 1998; Barger et al. 1998), may also be tracing dense regions of the mass distribution. These "submillimetre galaxies" (hereafter SMGs) appear to be very luminous in the rest-frame far-infrared, implying high star-formation rates (100 - 1000 $M_\odot$ yr^{-1}) in dusty galaxies

Lyman break spectral discontinuity (Steidel et al. 1996).

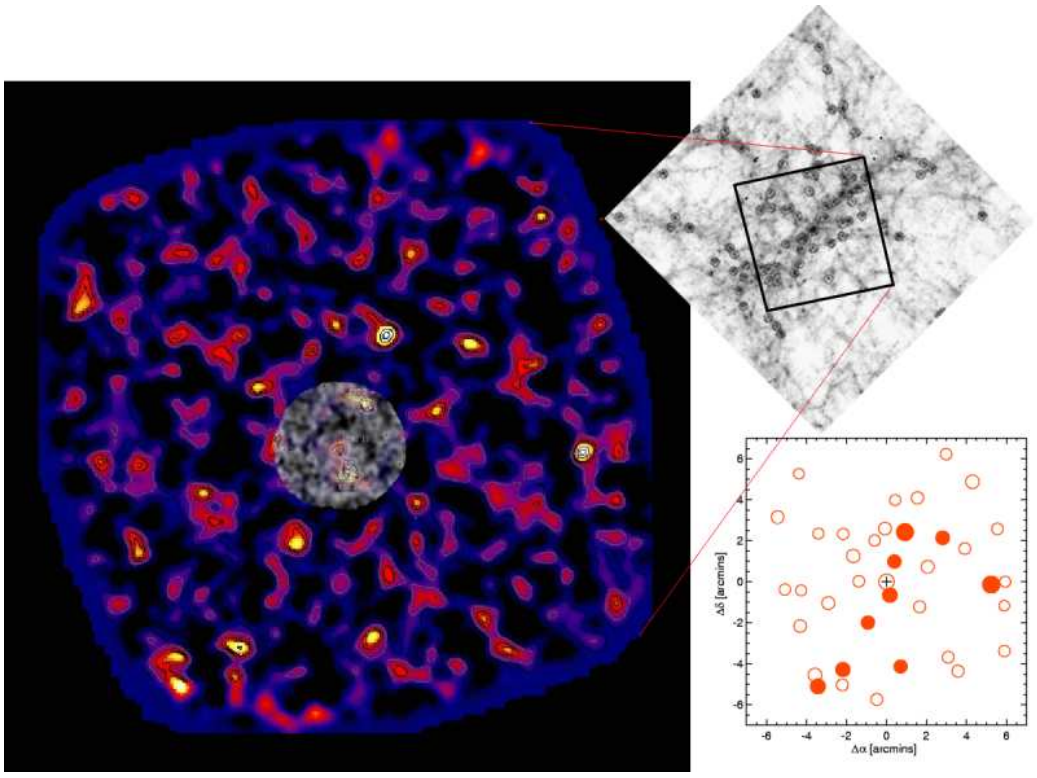

Figure 1.6: *(Left:)* 15'×15' AzTEC/JCMT 1.1 mm map of the region around 4C41.17, a z=3.8 radio galaxy suspected to be near the center of a large physical overdensity (Stevens et al. 2003). Under our assumed cosmology the AzTEC map samples a region ∼6.4×6.4 Mpc at z=3.8. Superimposed, in transparent black and white is the 5 sq. arcmin SCUBA image of the same field (Ivison et al. 2000). All 4 sources detected by SCUBA are confirmed by AzTEC. *(Top Right:)* A simulation of the progenitor of a rich cluster at $z \sim 3$ (Governato et al. 1998). The circles mark the positions of the most massive star-forming halos, some of which may appear as mm galaxies. The square marks the area of the AzTEC map. *(Bottom Right:)* Sketch of the location of 1.1mm AzTEC sources $<$ 6mJy (in empty circles) and high S/N $\geq$ 6 mJy sources (in solid circles) that trace a proposed proto-cluster filament (Hughes et al. 2006, in preparation).

at typical redshifts of $2-3$ (Chapman et al. 2003; Aretxaga et al. 2003)[4]. Based on similar co-moving number densities and clustering strengths (see Figure 1.3) it has been proposed that these objects represent an early phase in the formation of massive elliptical galaxies (Lilly et al. 1999; Scott et al. 2002), meaning that the SMGs may be highly biased tracers of the underlying mass distribution. Within this framework, wide-area submm/mm surveys of SMGs with single-dish submm/mm instruments ($\gg$1 sq. degree), or alternatively smaller area surveys using interferometer arrays, can be conducted in order to probe the galaxy distribution in dense regions at $z \gtrsim 1$.

Although it is appealing to think of the SMGs as the precursors to massive early-type galaxies, confirming this hypothesis requires larger area submm/mm surveys in order to constrain the number counts and clustering amplitude of this population. These outstanding problems are mainly related to the spatial and temporal distribution of the SMG population. Also important within the context of *observed* structure are the physical mechanisms responsible for the high far-infrared luminosities of the SMGs. Without optical spectra of a securely identified optical/infrared counterpart to an SMG, the most practical means of probing the molecular medium within these objects is through mm-wavelength spectroscopy of molecules such as CO and HCN.

Within the context of this work, the importance of understanding the physical characteristics of the various populations of luminous high redshift objects (i.e. star-formation rates, presence of outflows, dynamical masses, *etc.*) is that there remains a great deal of uncertainty regarding the sources responsible for the HI ionizing background at $z \gtrsim 2$. These objects may also be responsible for the feedback mechanisms which enrich the intergalactic medium (IGM) with metals early in the history of the Universe (e.g. Ellison et al. 2000). Over these redshifts, the most powerful means of quantifying the observed distribution of matter is through the Lyα forest of HI absorption lines. The distribution of HI gas in the IGM is likely the *only* observable means of tracing structure between the recombination epoch at $z \sim 1000$ and the reionization epoch at $z \sim 6-14$, the latter of which will soon be observable through low-frequency radio interferometry of the 21 cm transition of neutral Hydrogen. As such, a close link exists between studies of (un-

[4]The redshift distribution of SMGs remains the subject of intense study and debate, and the existence of a higher redshift population is entirely possible (e.g. Hughes et al. 2002).

)obscured objects at high-redshift, and the surrounding IGM.

1.1.4 The Co-evolution of Luminous Objects and the Intergalactic Medium

What is the impact of the most luminous high-redshift objects on the gas in their local environments? This question is most effectively addressed through studies of QSO absorption lines. Optical/ultraviolet spectroscopy of distant QSOs reveals a forest of absorption lines blueward of the redshifted 1216 Å Lyα emission line. Originally discovered by Lynds (1971), it is now generally accepted that this "Lyα forest" is due to absorption by neutral Hydrogen gas at different redshifts along the line of sight. The weak clustering strength of individual absorption lines relative to that of galaxies (Sargent et al. 1980), along with the power-law form of their distribution of column densities (Tytler 1987), implies that these absorbers have a common origin in the IGM. With the advent of large cosmological hydrodynamic simulations, the true context of the Lyα forest within the CDM structure formation scenario has been demonstrated. Simulations by Cen et al. (1993, 1994) showed that the Lyα forest arises naturally due to highly ionized HI gas ($n_{HI}/n_H \leq 10^{-4}$) in the IGM tracing the smoothly varying density field in the underlying dark matter distribution (Figure 1.7). Given that the observed strength of these absorption features does not suffer from cosmological dimming, they may be used as an unbiased probe of the $z > 2$ IGM, where most of the gas in the Universe should reside at this earlier epoch (e.g. Rauch 1998). At these redshifts the gas is likely kept warm ($\sim 10^4$ K) and ionized by UV photons from embedded objects, whose starburst and AGN activity has been fueled by IGM gas cool enough to collapse onto the early seeds of galaxies. Thus a synergy existed between luminous high-redshift objects and the surrounding IGM at these earlier epochs

1.2 Thesis Outline

The work presented in this thesis attempts to address a small fraction of the many outstanding problems related to the formation of large-scale structure, through the analysis and interpretation of observational data taken over wavelengths ranging from ∼4200 Å to ∼2 cm. These data do not only cover a broad range in wavelength, but also sample structure of various sizes and den-

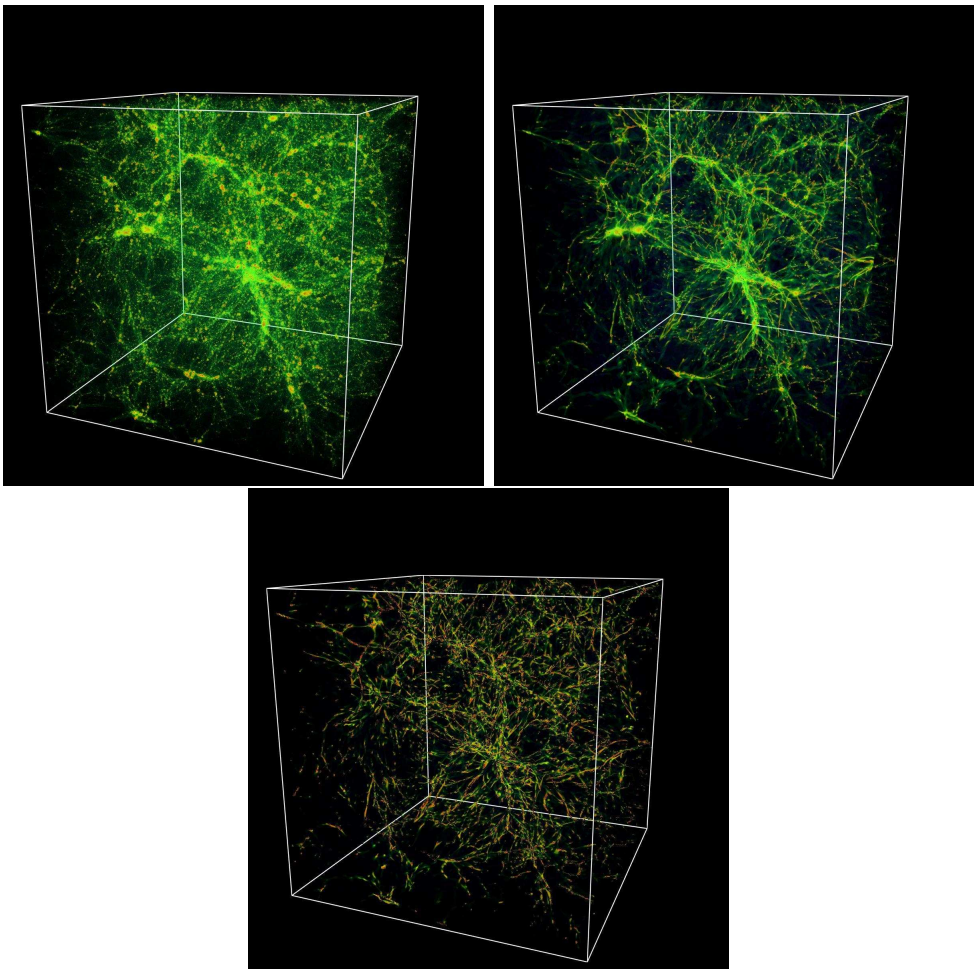

Figure 1.7: (clockwise from upper left) The simulated distribution of *i)* dark matter, *ii)* gas, and *iii)* neutral Hydrogen in a 25 Mpc comoving box at z=3 (simulation by Renyue Cen). The neutral Hydrogen component is believed to give rise to the Lyα forest of absorption lines observed in the optical/UV spectra of distant QSOs. This set of model predictions nicely illustrates how the sheets and filaments in the gas distribution should trace similar structures in the distribution of dark matter, as the overdensities in the gas are biased toward the overdense regions in the underlying mass distribution.

sities, from kpc scale fluctuations in the high-redshift intergalactic medium (IGM), to degree-scale anisotropies in the CMB radiation field. Combined studies of these various phenomena are required to build a coherent picture of the origin and evolution of structure in the Universe.

To begin, in chapter 2, I present an independent analysis and interpretation of the 850 μm survey data obtained as part of the SCUBA HAlf-Degree Extragalactic Survey (SHADES - PI: Jim Dunlop, Royal Observatory Edinburgh). SHADES is the largest single submm/mm survey conducted to date, with the primary goals of *i)* constraining the bright end of the number counts ($S_{850} \gtrsim$ 4-8 mJy), *ii)* measuring the spatial distribution of bright submm sources, and finally *iii)* constraining the redshift distribution for this population using photometric redshift techniques (e.g. Hughes et al. 2002; Aretxaga et al. 2003, 2005). Although a combined analysis of four independant reductions of the data is presented by Coppin et al. (2006), in this thesis I concentrate on the results of one of these reductions carried out at INAOE.

In addition to the independant analysis of the 850 μm data, I present a more detailed study of the complementary 450 μm maps of the two survey fields. As these data are of relatively poor quality[5], and a combined analysis of three independant reductions revealed acceptable agreement between only two of these, the relevance of these data has been down-weighted in Coppin et al. (2006). However, the 450 μm fluxes (or upper-limits) can provide powerful constraints on photometric redshift estimates for the SMGs.

Wide-area surveys can provide the source catalogues required to constrain the clustering strength of the bright SMG population, but the addition of accurate redshift information for these objects can be used to constrain both the global evolution of the obscured star-formation rate in the Universe, and add an extra dimension for constraining the clustering amplitude. Obtaining precise redshifts for SMGs has proven costly in terms of follow-up observing time on multi-wavelength facilities. Normally, deep 1.4 GHz radio interferometric imaging is used to identify the most probable radio counterpart(s) to the submm sources, which are then associated with optical/infrared counterparts (e.g. Ivison et al. 2002). Follow-up optical spectroscopy of these counterparts with 10 m class telescopes such as Keck, is then conducted in order to obtain SMG redshifts from rest-frame UV emission lines such as Hα

[5]The SHADES observations were conducted during non-optimal weather conditions, with 225 GHz zenith sky opacities in the range 0.05–0.10, while the atmospheric window at 450 μm is $\sim$6$\times$ more opaque than that at 850 μm.

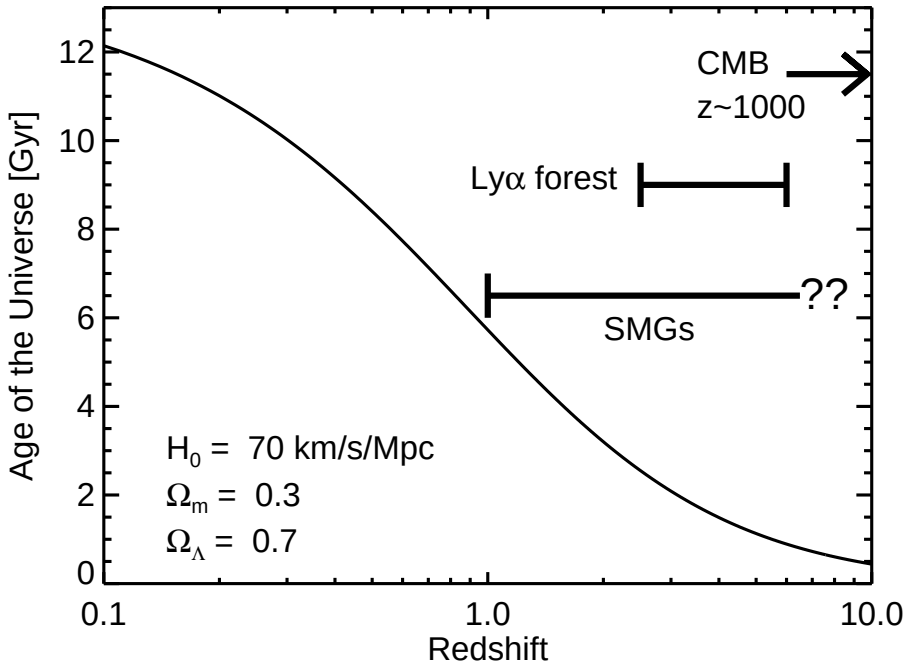

Figure 1.8: The age of the Universe as a function of redshift, adopting the parameters which define the ΛCDM model assumed throughout most of this work. I also plot the redshift intervals sampled by the various observational phenomena discussed in this thesis. As the submm galaxies (SMGs) discovered in blank-field extragalactic surveys (chapter 2) may potentially exist at redshifts $z > 6$, I denote the upper redshift limit of this population with '??'.

(Chapman et al. 2003, 2005). This process requires 10s of hours of observing time per object, so is not an efficient means of obtaining redshifts for the 1000s of objects that will be detected in upcoming surveys by facilities such as BLAST (Devlin et al. 2004), or the LMT (Serrano et al. 2006).

The far-infrared to radio photometric redshift technique, pioneered by Hughes et al. (1998), represents a more practical means of obtaining course redshifts ($\delta z \pm 0.3$) when observations of three or more fluxes at far-infared to radio wavelengths are available (Aretxaga et al. 2005). However, owing to the narrow bandwidths currently available with current submm/mm receivers, more accurate redshifts are required for follow-up studies of mm-wavelength emission lines such as [CI] and HCN (chapter 4), which can be used as diagnostic probes of the physical conditions in the gaseous medium of high-redshift SMGs. Given the relationship between far-infrared luminosity (or star-formation rate) and CO J=1-0 line luminosity (or molecular gas mass) observed in nearby galaxies (e.g. Young & Scoville 1991), the CO emission-lines, with rest-frame frequencies $\sim 115 \cdot J_{\rm upper}$ GHz, represent an ideal alternative for measuring redshifts of the far-infrared luminous SMGs. In chapter 3, I present the results of a broadband search for CO J=1-0 line emission in HDF850.1, the brightest submm object discovered in the confusion limited SCUBA/JCMT survey of the northern Hubble Deep Field (Hughes et al. 1998). This search with the 100 m Green Bank Telescope was motivated by the predictions of a photometric redshift technique, indicating a $\sim$90% probability that the CO J=1-0 line should emit in the frequency range of the $18.0 - 26.5$ GHz K-band receiver, corresponding to a redshift for HDF850.1 in the range $3.3 - 5.4$. Although the results of this experiment are found to be inconclusive, I discuss the potential for future wide bandwidth mm-wavelength spectroscopy of SMGs using telescopes such as the LMT, to rapidly obtain redshifts through simultaneous detection of multiple CO transition lines.

In chapter 4, I discuss the applications of observing various molecular emission line species in high-redshift objects, whose transitions are redshifted to submm-to-cm wavelengths. Given the sensitivities of current facilities, most of these species are only detectable in the most extreme, luminous high-redshift objects, possibly associated with denser regions of the matter distribution, as discussed earlier on. For this reason, the case study presented in chapter 4 is focused on the observation and interpretation of CO, HCN and [CI] line emission in the gravitationally lensed, ultraluminous quasar APM 08279+5255 at z=3.91. However, I conclude this chapter by discussing

the potential for upcoming facilities such as the Atacama Large Millimeter Array (ALMA) and the extended Very Large Array (eVLA), to detect these molecular emission line species in hundreds (or thousands) of less-luminous objects at high-redshift.

In chapter 5, I describe how studies of HI absorption lines in the optical spectra of high-redshift ($z \sim 3-4$) QSOs can be used to probe the UV radiation field and distribution of matter over the redshift interval $z \sim 2.5-3.7$. Determination of the background intensity of HI ionizing photons can provide clues as to the objects responsible for this emission, and, likely also those responsible for reionizing the Universe sometime between redshifts of 6 and 14 (Becker et al. 2001; Page et al. 2006). My analysis uses both high-resolution, high signal-to-noise QSO spectra, in conjunction with state-of-the-art ΛCDM hydrodynamic simulations, to show that, in addition to the UV photons emitted by luminous QSO at these redshifts, a significant contribution is also required from star-forming galaxies.

The final study presented in this thesis quantifies the spatial distribution of individual HI absorbers in both simulated and observed Lyα forest spectra. The purpose of this analysis is to determine if higher HI column density absorbers (typically found to be more metal rich; Ellison et al. 1999), exhibit stronger clustering than lower column density absorbers.

Unless otherwise stated, throughout this work I assume a Λ-dominated, cold dark matter cosmology (ΛCDM) with: $H_0 = 70$ km s^{-1} Mpc^{-1}, $\Omega_\Lambda = 0.7$, $\Omega_m = 0.3$ (Spergel et al. 2003, 2006; Sanchez et al. 2006).

Chapter 2

Blank-field (sub)mm wavelength surveys and the formation epoch of massive galaxies

2.1 Introduction

A powerful new window on galaxy and structure formation at redshifts, $1 < z < 10$, has been opened by the development of arrays of heat-sensitive bolometers operating at wavelengths between 250 μm and 3 mm. The first blank-field, extragalactic surveys at 850 μm with SCUBA (Holland et al. 1999) on the James Clerk Maxwell Telescope (JCMT), and also at 1.2 mm with MAMBO on the IRAM 30 m (Kreysa et al. 1998), have revealed that the far-infrared background radiation arises due to a population of dusty, high-redshift starburst galaxies (Smail, Ivison & Blain 1997; Hughes et al. 1998, Barger et al. 1998; Bertoldi et al. 2000; Scott et al. 2002; Borys et al. 2003; Greve et al. 2004; Laurent et al. 2005). The star-formation rates of these objects are inferred to be in the range 100–1000 $M_\odot$ yr^{-1}, which would be sufficient to produce the stellar mass component of a present-day, giant

elliptical galaxy. This interpretation is further supported by the agreement in the comoving number density of these two populations (Scott et al. 2002). If the submillimetre galaxies (hereafter SMGs) are truly massive galaxies undergoing their initial bursts of star formation, then hierarchical models of structure formation (described in chapter 1) would predict that the environments of these objects are most likely the overdense regions destined to evolve into massive, $M_c \gtrsim 10^{14-15}$ $M_\odot$, clusters of galaxies.

Detection of spatially resolved CO J=3-2 line emission on scales of $\sim$10 kpc in SMM J02399-0136 at z=2.8 (Genzel et al. 2003) demonstrated that SMGs contain large quantities of molecular gas (as inferred from the CO line-luminosity) within dynamically massive systems (as inferred from the CO line widths). Such observations were only possible using mm-wavelength interferometry, a relatively new observing technique which will be used to obtain the results presented in chapter 4. Comparison with the predictions of cosmological simulations that include galaxy formation implies that the number density of such obscured starburst galaxies, with baryonic masses $\geq 10^{11}$ $M_\odot$ at redshifts $z \sim 2.0 - 3.5$, may be as much as 15$\times$ greater than predicted by the models (see Figure 2.1). Although derived from comparison of an early generation of galaxy formation models with the observed properties of a small number of objects, such studies demonstrate the theoretical challenge posed by these new data, leading to exciting new insights as larger surveys and more advanced models become available in the near future.

A unique advantage of observing at (sub)mm wavelengths is that one may be equally sensitive to dusty starburst galaxies at $z = 1$, as to those at $z = 10$, making this wavelength regime a major focus for the next generation of planned telescopes and experiments. The physical mechanism behind this compensation for cosmological dimming, is that the far-infrared-to-mm spectral energy distribution of a far-infrared luminous galaxy such as Arp220 (thought to be representative of the SMG population), has a peak in intensity between rest-frame wavelengths of $\sim 60 - 100$ μm. This means that the SMG should exhibit a constant 850 μm flux density over the redshift interval $1 < z < 10$ (see Figure 2.2), making the SMGs an extremely powerful means of tracing structure in the high-redshift Universe.

The three main observables measured in an extragalactic (sub)mm wavelength survey are *i)* the flux densities of individual sources, *ii)* the number of sources with flux densities above a certain limit, and *iii)* the spatial distribution of sources. Each of these observables can provide clues as to the nature of the SMGs, and therefore the obscured star-formation rate at high-redshift.

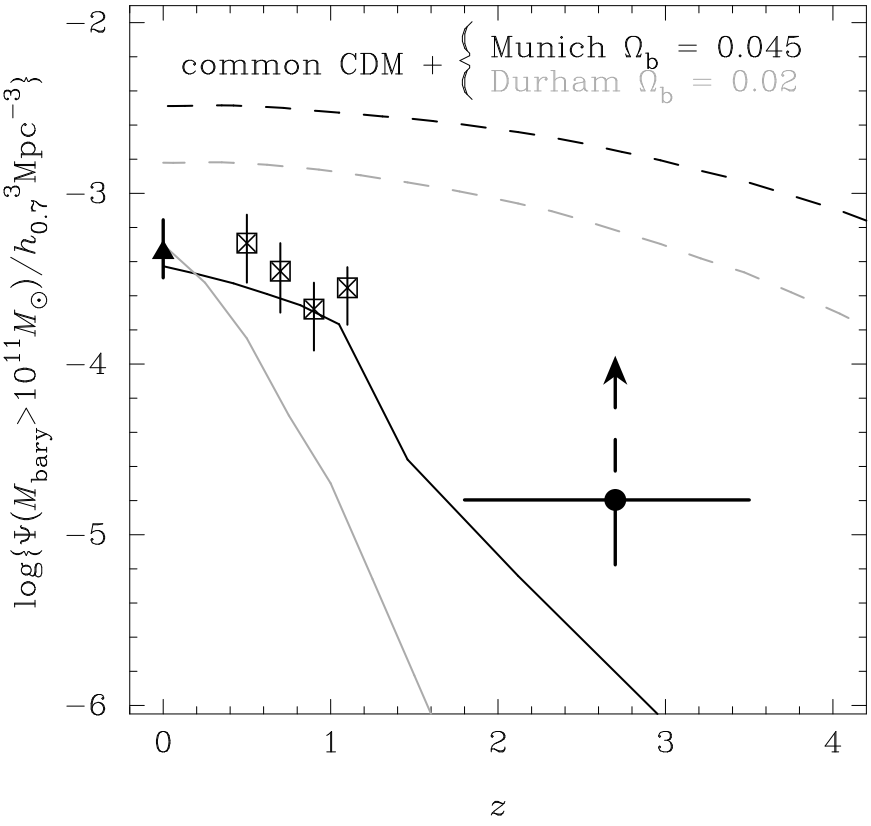

Figure 2.1: The co-moving number densities of high-mass objects (baryonic mass; $M_b \geq 10^{11}$ $M_\odot$) as traced by nearby 2dF and 2MASS galaxies with stellar masses $\geq 10^{11}$ $M_\odot$ (Cole et al. 2001) and high-redshift SMGs detected in CO line emission (Genzel et al. 2003). Also plotted are predictions by the semi-analytic models of two groups (Kauffmann et al. 1999; Baugh et al. 2003), with *dashed lines* showing the abundances of dark matter haloes containing *total* baryonic mass $\geq 10^{11}$ $M_\odot$, while the *solid lines* show the predicted number of starburst systems of the same mass (figure from Genzel et al. 2004).

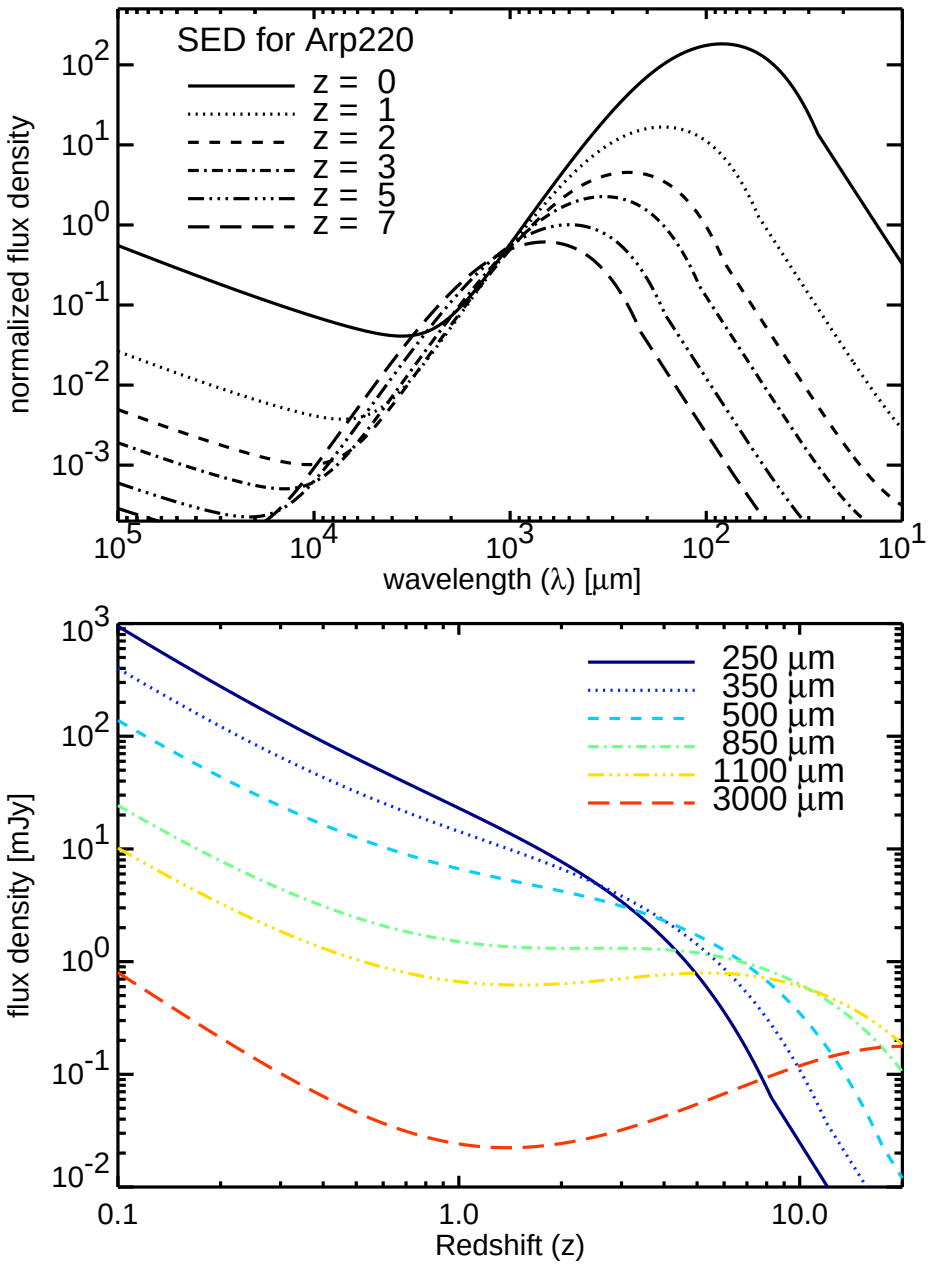

Figure 2.2: Evolution in the observed flux density of a galaxy with an Arp220 type SED ($T_{dust} \sim 60$ K, $\beta \sim 1.7$), as it is redshifted out to $z = 7$ (*top*). In the *bottom* panel the observed flux density from the same galaxy is plotted as a function of redshift, for a range of survey wavelengths. The important phenomena to note in this relation is that the observed 850 μm flux density remains roughly constant over the redshift interval $1 < z < 10$, and is even predicted to increase for objects at $z > 2$, when observed at longer wavelengths such as 3 mm, for example.

The number density of sources brighter than a certain flux limit (commonly referred to as the source counts), indicates the relative contribution of sources with different flux densities to the 850 μm extragalactic background intensity measured by COBE (Fixsen et al. 1998). Along with the source counts, the spatial distribution (or clustering strength) of the high-redshift SMGs can be compared to that of present-day galaxy populations (under the assumption of some evolutionary model) to provide insight into the fate of the SMGs at redshift, z=0. The current data suggest that the SMGs will evolve into massive, present-day elliptical galaxies (Lilly et al. 1999; Scott et al. 2002), commonly observed at the centers of galaxy clusters, and so the high-redshift SMGs should also be associated with regions of greater physical overdensity.

Up to now, blank-field extragalactic surveys at (sub)mm wavelengths have been limited by sensitivity, mapping speed, and low angular resolution. The sensitivity is determined by the collecting area of the antenna, the atmospheric opacity, and the bolometers themselves. The mapping speed is governed by sensivity along with the field of view of the instrument. The field of view of SCUBA on the JCMT is $\sim$2.3 arcmins, limited by the fact that only 37 bolometers in the 850 μm array, and 91 in the 450 μm array, were fabricated (by hand) for the original instrument. SCUBA-2, the successor to SCUBA, is composed of 10,000 pixels, and will have a field of view of $\sim$50 sq. arcmins (Holland et al. 2006). Although not yet commissioned on the telescope, SCUBA-2 is expected to begin taking scientific data on the JCMT in 2007, providing maps of incredible sensitivity over very wide areas. These wide-area surveys at 850μm will be complemented by wide-area surveys at 250, 350 and 500μm by the Balloon-Borne Large Aperture Submillimetre Telescope (BLAST; Devlin et al. 2005) and Herschel, and also at 1.1 mm with the 50 m diameter Large Millimetre Telescope (LMT; Serrano, Schloerb, Hughes & Yun 2006).

The low angular resolution of single-dish (sub)mm facilities (typically 10–15 arcsecs) creates a number of challenges for follow-up studies of SMGs. First and foremost, identification of the optical/infrared galaxy counterpart responsible for the submm emission is not immediately feasible, and so determination of redshifts, and hence far-infrared luminosities, has proven challenging (see chapter 3). Another limitation imposed by observing with a large beam is confusion noise, caused by the background population of faint sources on the scale of the telescope beam, effectively creating a depth threshold for deep surveys. Overcoming this problem requires the use of (sub)mm wavelength interferometers such as the SMA, PdBI or ALMA.

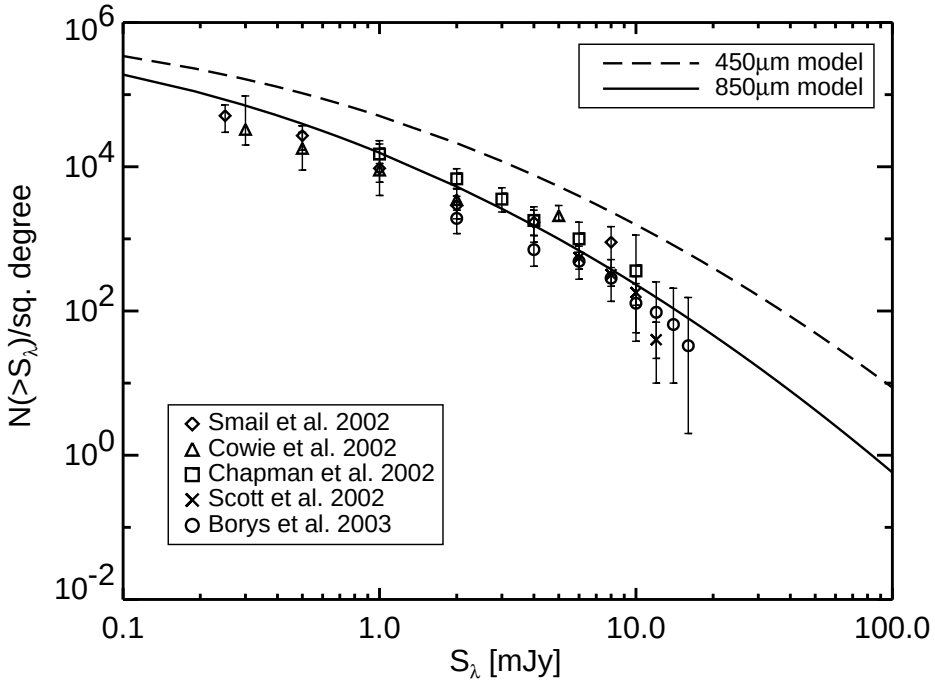

Figure 2.3: The constraints on the bright end of the 850 μm number counts provided by various surveys conducted prior to 2003. The *solid line* shows the 850 μm counts predicted by a model which assumes a single spectral energy distribution ($T_{dust} = 40$ K, $\beta = 1.2$) and a 60 μm luminosity function that evolves as $L_*(z) = L_*(z = 0) \cdot (1+z)^{3.2}$ out to $z = 2.2$, and then remains constant to $z = 6$. This same model also predicts the 450 μm number counts which are shown as the *dashed line*.

Until mid-2002, there remained important questions that had yet to be convincingly answered by any of the previous (sub)mm wavelength surveys. First, the area of any single survey field did not exceed 260 sq. arcmins. Measuring the angular clustering strength of SMGs, in order to compare with that of present-day galaxy populations, should require at least a one square degree submm wavelength survey (under our assumed cosmology), if the SMGs are clustered on scales of ∼30 Mpc at z=2 (Van Kampen et al. 2004). Second, the redshift distribution, and hence evolution of the obscured star formation rate, of the SMG population was not well constrained, yet simulations by Aretxaga et al. (2003) showed that a submm-to-radio photometric redshift technique (see chapter 3) applied to 100s of objects could accurately measure these globally averaged quantities. Finally, the results of the 850 μm analysis of the UK 8-mJy survey data (Scott et al. 2002) suggested a cut-off in the number density of bright ($S_{850} \gtrsim 8$ mJy) objects relative to that predicted by an extrapolation of the source count models (Figure 2.3). Although such an apparent turnover at the bright end of the source counts can be explained by selection effects (i.e. the fields observed in these surveys may simply be devoid of bright objects due to the limited co-moving volumes sampled), it is important that such a result be confirmed by wider area surveys over multiple regions of the sky.

2.2 SCUBA HAlf Degree Extragalactic Survey (SHADES)

Given the outstanding questions related to the nature of the high-redshift submm galaxy population at the beginning of 2002, it was clear that a wide-area 850 μm survey was in order, one that could benefit from additional observations at 250, 350 and 500 μm provided by the forthcoming BLAST experiment. The combination of multi-wavelength photometry and large areal coverage of these surveys would potentially be sufficient to constrain the angular clustering strength, photometric redshift distribution, and number counts of the bright (S(850μm) $\gtrsim$ 10 mJy) SMG galaxy population. As such, in June of 2002 the JCMT time allocation committee (TAC) awarded a total of 180×8 hour shifts to be dedicated to a SCUBA extragalactic survey, covering a half square degree divided between two fields to an 850 μm r.m.s.

of ∼2.2 mJy. The SCUBA HAlf Degree Extragalactic Survey (SHADES[1]; PI-Jim Dunlop) would be the largest submm survey to date, and would include over 75 astronomers from various institutions around the world (including the UK, Canada, Mexico, Italy, USA, Spain, Austria and Japan). A detailed overview of the survey science goals and observing strategy is presented in Mortier et al. (2005), but for completeness I provide a brief description of the SHADES observing strategy.

2.2.1 Observing Strategy for SHADES

The SHADES survey is divided between two fields with low Galactic cirrus contamination and plentiful complementary deep multi-wavelength data. The two fields are the Lockman Hole (LH; $\alpha = 10^h52^m$, $\delta = +57°$), and the Subaru/*XMM-Newton* Deep Field (SXDF; $\alpha = 2^h18^m$, $\delta = -5°$). Despite the original goal of mapping 0.5 sq. degree, the demise of SCUBA in early 2005 meant that only ∼40% of the original survey area was observed. However, the entire 0.5 sq. degree was eventually mapped in late 2005 using the 144 bolometer Astronomical Thermal Emission Camera (AzTEC; PI-Grant Wilson) operating at 1.1 mm. This instrument is destined to be one of the first-light instruments on the LMT when it begins operation in early 2008. The AzTEC observations of the SHADES fields are not presented here, but rather I focus on the analysis and interpretation of the 850 and 450 μm SCUBA data.

Although there are (or were) two SCUBA observing modes which have been used for extragalactic surveys (jiggle-mapping and scan-mapping), the mode most commonly adopted is the jiggle-map mode. Although neither observing mode is believed to be more efficient than the other, the jiggle-map mode is simpler and better characterized, and so is the mode adopted for the SHADES survey. Pointing drifts and calibration problems associated with SCUBA scan-mapping have been reported (Borys et al. 2002), further justifying the choice of observing mode for SHADES.

As the SCUBA bolometer arrays are feedhorn coupled, the 2-Fλ spacing between adjacent bolometers means that the 850 μm array is undersampling the sky by roughly a factor of 16. In jiggle-map mode, in order to fully sample both the 850 and 450 μm arrays, the secondary mirror is moved through a 64-point 'jiggle' pattern. Simultaneously, the secondary mirror is

[1] http://www.roe.ac.uk/ifa/shades/

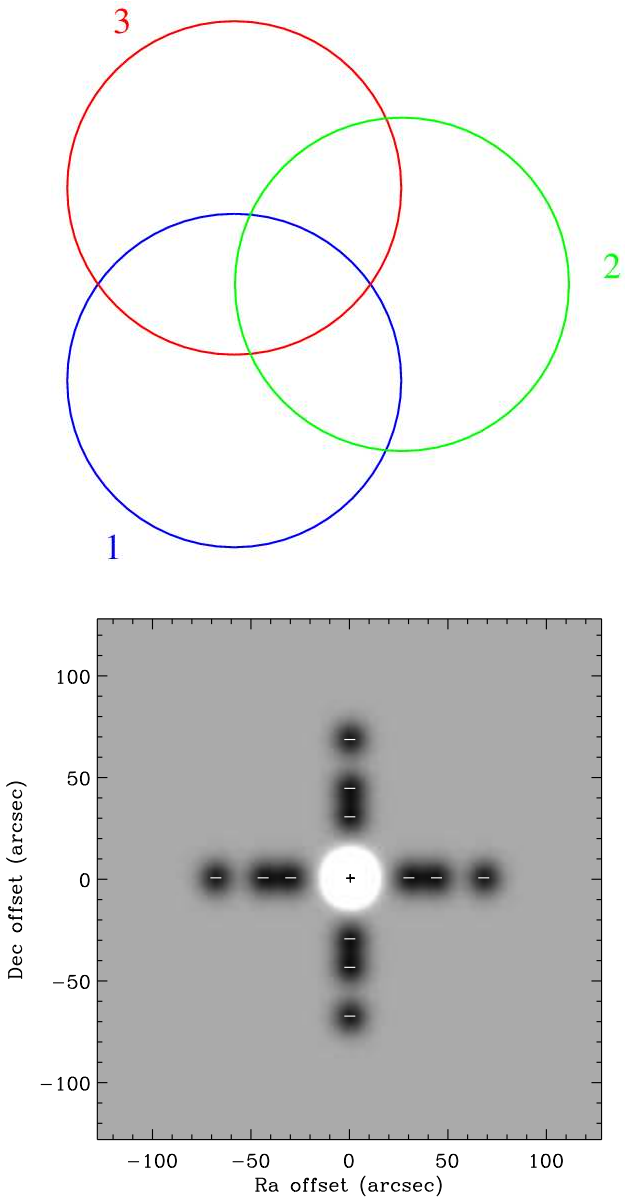

Figure 2.4: *top:* The three circles (each 2.3 arcmins diameter) show the relative overlap between consecutive jiggle-map pointings over the SHADES fields. This geometry is referred to as the 'tripos' positional scheme. A set of 3×15 minute jiggle-maps of a single 'tripos' is observed for each of the six chop throw angles: 30, 44 and 68 arcsecs with primary axes of 0 and 90 degrees with respect to the RA-DEC coordinate system. *bottom:* The SHADES point spread-function which results with the above chop throw angles, where each 'negative' image of the source revealed by the off-beams has -1/12th the peak flux of the central source.

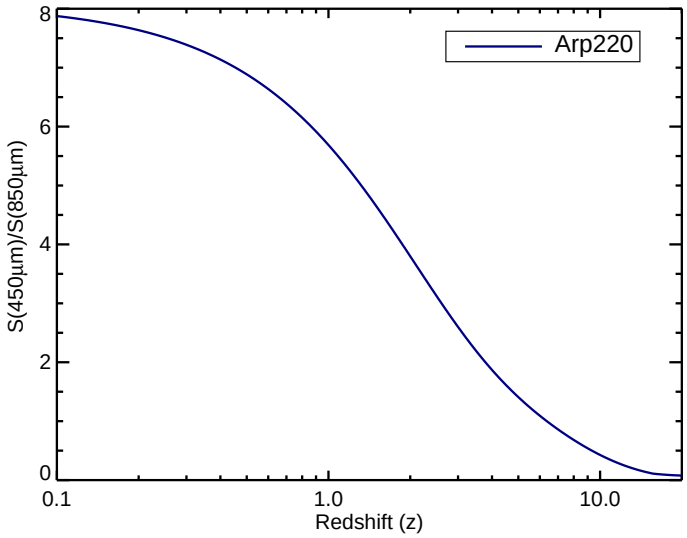

Figure 2.5: Assuming an Arp220 type spectral energy distribution, I plot the ratio between the 450 and 850 μm flux density against redshift. Note that for SHADES data the 850 μm maps are typically a factor of 10$\times$ deeper than the 450 μm maps, while we should expect the 450 μm counterparts to only be $\sim$1–4 times brighter than at 850 μm assuming redshifts in the range $z = 1 - 5$.

also 'chopping' along a fixed direction in the sky with a constant separation angle, at a frequency of 8 Hz. For SHADES, three chop-throws angles were used (30, 44 and 68 arcsecs), at two primary angles (0 and 90 degrees) for a total of six chop-throw configurations (Figure 2.4).

The pointing strategy for the individual SHADES jiggle-maps follows a scheme outlined in Figure 2.4. A set of three 15 minute duration jiggle-maps are observed consecutively with a common chop-throw angle, following the 'tripos' configuration shown in Figure 2.4. This same 'tripos' pointing scheme is repeated for the five additional chop-throw angles (though not necessarily in a consecutive sequence). The advantage of this mapping strategy is that the noisy edges of the individual jiggle-maps (due to undersampling of the array) are evened out over the survey area.

The results of the UK 8-mJy survey demonstrated that, although the

driest atmospheric conditions on Mauna Kea[2] are desirable for optimizing the sensitivity of the simultaneous 450 μm data, they are not required for conducting a sensitive 850 μm survey of bright SMGs (S(850μm) $\gtrsim$ 8 mJy). The main reason for this is that the depths achieved simultaneously in the 450 μm maps (more strongly dependant on the amount of water vapour in the atmosphere) are barely sufficient for detecting counterparts to $\sim$20% of the *most significant* 850 μm sources (e.g. Fox et al. 2002). Typically, the depths of the 450 μm SCUBA maps are $\sim$10$\times$ less sensitive than the 850 μm maps, whereas a galaxy with a far-infrared spectral energy distribution that varies as ν^3 in the Rayleigh-Jeans regime should only be $\sim$1-4$\times$ brighter at 450 μm, since at $z = 3$ the 450 μm observations are sampling the peak of the greybody spectrum (Figure 2.5). As such, the SHADES consortium requested only moderately good weather conditions for the survey (the median 225 GHz opacities for data contributing to the LH and SXDF maps were 0.068 and 0.069, respectively, see Figure 2.6), and the assumption by some consortium members was that the 450 μm data would add very little to the science goals of SHADES. However, the importance of detections (or secure upper-limits) at submm wavelengths shorter than 850 μm for subsequent photometric redshift analyses (Aretxaga et al. 2006) cannot be over-stressed, and in this thesis I provide an alternative analysis and interpretation of the 450 μm data to that presented in Coppin et al. (2006).

2.3 Data Reduction and Map-making

2.3.1 The INAOE Reduction

One of the benefits of having such a large consortium of astronomers committed to the SHADES survey is that it includes many of the world's top experts in the analysis of low signal-to-noise submm-wavelength data. This also means that there are a number of groups with competing ideas on how the data should be analyzed (and a sufficient number of willing graduate students and young post-docs), so that four entirely independent reductions of the 850 μm SCUBA data have been produced, with one at the IfA (Edinburgh; reduction A), one at Kent (reduction B), one at INAOE (reduction C) and finally, one at UBC (Vancouver; reduction D). In this Section, I describe

[2]At the JCMT, grade 1 weather is defined as that when the 225 GHz atmospheric opacity is $\tau_{225} < 0.05$, which occurs approximately 10% of the year on Mauna Kea.

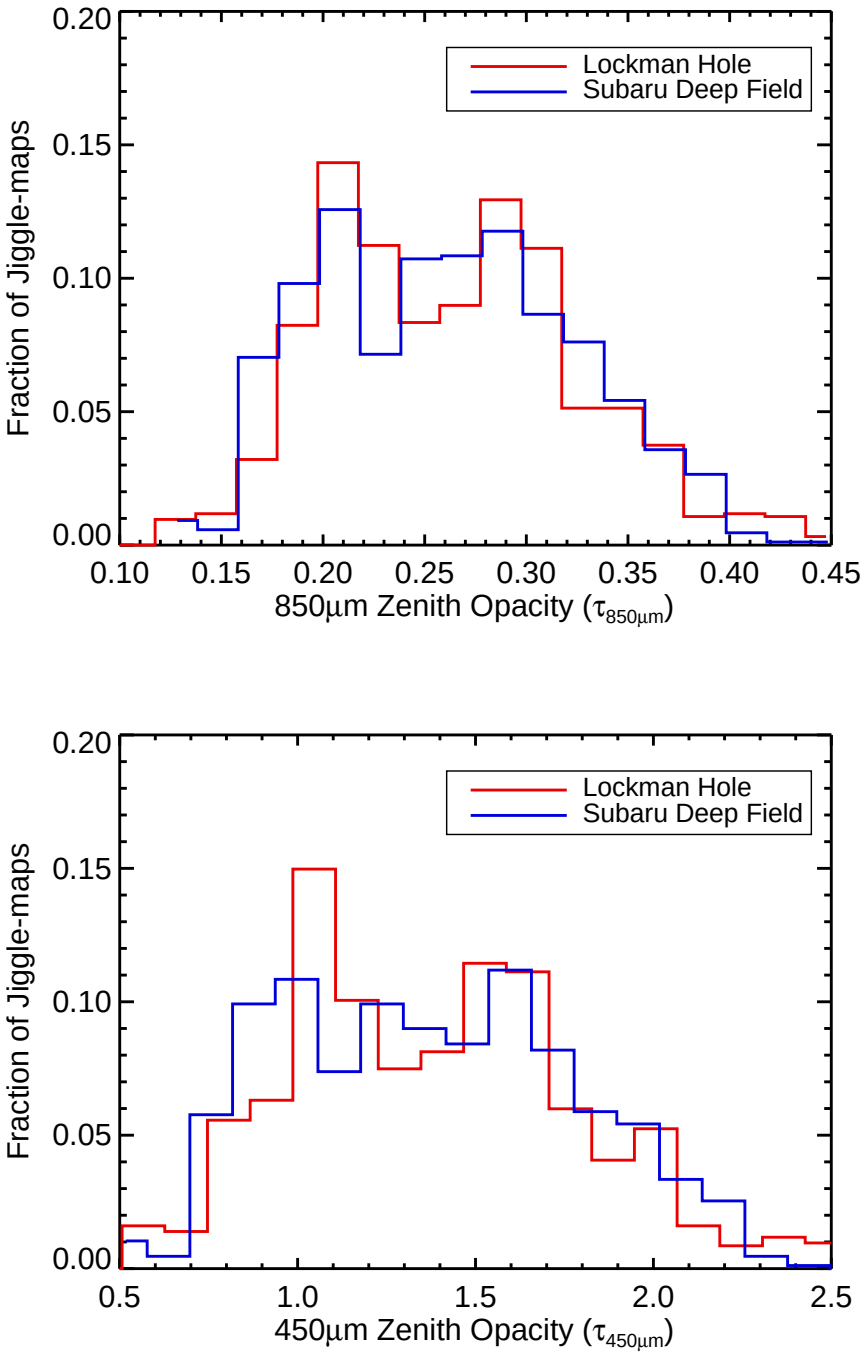

Figure 2.6: The *top* figure shows the normalized distribution of 850 μm zenith sky opacities which have been applied to individual jiggle-maps in the INAOE reduction of the SHADES data. Similarly, the *bottom* figure displays the corresponding histograms of 450 μm zenith sky opacities adopted in the INAOE reduction.

the analysis method of the INAOE team, which independently produced 850 and 450 μm maps of the two SHADES fields.

2.3.1.1 Calibration and Astrometry

Although the initial steps in the calibration of SCUBA jiggle-map data should be common to all four reductions of the SHADES data, the choice of gain parameters (atmospheric opacity and flux conversion factor) is found to vary considerably. The choice of gain parameters applied in the INAOE reduction presented here, was motivated by the procedure recommended by Archibald, Wagg, & Jenness (2001) and Archibald et al. (2002). All of the jiggle-map calibration steps were performed using the *SURF* data reduction package (Jenness & Lightfoot 1998).

Jiggle-map observations of primary (e.g. Mars, Uranus) and secondary calibrators (e.g. CRL618, 16293-2422), as well as jiggle-maps of the SHADES fields are reduced following the basic steps applied to all SCUBA jiggle-map data: nod correction, flat-fielding and correction for atmospheric opacity. The primary method which I adopt to correct for atmospheric extinction is based on a polynomial fit to the 225 GHz opacity measured every ten minutes at the adjacent Caltech Submillimeter Observatory (CSO). These values are then converted to estimates for the 850 μm and 450 μm zenith opacities following the relationships derived by Archibald, Wagg, & Jenness (2001) for the SCUBA wideband filters[3]:

$$\tau_{850\mu\mathrm{m}} = 4.02 \cdot (\tau_{225\mathrm{GHz}} - 0.001)\,, \tag{2.1}$$

$$\tau_{450\mu\mathrm{m}} = 26.2 \cdot (\tau_{225\mathrm{GHz}} - 0.014) \tag{2.2}$$

During those observing shifts when the CSO measurements were not available, interpolation between adjacent 850/450 μm skydip measurements (performed with the JCMT) were used to calculate the extinction correction. Figure 2.6 shows the distributions of 850/450 μm zenith sky opacities which were applied to the jiggle-maps that contribute to the final LH and SXDF maps.

Following the application of the opacity correction, a voltage offset due to sky noise is calculated and then removed from the bolometer time-streams.

[3]Note that a small subset of the LH data were observed prior to Oct. 10, 1999 when the narrow band SCUBA filters were in place, so that the opacity corrections applied to these data are slightly different than those quoted here.

For the maps of calibrator sources (which are generally unresolved on scales of the JCMT beam) the second from last ring of bolometers in the 850 μm array, and the outer most ring of bolometers in the 450 μm array are used to calculate the median sky signal. As the median voltage is the value adopted for the sky signal, I use all of the bolometers in the jiggle-map observations of the SHADES fields, as one does not expect to detect any sources in a single map at a high significance level. The sky-subtracted bolometer time-stream data for the calibrator observations are then rebinned to produce the final maps used to determine the flux conversion factors (in Jy/Beam/Volt).

The peak voltage of the rebinned calibration observation is determined from the maximum counts within a 10 arcsec aperture. The flux conversion factor (FCF) is derived using the expected flux (in Jy/beam) as provided either by the Starlink *fluxes*[4] program (for planets) or from the data on secondary calibrators provided by the JCMT staff. Once the FCFs are determined for each of the 3 chop throws, SHADES maps are then multiplied by the corresponding FCF (ie. derived from calibrators with the same chop throw). When calibrating the data, the applied FCFs come from the calibration observation which is closest in time to that of the SHADES jiggle-map. In cases where variable calibrators were observed (IRC+10216, OH231.8), attempts were made to cross-calibrate these sources with data taken on neighbouring shifts. For example, if IRC+10216 was the only calibrator observed on one half of a shift, the flux per beam could be determined if it was also observed on a previous night when another secondary or primary calibrator was observed closely in time. Histograms of the 850/450 μm FCFs applied to SHADES jiggle-maps in the INAOE reduction are shown in Figure 2.7.

Before rebinning, it is also important that any large pointing offsets be accounted for in the maps. An incorrect position for oCeti in the JCMT pointing catalogue meant that $\sim$11% of the jiggle-maps in the SXDF field were offset by 6.7 arcsecs in Declination, which was corrected in the reduction. The final number of 850 μm jiggle-maps contributing to the rebinned LH and SXDF maps are 926 and 863, respectively. The corresponding number of 450 μm jiggle-maps for these two fields are 952 and 868, respectively.

[4]http://docs.jach.hawaii.edu/star/sun213.htx/sun213.html

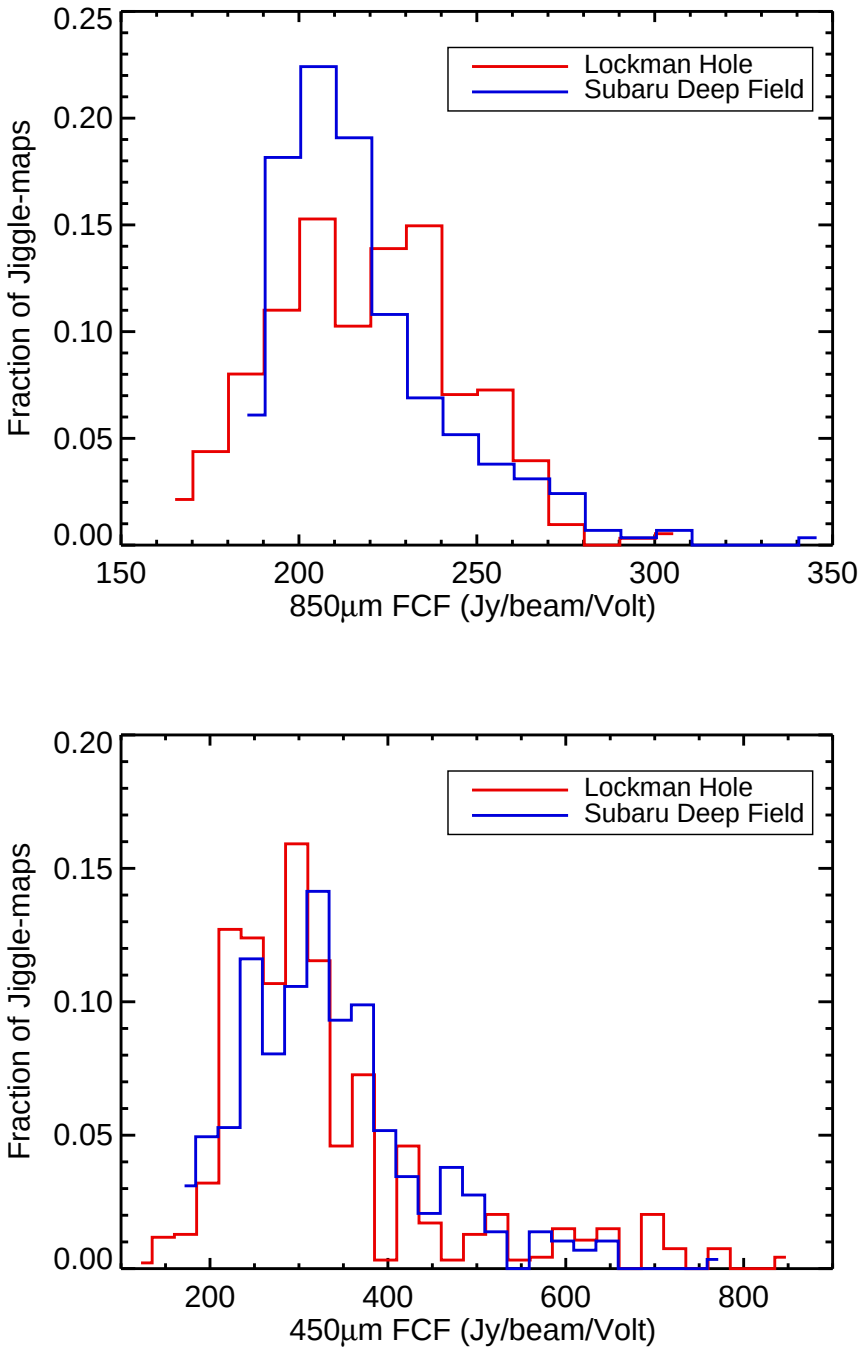

Figure 2.7: In a similar fashion to Figure 2.6, the *top* panel shows the normalized distribution of 850 μm FCFs which have been applied to individual jiggle-maps in the INAOE reduction of the SHADES data. The *bottom* panel displays the corresponding histograms of the 450 μm FCFs.

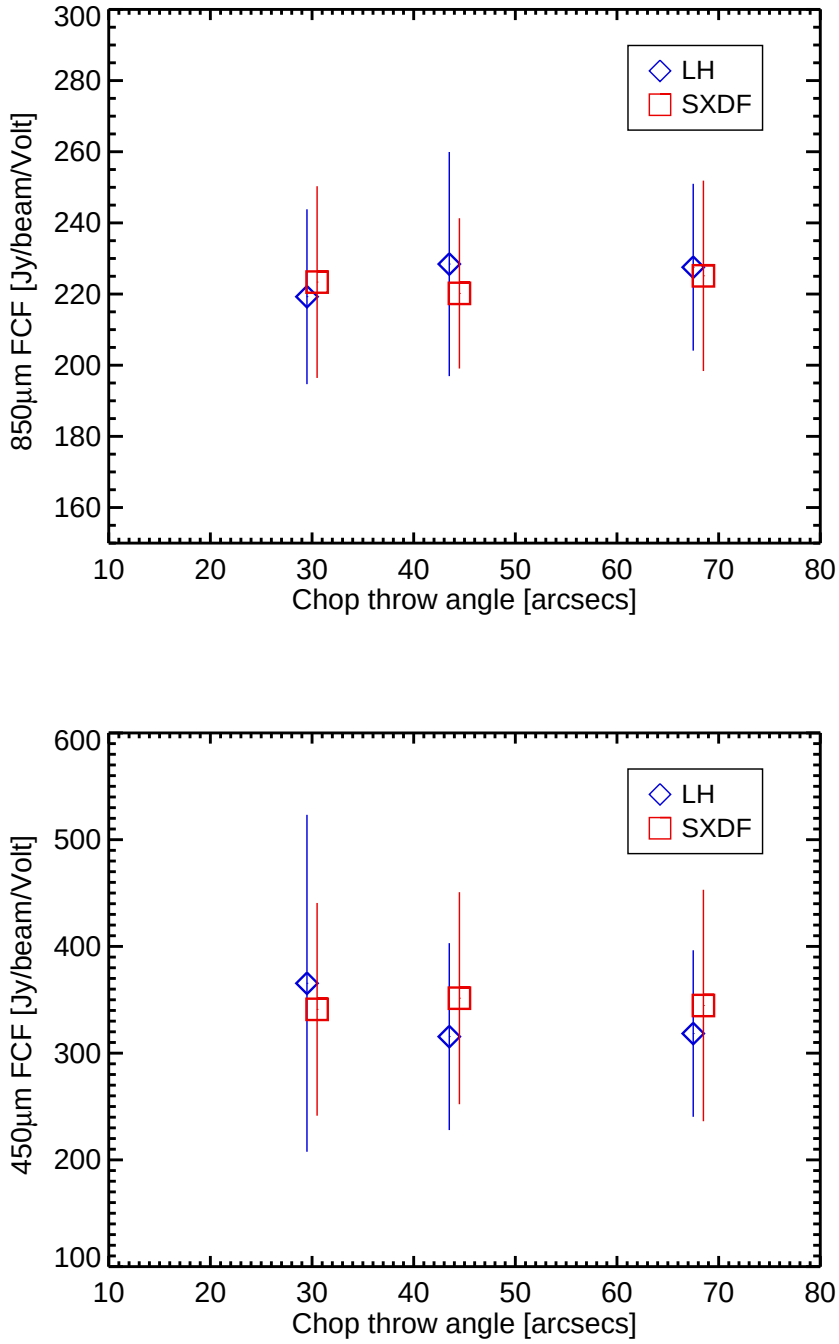

Figure 2.8: The mean flux conversion factors (FCFs) at 850μm (*top*) and 450μm (*bottom*) are plotted against chop throw angle for data taken during the SHADES survey.

2.3.1.2 Map-making

Once the individual SCUBA jiggle-maps are calibrated, the time-stream data are co-added on a grid and smoothed in order to create the final submm maps for each field. At this point, the *SURF* package is no longer sufficient for reduction of the data, partly due to memory restrictions implemented in the software, limits which are far exceeded by the unprecedented volume of data contributing to a single SHADES map. As such, all four reduction teams (IfA, Kent, INAOE and UBC) made use of pre-existing map-making code, or developed new software as in the case of the INAOE group. The development and testing of new map-making algorithms to handle large submm datasets is particularly important now, in order to prepare for the upcoming wide area SCUBA-2 and BLAST surveys. The INAOE map-making code has been written in the *idl* language and a preliminary version of the algorithm is described in Chapin (2004). Here, I describe the most recent algorithm which has been implemented by our group.

To begin, the bolometer time-stream measurements from every jiggle-map (having been calibrated in Jy/beam) are parsed into a single *idl* array along with the astrometry and chop throw angle for each measurement. The SCUBA data is initially sampled at 125 Hz, from which a mean and standard deviation are calculated following a 5-σ clip to remove noise spikes, over a 1 second timescale. Hence, each 15 minute duration jiggle-map contains 900 samples of this 1 Hz sampled time-stream per bolometer, each with a corresponding estimate of the variance. In order to account for the possibility of variations in the noise characteristics over longer timescales ($\gtrsim$1 min), the INAOE reduction instead calculates the variance for each sample over 100 sample intervals. The final processing step before the rebinning phase is to remove any time-stream samples which have S/N $>$ 5 and $\sigma >$ 300 mJy. Given the typically low 850 μm flux densities of the SMGs expected to be detected by SHADES (S_{850} $\sim$5-10 mJy), a single source would not stand out at high significance in a consecutive series of time-stream samples. It is only when the data are rebinned and smoothed that individual sources are identifiable.

The map-making algorithm adopted for our reduction is similar to that implemented in the group B (Kent) reduction (Mortier et al. 2005), with the exception that this group uses smaller, 1 arcsec pixels for their rebinning. In the INAOE reduction, the time-stream measurements are binned into 3

arcsec pixels in 1 of 6 different map grids, where each map corresponds to a different chop throw angle (Figure 2.4). We adopt 3 arcsec pixels in order to fully sample the map, as the sample spacing for the 64-point jiggle pattern is 3 arcsec. For each pixel, p, in the 6 maps the weight, W_p, is given by:

$$W_p = \sum_i 1/\sigma_i^2 \tag{2.3}$$

where i indicates the index of a single sample with variance σ_i. In a similar fashion, 6 signal maps are created by adding together the fluxes in a single pixel weighted by the variance:

$$F_p = \sum_i F_i/\sigma_i^2. \tag{2.4}$$

During this rebinning phase, the number of 'hits' per pixel (i.e. the number of bolometer samples in that pixel) is recorded, and any pixel with less than 10 'hits' is given no weight in the final, co-added map. The flux in the unsmoothed pixel maps, M_{u-p}, for each of the 6 chop throws are calculated following:

$$M_{u-p} = F_p/W_p, \tag{2.5}$$

while the uncertainty on this value is:

$$E_{u-p} = \sqrt{1/W_p}. \tag{2.6}$$

Before combining the 6 maps, each must be convolved with the point spread function (PSF) that corresponds to the chop throw pattern of the jiggle-maps that contributed data to each. Without applying some form of smoothing, it is not possible to identify the low signal-to-noise SCUBA sources in a particular map. PSFs are created for each of the 6 chop throws, c, by assuming a Gaussian beam of FWHM 14.7 arcsecs, where each PSF, P_c, is positive at the center and negative (-0.5× the central peak height) at each of the 2 chop positions (N-S or E-W, and seperated by ±30, 44, or 68 arcsecs). The smoothed flux maps for each chop throw, F_{s-c}, are produced following:

$$F_{s-c} = \left(M_{u-c}/E_{u-c}^2\right) \otimes P_c, \tag{2.7}$$

where $\otimes$ indicates a convolution, while the weight maps for each are:

$$W_{s-c} = \left(1/E_{u-c}^2\right) \otimes P_c^2. \tag{2.8}$$

The final, combined smoothed maps are then produced:

$$F_s = \frac{\sum_c F_{s-c}}{\sum_c W_{s-c}}, \tag{2.9}$$

while a map of the 1-σ rms in the map is also generated:

$$E_s = \sqrt{\frac{1}{\sum_c W_{s-c}}}. \tag{2.10}$$

The final maps for the LH and SXDF fields are shown in Figures 2.9 and 2.10. The typical 1-σ 850 μm rms in the LH and SXDF maps is 2.3 and 2.1 mJy, respectively.

The INAOE reduction also produces 450 μm maps following a similar map-making algorithm to that used to produce the 850 μm maps, with two exceptions. The 450 μm SCUBA array had 91 bolometers over the same field of view as the 850 μm array, so that the short wavelength jiggle-maps provide a better sampling of the sky. As such, I adopt smaller, 1 arcsec pixels when rebinning the 450 μm time-stream data onto the map grids. In addition, the FWHM of the PSF used to smooth these maps is 7.3 arcsecs. The 450 μm maps are shown in Figures 2.11 and 2.12, where the typical 1-σ rms in the LH and SXDF maps is 25 and 22 mJy, respectively.

2.4 Results

Many of the results described here are also presented in Coppin et al. (2006) as those of the 'group C' reduction (INAOE). Coppin et al. (2006) focus on the compilation of an 850 μm consortium source catalogue and corresponding source count estimates. A brief description of the 450 μm data analysis is presented, along with the claim that none of the 850 μm sources are detected at 450 μm, despite very good agreement between groups B and C (Kent and INAOE) on the fluxes and positions of a few potential 450 μm counterparts. As such, although much of the 850 μm analysis presented here is presented in Coppin et al. (2006), the results of this 450 μm analysis are unpublished, and will likely be the subject of a future SHADES publication.

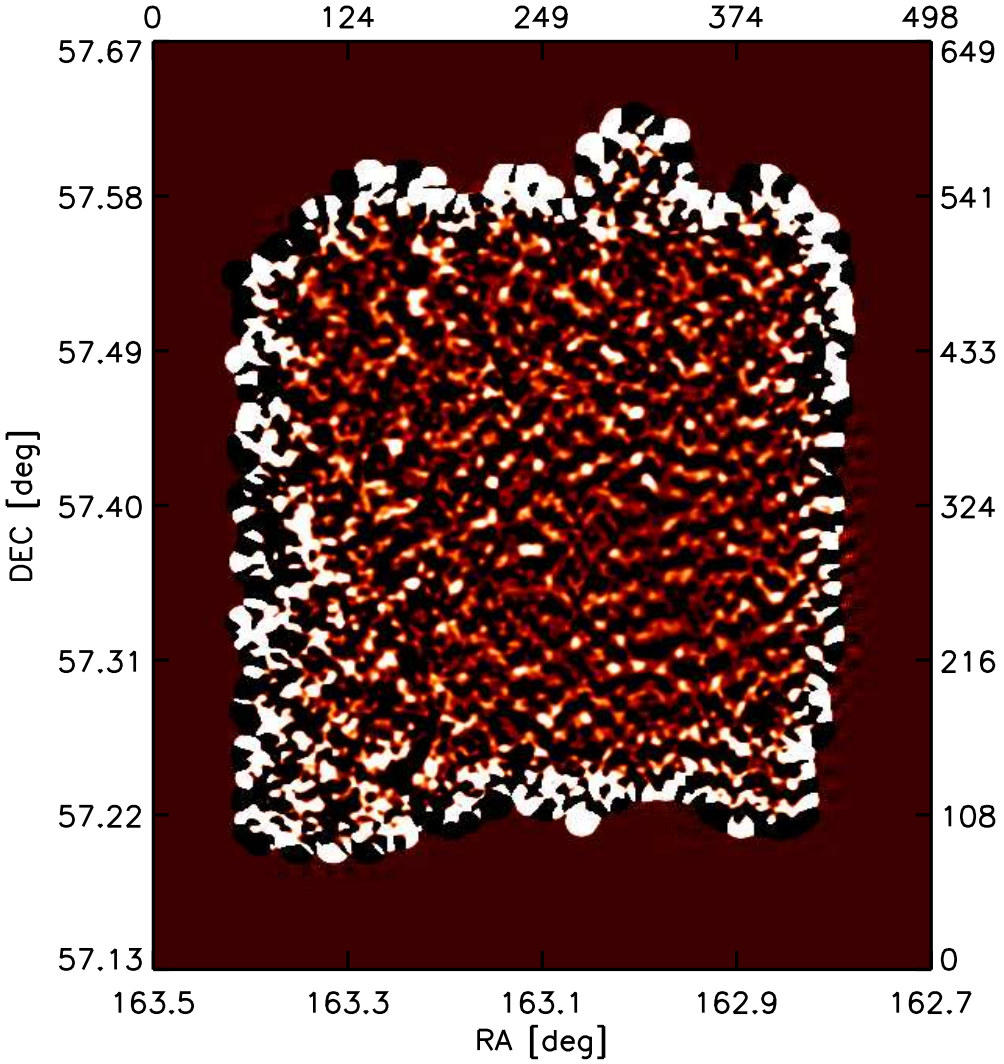

Figure 2.9: The INAOE 850 μm map of the LH field smoothed to 14.7 arcsecs resolution.

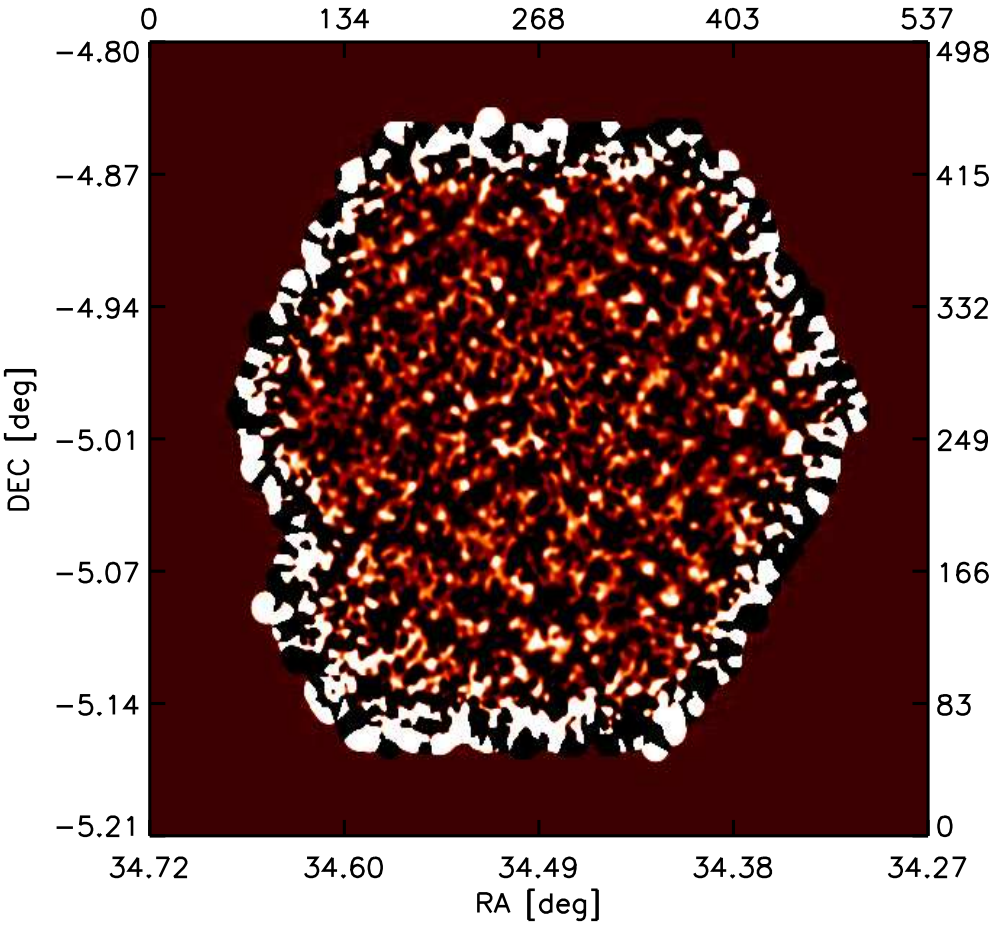

Figure 2.10: The INAOE 850 μm map of the SXDF field smoothed to 14.7 arcsecs resolution.

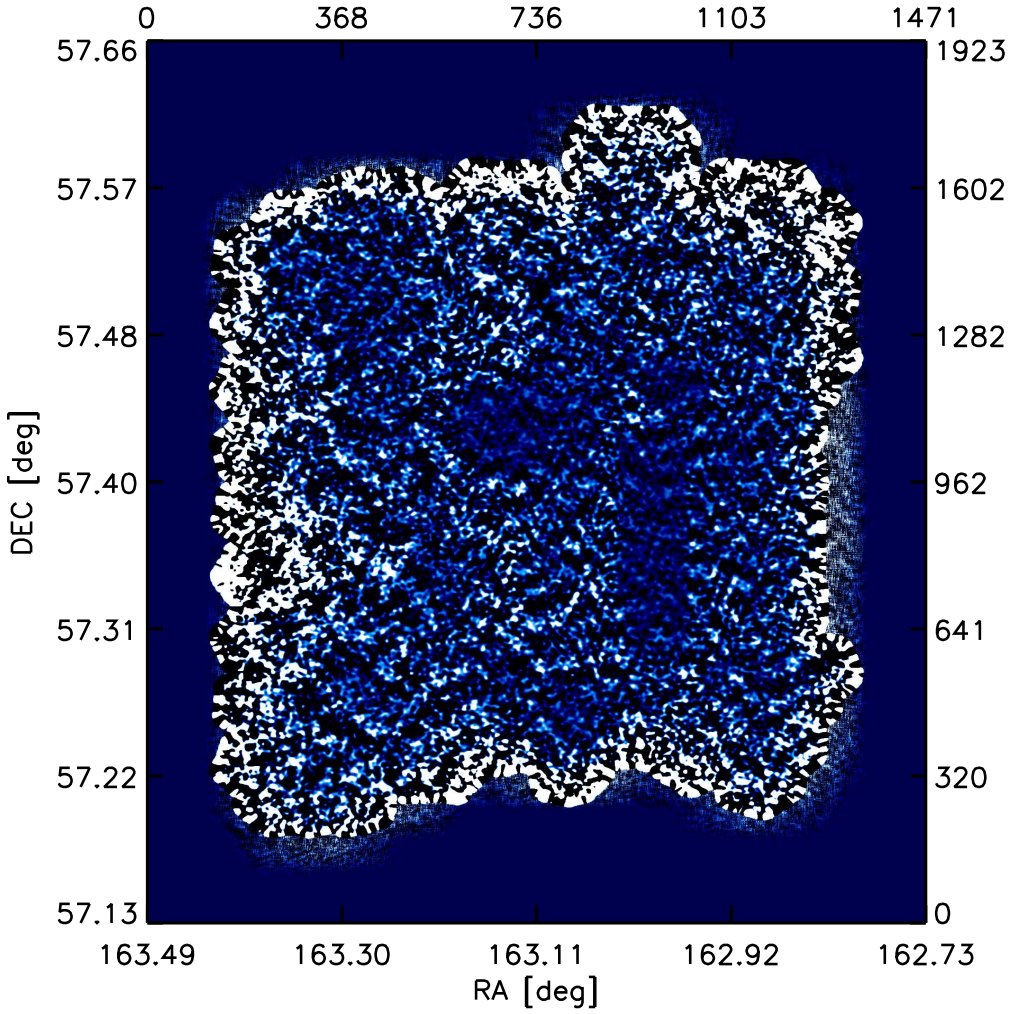

Figure 2.11: The INAOE 450 μm map of the LH field smoothed to 7.3 arcsecs resolution.

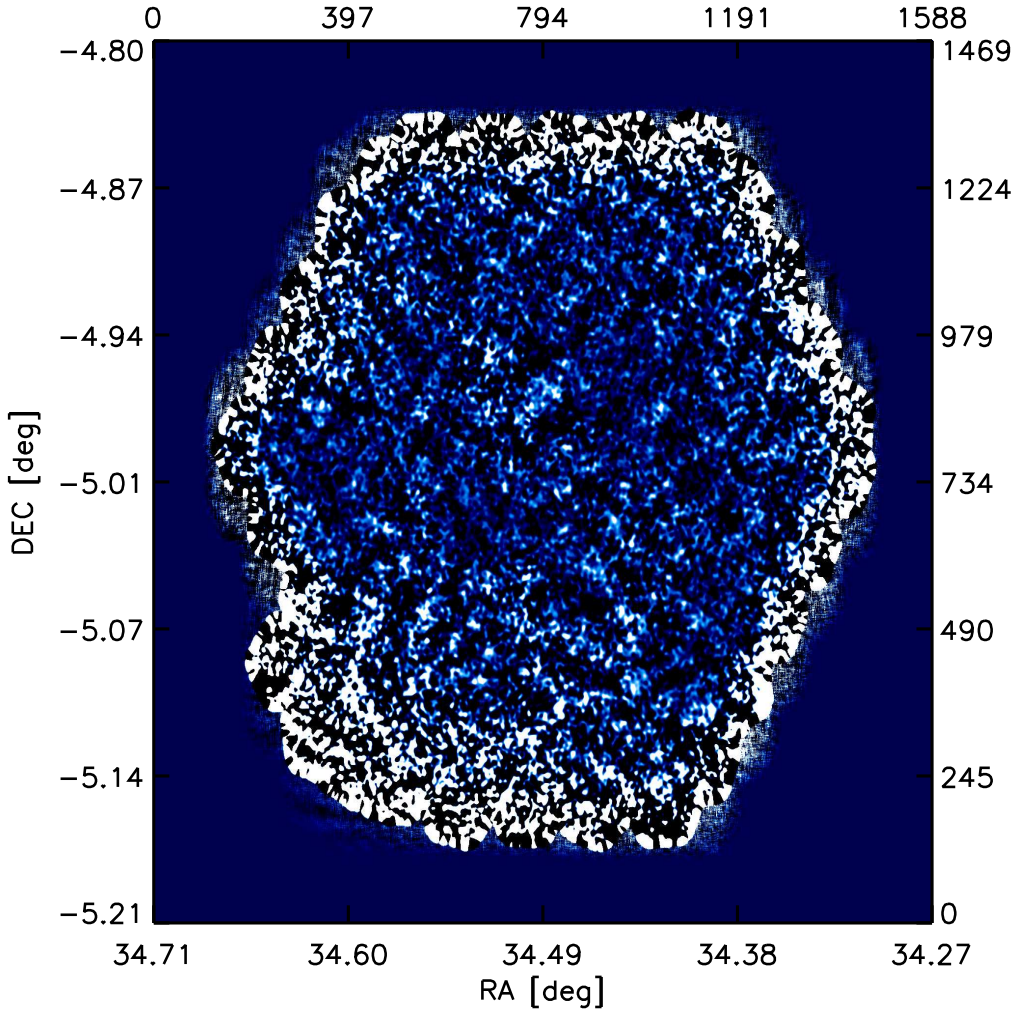

Figure 2.12: The INAOE 450 μm map of the SXDF field smoothed to 7.3 arcsecs resolution.

2.4.1 Combining Independent Reductions

The four independantly produced source catalogues were combined into a master catalogue reported by Coppin et al. (2006), which graded the robustness of each source candidate according to its consistency in position and statistical significance over multiple reductions. This is the first time that a multi-reduction catalogue of extragalactic submm sources has been produced from a single dataset. Independant analyses of such data are important as the low statistical significance of most SMG detections means that there is a non-zero probability for including spurious sources in published catalogues. Tables A.1 and A.2 give the deboosted 850 μm fluxes for the consortium list of LH and SXDF SHADES sources, along with either 3-σ upper limits, or peak 450 μm flux of any S/N>3.5 peak within 7.5 arcsecs of the 850 μm source in the INAOE maps. The details of how the combined 850 μm SHADES source catalogue is created are given in Coppin et al. (2006), while here I focus on the analysis method and results of the independent INAOE reduction. This work has been carried out in collaboration with Edward Chapin, and a further independent reduction of the INAOE data is presented in Chapin (2004), wherein a slightly different map-making algorithm is adopted, and the 450 μm SHADES data is not analyzed.

2.4.2 850 μm Source Candidates

The INAOE reduction finds 66 source candidates in the SXDF and 76 in the LH field at a significance >3-σ (see Tables A.3 and A.4). Though the details of the source extraction algorithm are not given here, the method is presented in Serjeant et al. (2003), Chapin (2004) and Mortier et al. (2005).

2.4.2.1 Spurious Sources

A frequent (and valid) criticism of most published SMG sourcelists is that some of the source candidates may turn out to be spurious, owing to the low signal-to-noise nature of the data. These are normally identified through cross-correlation of multi-wavelength source catalogues produced from data obtained with different instruments on different facilities. For instance, Laurent et al. (2005) compare their 1.1 mm Bolocam/CSO source candidates in the Lockman Hole with previous 850 μm SCUBA/JCMT and 1.2 mm MAMBO/IRAM 30 m source candidates (Scott et al. 2002; Greve et al.

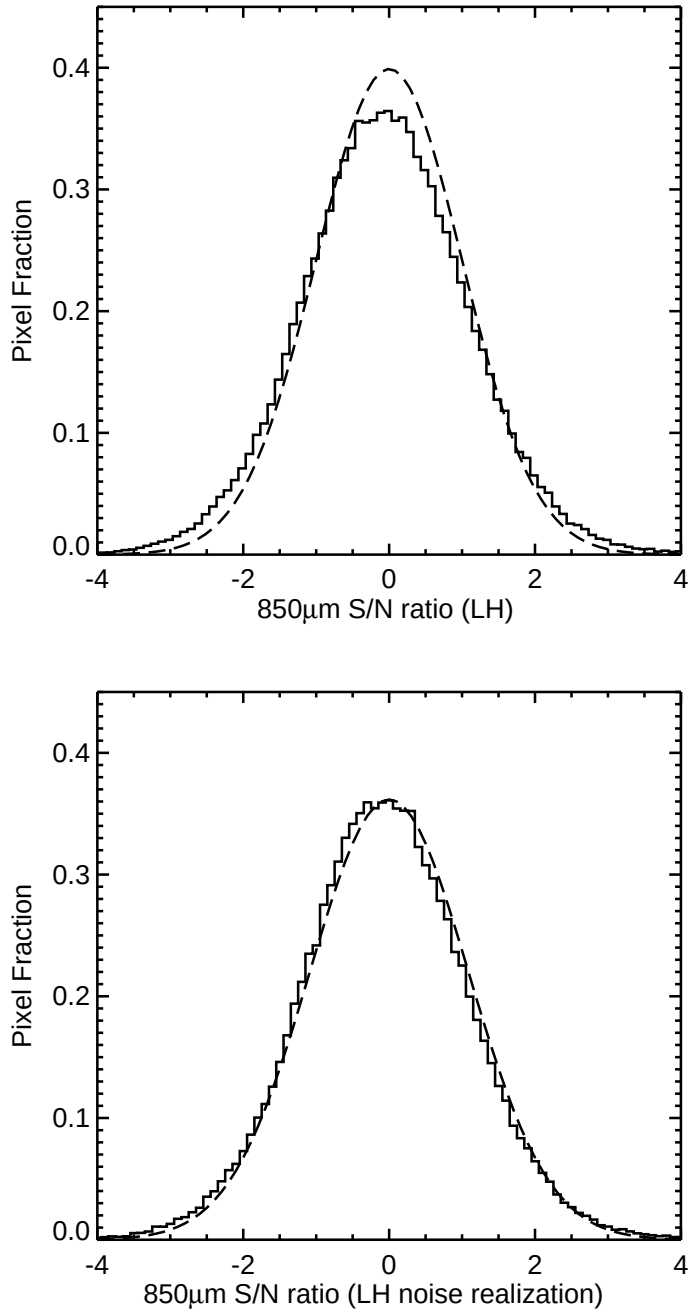

Figure 2.13: *top:* Normalized S/N histograms of pixels in the smoothed LH 850 μm map (*solid lines*). The *dashed lines* show Gaussians with $\sigma = 1$. The positive and negative skewness in the observed distributions imply the presence of real sources in the map, where the negative tail is due to the chop throw (Figure 2.4). The *bottom* figure shows the S/N histogram for a simulated map of pure noise, realized from the variance map of the LH.

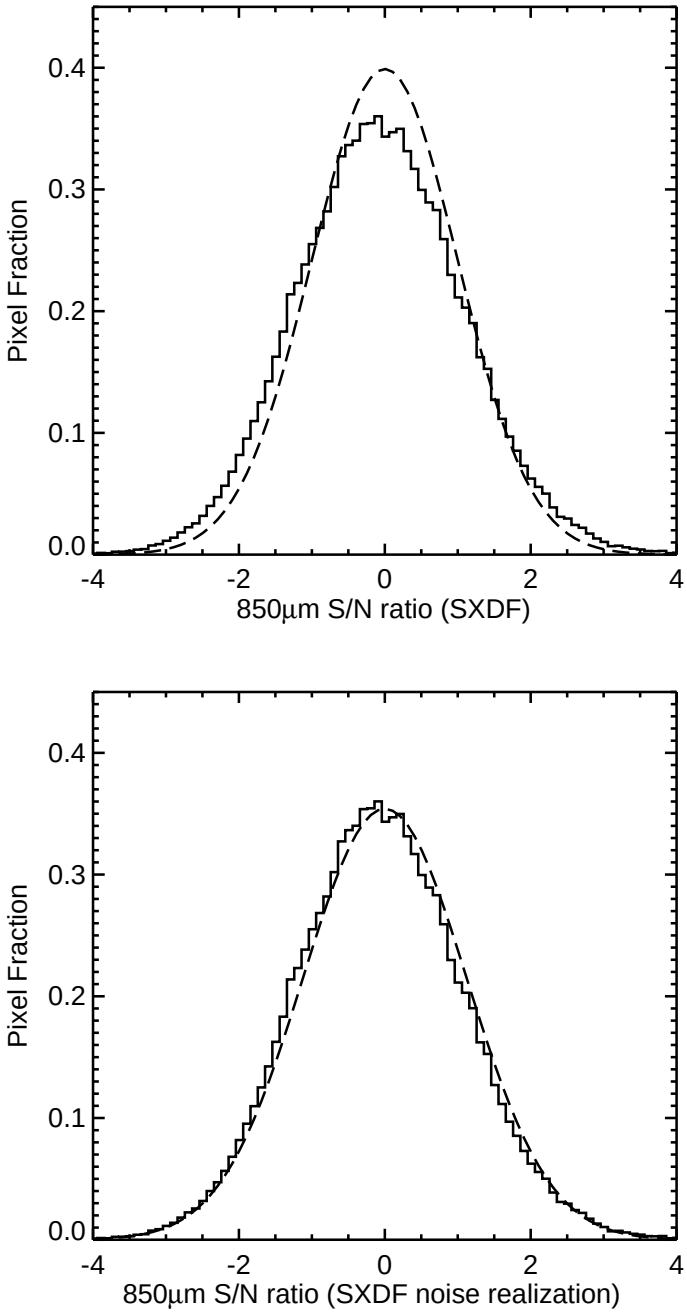

Figure 2.14: *top:* Normalized S/N histograms of pixels in the smoothed SXDF 850 μm map (*solid lines*). The *dashed lines* show Gaussians with $\sigma = 1$. The positive and negative skewness in the observed distributions imply the presence of real sources in the maps, where the negative tail is due to the chop throw (Figure 2.4). The *bottom* figure shows the S/N histogram for a simulated map of pure noise, realized from the variance map of the SXDF.

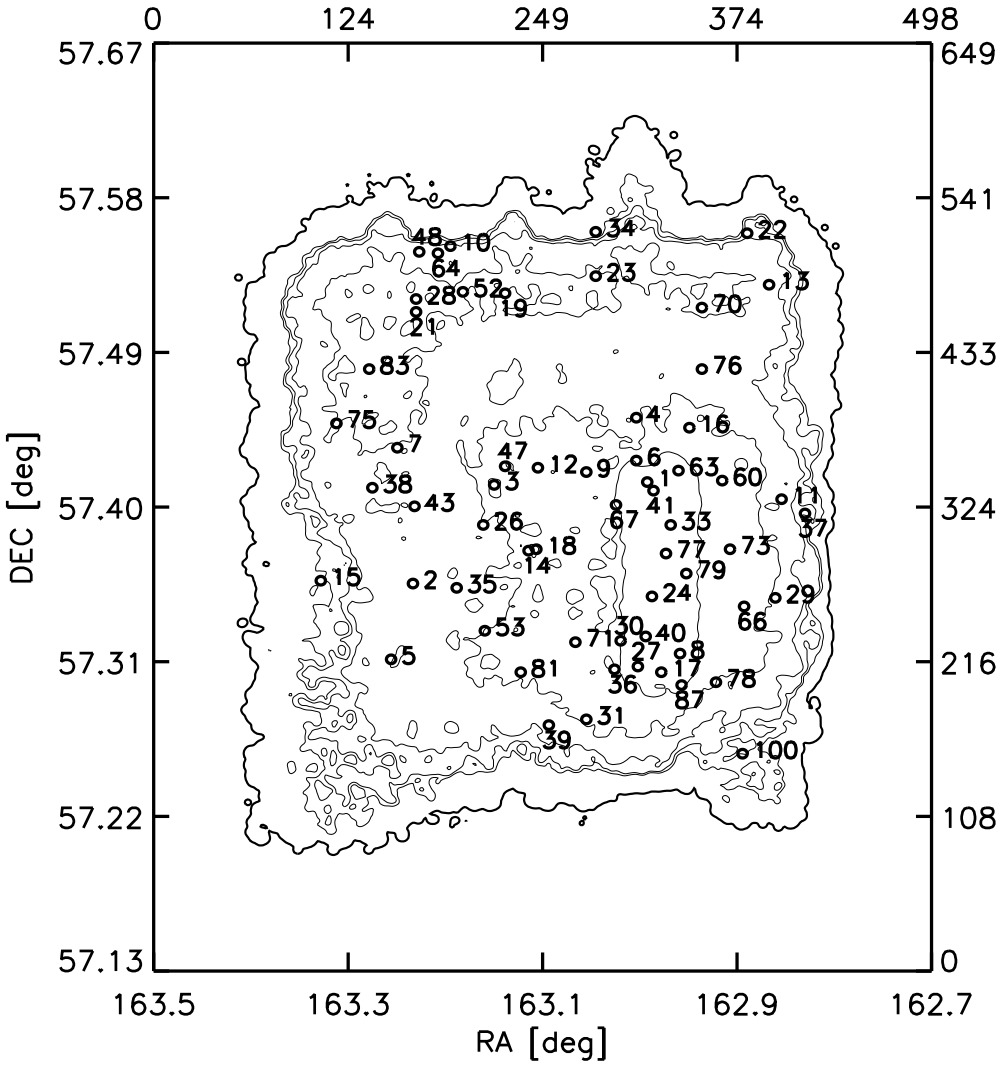

Figure 2.15: Positions of the 850 μm consortium sources overlaid on the noise map of the INAOE 850 μm LH reduction. Contour levels define regions with $\sigma_{850} \geq$1.5, 2.0, 3.0, 4.0 and 5.0 mJy.

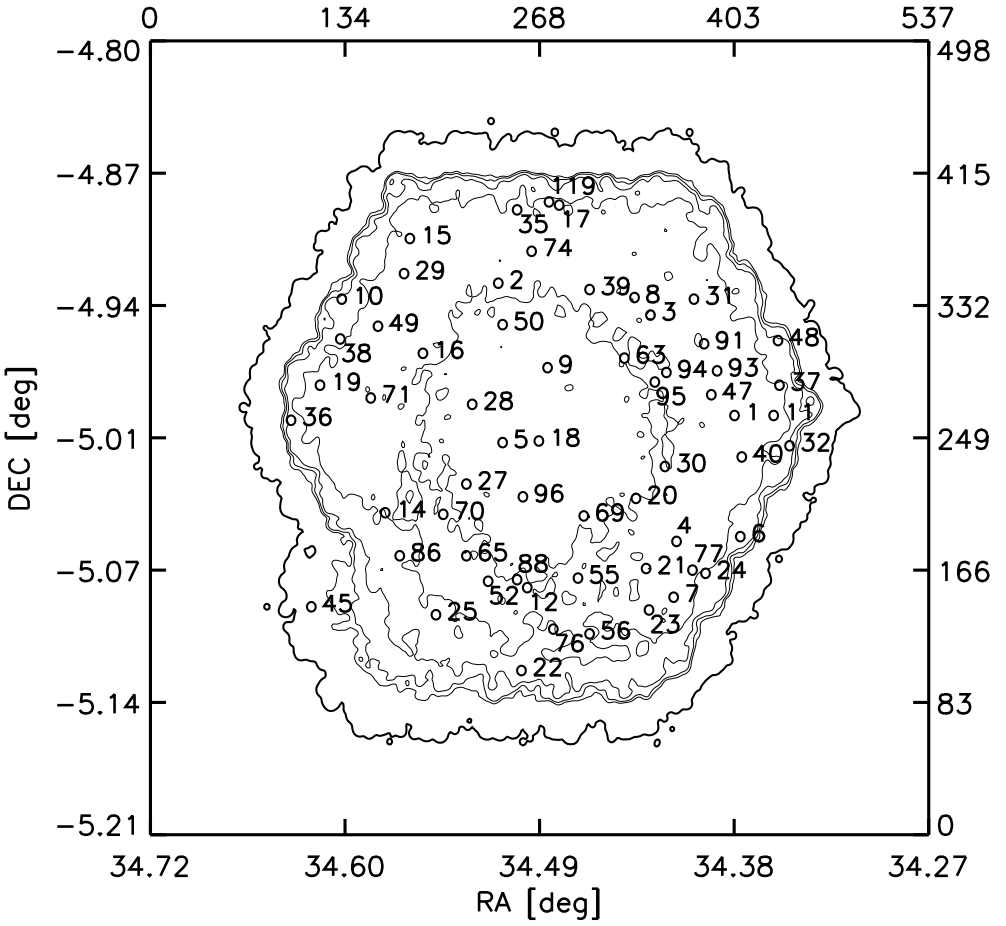

Figure 2.16: Positions of the 850 μm consortium sources overlaid on the noise map of the INAOE 850 μm SXDF reduction. Contour levels define reqions with $\sigma_{850} \geq$2.0, 3.0, 4.0, and 5.0 mJy.

2004). They find a broad range in the level of agreement between the 3 survey source catalogues in the region where all 3 overlap. The least successful comparison finds that only 7 of the 31 SCUBA sources are detected by Bolocam. Laurent et al. (2005) claim that the comparison between the different source catalogues takes into account the flux differences expected for the spectral energy distribution of a typical luminous infrared galaxy ($T_{dust} = 40$ K, $\beta = 1.6$) redshifted to z = 2.4.

Why should the submm survey data be inclined to produce such a high fraction of spurious extragalactic sources? The answer lies in the low signal-to-noise nature of the data, whereby sources are typically detected at the 3.5–5.0 σ significance level[5]. For purely Gaussian noise, as is assumed to be the case for this SHADES data (see Figures 2.13 and 2.14), one expects the number of noise peaks to decrease with increasing signal-to-noise, yet this number is non-zero even at the 3.5–4.0 σ significance level. In order to properly quantify the expected number of spurious sources due to noise, I adopt the following recipe:

1. The raw bolometer time-streams (before rebinning) have both a signal (*flux*) and standard deviation component (σ), where for the INAOE maps, the rms has been calculated over 100 sample intervals (recall that the sample rate of SCUBA is 1 Hz). In order to generate simulated maps of pure noise, the time-stream *flux* is substituted with a synthetic time-stream signal of *Gaussian random* values where σ is that of the sample in question.

2. The next step is to rebin the raw time-stream data onto the map grids following the same procedure for map-making that is applied to the real data, with the exception that the map *flux* is now a *random noise realization* of the true rms. Recall that in the map-making stage, six rebinned maps are created, where each includes only those individual jiggle-maps observed with a common chop-throw angle (±30, 44 and 68 arcsecs in both RA and DEC, see Figure 2.4). Each is then smoothed with a PSF appropriate to that chop-throw, and the six sub-maps are then co-added using inverse-variance weighting.

3. At this point the same source extraction algorithm applied to the real maps is applied to the *random noise realization map*, in order to gen-

[5]To date, the brightest submm source in the confusion limited 850 μm HDF survey of Hughes et al. (1998) is one of the highest significance SMG detections (∼14-σ).

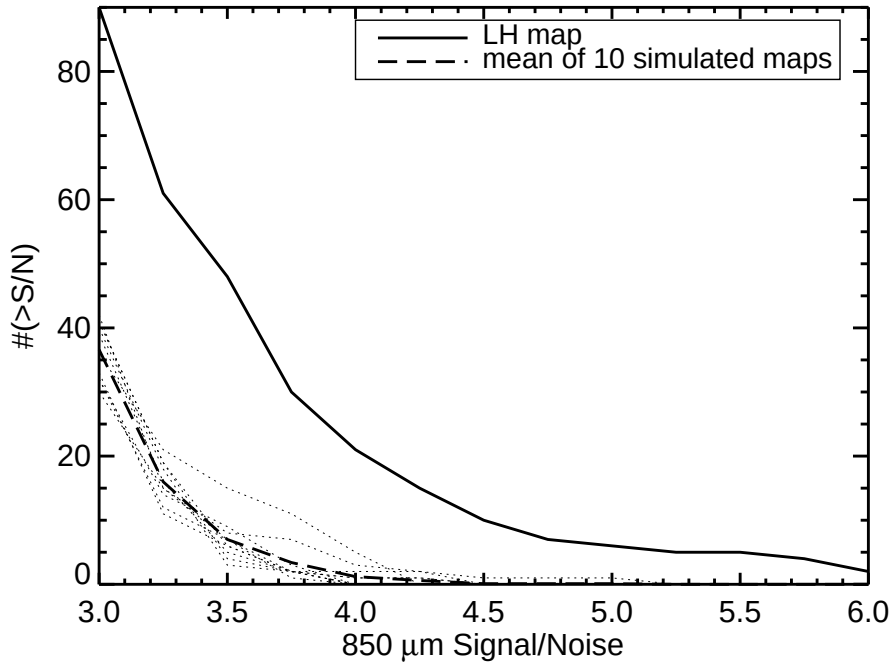

Figure 2.17: A comparison of the number of source candidates identified in the LH map (*solid line*) versus that identified in simulated maps generated from random realizations (*dotted line*) of the LH noise maps, plotted as a function of signal-to-noise threshold. The mean of 10 realizations is shown as the *dashed line*.

erate a catalogue of spurious sources (down to a 2.5 σ threshold). This algorithm (described in detail in Serjeant et al. 2003 and Chapin 2004) uses the full PSF shape to rank the robustness of each of the source candidates.

4. This process of generating random catalogues of spurious sources is repeated 10 times, and the number of spurious sources as a function of signal-to-noise ratio is compared to that observed in the real maps (see Figures 2.17 and 2.18).

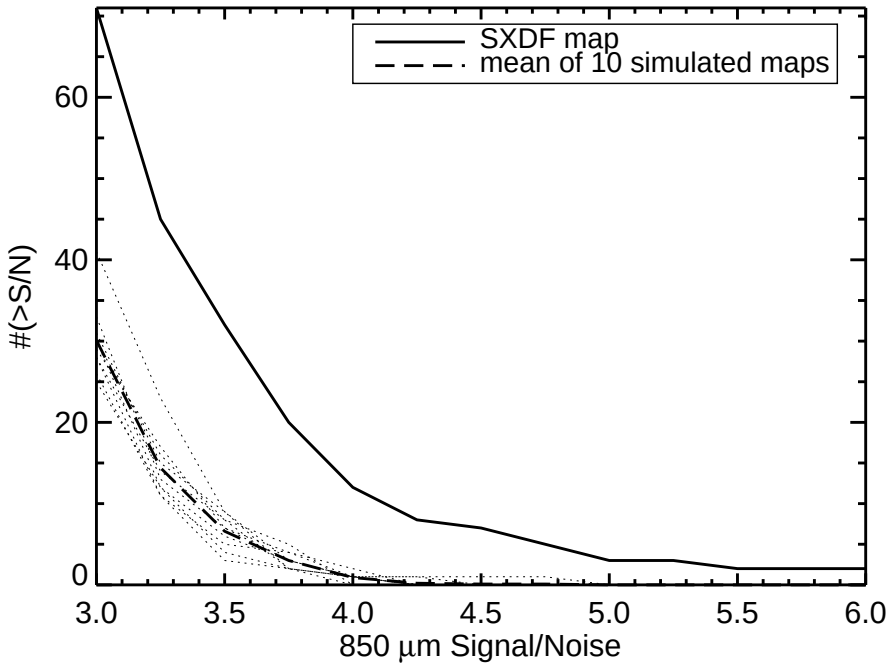

Figure 2.18: A comparison of the number of source candidates identified in the SXDF map (*solid line*) versus that identified in simulated maps generated from random realizations (*dotted line*) of the SXDF noise maps, as a function of signal-to-noise ratio. The mean of 10 realizations is shown as the *dashed line*.

Reduction	LH	SXDF
A	61.6%	80.0%
B	100.0%	91.7%
C (INAOE)	96.7%	98.3%
D	95.0%	98.3%

Table 2.1: The percentage of 850 μm SHADES consortium source catalogue recovered at $\geq$3-σ by each of the four reductions in the LH and SXDF fields ($\geq$3.5-σ in the case of reduction B).

2.4.2.2 Comparison with Consortium Catalogue

Of the source lists produced by each of the four independant reductions, not one of them recovers each individual source candidate in the combined consortium catalogue with a significance $\geq$3-σ. Table 2.1 summarizes the success rate of each of the four reductions at recovering sources in the master catalogue. It is apparent that reductions B (Kent), C (INAOE) and D (UBC) are equally successful at identifying robust source candidates, while reduction C (INAOE) does marginally better than the others. Although the reasons behind the varying degrees of success of each of the four reductions depends on the individual methods adopted (as outlined in Coppin et al. (2006)), a comparison of these methods is not carried out here, but rather I focus on the source candidates identified in the INAOE maps.

2.4.3 850 μm Source Counts

One of the primary goals of the SHADES survey is to provide stronger constraints on the bright end of the 850 μm source counts ($S_{850} \gtrsim 6$ mJy). With a similar goal in mind, Scott, Dunlop & Serjeant (2006) present a re-analysis of all existing SCUBA surveys conducted by the various groups, consistently employing a common data reduction and map-making technique. Although their data lack the survey area required to provide equally strong constraints on the source counts above $S_{850} \gtrsim 10$ mJy, they are consistent with the SHADES source count estimates (Coppin et al. (2006)) for flux densities $S_{850} \gtrsim 2$ mJy. Before presenting the INAOE source counts, I discuss the biases which must first be accounted for when estimating the source counts.

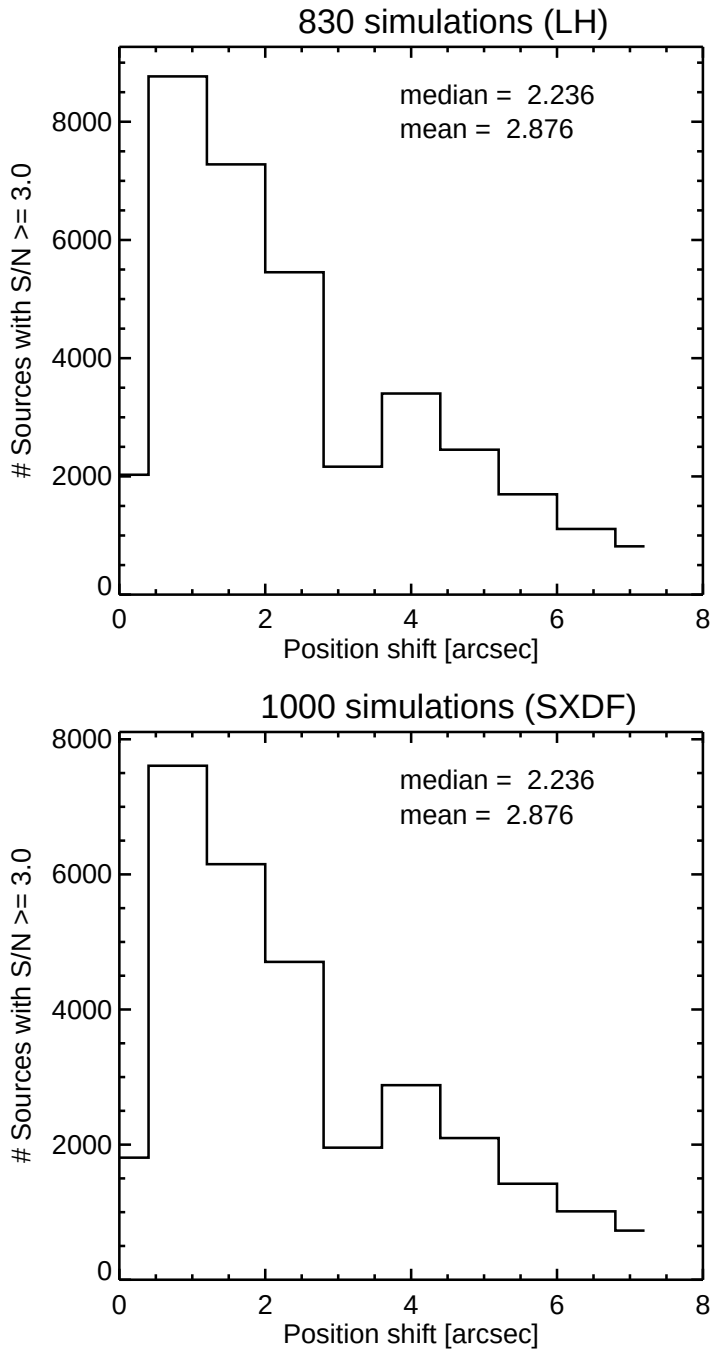

Figure 2.19: Histograms of the offset between the input and recovered positions of 850μm sources extracted from simulated SHADES maps which include noise realizations of the true variance.

2.4.3.1 Flux Boosting

The first bias introduced into the source counts estimate is due to the combination of a steep underlying source counts distribution (i.e. many more fainter sources) and the large uncertainties on the measured flux densities of recovered sources. This effect is referred to as *Malmquist bias*. A similar effect, called *Eddington bias*, is due to sources with fluxes at, or below the detection threshold having their fluxes artificially 'boosted' by measurement uncertainties or faint source confusion. In order to correct for these biases, I follow a recipe similar to that described in Section 2.4.2.1 for quantifying the expected number of spurious sources, with the exception that simulated sources are now included in the noise realization maps.

1. The raw bolometer time-stream samples (before rebinning) have both a signal (*flux*) and standard deviation component (σ), where I have calculated the rms over 100 sample intervals (recall that the sample rate of SCUBA is 1 Hz). In order to generate simulated maps of pure noise, the time-stream *flux* is replaced by a synthetic time-stream signal of *Gaussian random* values where σ is that of the original sample.

2. The next step is to rebin the raw time-stream data onto the map grids following the same procedure for map-making that is applied to the real data, with the exception that the map *flux* is now a *random noise* realization of the raw σ. Recall that in the map-making stage, six rebinned maps are created, each including only those individual jiggle-maps observed with a single chop-throw configuration (angles of 30, 44 and 68 arcsecs in both RA and DEC, see Figure 2.4). These maps are not smoothed at this stage as they were in Section 2.4.2.1.

3. A grid of randomly distributed sources (represented by δ functions) is created, where the flux for each source is assigned according to a probability distribution defined by a model for the observed 850 μm source counts (Borys et al. 2003). This map of δ functions is then convolved with the PSF defined by each of the six chop throws, resulting in six new maps.

4. Each of the six 'source maps' is added to the corresponding map of random noise, and then smoothed with the appropriate chopped PSF. The six simulated maps are co-added using inverse variance weighting

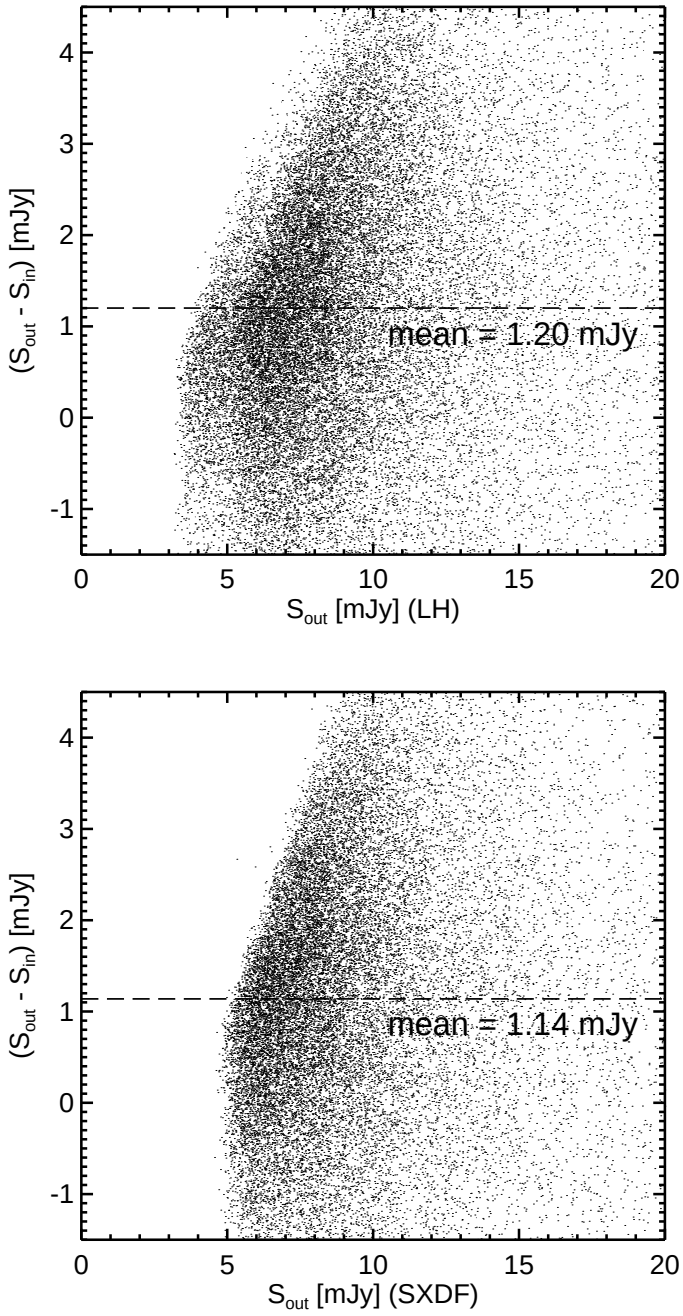

Figure 2.20: Difference in the 850 μm flux density of sources > 3-σ recovered from simulated source maps which include noise realized from the variance of the real maps. The *dashed lines* show the mean flux difference calculated from all simulated sources.

as in the case of the real data. The result is a *simulated source map* which may be used to estimate the flux biases.

5. At this point the same source extraction algorithm applied to the real maps is applied to the *simulated source maps*, in order to generate a catalogue of fake sources (above a 2.5-σ threshold). This algorithm (described in detail in Serjeant et al. 2003 and Chapin 2004) uses the full PSF shape to rank the robustness of each of the source candidates. 1000 *simulated source maps* are generated for the SXDF field, while 830 are generated for the LH field.

In addition to providing estimates of the flux bias, by applying the source extraction algorithm to simulated source maps one is able to estimate the positional uncertainty inherent in low signal-to-noise SCUBA sources. Figure 2.19 shows histograms of the offsets between the input source position and the position of the same source after extraction from the map. The median offset found for sources in both fields is $\sim$2.2 arcsecs, consistent with the range $2-3$ arcsecs typically quoted in the literature.

Figure 2.20 shows the difference between the input and recovered source flux density for sources in the simulated maps, plotted against the original input 850 μm flux density. Although there is a weak dependance of flux increase on output flux density, the scatter is quite large. The important point is that the true flux of a source (S_{in}) is typically 15–25% lower than that observed for sources with measured 850 μm flux densities (S_{out}) in the range 5–8 mJy.

2.4.3.2 Estimating Source Counts for SHADES

The 850 μm source counts are estimated for each SHADES field separately. To begin, the fluxes of all sources detected at $\geq$3-σ are corrected for the flux boosting described in the previous section, and illustrated by Figure 2.20. The correction factor applied to each source candidate's flux is the mean flux difference ($S_{out}-S_{in}$) found for simulated sources with the same *measured* flux density (S_{out}) as the source candidate in question. For each flux density bin, the cumulative source counts per square degree is the total number of sources with corrected flux densities brighter than that flux limit, minus the number of spurious sources expected from the noise simulations (section 2.4.2.1), divided by the area of the map over which these sources would be detected. The uncertainty on each value is assumed to be Poisson random, though

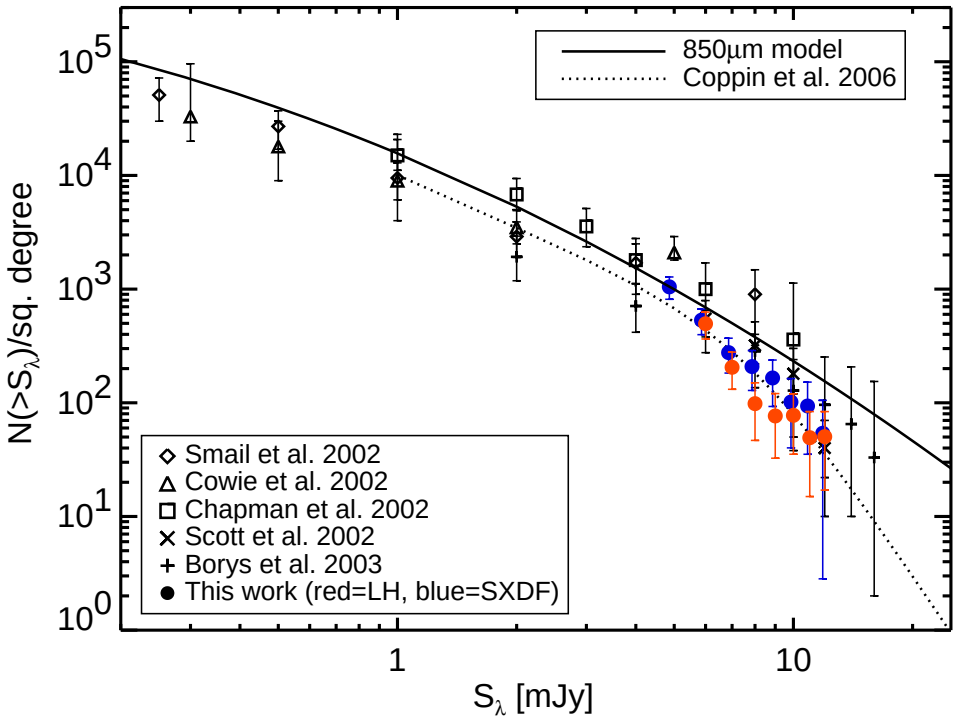

Figure 2.21: The 850 μm number counts calculated from the SHADES data analyzed in this work, compared with estimates presented previously in the literature, and the model fit to the combined SHADES counts presented by Coppin et al. (2006).

there may be an additional contribution from source clustering which I do not include since the clustering amplitude of SMGs is not well constrained. The results are shown in Figure 2.21.

Although the original survey area proposed for SHADES was not observed, it is clear from both the results presented here and by Coppin et al. (2006), that the cutoff in the number of bright 850 μm sources first observed by Scott et al. (2002) is confirmed. The fact that such a deficit is observed for sources in both the Lockman Hole and the Subaru XMM Deep Field, would imply that 'Cosmic variance' is not responsible. Within this context, 'Cosmic variance' is the result of density fluctuations in the matter distribution, whereby a small survey area may happen to be sampling an under-dense region with very few bright SMGs. For this reason the SHADES survey was designed to cover 0.5 square degree divided between two seperate fields.

2.4.4 450 μm Counterparts to 850 μm Sources

Although the conclusion of the combined analysis of three independant 450 μm reductions presented in Coppin et al. (2006) is that none of the consortium 850 μm sources are detected in the shorter wavelength maps, my aim here is to present an alternative and independent conclusion based only on the INAOE 450 μm data reduction.

Before considering potential 450 μm counterparts, it is important to determine whether the 450 μm maps are consistent with the presence of real sources. Figure 2.22 plots the distribution of pixel S/N values in the 450 μm maps which have been smoothed using a 7.3 arcsecs (FWHM) Gaussian PSF. For a map of pure noise, one would expect a Gaussian distribution of S/N values with σ=1, such as that shown by the *dashed lines*. The fact that the observed distributions from both fields appear to be skewed (both positive and negative skewness is expected due to the chop pattern; Figure 2.4), implies that flux from real sources is present in the 450 μm maps. If the excess 450 μm flux in the maps is due to the presence of a few bright, high S/N sources, then the best place to search for such objects is near the positions of the 850 μm source candidates.

The recipe adopted for selecting potential 450 μm counterparts to 850 μm sources, is to identify any peak within 7.5 arsecs of the 850 μm source position that has a SNR greater than 3.5-σ in the 450 μm map. The 1-σ rms in the 450 μm maps, at the positions of the 850 μm sources, varies from $8-90$ mJy in the LH field, and $13-106$ mJy in the SXDF field. The JCMT dish is

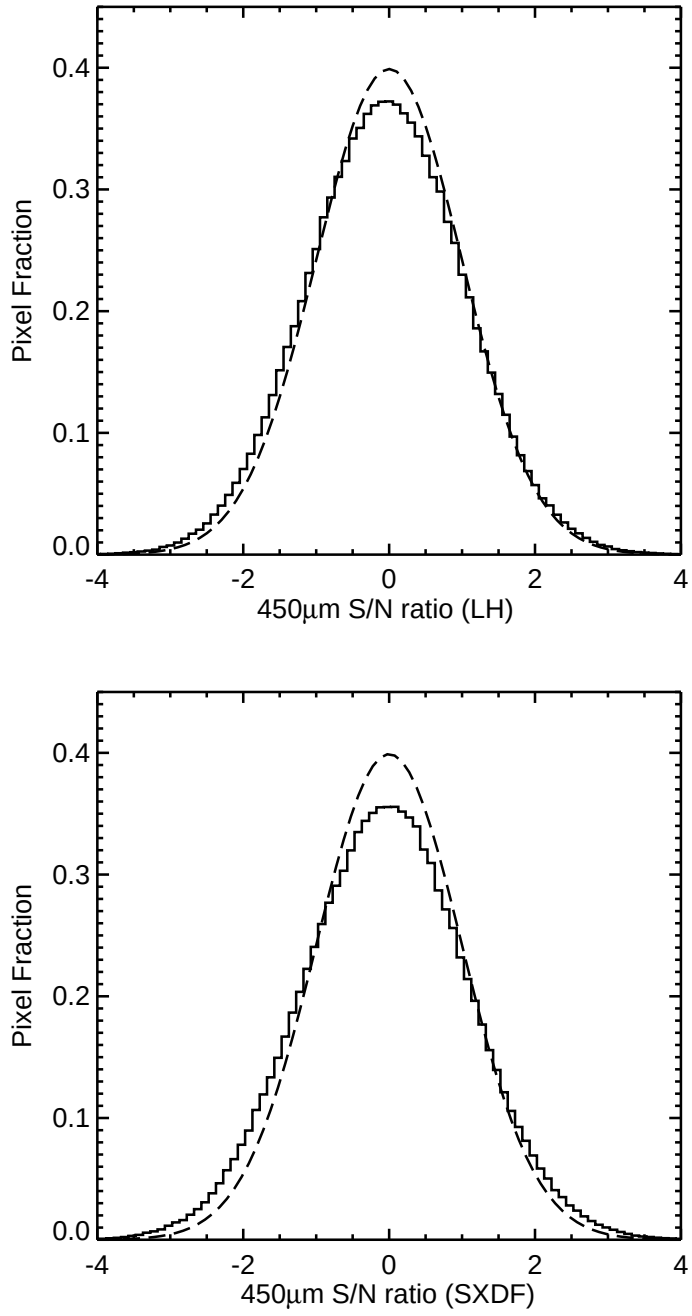

Figure 2.22: Normalized S/N histograms of pixels in the smoothed 450 μm maps (*solid lines*) of the Lockman Hole (LH; *top*) and the Subaru XMM Deep Field (SXDF; *bottom*). The *dashed lines* show Gaussians with $\sigma = 1$. The positive and negative skewness in the observed distributions imply the presence of real sources in the maps.

not optimized for observations at 450 μm, so that the shape of the PSF is not strictly Gaussian for point sources. As such, rather than use the full, chopped PSF for source extraction, as in the case of 850 μm sources, the flux in the pixel with the highest SNR is taken as the flux in the beam, and the negative sidelobes are not included in the flux estimates. Uncertainties are taken as the median 450 μm rms within a 20×20 arcsec box centered on the position of the 850 μm source. This recipe for identifying *potential* 450 μm candidates is applied to both the consortium 850 μm source list (Tables A.1 and A.2) and the INAOE 850 μm lists presented here (Tables A.3 and A.4). Coincidently, three 450 μm candidates are found for each of the four 850 μm lists.

Given that the smaller JCMT beamsize at 450 μm will lead to a greater number of spurious sources compared to 850 μm, it is essential to characterize the probability of finding a 450 μm candidate for a random 850 μm source position using the above recipe.

2.4.5 Blank-field 450 μm Source Candidates

The low signal-to-noise ratio (SNR) nature of SMG candidates identified with the large JCMT beam at 850 and 450 μm ($\sim$15 and 7.5 arcsecs respectively), means that a significant fraction of these (depending on the SNR threshold) will be spurious. Figure 2.23 compares the number of 450 μm objects extracted from the SHADES maps as a function of SNR, with the mean number extracted from 10 maps which are random noise realizations of the true variance maps. It is apparent that even at the 4-σ significance level, we should expect $20-50\%$ of the sources to be spurious. As such, it is a non-trivial task to determine which, if any of the blank-field 450 μm source candidates are real.

One way to test the robustness of a blank-field 450 μm source is to search the 850 μm map for potential counterparts. In Figure 2.5, I showed that for an Arp220 type SED at $1.5 \leq z \leq 3.5$, the 450 μm flux would be $\sim$2.2–4.6× greater than the 850 μm flux. As such, I am not able to use the 850 μm data to confirm the validity of any blank-field 450 μm candidate, since the sensitivity of the 450 μm data with respect to the 850 μm data, is too low.

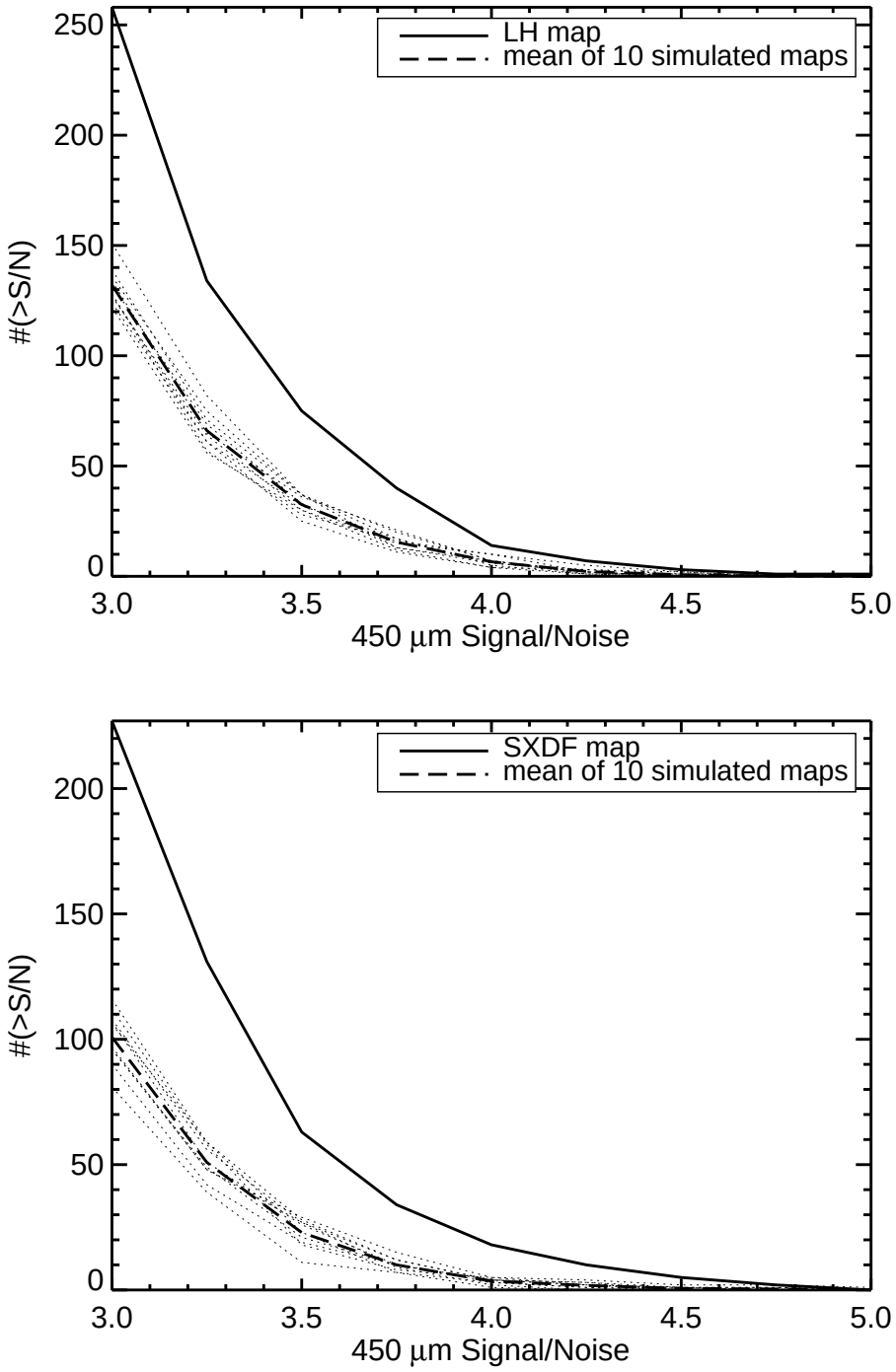

Figure 2.23: A comparison of the number of 450 μm source candidates identified in the LH and SXDF maps (*solid lines*) versus that identified in simulated maps generated from random realizations (*dotted lines*) of the variance maps. The mean of 10 realizations are shown as the *dashed lines*.

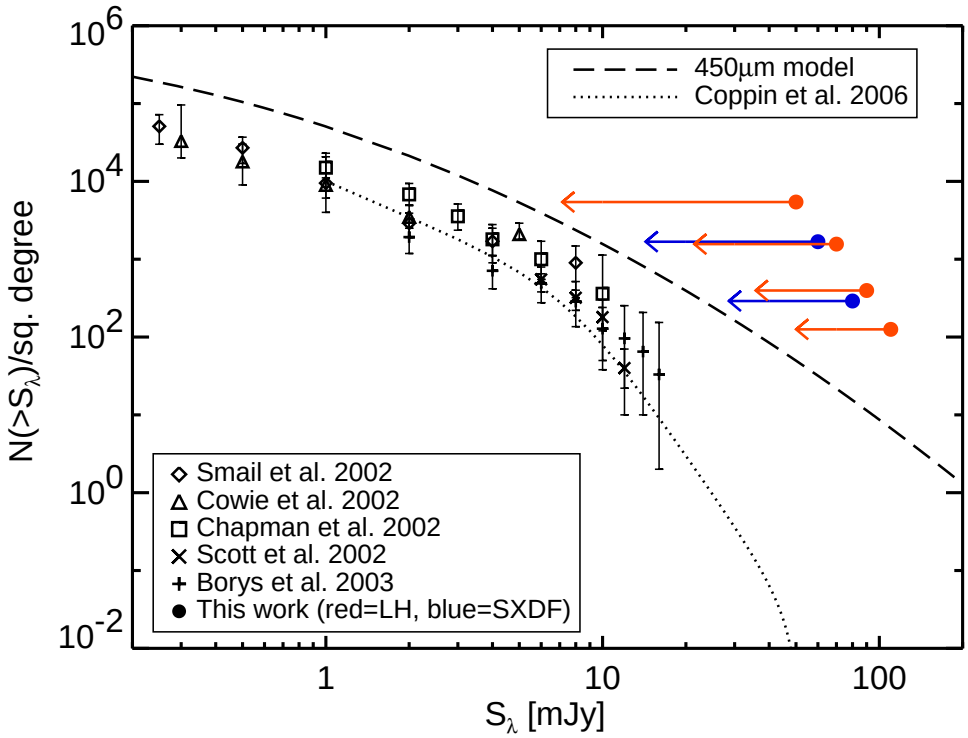

Figure 2.24: The 450 μm source counts calculated from the SHADES data analyzed in this work, compared with estimates of the 850 μm source counts presented previously in the literature, and the model fit to the combined SHADES counts presented by Coppin et al. (2006). The *dashed line* shows the counts predicted by assuming a greybody spectral energy distribution ($T_{dust} = 40$ K, $\beta = 1.2$) and the 60 μm luminosity function calculated from IRAS galaxies (Saunders et al. 1990) which evolves as $L_*(z) = L_*(z = 0) \cdot (1 + z)^{3.2}$ out to $z = 2.2$ and then remains constant to $z = 6$.

2.4.6 450 μm Source Counts

The source counts at 450 μm are estimated following the same recipe used to estimate the 850 μm source counts (Section 2.4.3.2), with two exceptions. The first difference is that I only consider 450 μm source candidates with S/N $\geq$ 3.5, as we expect a greater number of spurious sources above each signal to noise threshold in the 450 μm map due to the smaller beamsize. The second difference is that I do not correct for flux boosting as I did in the case of the 850 μm source candidates. The reason for this is that there are currently no strong constraints on the 450 μm source counts, which are needed to populate the fake source maps used to estimate the flux boosting factors. If the 450 μm extragalactic background population is the same as the 850 μm population, then it is possible to predict the shape and amplitude of the 450 μm source counts under the assumption of a single spectral energy distribution (e.g. Figure 2.3). Comparing the SHADES 450 μm source count estimates plotted in Figure 2.24 with the predictions of such a model, implies that the true 450 μm fluxes should be $\sim$40 mJy lower than observed over the flux density interval S_{450} $\sim$50–110 mJy.

To conclude, although the 450 μm data does appear to provide counterparts to a few of the 850 μm source candidates, the uncertainty in the number and measured fluxes of secure sources has not yet reached the level for robust estimates if the 450 μm source counts. This situation is likely to improve for future surveys with the more sensitive 450 μm array on the new SCUBA-2 instrument to begin operation on the 15 m diameter JCMT in early 2007.

2.4.7 450 μm Stacking Analysis

I have demonstrated that the 450 μm SHADES data do not provide reliable detections for the majority of individual 850 μm source candidates, nor is it possible to place strong constraints on the 450 μm source counts, yet one may still ask if the population as a whole is detected in the SHADES data. In order to address this question, I perform a 'stacking analysis', whereby the 450 μm fluxes and uncertainties in the pixels nearest to the central positions of sources in a particlular subsample are averaged:

$$\mathrm{w_{450-i}} = \frac{1}{\sigma^2_{\mathrm{450-i}}} \tag{2.11}$$

$$\mathrm{S_{450-stacked}} = \frac{\sum_{\mathrm{i}} \mathrm{w_{450-i}}\ \mathrm{S_{450-i}}}{\sum_{\mathrm{i}} \mathrm{w_{450-i}}}. \tag{2.12}$$

The uncertainty on this value is then:

$$\sigma_{450-\mathrm{stacked}} = \frac{1}{\sqrt{\sum_{\mathrm{i}} \mathrm{w}_{450-\mathrm{i}}}}. \quad (2.13)$$

In this analysis, the 450 μm stacked fluxes are calculated at the positions of sources in five different subsamples: *i)* 850 μm consortium source catalogue, *ii)* 850 μm INAOE source catalogue, *iii)* 850 μm consortium sources with radio IDs, *iv)* 850 μm consortium sources without radio IDs, and *v)* 850 μm consortium sources with radio counterparts at the position of the radio source[6]. Table 2.2 gives the stacked 450 μm flux along with the weighted mean of the 850 μm flux for the corresponding subsample.

The results presented here are in broad agreement with those of two additional independant analyzes of the 450 μm SHADES data (see Coppin et al. 2006). I note however, that the uncertainties on the 450 μm stacked fluxes in this reduction are, on average, $\sim$17% lower than those obtained by 'Group D' (UBC) whose calibration strategy is to adopt monthly average flux conversion factors (FCFs) provided by the JCMT staff, rather than calculating their own FCFs from nightly calibration observations as I have done for the INAOE reduction ('Group C'). As the analysis of 450 μm wavelength data will be more sensitive to differences in the calibration strategy than that of the 850 μm data, I suggest that the lower uncertainties on the INAOE stacked fluxes, relative to those of UBC, indicate that calibration factors determined on a nightly basis are more accurate than those derived from a monthly average.

It is evident from the stacked flux values in Table 2.2 that all 850 μm selected subsamples in both fields are detected, on average, at 450 μm. Interestingly, the average 450 μm flux of 850 μm sources with 1.4 GHz radio counterparts is higher than that of those without radio counterparts. This is most likely due to the 1.4 GHz detected sources being at lower redshifts, as there is a positive K-correction to the radio fluxes of SMGs, so the radio detected objects should also exhibit larger 450 μm fluxes (Figure 2.5) than those without radio counterparts. Figures 2.25 and 2.26 show postage stamps of the stacked 450 μm flux images of the radio detected (at the 1.4 GHz counterpart position) and undetected subsamples, along with the stacked 450 μm

[6]The 1.4 GHz VLA observations will be presented in Ivison et al. in preparation, but it is important to mention here that the synthesized beamsize of the radio images range from $1.3 - 3.9$ arcsecs

LH	$S_{450-\mathrm{stacked}}$ [mJy]	$\bar{S}_{850}$ [mJy]
850 μm consortium sources:	12.4±2.1	5.29±0.22
850 μm INAOE sources:	7.1±1.8	6.52±0.20
850 μm consortium with 1.4 GHz ID (850 μm pos.):	20.8±3.3	6.37±0.38
850 μm consortium without 1.4 GHz ID:	7.4±2.7	4.76±0.26
850 μm consortium with 1.4 GHz ID (radio pos.):	22.0±3.3	6.37±0.38
SXDF		
850 μm consortium sources:	12.5±2.4	5.33±0.24
850 μm INAOE sources:	8.6±2.3	7.11±0.24
850 μm consortium with 1.4 GHz ID (850 μm pos.):	14.1±3.9	6.25±0.40
850 μm consortium without 1.4 GHz ID:	11.4±3.1	4.77±0.31
850 μm consortium with 1.4 GHz ID (radio pos.):	17.9±3.8	6.25±0.40

Table 2.2: 450 μm stacked fluxes in mJy for various subsamples of the 850 μm SHADES source catalogue.

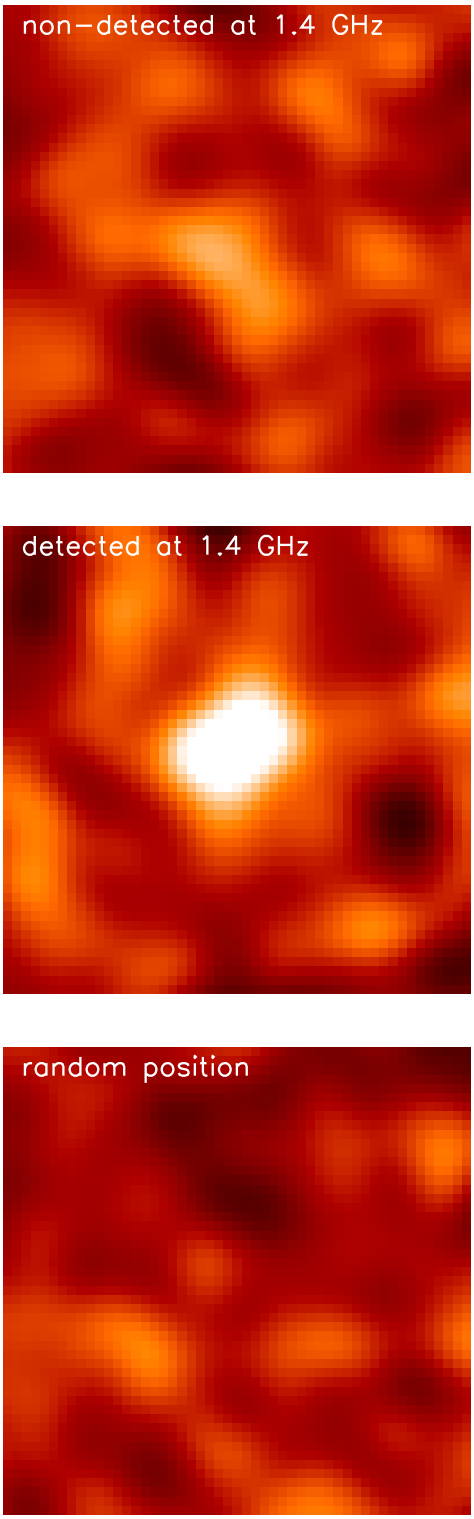

Figure 2.25: Postage stamps of the signal-to-noise ratio for the stacked 450 μm flux in $50'' \times 50''$ regions of the Lockman Hole map centered at the positions of *top:* 850 μm consortium sources without radio detections, *middle:* the radio ID for 850 μm consortium sources with radio detections, and *bottom:* 60 randomly chosen locations in the 450 μm Lockman Hole map. In all 3 cases the colour scale runs from -5 to +5-σ.

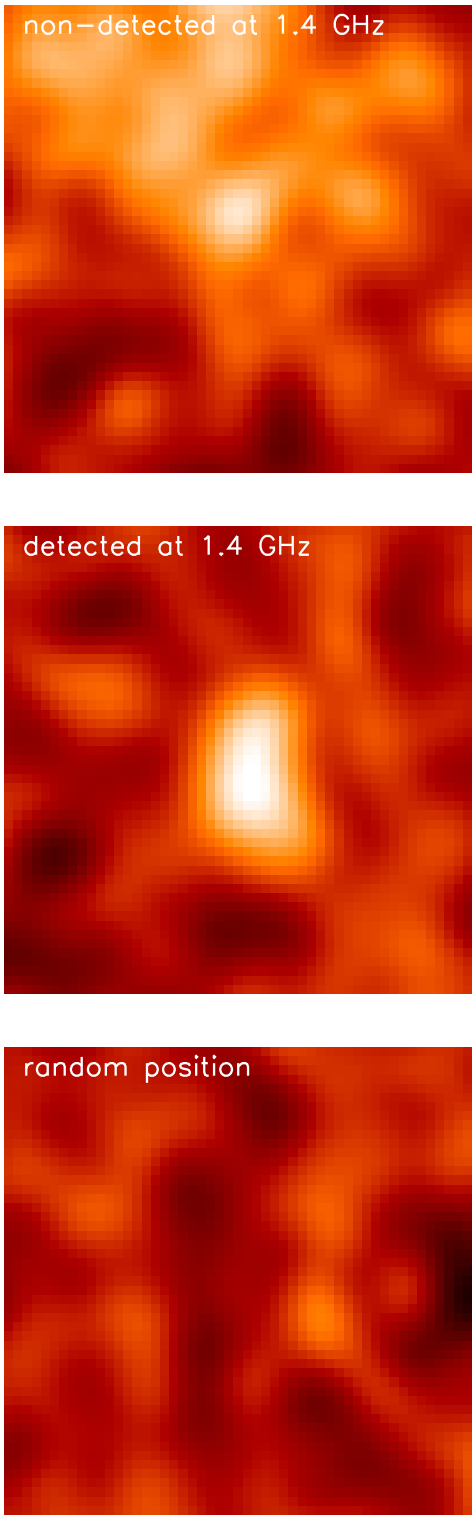

Figure 2.26: Postage stamps of the signal-to-noise ratio for the stacked 450 μm flux in $50'' \times 50''$ regions of the SXDF map centered at the positions of *top:* 850 μm consortium sources without radio detections, *middle:* the radio ID for 850 μm consortium sources with radio detections, and *bottom:* 60 randomly chosen locations in the 450 μm SXDF map. In all 3 cases the colour scale runs from -5 to +5-σ.

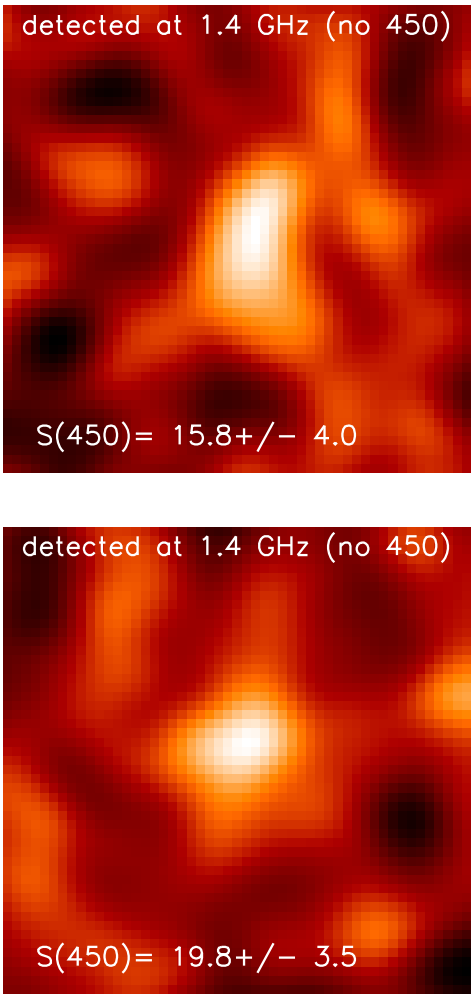

Figure 2.27: Postage stamps of the stacked 450 μm fluxes at the positions of radio detected 850 μm consortium sources in the Subaru XMM Deep Field (*top*) and the Lockman Hole (*bottom*), where I have excluded the sources which I believe to have secure 450 μm counterparts (see Tables A.1 and A.2).

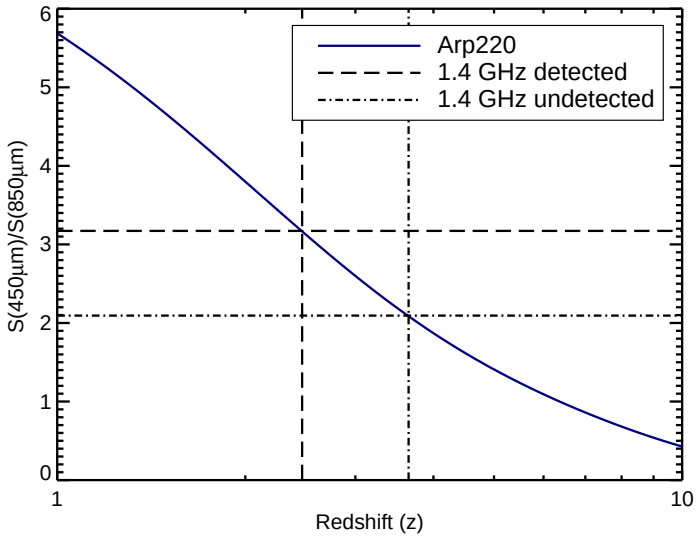

Figure 2.28: Assuming an Arp220 type spectral energy distribution, I plot the ratio between the 450 and 850 μm flux density as it evolves with redshift. The *long dashed* lines show the mean ratio of the stacked fluxes for the radio detected subsample of sources in both fields. Likewise, the *dot-dashed* lines show the mean ratio of the stacked fluxes for the radio undetected subsample. The mean redshifts for the radio detected and undetected samples are z=2.5 and 3.7, respectively, under the assumption of an Arp220 spectral energy distribution.

flux images corresponding to 60 positions chosen at random in each of the two fields. In order to determine whether the detection of the radio subsamples in the 450 μm stacked flux analysis could be due to the contribution from a few objects detected individually at high significance, I repeat the stacking analysis for the radio detected subsample of 850 μm consortium sources while excluding those sources believed to be detected at 450 μm (Section 2.4.4). The results of this calculation are shown in Figure 2.27, which demonstrates that the small number of bright 450 μm counterparts are not responsible for the measured signal.

Taking into account the uncertainties on the stacked fluxes given in Table 2.2, I calculate the average 450-to-850 μm flux density ratio for the 850 μm consortium sources in both the radio detected and undetected subsamples.

Figure 2.28 compares these ratios to the expected ratio for an object with the same far-infrared spectral energy distribution (SED) as Arp220, redshifted out to $z > 10$. Under this assumed SED shape, the mean redshift of the radio undetected sources is $z = 3.7^{+1.3}_{-1.0}$, while the mean redshift of the radio detected sources is $z = 2.5^{+0.7}_{-0.6}$. Although the uncertainties on these mean redshifts are large, the result still supports the suggestion that there exists a high-redshift tail ($z \gg 3$) to the (sub)mm galaxy population. If these radio undetected 850 μm SHADES sources do indeed lie at higher redshifts, then that would imply that the current redshift surveys of optical counterparts to SMGs identified through radio interferometry (Chapman et al. 2003, 2005), are missing members of a high-redshift tail (i.e. $z \gg 3$) of this population. Obtaining redshifts for individual objects associated with this high-redshift tail is more challenging, as the optical/infrared counterparts are harder to identify given the optical/infrared K-correction. To address this problem, I present an alternative approach to measuring redshifts for these objects in chapter 3.

2.5 Clustering of (Sub)mm Galaxies

One of the initial goals of the SHADES survey was to measure the angular clustering strength of the bright (S_{850} >8 mJy) population in order to test the hypothesis that these SMGs are indeed the progenitors of massive elliptical galaxies. Without the additional spatial constraint provided by the redshift information (which will be addressed in chapter 3), one must rely on the angular correlation function statistic discussed in Section 1.1.1. Although the results presented here are preliminary, the full analysis will be presented in Gaztañaga, Wagg et al. (in preparation).

Figure 2.29 shows the results of combining the 2-point angular correlation function measured from the LH and SXDF consortium sources. Although the significance of the positive correlation on small scales is small, there is a 2-σ measurement of bias (see Section 1.1.1) with respect to local APM galaxies ($b = 1.17^{+0.24}_{-0.31}$) whose measured correlation function (Baugh & Efstathiou 1993) has been projected out to z=2–3, the median redshift of the bright SMG population (Aretxaga et al. 2003, 2005; Chapman et al. 2003, 2005). The data are inconsistent with the projected bias of massive galaxy clusters ($b \sim 3$; Gonzalez et al. 2002) at the 3-σ level.

The bias may be converted to a correlation length assuming that the

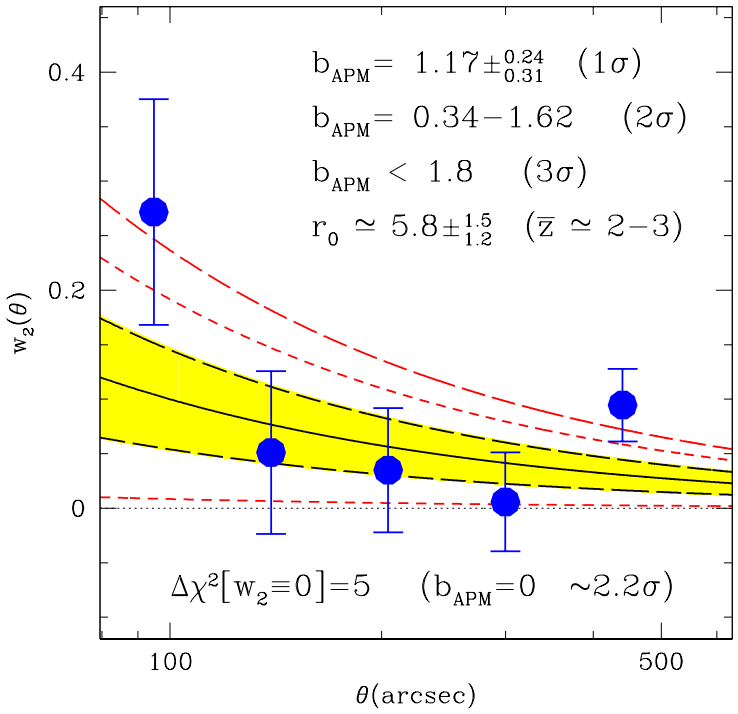

Figure 2.29: The combined angular 2-point correlation function of 850 μm sources in the SHADES SXDF and LH consortium catalogues (*filled circles*). This measurement is compared to w_2 measured for nearby APM galaxies (Baugh & Efstathiou 1993) projected out to z=2–3, by fitting the bias parameter presented in Section 1.1.1. The *shaded region* defines the 1-σ confidence interval while the *short* and *long dashed* lines show the 2-σ and 3-σ bounds respectively (Gaztañaga, Wagg et al. in preparation).

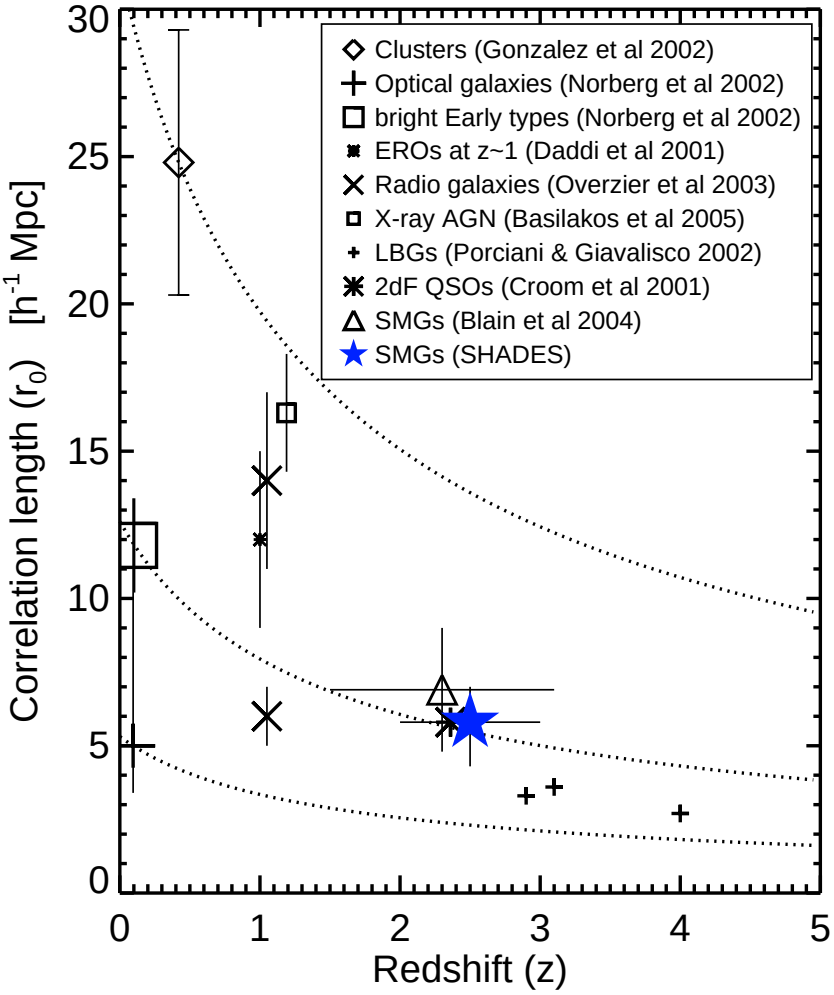

Figure 2.30: The correlation length of the clustering strength for different populations of objects at low and high redshift, compared with that of SMGs in SHADES, $r_0 = 5.8 \pm 1.4h^{-1}$ Mpc. The *dotted lines* show the predictions of the stable clustering model of Carlberg et al. (1997), normalized to the correlation lengths of 3 low-redshift populations.

SHADES sources lie at redshifts z=2–3. We find, $r_0 = 5.8 \pm 1.4h^{-1}$ Mpc which is consistent with $r_0 = 6.9 \pm 2.1h^{-1}$ Mpc found by Blain et al. (2004) in their sample of SMGs with measured redshifts. The implication of this result is that the SMGs appear to exhibit a clustering strength which is closer to that of nearby early type galaxies (Norberg et al. 2002) and 2dF QSOs at $z \sim 2.4$ (Croom et al. 2001) than to that of massive clusters. Wider area surveys with future facilities such as the LMT, or SCUBA2 on the JCMT, will lead to much tighter constraints on the angular clustering strength of the SMG population.

2.6 Future Work

The demise, and subsequent retirement of SCUBA in early 2005 meant that only ∼40% of the SHADES survey area was observed. Without the availability of a continuum instrument on the JCMT until the arrival of SCUBA-2 in early 2007, an opportunity arose for the commissioning of a new instrument; the 144 bolometer Astronomical Thermal Emission Camera (AzTEC; PI - Grant Wilson), destined to be the first light 1.1 mm camera on the 50 m LMT when it begins operation in early 2008. The combination of a larger field of view (∼4×4 square arcmins compared to ∼2×2 square arcmins), greater number of bolometers (144 versus 37), and operating in the more transparent 1 mm atmospheric window, meant that the mapping speed of AzTEC on the JCMT would be a factor of ∼15× faster than SCUBA. As such, a number of Galactic and extragalactic projects were conducted with AzTEC on the JCMT during the last half of 2005.

One of the JCMT/AzTEC projects was a continuation of the SHADES survey, reaching a typical 1-σ depth of ∼0.8 mJy at 1.1 mm over the entire 0.5 square degree area originally proposed. In addition to increasing the number of source candidates in the SHADES catalogue and tightening the constraints on both the bright end of the 850 μm source counts and the angular clustering strength of SMGs, this new survey will lead to a more robust sample of 850 μm source candidates which will benefit from an additional flux measurement in order to better constrain the SED shapes. The results of this new survey will be presented in an upcoming SHADES publication.

In early 2008, the LMT is expected to begin operation as the world's largest single-dish mm-wavelength facility. With AzTEC on the LMT, the expected mapping speed is ∼0.36 square degrees per hour to a 1-σ rms of

1 mJy at 1.1 mm. Figure 2.31 compares the expected fraction of the 200 μm extragalactic background[7] that has been resolved by current 850 μm SCUBA surveys, with that expected to be resolved by 4 proposed 1.1 mm surveys with AzTEC on the LMT. Each of these surveys would only require $\sim$4.3 hours of on-source observing time assuming the above mapping speed. It is clear that the greater mapping-speed and higher angular resolution ($\sim$6 arcsec - which lowers the confusion limit) will mean that the proposed LMT/AzTEC surveys should collectively resolve most of the 200 μm extragalactic background population. Combined with redshifts for individual objects (discussed in chapter 3), these proposed surveys would result in the first concrete estimates of the obscured cosmic star formation rate over redshifts $z \sim$1–10.

[7]The intensity of the FIR background radiation peaks at $\sim$200 μm.

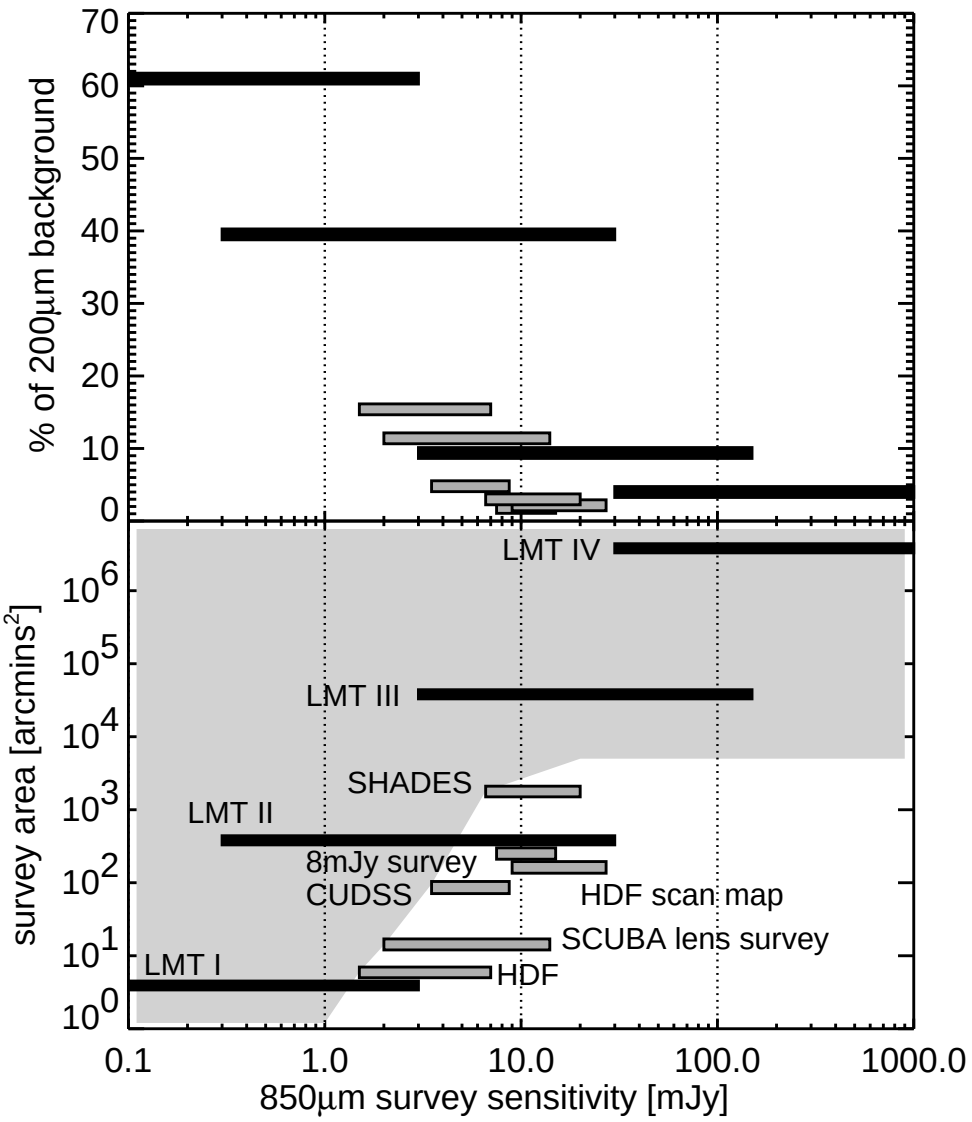

Figure 2.31: A summary of past and present, blank-field extragalactic 850 μm surveys, and future LMT surveys at 1.1 mm. In the *bottom* panel, each survey is represented by a shaded bar which extends from the 3-σ flux density limit of the survey, to the flux density of the brightest source detected in the survey. The grey shaded region shows the parameter space which has not been sampled by the present generation of surveys, but that will be explored by upcoming surveys with the LMT. The *top* panel shows the percentage of the 200 μm extragalactic background which should be resolved by each of these surveys, under the assumption of an Arp220 type galaxy SED model, which is used in conjunction with an evolving 60 μm luminosity function, to reproduce the observed intensity of the 200 μm extragalactic background radiation.

Chapter 3

Obtaining redshifts for submm galaxies using broadband cm wavelength spectroscopy

3.1 Introduction

Although the wide-area extragalactic surveys discussed in Chapter 2 can provide constraints on the angular distribution of submm galaxies (SMGs), redshifts for individual objects provide tighter constraints on their clustering strength, which is important for showing how these objects fit into the hierarchical framework of large-scale structure formation. In addition, redshifts for the SMGs are required to measure their far-infrared luminosities, a quantity that may then be converted into an estimate of the global rate of obscured star-formation[1] in the Universe over the redshift range $1 \lesssim z \lesssim 6$. The importance of this last point will be revisited in Chapter 5, where I discuss the impact of high-redshift galaxies and AGN on the gas in the surrounding intergalactic medium.

[1] An estimate of an object's obscured star-formation rate may be obtained from its' total infrared luminosity ($[L_{\odot}]$) following the approximation, $SFR \approx 1.2 \times 10^{-10} L_{IR}$ [$M_{\odot}$ yr^{-1}] (Kennicutt 1998).

Due partly to their obscured nature, identification of optical counterparts, and subsequent spectroscopic redshift determination for the members of the population of high-redshift, dusty starburst galaxies discussed in Chapter 2, has proven challenging and costly in terms of the observing time required for follow-up radio, and optical observations (e.g. Ivison et al. 2002; Chapman et al. 2003). The large beamsizes of the submm/mm instruments used to discover these SMGs (typically 10-15″), means that a number of optical/infrared counterparts could potentially be responsible for the submm emission. There are currently three main avenues available for obtaining the redshift of an individual SMG:

1. Identification of an optical/infared counterpart through *i)* radio-wavelength interferometry (e.g. Smail et al. 2000; Ivison et al. 2002), *ii)* deep near-infrared imaging (e.g. Egami et al. 2004), or (preferably) *iii)* submm/mm-wavelength interferometry (e.g. Downes et al. 1999), whose redshift is subsequently determined through optical spectroscopy with large, 10-meter class telescopes (e.g. Chapman et al. 2003, 2005).

2. By adopting a range of template, far-infrared-to-radio wavelength spectral energy distributions of far-infrared luminous galaxies, the observed photometric data (or limits) for an individual SMG may be used to estimate its most probable photometric redshift (e.g. Carilli & Yun 1999, 2000). This technique has proven to be accurate to, $\triangle z \pm 0.5$, when four, or more observations at submm-to-radio wavelengths are available (Hughes et al. 2002; Aretxaga et al. 2003, 2005).

3. Broadband mm-to-cm wavelength spectroscopy of an individual SMG, using sensitive, large beamsize instruments ($5'' - 1'$), can potentially provide an accurate redshift through detection of one, or more CO emission line transitions, where the observed separation between adjacent transitions is given by, $\triangle\nu_{obs} = 115/(1+z)$ GHz.

Of these three techniques, the most desirable means of redshift determination for SMGs is through the use of broadband mm-to-cm wavelength spectroscopy, as this method eliminates any ambiguity associated with the optical/infrared counterpart to the SMG, and minimizes the observing time required on the various multi-wavelength facilities. This method should also be more accurate than either photometric redshift estimates, or even optical redshift estimates, given the commonly large velocity difference between a

molecular CO line redshift (assumed to originate at the intrinsic velocity of the galaxy), and an optical emission/absorption line redshift, as the latter may be biased due to galactic winds, or absorption by dust.

Unfortunately, as opposed to the wide velocity coverage traditionally available with optical spectrographs, the mm-to-cm wavelength regime has suffered due to the narrow bandwidth provided by the current generation of receivers (typically 500-1000 MHz, or ∼1000-3000 km s^{-1} at mm-wavelengths). This issue is being addressed by the upcoming generation of broadband receivers set to be commissioned, or already in place, on large existing facilities such as the Green Bank Telescope (GBT[2]). It is anticipated that the most powerful instrument for such redshift searches will be the 50-meter diameter, Large Millimeter Telescope (LMT/GTM[3]), currently under construction in the state of Puebla, Mexico, and set to begin operation in early 2008. The first generation of instruments for the LMT will include a 'redshift machine' heterodyne receiver, operating at ∼90 GHz with an instantaneous bandwidth of ∼35 GHz (P.I. Neal Erickson).

Even with the capability of wide bandwidth, mm-to-cm wavelength receivers on large telescopes, it is important to have an independant, photometric estimate of the redshift for a SMG. This estimate may be used either to guide the choice of the initial frequency tuning for a CO line search, or otherwise guide the choice of follow-up frequency tuning in those cases where only one CO line transition is detected. In this chapter, I describe the results of an experiment whereby the photometric redshift estimate for HDF850.1 (based on the technique described in Hughes et al. 2002; Aretxaga et al. 2003; illustrated in Figure 3.1), the brightest SMG in the confusion limited, 850 μm JCMT/SCUBA survey of the *Hubble Deep Field* by Hughes et al. (1998), is used to motivate a GBT search for CO J=1-0 and CO J=2-1 line emission in this object. This is the first time that such a wide redshift-interval has been covered in a search for CO line emission in a high-redshift object, and the results are also presented in Wagg et al. (2006b).

[2]The Green Bank Telescope is a facility of the National Radio Astronomy Observatory, operated by Associated Universities, Inc. under a Cooperative Agreement with the National Science Foundation.

[3]http://www.lmtgtm.org

3.2 Observations of molecular CO line emission in far-infrared luminous galaxies at high-redshift

Over the past 15 years, observing CO line emission in high-redshift objects has become a powerful means of constraining the physical conditions of the gas within their molecular ISM (for an excellent review see Solomon & Vanden Bout 2005). The luminosity in the CO J=1-0 line is the optimal estimator of the total molecular gas mass, yet for practical reasons, in gas-rich objects at high-redshift (z $\gtrsim$ 2), searches are normally first conducted for emission from high-J ($J_{\rm upper} \geq 2$) CO line transitions, and subsequent searches for CO J=1-0 emission are carried out if the mm-wavelength searches for high-J CO lines are successful. This approach can bias the sample of objects detected in CO line emission to those with hotter, and denser gaseous mediums.

To date, high-J CO line emission has been detected in 12 SMGs (Frayer et al. 1999; Neri et al. 2003; Genzel et al. 2003; Greve et al. 2005; Tacconi et al. 2006), while the CO J=1-0 line has been detected in only one of these (Hainline et al. 2006). In addition to the faintness of molecular emission lines in high-redshift SMGs, searches have been hindered by the limited spectral bandwidth of current mm-wavelength facilities, generally covering $\sim$1700 km s^{-1} at 3 mm, while the typical SMG CO linewidth is $\sim$800 km s^{-1} FWHM. This narrow bandwidth can also be restrictive as galactic outflows in many high-redshift SMGs may lead to large velocity offsets between the redshifts derived from Lyα, and those derived from CO emission lines. In some SMGs this difference may be greater than 600 km s^{-1} (e.g. Greve et al. 2005), due possibly to galactic outflows, or scattering of Lyα photons by dust. As CO emission-line frequencies are not expected to be biased with respect to the systematic redshift, broadband spectroscopic searches for CO line-emission should be a powerful means of obtaining redshifts for the SMG population.

Educated searches for mm-to-cm wavelength molecular CO line emission in far-infrared luminous objects with no prior redshifts, are now becoming feasible as wideband spectrometers become available on large mm-to-cm wavelength telescopes, such as the 100 m diameter Green Bank Telescope (GBT; Jewell & Prestage 2004), or the 50 m Large Millimeter Telescope (LMT[4]; Ser-

[4]http://www.lmtgtm.org

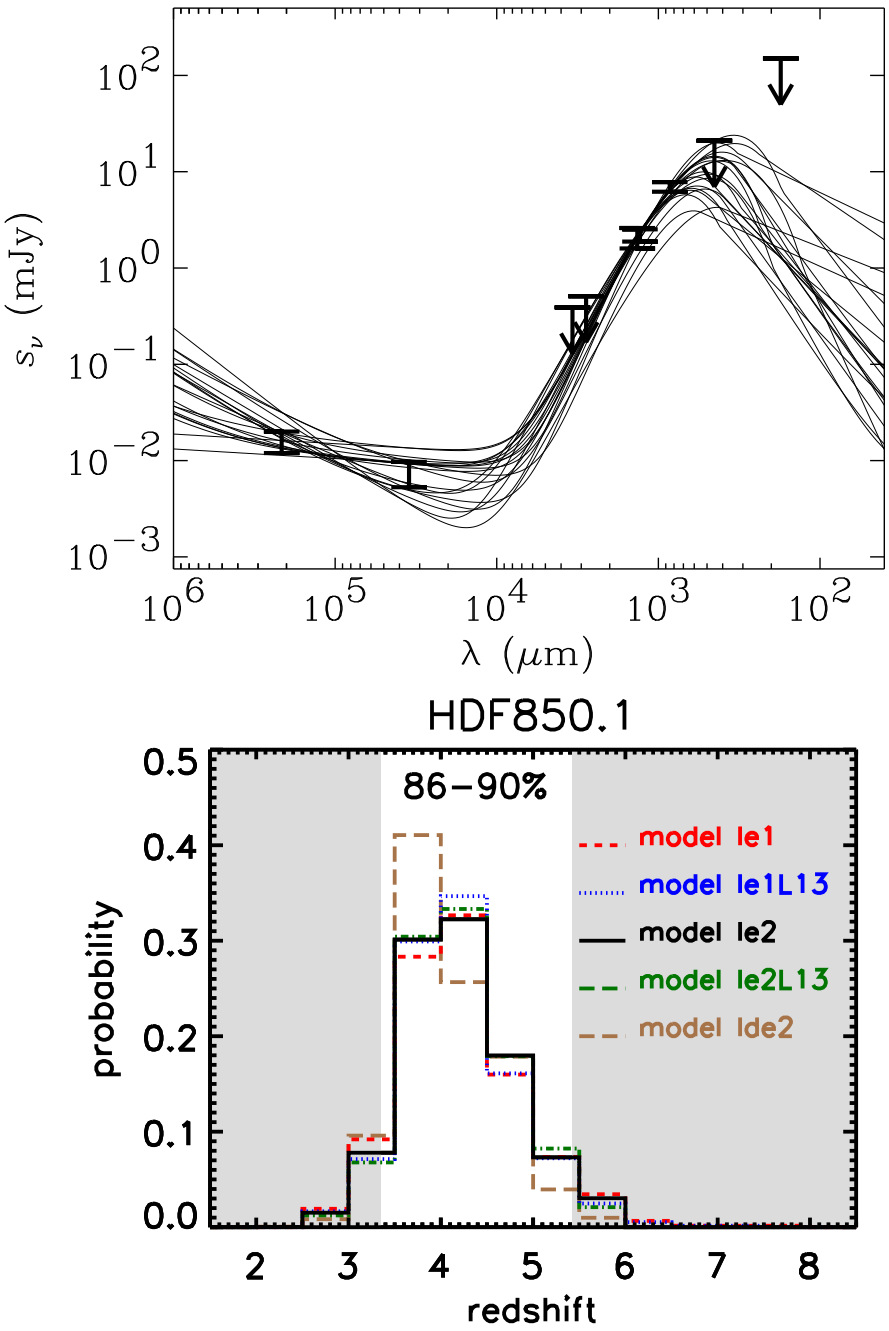

Figure 3.1: **a)** Photometric data for HDF850.1 over observed far-infrared to radio wavelengths. Also shown are a range of template spectral energy distributions, adopted from nearby starbursts, ultraluminous infrared galaxies, and AGN, all redshifted to fit the data for HDF850.1 (taken from Chapin 2004). **b)** The predicted photometric redshift distribution for HDF850.1, derived from various evolutionary models of the 60 μm luminosity function which is adopted as a prior in these calculations (see Hughes et al. 2002; Aretxaga et al. 2003, 2005; Chapin 2004). The shaded region defines the redshift boundaries for which the 115.2712 GHz CO J=1-0 line would emit at frequencies outside the GBT K-band receiver window. The models predict an 86-90% probability that the CO J=1-0 line is redshifted to K-band frequencies (Aretxaga et al. 2003; Dunlop et al. 2004).

rano et al. 2006). In order to obtain preliminary redshift estimates and guide the frequency tunings of these spectroscopic searches for molecular line emission in SMGs, some groups have developed photometric redshift techniques which exploit the far-infrared-to-radio wavelength correlation in star-forming galaxies (Helou et al. 1985), or adopt template far-infrared spectral energy distributions (SEDs) based on nearby galaxies (Carilli & Yun 1999, 2000; Dunne, Clements & Eales 2000a; Rengarajan & Takeuchi 2001; Hughes et al. 2002; Aretxaga et al. 2003; Wiklind 2003). These techniques can potentially provide redshift estimates for large samples of SMGs with individual accuracies, $\delta z \sim \pm 0.3$, when photometric flux measurements of 3 or more far-infrared-to-radio wavelengths are available (Aretxaga et al. 2005).

The GBT is the only operational mm-to-cm wavelength telescope in the world with instruments that have both sufficient spectral line sensitivity and receiver bandwidth to conduct guided searches for CO line emission in SMGs at redshifts $z \gtrsim 0.9$. This lower redshift limit is set by the current GBT frequency limit of 60 GHz and the CO J=1-0 line rest frequency of 115.2712 GHz. Given this restriction, an excellent candidate for conducting a blind search for CO line emission is HDF850.1 (Hughes et al. 1998), one of the most well studied SMGs, and the brightest 850 μm source in the confusion limited JCMT/SCUBA survey of the northern *Hubble Deep Field*. Due partly to the extreme optical faintness ($K \simeq 23.5$, $I - K > 5.2$) of the gravitationally lensed galaxy counterpart to HDF850.1 (Dunlop et al. 2004), the redshift of this object has proven elusive. A wealth of deep rest-frame far-infrared-to-radio wavelength observations of HDF850.1 provide the basis for a photometric redshift z=4.1±0.5 (Yun & Carilli 2002; Aretxaga et al. 2003). In principle, HDF850.1 presents an ideal target for the GBT with which to test the accuracy of our photometric redshift technique, and thus has motivated a GBT search for CO J=1-0 and CO J=2-1 line emission over the redshift interval, $3.3 \lesssim z \lesssim 5.4$.

3.3 Observations and Data Reduction

The far-infrared-to-radio wavelength photometric redshift estimate of Aretxaga et al. (2003) implies an 86 to 90% probability that HDF850.1 has a redshift in the range, $3.3 \leq z \leq 5.4$. Over this redshift interval, the 115.2712 GHz CO J=1-0 line is redshifted into the 18.0 to 26.5 GHz frequency window of the K-band receiver on the GBT. Motivated by this prediction, we have

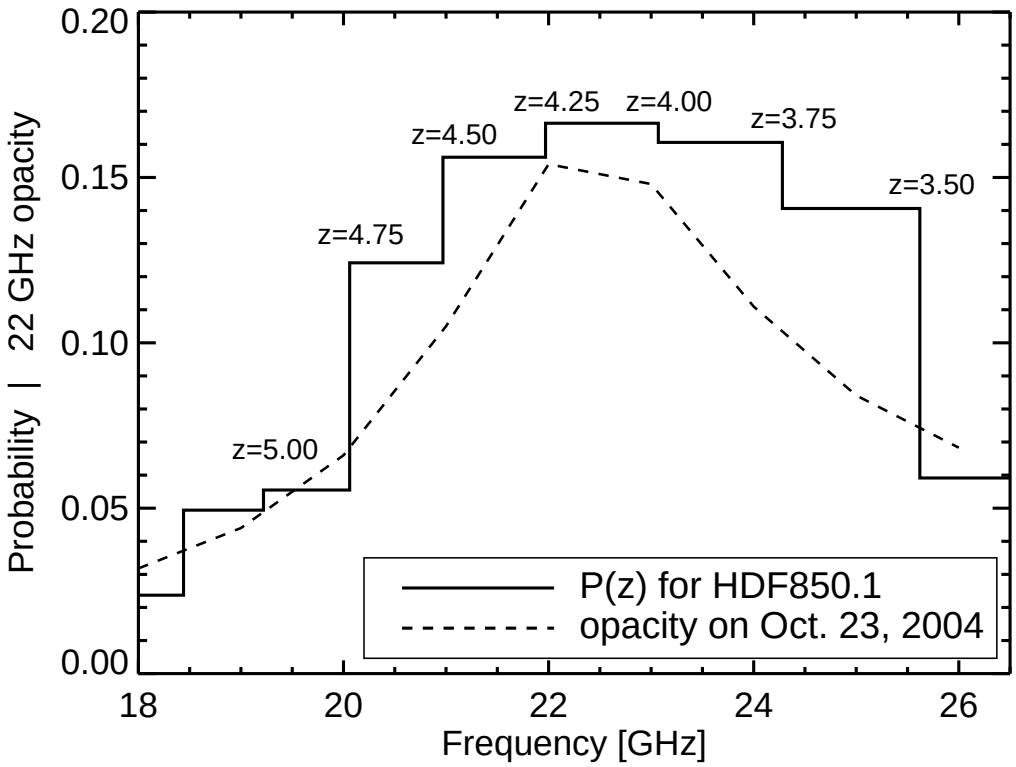

Figure 3.2: The most recent submm-to-radio-wavelength photometric redshift estimate for HDF850.1, plotted as a function of redshifted (115.2712 GHz) CO J=1-0 line frequency (*solid line*). The *dashed line* shows an example of the opacity across the K-band due to the atmospheric water vapour line at ∼22 GHz.

obtained a complete K-band spectra of HDF850.1 in order to search for redshifted CO J=1-0 line emission.

I carried out observations in nod mode with the GBT K-band receiver during October 2004 and May 2005. All of the K-band observations were conducted under reasonably dry conditions, with an average 22 GHz zenith opacity, $\tau_{22\mathrm{GHz}} \sim 0.09$. The nearby quasar 3C295 was used for pointing purposes, as well as baseline and flux calibration throughout the K-band observations. To correct for slowly varying, large-scale spectral baseline features, the observations were made by alternately nodding two beams seperated by 178.8 arcsecs, between the source and blank sky. The GBT spectrometer

allows a maximum instantaneous frequency coverage of 800 MHz bandwidth in each of four independent quadrants. For the observations presented here, one pair of quadrants was used to measure a ∼1.5 GHz wide spectra on the source, while the other pair measured blank sky in the off-beam. A total of 6 tunings (or sequences) were therefore used to cover the entire K-band window. Each spectral channel was 0.39 MHz wide so that the velocity resolution varied from ∼4.4 km s^{-1} to ∼6.5 km s^{-1} across the band. A total of 28.2 hours of integration time was devoted to the HDF850.1 K-band spectra. The time spent on each ∼1.5 GHz tuning sequence was varied to compensate for the increased opacity towards the center of the band, due to the 22 GHz atmospheric water vapour line. The goal was to obtain a spectra with uniform noise across the K-band. Overheads such as pointing, focusing, acquisition of baseline calibration spectra, and follow-up of potential CO line detections, amounted to an additional factor of ∼2 increase in the observing time.

In December 2005, a search was also conducted for CO J=2-1 emission using the GBT Q-band receiver (40 to 48 GHz), over the redshift interval, $3.91 \lesssim z \lesssim 4.25$. As in the case of the K-band observations, the nod observing mode was adopted, while the spectrometer was set up in wide bandwidth, low resolution mode. The velocity resolution varied from ∼2.5 km s^{-1} to ∼2.7 km s^{-1} across our Q-band spectra. As there is a dearth of bright, compact calibration sources at these higher frequencies, the primary flux calibrator was 3C286, while the nearby quasar 1153+495 (∼17^o separation) was used for pointing.

Obtaining quality spectra with the GBT Q-band receiver generally requires low wind speeds (≤3 m s^{-1}), and an extremely dry, stable atmosphere. Only on a single night in December 2005, was data obtained under just such conditions, with a median $\tau_{44\mathrm{GHz}} \sim 0.1$ and negligible wind speeds. Despite acceptable Q-band weather conditions during this, and possibly one other observing shift, only the left polarization Q-band spectra is included in our analysis, as the majority of the right polarization spectra suffer from a severe baseline ripple of unknown origin (see §3.3.1).

Both the K-band and Q-band spectra were reduced using the *gbtidl*[5] data analysis package. For a series of consecutive scans, a co-added spectra

[5]http://gbtidl.sourceforge.net

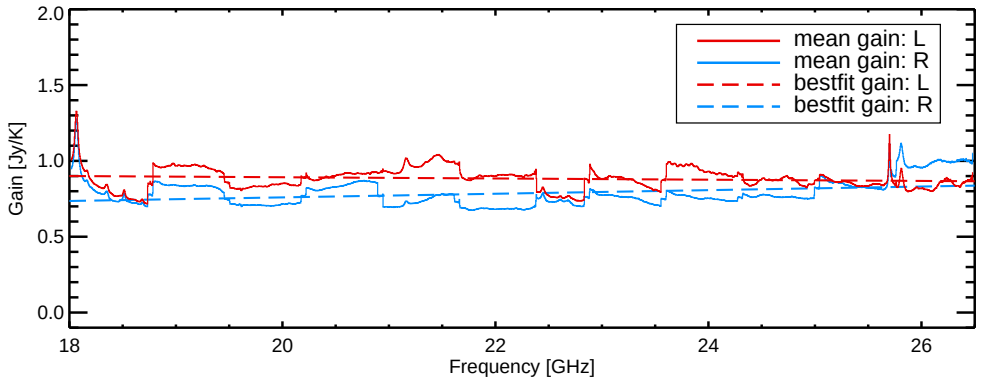

Figure 3.3: The GBT K-band gain (in Jy/K) for the left and right polarizations, averaged over all observations of the calibrator, 3C295 (*solid lines*). Also plotted as *dashed lines* are the bestfit linear regression curves to the data. These fits are then used to calibrate the combined HDF850.1 spectra, and are in good agreement with the values quoted in the GBT observing guide.

is produced following the standard procedures described by Vanden Bout, Solomon & Maddalena (2004), which are only outlined here for completeness.

For simplicity, I will consider the spectra in only one quadrant, and one polarization from each of the two beams in the discussion that follows. I refer to these spectra as $B_1(\nu)$ and $B_2(\nu)$, where one of the two beams is always pointed 'ON' the source, while the 'OFF' beam is observing blank sky separated from the source by 178.8 arcsecs in azimuth. A single scan is the time that one beam spends on-source before nodding to the off-source position, when the other beam is nodded onto the source. For our observations, a scan duration of 1 minute was adopted. This scan length minimizes the frequency dependant variation in the sky brightness temperature between succesive scans, while also minimizing the time devoted to overheads such as nodding. Assuming that $B_1(\nu)$ begins on-source at scan i, then a series of normalized spectra are produced by subtraction of the off-source scan from the on-source scan (note that from this point on, the ν dependance will not be made explicit):

$$\left(B^{(i)}_{1-\mathrm{ON}} - B^{(i+1)}_{1-\mathrm{OFF}}\right) / B^{(i+1)}_{1-\mathrm{OFF}},$$

$$\left(B^{(i+1)}_{2-\mathrm{ON}} - B^{(i)}_{2-\mathrm{OFF}}\right)/B^{(i)}_{2-\mathrm{OFF}},$$
$$\left(B^{(i+2)}_{1-\mathrm{ON}} - B^{(i+3)}_{1-\mathrm{OFF}}\right)/B^{(i+3)}_{1-\mathrm{OFF}},$$
$$\left(B^{(i+3)}_{2-\mathrm{ON}} - B^{(i+2)}_{2-\mathrm{OFF}}\right)/B^{(i+2)}_{2-\mathrm{OFF}},$$
$$\left(B^{(i+4)}_{1-\mathrm{ON}} - B^{(i+5)}_{1-\mathrm{OFF}}\right)/B^{(i+5)}_{1-\mathrm{OFF}},$$
$$\left(B^{(i+5)}_{2-\mathrm{ON}} - B^{(i+4)}_{2-\mathrm{OFF}}\right)/B^{(i+4)}_{2-\mathrm{OFF}},$$
etc....

It is important that each normalized spectra be created from the 'ON'-'OFF' scan pair that travel down the same signal path (ie. the signal from a single beam and polarization), so that any path-dependant sources of baseline structure may be properly subtracted. An average of these normalized spectra is then calculated, with each spectrum weighted simply by the inverse square of the system temperatures, T_{sys}^{-2}. The units of this mean spectrum are then calibrated from [K] to [Jy] using the best-fit gain curves shown for the K-band observations in Figure 3.3. The gain curves were derived from observations of objects with known (and non-variable) radio flux densities (3C295 for the K-band spectra and 3C286 for the Q-band spectra).

The left and right polarization spectra are analyzed separately so that any potential detection of CO line emission would have to be confirmed in both polarizations. A large fraction of the data ($\sim$53%) were considered unusable due to various forms of spectral baseline irregularities and contamination which could not be removed reliably during the data reduction process (see §3.3.1). I attempted to use spectra of the bright pointing sources to correct the baseline shapes in these spectra (Vanden Bout, Solomon & Maddalena 2004), however I found that this did not improve the quality of the final spectra. After removal of the poor quality data, the total on-source integration time devoted to the final K-band spectra is 12.3 hours in the left polarization spectra, and 13.9 hours in the right polarization spectra (see Table 3.1).

3.3.1 Spectral Baselines

A major obstacle faced by searches for faint, broad emission lines, is the presence of variations in the spectral baseline shape, with a characteristic scale similar to the expected CO linewidths. These features are not uncommon in mm/cm wavelength spectra obtained with single-dish instruments, and can easily be mistaken for detections of weak, broad emission lines. There are a

Table 3.1: Summary of K-band observations of HDF850.1. The total integration time, $t_{\rm int}$, is based on the data which contributes to the final, left (L) and right (R) polarizaion spectra.

Seq.#	$\nu_1 - \nu_2$[GHz]	$t_{\rm int}$ (L/R) [hrs]	$\bar{\sigma}$ (L/R) [mJy]
K1	$22.10 - 23.62$	2.7 / 3.1	0.58 / 0.69
K2	$23.54 - 25.06$	2.2 / 1.8	0.51 / 0.61
K3	$20.88 - 22.40$	2.1 / 3.1	0.50 / 0.52
K4	$19.44 - 20.96$	1.8 / 2.6	0.60 / 0.46
K5	$24.98 - 26.50$	1.5 / 1.2	0.98 / 0.85
K6	$18.00 - 19.52$	1.9 / 2.1	0.77 / 0.72

number of instrumental, as well as atmospheric effects which may produce spectral baseline artefacts. Here, I summarize a few such artefacts which have been identified in our GBT (K and Q-band) spectra of HDF850.1:

- Weather variations over short timescales (on order of the length of a single scan of 1 minute duration) may result in inaccurate subtraction of the atmospheric contribution to the system temperature across the band. This is particularly problematic at Q-band frequencies, where clouds passing overhead may lead to rapid changes in the temperature of the atmosphere within a single beam.

- There may be interference from sources along the path of the analog signal, originating at the receiver on the telescope and traveling to the spectrometer backend in the GBT control room. An example of this is the 50 MHz ripple which appears in the left polarization K-band spectra taken during May, 2005 (Figure 3.4), and is due to temperature variations in the equipment room where the spectrometer is located. These variations cause standing waves in the connectors which manifest themselves as ripples in the spectral baseline.

- Resonances in the receiver feeds may cause a loss of power at certain frequencies, leading to emission or absorption lines, sometimes referred to as 'suck-outs'. When calculating (ON − OFF)/OFF from the on-source and off-source spectra, there will be a feature which is either in emission or absorption, depending on whether the power loss is in

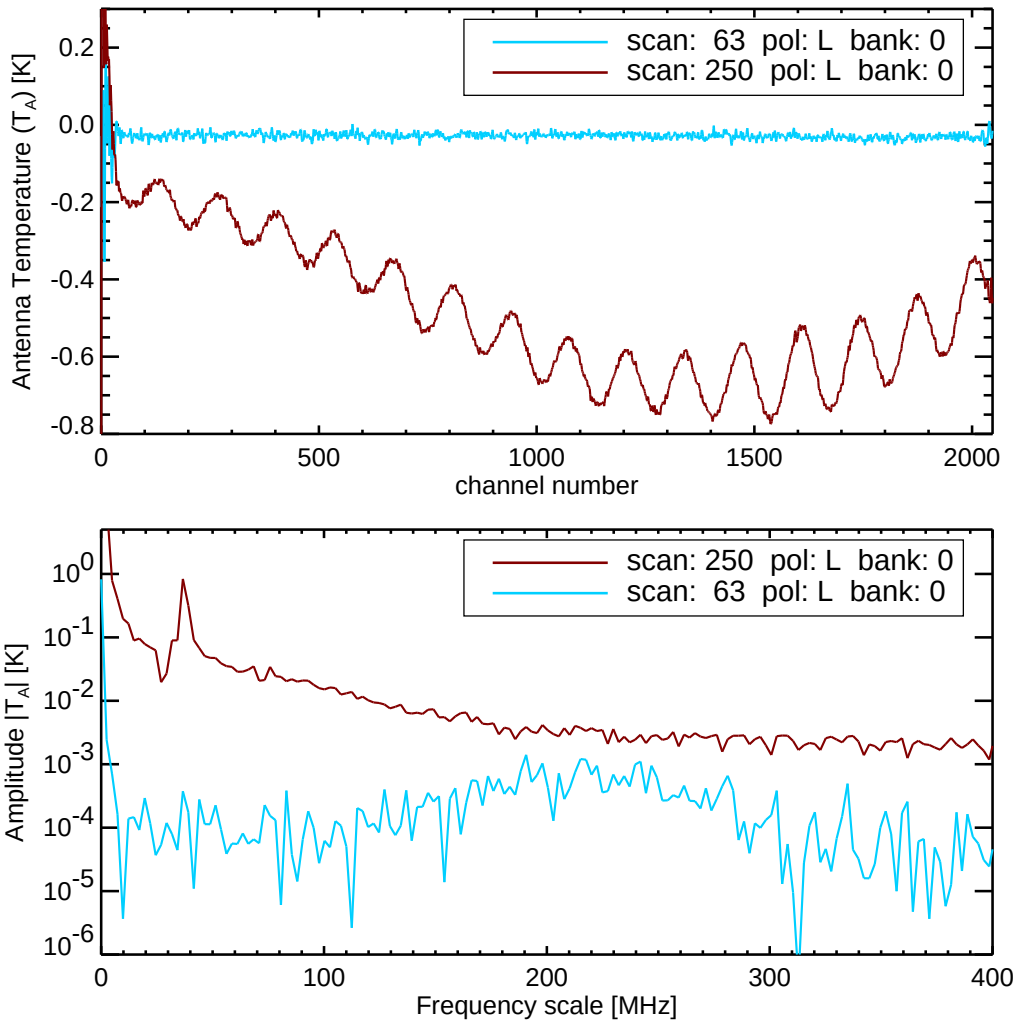

Figure 3.4: *top:* An example of the ∼50 MHz ripple which infected much of the left polarization, K-band spectra during the May, 2005 observing run. For comparison, I plot a spectra of the same frequency tuning and polarization obtained on a different date. *bottom:* The power spectra of the two spectra, exemplifying the prominant spike on scales of ∼50 MHz in one of the two. This excess in power is likely due to temperature variations in the spectrometer room, which can result in the creation of standing waves in some of the signal connectors.

the on, or the off-beam. These 'suck-outs' are apparent in the K-band receiver temperature curve shown in Figure 3.5(a) (e.g. at frequencies of ∼22.6 GHz and ∼25.7 GHz), and may also be present in the Q-band receiver system (however at present, no high-resolution receiver temperature data are available for this receiver).

- A high-frequency ripple severely affected the right polarization Q-band spectra taken in December, 2005 (but may also be present in the left polarization at a lower amplitude), and is of an unknown origin.

Data which was infected by any of these artefacts was not included when creating the final spectra. Thus ∼53% of the original data were discarded.

3.4 Results and Discussion

I do not find any evidence for CO J=1-0 line emission in our K-band spectra. Figure 3.5(a) shows the final K-band spectra of HDF850.1 over the observed frequency range, $\nu_{\rm obs}$ = 18.0 to 26.5 GHz. Due to the presence of residual baseline features, ∼53% of the raw data are not included in the final, co-added spectra shown here. The most noticeable contaminant of our spectra are the receiver resonance features, appearing at various frequencies along the K-band receiver temperature spectra (top curve, Figure 3.5(a)). These resonances originate within the feed horns and their amplitudes depend strongly on the weather conditions. Although these features prevent us from placing any constraints on the presence of CO J=1-0 line emission over certain redshift intervals, it is still possible to obtain CO J=1-0 line luminosity limits over much of the K-band window.

3.4.1 CO line luminosity limits

I calculate 3-σ upper limits to the CO J=1-0 and CO J=2-1 line luminosities across the available K-band and Q-band spectra, respectively. I assume a range of CO line widths, $\Delta V_{\rm line}$ = 460, 780 and 1100 km s^{-1}, which represent the first, median and third quartiles of the linewidths in the 12 SMGs detected in high-J CO line emission (see Greve et al. 2005). The 3-σ upper limit to the CO line integrated intensity is given by (e.g. Isaak, Chandler & Carilli 2004), $3 \cdot \sqrt{\Delta V_{\rm line}/\Delta V_{\rm channel}} \cdot \sigma_{\rm channel} \cdot \Delta V_{\rm channel}$ (in units of Jy km s^{-1}), where the velocity width of a channel, $\Delta V_{\rm channel}$, and the r.m.s. per channel,

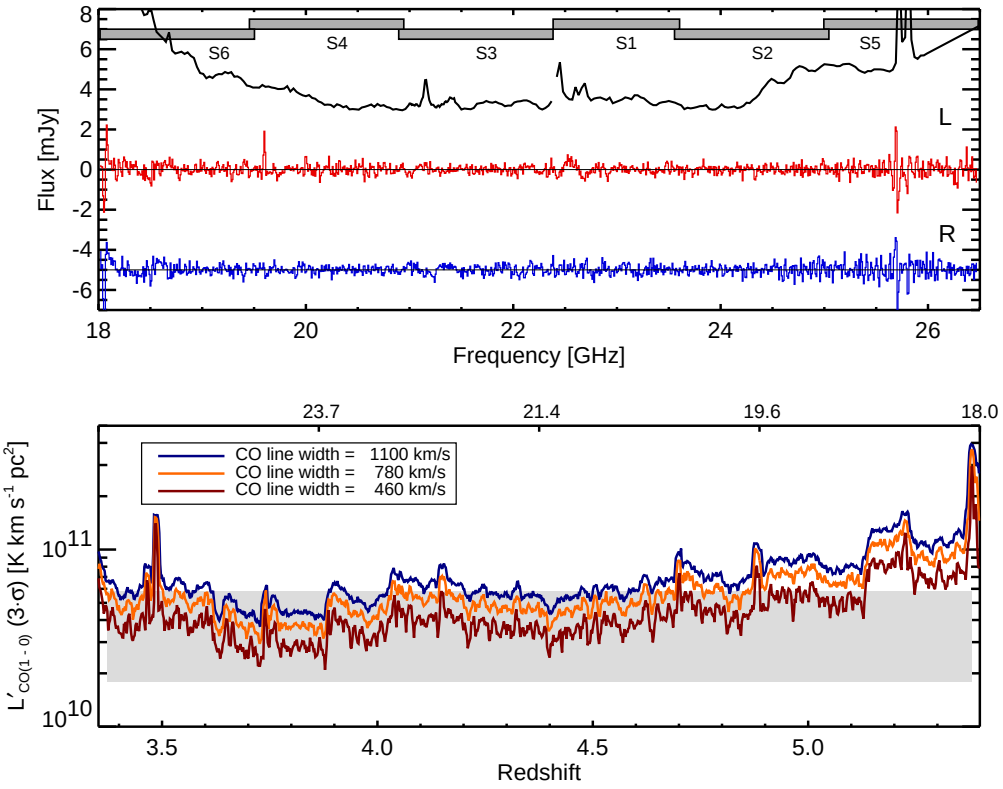

Figure 3.5: *top:* K-band spectra of HDF850.1 produced from the best 50% of the data, or 12.3 and 13.9 hours of on-source integration time included in the left and right polarization spectra, respectively. Channel widths are 8.786 MHz. The black solid-line shows the scaled K-band receiver temperature sampled at 30 MHz resolution. Receiver resonance lines appear at various frequencies across the band. Grey boxes show the 6 frequency tunings (each ∼1.5 GHz wide) adopted to cover the full K-band window. Receiver resonances, such as the one at 25.7 GHz, also appear in the HDF850.1 spectra. Another noteworthy feature is the emission line at 19.6 GHz seen in the left polarization spectra but not in the receiver temperature curve. This emission feature is also observed in the calibration spectra of 3C295, so I believe it to be another receiver resonance line. *bottom:* The 3-σ upper-limits to the CO J=1-0 line luminosity calculated from the co-added left and right polarization spectra, assuming CO line widths of 1100, 780 and 460 km s^{-1}. Also shown as the shaded region, is the range encompassed by the first and third quartiles of the CO line luminosities in the 12 SMGs detected so far in high-J CO line emission (see Greve et al. 2005).

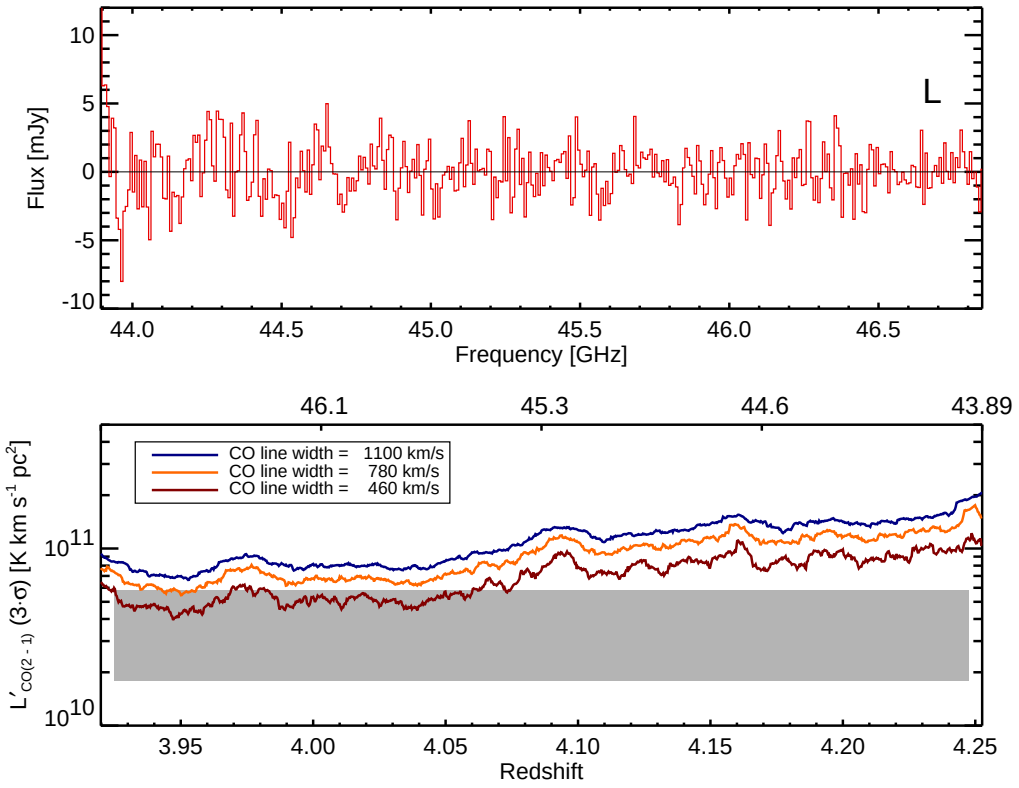

Figure 3.6: **a)** The Q-band spectra of HDF850.1 showing only the best of the combined left polarization spectra sampled at 7.813 MHz resolution. The right polarization spectra suffered from a severe baseline ripple of unknown origin so is not included here. The redshift range (z $\sim$ 3.91 - 4.25) covered by this search for CO J=2-1 improves upon the K-band spectra centered at 22.5 GHz, where receiver resonance lines made it difficult to place constraints on the presence of CO J=1-0 line emission. **b)** The luminosity limits on CO J=2-1 derived from the noise in the left polarization, Q-band spectra, assuming CO linewidths of 1100, 780 and 460 km s^{-1}. As in Figure 3.5(b), I also show the range defined by the first and third quartiles of the CO line luminosity (median $L'_{CO} = 3.8 \times 10^{10}$ K km s^{-1} pc^2), as given in Greve et al. (2005).

$\sigma_{\rm channel}$, both vary across the combined spectra. The limits to the integrated line intensity are converted to 3-σ upper limits to the CO line luminosity, $L'_{\rm CO}$, following the expression given by Solomon, Downes & Radford (1992). These limits are shown in Figure 3.5(b) for the CO J=1-0 line in the K-band spectra, and in Figure 3.6(b) for the CO J=2-1 line in the Q-band spectra. For comparison, I also plot the median CO line luminosity measured in the current sample of SMGs detected in high-J ($J_{\rm upper} \geq 2$) CO line emission (see Greve et al. 2005).

The fact that neither CO J=1-0 , or CO J=2-1 line emission is detected in HDF850.1, can be explained by three possible scenarios; *i)* the total molecular gas mass in this object is low, resulting in CO line emission that is weaker than our line luminosity limits, *ii)* the frequency of the emission line coincides with that of a receiver resonance feature, or *iii)* the redshift of this object is such that the emission frequency of the CO J=1-0 line is outside the range accessible to the K-band receiver, a possibility which has a 10-14% probability according to the photometric redshift estimate of Aretxaga et al. (2003).

Under the assumption that *i)* is the correct scenario, the limits to the CO J=1-0 line luminosity can be used to estimate the limits on the total molecular gas mass, $M_{\rm H_2}$, in HDF850.1. Adopting the relationship: $M_{\rm H_2} = \alpha L'_{\rm CO(1-0)}$ ($\alpha \sim 1$ M$_\odot$(K km s^{-1} pc^2)$^{-1}$), appropriate for nearby ultraluminous infrared galaxies (Downes & Solomon 1998), I estimate an upper limit to the molecular gas mass contained within HDF850.1, under the assumption that its redshift is in the range, $3.3 \leq z \leq 5.4$. The 3-σ limit to the CO J=1-0 line luminosity is in the range, $L'_{\rm CO} \lesssim (3-9) \times 10^{10}$ K km s^{-1} pc^2, depending on the assumed line width and redshift. By first accounting for a lensing amplification factor of 3 (Dunlop et al. 2004), these limits on the CO line luminosity translate directly to a molecular gas mass, $M_{\rm H_2} \lesssim (1-3) \times 10^{10}$ M$_\odot$. The lensing amplification factor has been calculated for the FIR/submm emission region, which I am assuming is co-spatial with the low-J CO line emission region, resulting in an equal lensing factor. This assumption may not be valid, but without high angular resolution observations of both the FIR/submm and the low-J CO emission line regions, it remains uncertain.

3.4.2 CO and Far-Infrared luminosities

I now assess whether the CO line luminosity limits achieved here, are sufficient to have detected CO line emission over the observed redshift interval,

by considering the CO line luminosity ($L'_{\rm CO}$) predicted by the estimated far-infrared luminosity ($L_{\rm FIR}$) of HDF850.1 within the context of the locally observed $L_{\rm FIR} - L'_{\rm CO}$ relation. In nearby galaxies there exists a well-established correlation between far-infrared luminosity and CO line luminosity (eg. Young & Scoville 1991), though it is unclear whether this relation truly arises from a direct dependance of star-formation rate (as traced by $L_{\rm FIR}$) on the total molecular gas mass (as traced by $L'_{\rm CO}$). Furthermore, this relationship appears to deviate from a power-law at high far-infrared luminosities ($L_{\rm FIR} \gtrsim 10^{12}$ L$_\odot$), which are characteristic of the SMG population. Despite the uncertainties in this relation, I convert the estimated far-infrared luminosity in HDF850.1 to an expected CO J=1-0 line luminosity, in order to determine if our limits on the CO J=1-0 and CO J=2-1 line luminosities are sufficiently sensitive for us to have confidently expected a CO detection.

Following Neri et al. (2003) and Greve et al. (2005), I calculate the far-infrared luminosity for HDF850.1 according to, $L_{\rm FIR} \sim 1.9{\times}10^{12} S_{850}({\rm mJy})$ L$_\odot$ (Blain et al. 2002), under the assumption of a modified greybody with dust temperature $T_{\rm d} = 40$ K, and emissivity index $\beta = 1.5$, where S_{850} is the observed 850 μm flux density. Although various measurements of the 850 μm flux density in HDF850.1 exist in the literature, the differences are not significant and I adopt the original value presented by Hughes et al. (1998), $S_{850} = 7.0 \pm 0.5$ mJy. This leads to an estimated far-infrared luminosity, $L_{\rm FIR} \sim (13.3 \pm 1.0) m^{-1} \times 10^{12}$ L$_\odot$ (where m is the magnification factor due to gravitational lensing, believed to be $\sim$3; Dunlop et al. 2004).

In Figure 3.7, I compare the estimated limits on the $L_{\rm FIR} - L'_{\rm CO}$ parameter space obtained here for HDF850.1, with the $L_{\rm FIR} - L'_{\rm CO}$ relation observed in other SMGs and various low-redshift galaxy samples. The ultraluminous infrared galaxy (ULIRG) sample observed in CO J=1-0 by Solomon et al. (1997) is also included, along with the SLUG sample of Dunne et al. (2000b) with CO J=1-0 line luminosities taken from the literature (Sanders et al. 1985, 1986, 1991; Young et al. 1995; Casoli et al. 1996; Chini, Krügel & Lemke 1996; Maiolino et al. 1997; Solomon et al. 1997; Lavezzi & Dickey 1998). More recent measurements of the nuclear CO J=1-0 and CO J=3-2 line emission in a subset of the SLUGS are presented in Yao et al. (2003). The SMG sample consists of only those objects in which searches have been made for high-J CO line emission (Frayer et al. 1999; Neri et al. 2003; Genzel et al. 2003; Greve et al. 2005; Tacconi et al. 2006). The far-infrared luminosities for these objects are calculated following the same prescription as that adopted for HDF850.1, with submm/mm flux densities taken from the literature (Smail et al. 1997,

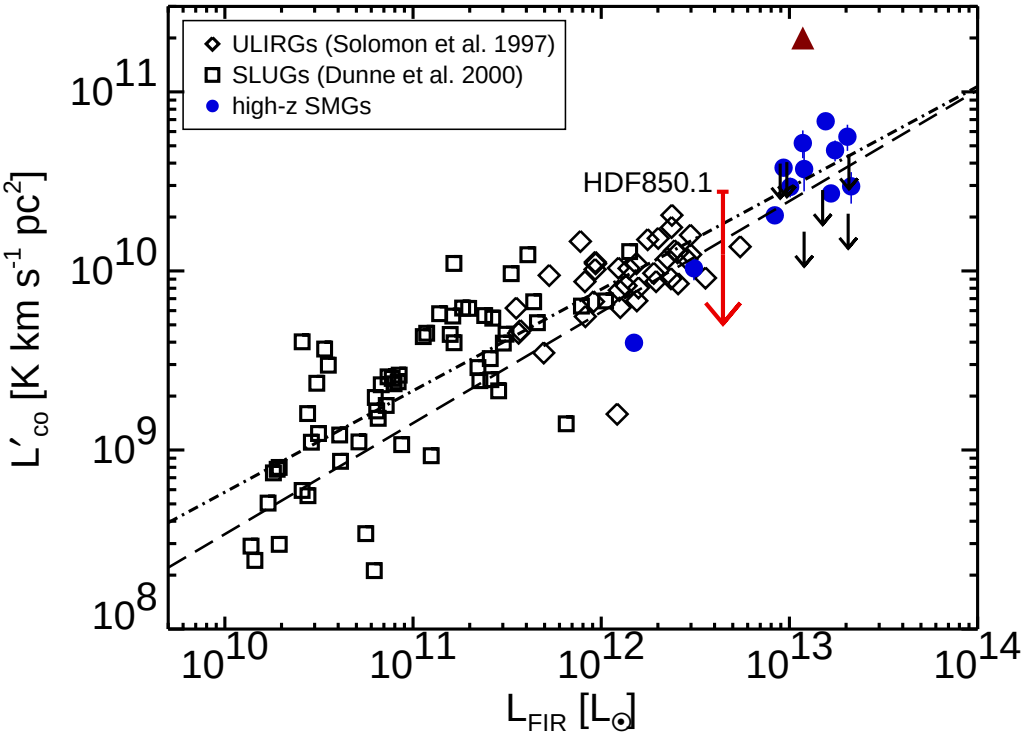

Figure 3.7: The relation between CO line luminosity and far-infrared luminosity in various samples of luminous infrared galaxies and AGN. The *diamonds* are from the CO J=1-0 line observations of nearby ULIRGs presented in Solomon et al. (1997), while the *squares* are from the SLUGS sample of nearby LIRGs/ULIRGs observed at submm wavelengths by Dunne et al. (2000b). The *solid circles* are the sample of high-redshift SMGs which have been observed in high-J CO line emission, while the *solid triangle* is for the one SMG detected in CO J=1-0 line emission (Hainline et al. 2006). The range in limits to the CO line luminosity in HDF850.1 measured here (under the assumption of a redshift, $3.3 \leq z \leq 5.4$) are shown as the *long arrow*, and have been corrected for a lensing magnification factor of 3. I show the fit presented in Greve et al. (2005) to a ULIRG+SMG sample (*dashed line*), along with the fit derived here to the low-redshift objects plotted, and only those SMGs which are detected in CO line emission (*dot-dashed line*).

1998; Ivison et al. 1998; Barger, Cowie, & Sanders 1999; Dey et al. 1999; Cowie, Barger, & Kneib 2002; Scott et al. 2002; Chapman et al. 2003b, 2005; Greve et al. 2004). For the purpose of comparison with the nearby galaxies detected in CO J=1-0 , I follow Greve et al. (2005) and assume that for the high-J CO lines observed in SMGs, $L'_{\rm CO(4-3)}/L'_{\rm CO(1-0)} = L'_{\rm CO(3-2)}/L'_{\rm CO(1-0)} = L'_{\rm CO(2-1)}/L'_{\rm CO(1-0)} = 1$, corresponding to optically-thick, thermalized CO lines. These data are plotted in Figure 3.7, with appropriate corrections applied to both $L_{\rm FIR}$ and $L'_{\rm CO}$ to account for magnification by gravitational lensing in the 6 SMGs believed to be lensed (assuming co-spatial far-infrared and CO emission line regions).

Also plotted in Figure 3.7 is a fit to the $L_{\rm FIR} - L'_{\rm CO}$ relation derived from a combined sample of ULIRGs and SMGs by Greve et al. (2005) where $\log L'_{\rm CO} = (0.62 \pm 0.08) \log L_{\rm FIR} + (2.33 \pm 0.93)$. I find a similar relation when I fit to the luminosities in the combined low-redshift LIRGs/ULIRGs and SMG sample plotted here, $\log L'_{\rm CO} = (0.57 \pm 0.03) \log L_{\rm FIR} + (3.05 \pm 0.34)$. These fits may be used to compare the estimated far-infrared luminosity in HDF850.1 to the measured CO line luminosity limits. After correcting for amplification by gravitational lensing, the estimated far-infrared luminosity in HDF850.1 makes it one of the least intrinsically luminous SMGs that has been searched for CO line emission, as most are believed to be unlensed (see Greve et al. 2005). Adopting the estimate for $L_{\rm FIR}$ in HDF850.1, the fit to the $L_{\rm FIR} - L'_{\rm CO}$ relation by Greve et al. (2005) would predict, $L'_{\rm CO} = 2.9m^{-1} \times 10^{10}$ K km s^{-1} pc^2, while the fit presented here would predict, $L'_{\rm CO} = 3.4m^{-1} \times 10^{10}$ K km s^{-1} pc^2. These values are generally lower than the 3-σ CO line luminosity limits achieved in our K-band and Q-band spectra.

I am unable to draw any conclusions as to the validity of the photometric redshift technique applied to HDF850.1. Although I have removed $\sim$53% of the original K-band data due to various spectral baseline irregularities, a further $\sqrt{2}$ decrease in the noise would still not be sufficient to obtain an L'_{CO} limit that was significantly inconsistent with the expected CO content, given the uncertainties and the dispersion in the estimated gas masses of SMGs with CO detections. The CO J=1-0 and CO J=2-1 line luminosity limits presented here are not of sufficient depth to exclude the presence of CO line emission within the redshift interval, $3.3 \lesssim z \lesssim 5.4$.

3.5 Summary and Future Work

In this Chapter I have presented a broadband, GBT spectroscopic search for CO J=1-0 and CO J=2-1 line emission in the high-redshift SMG, HDF850.1 using the K-band (18.0 to 26.5 GHz) and Q-band (40.0 to 48.0 GHz) receivers. Although I do not detect any CO line emission in this object, the constraints on the CO line luminosity are approaching that predicted by the far-infrared luminosity, within the context of the local $L_{\rm FIR} - L'_{\rm CO}$ relation. These GBT results are still consistent with HDF850.1 lying in the redshift interval, $3.3 \lesssim z \lesssim 5.4$, based on the previous rest-frame far-infrared-to-radio photometric redshift estimate of Aretxaga et al. (2003).

In Figure 3.8, I show simulated K-band spectra of an object at z=4.0 with $L_{\rm FIR} = 10^{13}$ L$_\odot$, characteristics similar to what we expect for HDF850.1. The CO J=1-0 line luminosity is derived assuming, $\log L'_{\rm CO} = 0.62 \cdot \log L_{\rm FIR} + 2.33$ (Greve et al. 2005), while for the high-J CO line transitions I assume optically thick, thermalized gas, which would lead to $L'_{CO(1-0)} = L'_{CO(2-1)} = L'_{CO(3-2)} = etc...$. From the CO line luminosity, the luminosity in other molecular line species is derived assuming luminosity ratios observed in local galaxy samples (e.g. I adopt $L'_{HCN}/L'_{CO} = 0.2$, as Gao & Solomon (2004a) measure 0.10-0.25 in their sample of nearby infrared luminous galaxies). To simulate the K-band spectra shown in Figure 3.8, I adopt the rms achieved in our combined L+R polarization spectra of HDF850.1 ($\sim$190 μJy per 5.9 MHz channel), and also that obtained by Riechers et al. (2006) in their K-band spectra of the lensed quasar APM 08279+5255 with an apparent $L_{\rm FIR} = 10^{15}$ L$_\odot$ ($\sim$65 μJy per 5.9 MHz channel in 22 hours on-source observing time). It is apparent that under the aforementioned assumptions, even if we were to have observed HDF850.1 for $6 \times 22 = 132$ hours ($\sim$180 hours total), we would likely not have detected the CO J=1-0 line. However, it is important to point out that the assumptions used to predict the CO J=1-0 line luminosity are based on extrapolation from observations of high-J CO lines published during the past two years, while our project was originally awarded time in 2002. Until observations of CO J=1-0 in a large sample of SMGs is undertaken, there will remain a great deal of uncertainty in the *expected* CO J=1-0 line intensity.

Although the results of this experiment do not yield strong constraints on either the validity of the photometric redshift technique, or the CO J=1-0 line luminosity in HDF850.1, I note that this is one of the first times that such a search as been conducted at these frequencies. In the very near future,

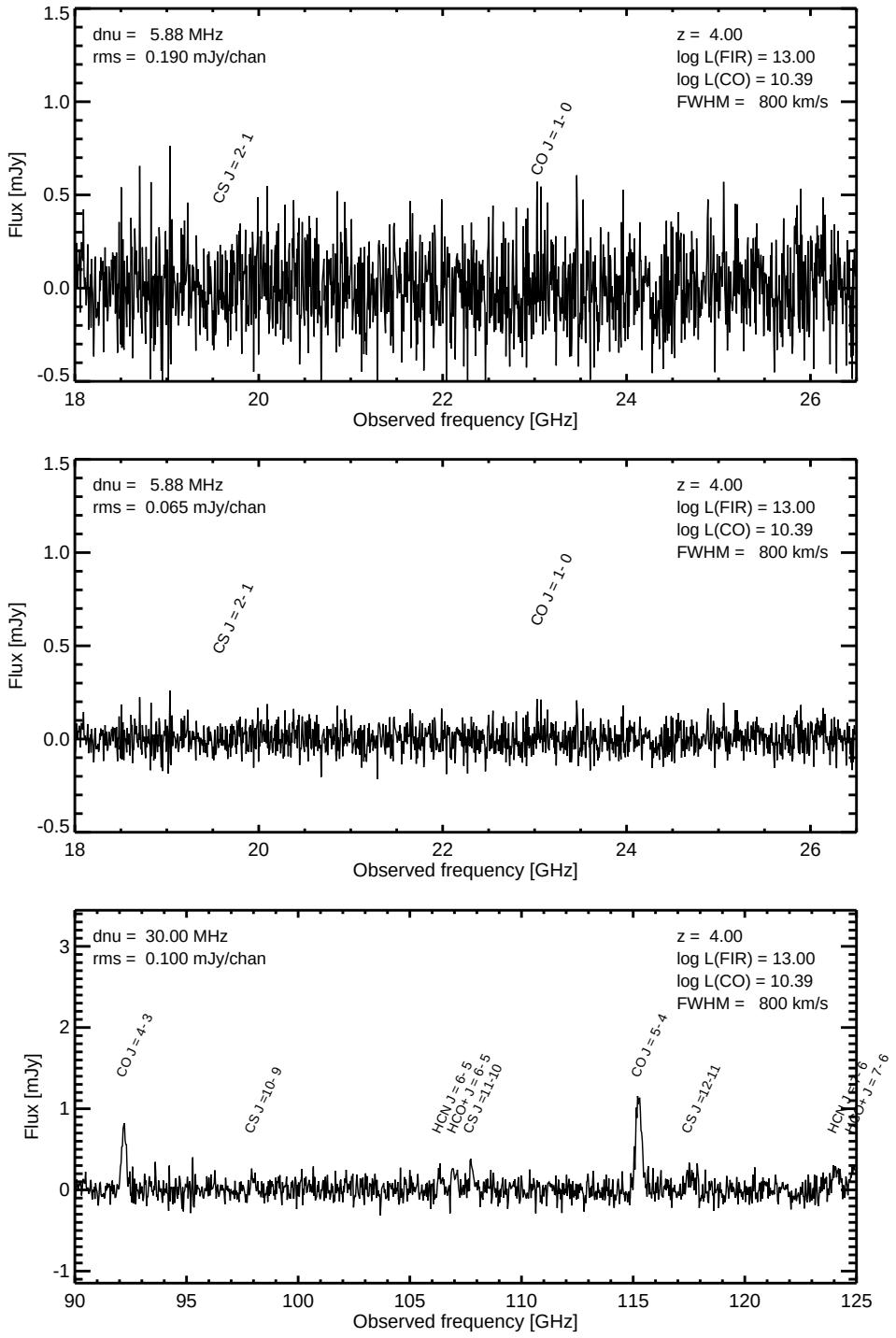

Figure 3.8: *top:* Simulated K-band spectra of an SMG at z=4.0 with $L_{\rm FIR} = 10^{13}$ $L_\odot$ adopting the sensitivity achieved in our observations. *middle:* Simulated spectra of the same object, only now with the same depth achieved by Riechers et al. (2006) in their APM 08279+5255 spectra. Their on-source integration time for a single tuning was 22 hours (30 total), so these simulated observations would require $6 \times 30 = 180$ hours of GBT observing time. *bottom:* The same object observed with the "Redshift Receiver" on the LMT.

the instrumental effects which led to much of the K and Q band spectra being unusable, will be resolved thanks to the ongoing efforts of the GBT staff and user community. In addition, a wide bandwidth receiver backend ($\sim$4 GHz) called "Zspectrometer" operating at 26-40 GHz (PI-Andy Harris, U. Maryland) will soon be commissioned on the GBT[6], in principle reducing the observing time for an experiment such as this by a factor of $\sim$6, or more. A new correlator for the VLA will provide similar wide bandwidth capabilities when the EVLA begins operation in three years time.

Given that the gaseous medium within SMGs is likely to be warm and dense, the high-J CO line transitions ($J \geq 3$) should be more intense than the J=1-0 transition (see Figure 4.2), so that redshift searches using broadband mm-wavelength receivers on large telescopes, such as the 50-m LMT should be more successful in obtaining redshifts for the SMG population of starburst galaxies. The simulated 3 mm spectra of an HDF850.1 type SMG shown in Figure 3.8, illustrates the potential for the $\sim$35 GHz bandwidth "redshift receiver" to obtain CO redshifts for SMGs like HDF850.1. Even in those cases where only a single CO line transition is observed, additional redshift constraints may be possible thanks to high-J line emission from other molecular species such as HCN and CS.

With the aforementioned ensemble of wide bandwidth heterodyne receivers on new facilities set to begin operation over the next five years, exploiting mm-to-cm wavelength line emission to obtain redshifts for SMGs will become routine. As such, the groundwork laid by experiments such as the one presented here, are necessary in order to help build the foundation for the exciting decade of research to come.

[6] *http://www.astro.umd.edu/∼harris/kaband/index.html*

Chapter 4

Probing the physical conditions in high-redshift objects using mm-wavelength spectroscopy

4.1 Introduction

The importance of measuring redshifts for distant (z $\gtrsim$ 1), far-infrared luminous objects (as discussed in Chapter 3), is not only to determine their far-infrared luminosities (which provide an estimate of the obscured star-formation rates), but also to guide the tuning frequencies of submm-to-cm wavelength receivers in subsequent searches for emission from various molecular line species. Due to its relative brightness in luminous infrared galaxies, CO line emission is the most common, and powerful means of probing the interstellar medium within high-redshift infrared luminous galaxies ($L_{\rm FIR}$ $\gtrsim$$10^{12}$ L$_{\odot}$), such as the submm galaxies (SMGs; see Chapter 2). However, the typically optically-thick nature of CO line emission means that one must measure the relative brightnesses of a number of transition lines, and invoke the use of radiative transfer models in order to constrain the density and temperature of the gas in the emission-line region. As such, observations of other molecular line species can provide further, often unique, constraints

on the physical conditions of the gas in high-redshift objects. In this chapter I discuss the potential for submm-to-cm wavelength molecular emission lines to serve as diagnostic probes of the gas in high-redshift objects. Although the spectral line-sensitivity of current instruments limits us to studying only the most luminous high-redshift objects (such as APM 08279+5255, a lensed ultraluminous quasar at z = 3.9), these objects are likely to have the greatest impact on the surrounding intergalactic medium (i.e. outflows or large HI photo-ionization rates, provided the UV escape fraction is high). As such, exploiting the molecular line-emission to measure physical properties, such as star-formation rates, total gas masses and dynamical masses (inferred from the linewidths) in the most extreme objects, is crucial in order to determine their link to other observed phenomena discussed in this thesis, such as the ionization state of the gaseous IGM discussed in Chapter 5. I also describe the results of PdBI observations of HCN and [CI] in the ultraluminous quasar APM 08279+5255 at z = 3.9, which are published in Wagg et al. (2005, 2006a).

Before summarizing the diagnostic application of a few molecular emission line species whose emission is redshifted to submm/mm wavelengths for $z \gtrsim 2$, it is important to emphasize the impact that observations of these lines in high-redshift objects can have on our understanding of the first bound, small-scale structures in the Universe. The detection of large masses of molecular gas and dust in high-redshift (z > 2) objects poses a challenge to models of galaxy and structure formation. For example, the detection of CO line emission by Walter et al. (2003) in the host galaxy to the quasar J1148+5251 at z = 6.42 (Fan et al. 2003), implies that this object contains $>10^{10}$ $M_\odot$ of molecular H_2 gas at a time when the Universe was less than 1 Gyr old (under our assumed cosmology - see Figure 1.8). Most heavy elements, such as Carbon and Oxygen, form through stellar nucleosynthesis processes and are thought to be redistributed into the surrounding medium by supernova explosion (or stellar winds). A detectable quantity of CO emission in J1148+5251 would suggest that the first generations of high-mass stars ($\sim$100 $M_\odot$) in this object must have gone through their life-cycle of formation and death as supernova type II in an unusually rapid fashion[1]. This may then provide an important clue as to the predicted existence of a class of massive population III stars, and thereby the sources responsible for reionizing the Universe at

[1]To reproduce the CO mass observed in J1148+5251 would take $\sim 10^7$ high-mass population III stars with lifetimes of less than $\sim 10^7$ years (Cen 2003).

z > 6. Interestingly, in order to reproduce the observed number density of bright SMGs (Chapter 2), cosmological hydrodynamic simulations which include galaxy formation require a "top-heavy" initial mass function for stars which form in these objects at high-redshift (Baugh et al. 2005). Given the unique nature of high-redshift objects such as J1148+5251 and the SMGs, observations of redshifted molecular line emission at submm-to-cm wavelengths can yield insight into the physical processes, such as star-formation rate and gas density, responsible for their behaviour. Understanding such behaviour will help us to understand the co-evolution of these objects and their surrounding IGM, which is one of the most powerful tracers of large-scale structure out to $z \lesssim 6$ (as discussed in Chapter 5).

The spectral line sensitivity of submm-to-cm wavelength instruments has only recently reached the level sufficient to detect faint molecular emission lines such as CO, in even the most apparently luminous high-redshift (z $\geq$1) objects. There currently exist only 36 z $\geq$ 1 objects which have been detected in either CO, [CI], CII, HCN, or HCO^+ line emission. Future submm/mm wavelength instruments such as the LMT and the Atacama Large Millimeter Array (ALMA[2]), along with cm-wavelength instruments such as the extended Very Large Array (EVLA[3]) and the Square Kilometer Array (SKA[4]), should expand this number of detectable objects into the hundreds, or thousands (Carilli & Blain 2002, see Figure 4.1).

I now give a brief overview of the diagnostic application of each of the five submm-to-cm wavelength molecular species which have currently been detected in high-redshift objects. For an excellent review of this subject, the reader is referred to Solomon & Vanden Bout (2005).

4.1.1 CO

As discussed in Chapter 3, observing redshifted CO line-emission is the most powerful means of probing the gaseous medium within far-infrared luminous objects at high-redshift. CO line-emission is typically intense in dust-rich systems with high star-formation rates or AGN activity, as it is the most abundant molecule after molecular Hydrogen (H_2), and is excited at relatively low gas densities (n_{H_2} ~300 cm^{-3}). As molecular Hydrogen does not have a

[2]http://www.alma.nrao.edu
[3]http://www.aoc.nrao.edu/evla/
[4]http://www.skatelescope.org/

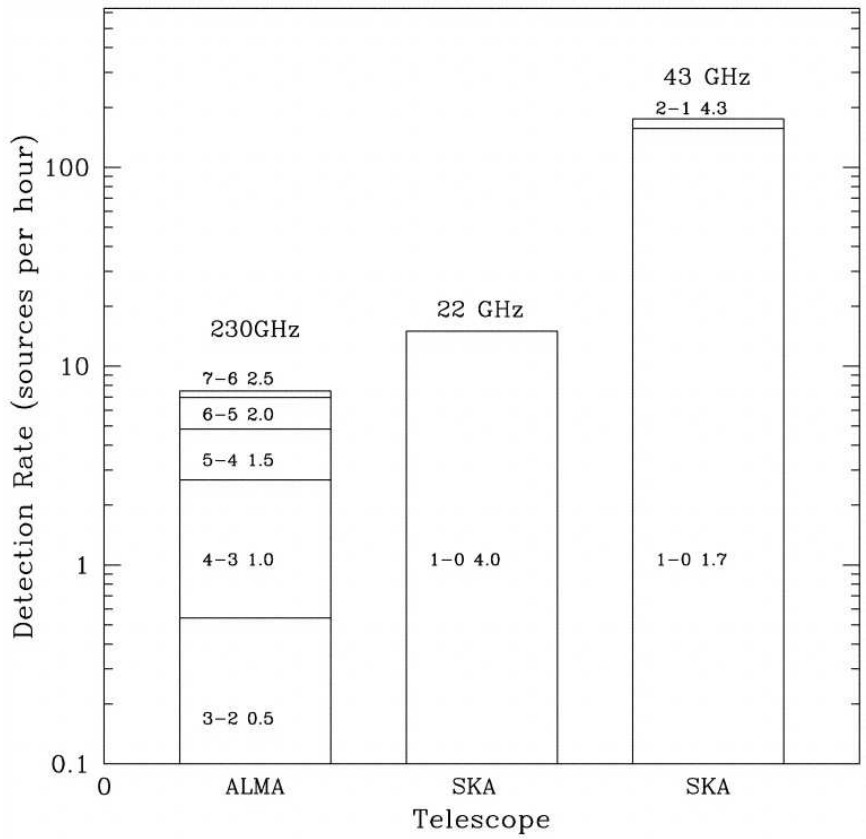

Figure 4.1: The anticipated detection rate of CO emission lines using ALMA at 230 GHz and SKA at 22 and 43 GHz in high-redshift objects. Each histogram is labelled with the CO transition line which is detected from a galaxy at the indicated redshift (Carilli & Blain 2002).

line transition at these frequencies, the integrated intensity in the CO J=1-0 line ($S_{CO}\triangle V$ [Jy km/s]) is often measured in order to estimate the total molecular gas mass in extragalactic objects. In distant objects, the integrated CO line intensity redshifted to an observed frequency, ν_{obs} ([GHz]), can be converted to a line luminosity,

$$L'_{CO} = 3.25 \times 10^7 \; S_{CO}\triangle V \; \nu_{obs}^{-2} \; D_L^2 (1+z)^{-3} \; [\mathrm{K\ km/s\ pc^2}] \tag{4.1}$$

(Solomon et al. 1992b), where D_L is the luminosity distance ([Mpc]) to the observed redshift, and depends on the assumed cosmology[5]. From L'_{CO}, one is able to estimate the total molecular gas mass in a far-infrared luminous object at high-redshift,

$$M(H_2) = \alpha L'_{CO}, \tag{4.2}$$

where most studies adopt $\alpha = 0.8$ [$\mathrm{M_\odot}$ (K km/s pc^2)$^{-1}$] as determined from nearby luminous infrared galaxies (Downes & Solomon 1998). I should note that α is likely to be a factor of $\sim$5 higher for more quiescent objects such as spiral galaxies, and has recently been shown to depend on the physical conditions in the gas (Yao et al. 2003).

Although by itself, the CO J=1-0 line luminosity is believed to provide a good estimate of the total molecular gas mass, observations of multiple CO line transitions can provide constraints on the kinetic temperature and density of the gas in the emission-line region through the use of large velocity gradient (LVG) models (Scoville & Solomon 1974; Goldreich & Kwan 1974). Intense emission in the high-J CO line transitions (such as CO J=4-3 or CO J=5-4) indicate regions of warmer, denser gas. Figure 4.2 demonstrates how the CO line flux density (normalized to the flux in the CO J=1-0 line) depends on the physical conditions within the emission line region for an object at z=3. The relative line fluxes are predicted using the *RADEX*[6] (Schöier et al. 2005) software, which calculates the brightness temperatures for transitions of the selected molecular species given a set of input physical conditions (T_{CMB}, n_{H_2}, T_{kin}, and $N(CO)$).

High-redshift objects found to be far-infrared luminous through their submm/mm wavelength continuum emission are typically first observed in the high-J ($J \geq 2$) CO transition lines redshifted to mm-wavelenths. If detected, follow-up searches for cm-wavelength emission in the CO J=1-0 lines are often conducted. This selection process may introduce a bias

[5] $D_L = (1+z)\frac{c}{H_0}\int_0^z \frac{dz\prime}{E(z\prime)}$, where $E(z) = \sqrt{\Omega_m(1+z)^3 + \Omega_k(1+z)^2 + \Omega_\Lambda}$

[6] http://www.strw.leidenuniv.nl/~moldata/radex.html

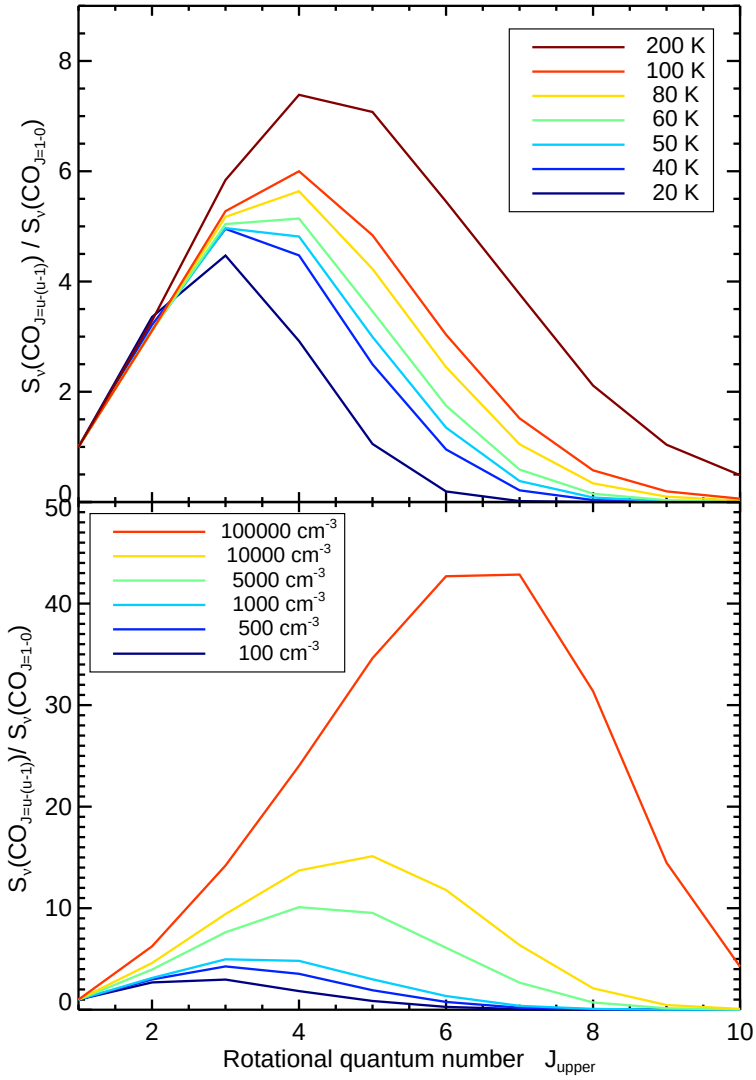

Figure 4.2: The CO line flux density, $S_\nu(CO_{J=u-(u-1)})$, in the J_{upper} to $J_{upper}-1$ transition relative to the flux density in the CO J=1-0 line flux, predicted by a large velocity gradient (LVG) model (Schöier et al. 2005), assuming different physical conditions for the gas in a z=3 object ($T_{CMB} = 2.73\ (1 + z) = 10.92$ K). All models adopt a CO column density per unit linewidth, $N(CO)/\Delta v = 1 \times 10^{17}$ cm^{-2} (km s^{-1})$^{-1}$. The *top* panel shows the effects of a changing the kinetic temperature at a constant gas gas density, $n_{H_2} = 1,000$ cm^{-3} where the temperature ranges from the coolest *dust* temperature of any SLUGS galaxy in the sample of Dunne et al. (2000), to that of the high-redshift ultraluminous quasar APM 08279+5255 (Lewis et al. 1998). For the models shown in the *bottom* panel, the gas density is varied at a constant kinetic temperature, $T_{kin} = 50$ K, from values found for the Milky Way disk (Helfer and Blitz 1997), to those inferred from observations of high-J HCN line emission in ultraluminous objects at high-redshift (Wagg et al. 2005).

towards detection of CO line emission in objects with warmer, denser gas regions, and it has been suggested that objects with a significant cool, diffuse component of molecular gas may be missed by the CO line surveys (e.g. Riechers et al. 2006a). Detection of a massive ($\sim 10^{11}$ $M_{\odot}$), extended component ($\sim$50 kpc under our assumed cosmology) in the ultraluminous quasar APM 08279+5255 at z=3.91 has been claimed by Papadopoulos et al. (2001), using high-resolution VLA observations of CO J=1-0 and CO J=2-1 line emission (cf. Riechers et al. 2006a).

The receiver bandwidth and spectral line sensitivity of current cm wavelength interferometers such as the VLA ($\sim$300 km s^{-1} at 40 GHz), or the Australia Telescope Compact Array (ATCA), are barely adequate for detecting CO J=1-0 line emission in even the most luminous high-redshift objects. As such, these facilities have only detected CO J=1-0 line emission with relatively poor spectral resolution[7] in two QSO and two radio galaxies at redshifts, z $>$ 3 (Papadopoulos et al. 2001; Lewis et al. 2002; Carilli et al. 2002; Greve et al. 2004; Klamer et al. 2005). Observations of CO J=1-0 at higher spectral resolution ($\triangle V_{chan} \lesssim 0.1 \cdot \triangle V_{FWHM}$) are required in order to constrain the linewidths, which provide an estimate of the dynamical mass interior to the emission line region. If the linewidth of a CO J=1-0 line is similar to the linewidths of the high-J CO lines detected at mm-wavelengths[8], then it can be argued that all of the observed CO line transitions orginate from within a common molecular gas region.

Sensitive, high spectral resolution observations at cm-wavelengths are now possible with the world's only 100 m diameter steerable antennas: the NRAO GBT and the MPIfR Effelsberg telescope. The low spatial resolution of these instruments may be beneficial for observations of the CO J=1-0 line in high-redshift objects, as the large beamsizes ($\sim$30-35 arcsec at 22 GHz, or $\sim$210-240 kpc at z=4 in our assumed cosmology) ensure that any emission from a lower excitation extended component will be observed, given that this component should be on the order of 50 kpc (Papadopoulos et al. 2001). While in the process of writing this dissertation, detections of CO J=1-0 line emission in BR1202-0725 at z=4.7, PSS J2322+1944 at z=4.1 and APM 08279+5255 at z=3.9, using the GBT and the Effelsberg telescope,

[7] At an oberving frequency of 22 GHz, the channel width of the VLA correlator at the maximum bandwidth of 100 MHz is $\sim$85 km s^{-1}.

[8] Typical values for the FWHM are a few$\times$100 km s^{-1}, whereas the uncertainties can be as great as $\pm$100 km s^{-1} due to the low signal-to-noise per spectral channel (e.g. Greve et al. 2005).

were presented by Riechers et al. (2006a). In all three quasar host galaxies they find that the linewidths of the CO J=1-0 lines are consistent with the linewidths of previously detected high-J CO emission lines, implying that all of the CO line emission arises within a common region. In addition, their LVG modelling of the CO line intensity ratios in these objects, indicates that the relative intensities are in good agreement with a single gas component in each case. Riechers et al. conclude that for the objects in their sample, any extended component of cold molecular gas would contribute <30% of the overall CO J=1-0 line luminosity, in contradiction to the interpretation of Papadopoulos et al. (2001).

4.1.2 HCN

Due to a large dipole moment ($\mu_D^{HCN} = 2.98$) relative to CO ($\mu_D^{CO} = 0.1$), the HCN molecule is much harder to collisionally excite than CO (the critical density for excitation[9] of the HCN J=1-0 line is, $n_{H_2} \gtrsim 10^4$ cm^{-3}, compared to, $n_{H_2} \gtrsim 300$ cm^{-3}, for the CO J=1-0 line), so strong HCN line emission in high-redshift objects may be interpreted as a signature of star-formation in dense gas (eg. Solomon et al. 2003). In the Milky Way galaxy, while CO line emission is generally observed to trace diffuse gas in the interstellar medium, HCN line emission primarily arises from dense gas regions, such as the cores of molecular clouds, where active star-formation is taking place (Helfer & Blitz 1997).

In a survey of HCN J=1-0 line emission in quiescent spirals and luminous infrared galaxies (Solomon, Downes & Radford 1992a), it was first shown that a galaxy's global star-formation rate (as traced by its infrared/far-infrared luminosity), is more tightly correlated with the HCN line luminosity than with the CO line luminosity. This correlation has recently been better quantified using a larger sample of nearby galaxies (see Figure 4.3(a)) by Gao & Solomon (2004a, b), who found that the power law coefficient in this relation is consistent with unity over nearly 3 orders of magnitude in luminosity. Wu et al. (2005) have shown that this correlation extends down to the faint infrared luminosities of dense cores in the Milky Way, $L_{IR} \gtrsim 10^{4.5}$ L$_\odot$, so that it is valid over $7-8$ orders of magnitude in L_{IR}. By observing the HCN line

[9]The critical density for excitation of a molecular line transition from state J=l to J=m is defined as, $n_{crit} = A_{lm}/K_{lm}$, where A_{lm} is the Einstein coefficient equal to the rate of spontaneous emission, and K_{lm} is the collision rate coefficient defined as the velocity averaged cross section for that molecule.

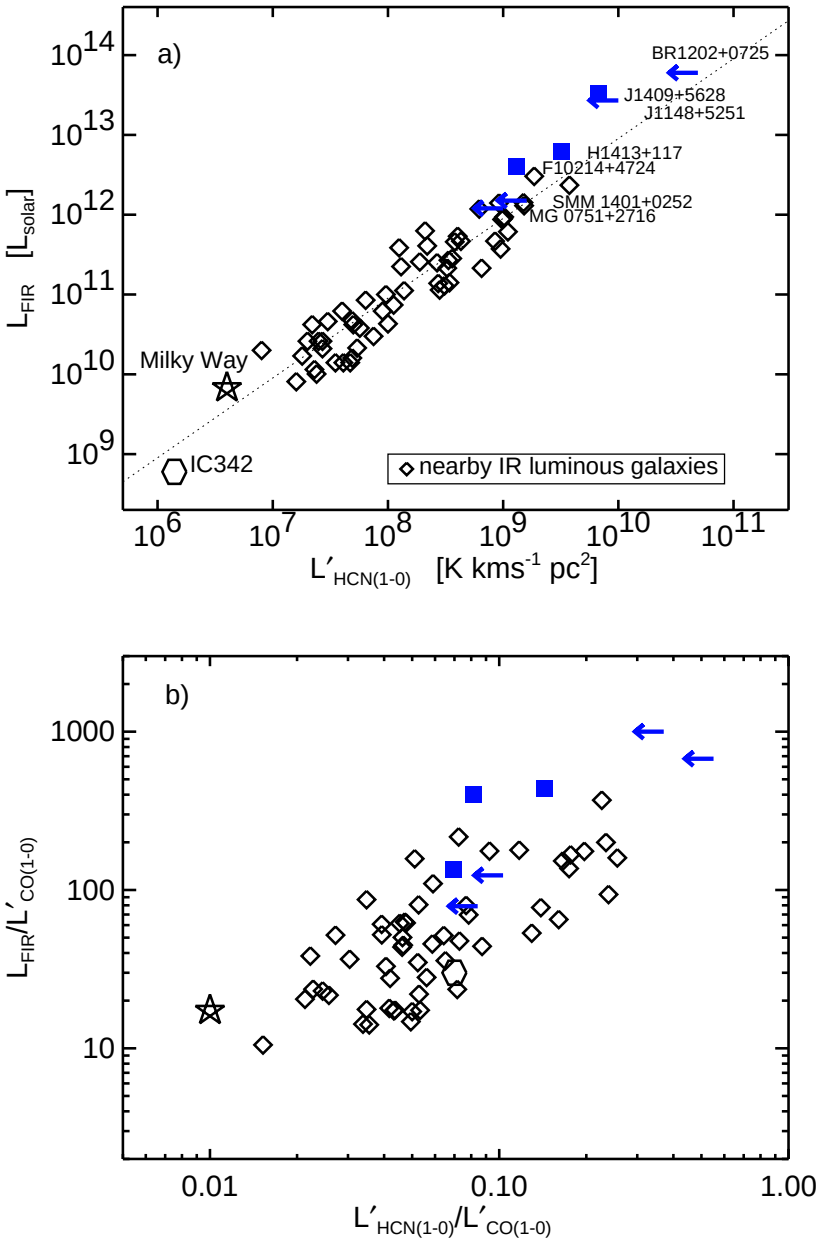

Figure 4.3: (a) The relationship between far-infrared (FIR) luminosity and HCN J=1-0 line luminosity in galaxies and AGN with a broad range of far-infrared luminosities, observed at both low-redshift (Gao & Solomon 2004) and high-redshift (Solomon et al. 2003; Vanden Bout et al. 2004; Carilli et al. 2005; Isaak et al. 2005). The *open star* and *open hexagon* indicate the values in the Milky Way and the nearby spiral galaxy IC342, respectively. *Open diamonds* represent values measured in local Universe galaxies with infrared luminosities in the range, $8 \times 10^9 \lesssim L_{IR}/L_\odot \lesssim 3 \times 10^{12}$. At the high end of the luminosity scale are the FIR luminous galaxies and AGN at $z > 2$, which have been detected (*filled squares*) or searched (*arrows*) for HCN J=1-0 line emission. (b) The ratio of bolometric FIR luminosity to CO J=1-0 line luminosity, as it depends on the HCN J=1-0 to CO J=1-0 line luminosity ratio in the sample of galaxies shown in (a).

luminosity in far-infrared luminous objects at high-redshift, this correlation may be tested for $L_{FIR} \gtrsim 10^{12}$ $L_\odot$ (e.g. Carilli et al. 2005).

If the ratio of far-infrared luminosity to CO line luminosity can be interpreted as the dependance of star-formation rate on the *total* molecular gas mass, then the ratio of far-infrared luminosity to HCN line luminosity is equivalent to the dependance of star-formation rate on the mass in *dense* molecular gas. Following this line of reasoning, the ratio of the HCN to the CO line luminosity should provide an estimate of the dense gas fraction. From Figure 4.3(b), it is clear that the star-formation rate per unit molecular gas mass (L_{FIR}/L'_{CO}), depends strongly on the fraction of gas which is dense (L'_{HCN}/L'_{CO}). Further discussion on the merits of HCN as a dense gas tracer are presented throughout Section 4.2.

4.1.3 [CI]

In the Milky Way and nearby galaxies, it is found that atomic Carbon ([CI]) line emission is spatially coincident with CO line emission (Ojha et al. 2001; Gérin & Phillips 2000). If the [CI] and CO are co-spatial, then [CI] line emission may serve as an altervative measure of the total H_2 gas mass in high-redshift objects. Testing this assumption in nearby galaxies has proven challenging, as compilation of large samples of [CI] line measurements is inhibited by the fact that the intensity in the 492.161 GHz [CI] $^3P_1 - ^3P_0$ line is strongly attenuated by water vapour absorption in the atmosphere. However, this line is redshifted into more transparent atmospheric windows for objects at, $z \gtrsim 1$. The potential merit of observing [CI] line emission in high-redshift objects, and also the potential for using the [CI] line luminosity as an estimator of a galaxy's total molecular gas mass, is further discussed in Section 4.3.

4.1.4 CII

Emission from the 157.7 μm CII line is believed to arise mainly in regions of high UV photon flux, or photo dissociation regions at sites of star-formation activity. CII line emission is expected to be a major coolant in such regions, possibly more important than either CO or [CI] line emission, while able to account for ∼0.1 - 1.0% of the total luminosity in some galaxies. Early searches for CII line emisssion in high-redshift objects lacked the sensitivity

for detection (Bolatto et al. 2004; Marsden et al. 2005) primarily due to baseline structures in the single-dish spectra.

The first high-redshift object in which CII line emission has been detected is SDSS J1148+5251 at z = 6.42 (Maiolino et al. 2005), the most distant quasar currently known. The CII line luminosity in this object implies a star-formation rate, SFR $\sim$3000 $M_\odot$ yr^{-1}. As such, future observations of CII line emission in high-redshift objects have the potential to provide an independent measure of star-formation activity.

While writing this thesis, the first interferometric observation of CII line emission at high-redshift was presented by Iono et al. (2006) in BR1202-0725 at z=4.7. They measure the ratio of CII to far-infrared luminosity in one of the two components to be 0.04%, which is consistent with that measured in nearby ULIRGs.

4.1.5 HCO^+

On an anecdotal note, the day that I began writing this chapter there were only four mm-to-cm wavelength molecular emission line species that had been detected in high-redshift (z > 2) objects. The very next day an article appeared on *astro-ph*, presenting the first detection of HCO^+ J=1-0 line emission in "the Cloverleaf" quasar at z = 2.56 (Riechers et al. 2006b). Suffice to say, on that day I began writing this description of the fifth detectable molecule, and one that is complementary to those previously detected. A few weeks later, the first detection of HCO^+ J=5-4 was presented for APM 08279+5255 at z=3.91 (Garcia-Burillo et al. 2006). These detections of HCO^+ line emission each required 10+ of hours of observing time on the world's largest mm/cm wavelength interferometers. Motivating the feasibility of such large quantities of observing time required the results of a large survey of HCO^+ in a sample of 16 nearby luminous, and ultra-luminous infrared galaxies (Graciá-Carpio et al. 2006).

Like the HCN molecule, the HCO^+ molecule is believed to trace regions of dense gas, and so is likely a good indicator of star-formation activity. HCO^+ has a high dipole moment ($\mu_D^{HCO+} = 4.48$), with a critical density for excitation of the J=1-0 transition, $n_{H_2} \gtrsim 10^4$ cm^{-3}. In a recent survey of HCO^+ J=1-0 in 16 luminous and ultralumious infrared galaxies (Graciá-Carpio et al. 2006), it was shown that the HCO^+ J=1-0 line luminosity is correlated with the star-formation rate inferred from the far-infrared luminosity, as in the case of the HCN J=1-0 line luminosity. It has been argued

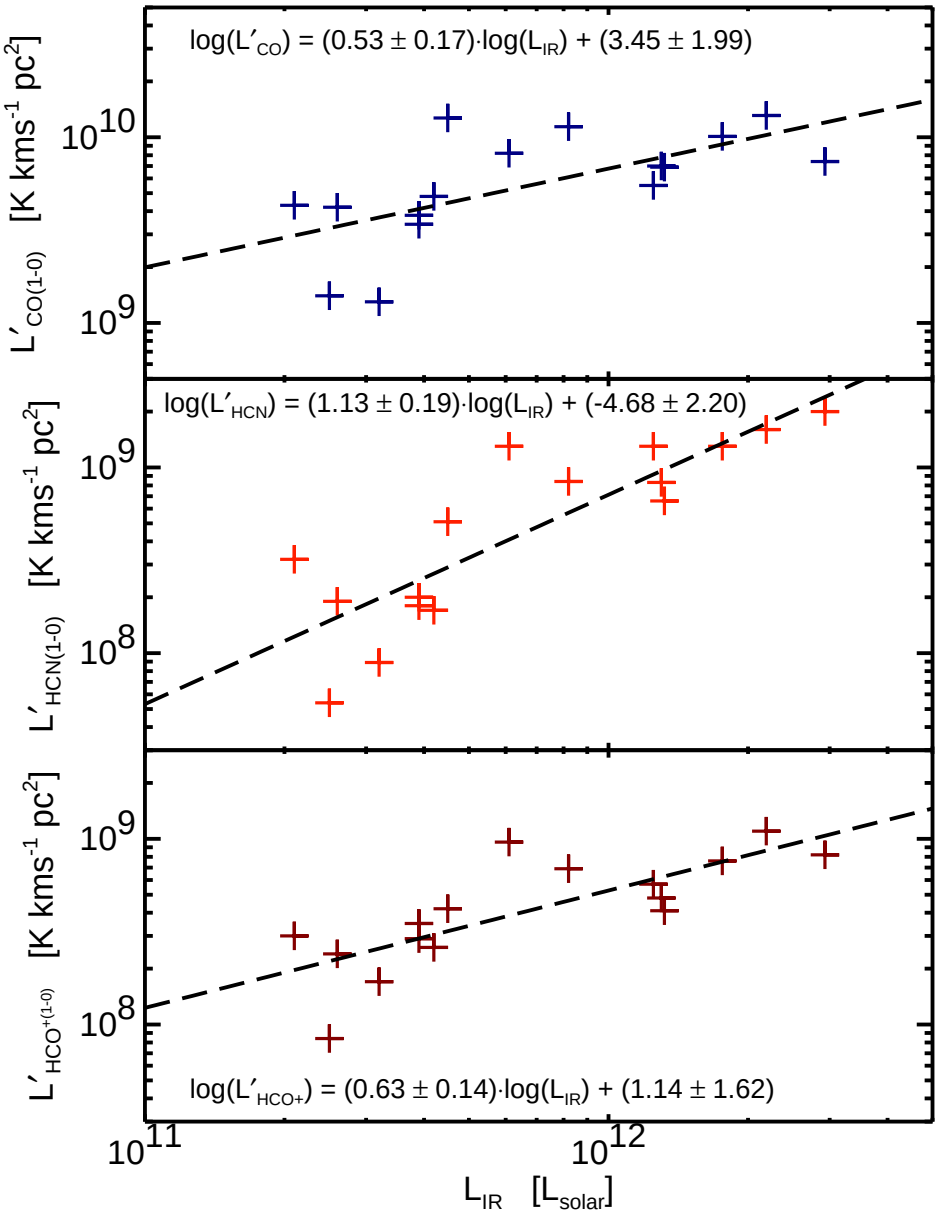

Figure 4.4: Dependance of the CO J=1-0, HCN J=1-0 and HCO^+ J=1-0 line luminosities on infrared luminosity in the luminous and ultraluminous infrared galaxy sample studied by Graciá-Carpio et al. (2006).

by Graciá-Carpio et al. (2006) that the HCO^+ line luminosity provides a better measure of the star-formation rate than the HCN line luminosity, as AGN-dominated systems have higher HCN/HCO^+ and HCN/CO line luminosity ratios than those systems whose far-infrared luminosity is dominated by starburst activity (Kohno et al. 2001; Kohno 2005; Imanishi et al. 2006). A number of explanations for the increased HCN line luminosities have been put forward, including: (1) an enhanced HCN abundance relative to CO, due to increased ionization near the AGN (Lepp & Dalgarno 1996), (2) selective depletion of Oxygen relative to Carbon in the nuclear region, or (3) infrared pumping, through a 14 μm vibrational band, may increase the excitation of HCN (Aalto et al. 1995). In spite of any possible biases inherent in the use of HCN emission as a tracer of dense gas, Riechers et al. (2006b) show that the HCN/HCO^+ line luminosity ratio is consistent with unity over a wide range in far-infrared luminosities, implying that both HCN and HCO^+ likely trace the same, dense gas regions of star-forming galaxies.

In the following two sections, I present new observations of HCN and [CI] line emission in the ultraluminous quasar APM 08279+5255 at z=3.9 (Wagg et al. 2005, 2006a). Although this object represents an extreme case in which to study molecular line emission at high-redshift, the limited spectral line sensitivity of current mm-wavelength instruments prohibits these types of studies in less luminous objects, until instruments such as ALMA come online.

4.2 HCN J=5-4 emission in APM 08279+5255 at z = 3.9

The quasar APM08279+5255, serendipitously discovered by Irwin et al. (1998), has become an archetypical ultraluminous high redshift source for study at all wavelengths, from X-ray to radio (e.g. Ellison et al. 1999, Gallagher et al. 2002, Soifer et al. 2004). The popularity of this source may be attributed, in part, to its tremendous apparent luminosity, of which $\sim 10^{15}$ $L_\odot$ emerges in the far-infrared (Lewis et al. 1998). Optical imaging reveals multiple source components and suggests that the object is strongly gravitationally lensed (Ledoux et al. 1998, Ibata et al. 1999, Egami et al. 2000). Even after correction for the lensing amplification, APM08279+5255 remains one of the most

intrinsically luminous objects known in the Universe.

The extreme luminosity of APM08279+5255 is provided by a combination of an active galactic nucleus (AGN) and star formation activity. Downes et al. (1999, hereafter D99) used the IRAM Plateau de Bure interferometer (PdBI) to detect dust continuum and CO J=4-3 and J=9-8 emission at arcsecond scales in APM08279+5255, proposing that the emission originates in a warm, dense circumnuclear disk of sub-kpc size. APM08279+5255 is the only high redshift source where CO emission from such highly excited levels as J=9 has been observed, indicative of extreme conditions in the molecular gas. In order to better understand the excitation of the molecular material and its physical nature, observations of additional diagnostic lines are needed.

The HCN molecule, which requires substantially higher densities ($n_{H_2} > 10^4$ cm^{-3}) than CO for collisional excitation due to its large dipole moment, is a promising tracer of environments such as the nucleus of APM08279+5255. In the Galaxy, HCN emission selectively traces the high density gas where star formation takes place (Helfer & Blitz 1997). In nearby star forming galaxies, the HCN J=1-0 line luminosity is found to correlate tightly with infrared/far-infrared luminosity (Solomon, Downes & Radford 1992a, Gao & Solomon 2004a, 2004b). At high redshifts, detection of HCN emission has proven challenging for the current generation of radio telescopes. The J=1-0 line has been clearly detected in H1413+117 (the strongly lensed "Cloverleaf" at z=2.6, Solomon et al. 2003), and in the strongly lensed IRAS F10214+4724 at z=2.3 (Vanden Bout et al. 2004), and tentatively detected in J1409+5628 at z=2.6 (Carilli et al. 2005). The higher excitation HCN J=4-3 line was also tentatively detected in H1413+117 (Barvainis et al. 1997, although see Solomon et al. 2003). Here I present the detection of strong HCN J=5-4 line emission in APM08279+5255 at z=3.9 and discuss the implications for the physical conditions in this remarkable object.

4.2.1 HCN Observations

The IRAM PdBI was used to observe APM08279+5255 in the HCN J=5-4 line, redshifted to the 3-millimeter band, on six dates in 1999 and 2001. As the scheduling of the PdBI is subject to weather conditions, and the array is rarely visited by outside observers due to a pair of fatal accidents in 1998 involving both a gondola and a helicopter, the observations are carried out by the telescope operators. All of the observations were made in compact configurations of the four or five available antennas. The phase center was offset by

HCN J=5-4 peak:	2.01 ± 0.51 mJy
HCN J=5-4 $\Delta V_{\rm FWHM}$:	440 ± 59 km s^{-1}
HCN J=5-4 v_0:	83 ± 26 km s^{-1}
$I_{HCN(J=5-4)}$:	0.98 ± 0.12 Jy km s^{-1}
$L'_{HCN(J=5-4)}$:	$4.0 \pm 0.5 \times 10^{10}$ K km s^{-1} pc^2
90.2 GHz continuum:	0.66 ± 0.18 mJy

Table 4.1: HCN J=5-4 line parameters for APM08279+5255. The velocity of the HCN line is given with respect to z=3.911, determined from the CO lines. The HCN J=5-4 luminosity is uncorrected for lensing magnification.

1.25″ from the CO peak position. The receivers were tuned to 90.229 GHz, corresponding to the HCN J=5-4 line (rest frequency of 443.1162 GHz) at z=3.911, determined from the earlier CO line observations. Spectral correlators covered a velocity range of ∼1600 km s^{-1}. The baseline lengths ranged from 17 to 81 meters, leading to a beam size of $7.4'' \times 6.2''$ (position angle 79^o). The nearby quasar 0749+540 was used for complex gain calibration. The flux scale was set using standard sources and other strong sources including MWC349, CRL618, 3c345.3 and 0923+392, and should be accurate to better than 20%. The integration time on source was about 32 hours (equivalent to 11.9 hours with the current six antenna array). The average rms noise is 0.47 mJy beam^{-1} in each 100 km s^{-1} channel.

4.2.2 Results

Figure 4.5 shows a series of 100 km s^{-1} channel maps across ∼900 km s^{-1} of the bandwidth. Compact HCN J=5-4 line emission is clearly evident. Figure 4.6 shows the spectrum at the position of peak intensity in Figure 4.5. This position is consistent with that found by D99 for the CO emission within the uncertainties. The bandwidth is barely adequate to span the full extent of the HCN line emission. As indicated in Figure 4.6, we adopt narrow continuum regions at both ends of the spectrum to derive the HCN line properties. The 90.2 GHz continuum flux from the combination of these "line-free" spectral regions is 0.66 ± 0.18 mJy, in line with the value of 1.2 ± 0.3 mJy at 93.9 GHz found by D99, within the uncertainties. A Gaussian fit to the continuum subtracted spectrum gives a peak flux of 2.01 ± 0.51 mJy beam^{-1}, central velocity $v_0 = 83 \pm 26$ km s^{-1} (z=3.9124 ± 0.0004),

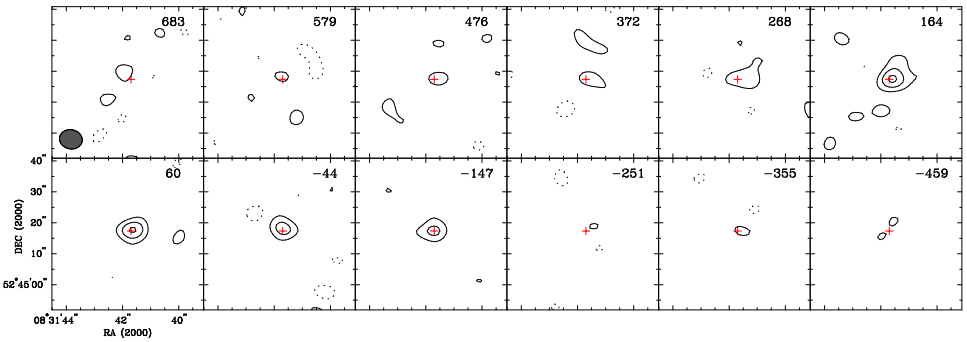

Figure 4.5: Channel maps of 90.2 GHz redshifted HCN J=5-4 emission plus continuum emission in APM08279+5255. The cross marks the position of the CO peak position from D99, offset by (1″.19, −0″.36) from the phase center ($08^h31^m41^s.57$, $52^o45^m17^s.7$). The contour intervals are -2, 2, 4, and 6×σ (0.47 mJy beam^{-1}). The filled ellipse shows the 7″.4 × 6″.2 PA 79.0° synthesized beam. The numbers in each panel indicate the velocity relative to z=3.911.

and $\Delta V_{\rm FWHM} = 440 \pm 59$ km s^{-1}. The HCN J=5-4 line integrated intensity determined by integrating over the velocity range −200 to +500 km s^{-1} is 0.98 ± 0.12 Jy km s^{-1}. The line luminosity is $L'_{HCN(J=5-4)} = 4.0 \pm 0.5 \times 10^{10}$ K km s^{-1} pc^2 using equation (3) of Solomon et al. (1992b). Table 4.1 lists the fitted and derived HCN line parameters.

4.2.3 Discussion

4.2.3.1 HCN and CO emission region

The HCN J=5-4 central velocity and line width, $\Delta V_{\rm FWHM} = 440 \pm 59$ km s^{-1}, are very similar to that found for the CO J=4-3 line, $\Delta V_{\rm FWHM} = 480 \pm 35$ km s^{-1} (D99). This close correspondence suggests a co-spatial origin for the emission from these lines. Both species likely arise from the same dynamical structure, presumably a warm, dense circumnuclear disk.

If the high-J HCN and high-J CO lines emerge from the same region, then it is reasonable to assume that the HCN luminosity is magnified by gravitational lensing by the same factor as the CO luminosity. D99 argue that the magnification factor is 7 to 20 for an intrinsic CO source size of 160 to 270 pc (173 to 290 pc for the cosmology adopted here). Lewis et al. (2002) argue for a somewhat lower magnification factor of ~ 3 based on the

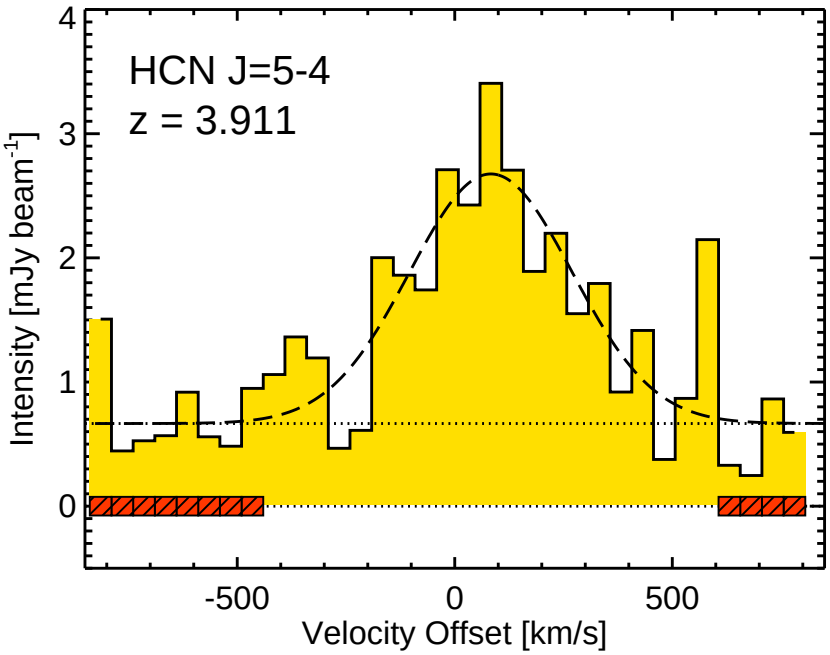

Figure 4.6: Spectrum of HCN J=5-4 emission from APM08279+5255 at 90.229 GHz, where the velocity scale is relative to the CO redshift of 3.911. The hatched regions mark the channels assumed to represent the line-free continuum level. The dashed line shows a Gaussian fit.

brightness of CO J=1-0 and CO J=2-1 lines in sub-arcsecond resolution VLA images (Papadopoulos et al. 2001, Lewis et al. 2002). Since the low-J CO line shapes are not well measured, it is not clear if the low-J and high-J CO lines are co-spatial. In any case, there is considerable uncertainty in the lensing model, and a wide range of magnification factors are viable. Observations that spatially resolve the high-J CO line emission would be useful to directly probe the line brightness and distribution.

4.2.3.2 HCN/CO ratio and Physical Conditions

The L' ratio for two lines equals the intrinsic brightness temperature ratio averaged over the velocity and physical extent of the source, and may be used to constrain the physical conditions of the gas (Solomon, Downes & Radford 1992b). D99 reproduce the CO J=9-8/J=4-3 line luminosity ratio of 0.48 ± 0.07 using escape-probability radiative transfer and deduce a gas temperature, T_{kin} ∼140 - 250 K and a molecular hydrogen density, $n_{H_2} \sim 4,000$ cm^{-3}. The CO J=9-8/J=4-3 ratio and the CO J=4-3/J=1-0 ratio also may be reproduced by gas with a lower temperature and higher density. Using the *RADEX*[10] (Schöier et al. 2005) software, we find that T_{kin} ∼80 K and $n_{H_2} \sim 40,000$ cm^{-3} matches the CO line ratios, with $N(CO)/\Delta v = 4 \times 10^{17}$ cm^{-2} (km s^{-1})$^{-1}$. This single component model also provides a good fit to all the observed lines in the CO ladder, up to the J=11-10 transition, as shown by Weiß et al. (2005, in prep.) who reach similar conclusions about the gas density and temperature.

These radiative transfer calculations assume that the HCN molecules are excited by collisions. It is possible that radiative excitation plays a role, as infrared radiation from dust heated by the AGN may excite HCN through stretching and bending vibrational modes at (rest frame) 3, 5 and 14 μm. However, as argued by D99 for CO excitation in this source, the large dust mass and consequent high opacity likely prohibits the short wavelength infrared radiation from affecting a large volume of the gas.

If we assume the conditions inferred from the CO line ratios, and a nominal [HCN/CO] abundance ratio of 10^{-3}, as found in Galactic star forming cores (Helfer & Blitz 1997), then the single component radiative transfer model predicts a magnified luminosity $L'_{HCN(J=5-4)} = 3.9 \times 10^9$ K km s^{-1} pc^2, which is a factor of 10 lower than the observed value. A plausible way to

[10] http://www.strw.leidenuniv.nl/~moldata/radex.html

produce a higher HCN J=5-4 line luminosity is with a higher [HCN/CO] abundance ratio. From the radiative transfer model, this ratio must be in the range (1 - 2) $\times 10^{-2}$ to match the data. There are at least two plausible scenarios that could lead to a higher [HCN/CO] abundance ratio: (1) an increased ionization rate in the vicinity of the AGN that enhances the HCN abundance (Lepp & Dalgarno 1996); (2) selective depletion of oxygen relative to carbon in the nuclear region. A combination of these two effects has been proposed to explain observations of HCN and CO in the nearby active nucleus NGC 1068 (Sternberg et al. 1994, Shalabiea & Greenberg 1996, Usero et al. 2004). If there has been selective depletion of oxygen in APM08279+5255, then the super-solar Fe-to-O ratio found from X-ray data (Hasinger et al. 2002) may not provide a relevant constraint on metal enrichment (or age) at high redshift.

Observations of additional HCN transitions would allow the physical conditions of the HCN emitting material to be determined independently of the constraints provided by CO observations. The single component model (with enhanced [HCN/CO] = 10^{-2}) predicts $L'_{HCN(J=1-0)} = 4.4 \times 10^{10}$ K km s^{-1} pc^2. A secure detection of the HCN J=1-0 line at this luminosity (redshifted to 18.05 GHz) would require $\sim$ 100 hours of integration time using a 100 meter diameter class radio telescope.

The mass of dense gas may be estimated from the HCN line luminosity, $M_{dense} = \alpha L'_{HCN(J=1-0)}$, where α for warm gas ($\sim$ 50 K) is $\sim 7\ M_\odot (\mathrm{K\ km\ s^{-1}\ pc^2})^{-1}$ (Gao & Solomon 2004b). For the HCN J=1-0 line luminosity estimated from our radiative transfer calculation, $M_{dense} = 3.1 \pm 0.4 \times 10^{11}$ M$_\odot$ uncorrected for amplification by gravitational lensing. A conventional estimate of the (total) molecular gas mass from the nuclear CO line luminosity (Lewis et al. 2002) results in a comparable value, i.e. $M_{H_2} = \beta L'_{CO(1-0)}$, where $\beta \sim 1 - 5\ M_\odot (\mathrm{K\ km\ s^{-1}\ pc^2})^{-1}$ (Downes & Solomon 1998, Young & Scoville 1991). In this regard, APM08279+5255 is somewhat similar to IRAS F10214+4724, where the molecular medium is also dense.

4.2.3.3 Far-infrared, CO and HCN Luminosities

According to Solomon et al. (2003), the presence of strong HCN emission from a high redshift object is an indicator of an ongoing starburst. A tight correlation exists between far-infrared luminosity and HCN J=1-0 line luminosity in star forming galaxies (Solomon, Downes & Radford 1992). The far-infrared luminosity is primarily due to dust heated by young, high mass

stars. To the extent that AGN activity is not important, the ratio L_{FIR}/L'_{CO} measures the star formation rate per unit molecular gas mass, while the ratio L_{FIR}/L'_{HCN} measures the star formation rate per unit dense molecular gas. For the sample of star forming galaxies examined by Gao & Solomon (2004a, 2004b), L_{FIR}/L'_{CO} increases with far-infrared luminosity, while L_{FIR}/L'_{HCN} does not.

To examine APM08279+5255 in the context of the correlations established from nearby galaxies, we must appeal to the results of the radiative transfer calculation (§ 4.2.3.2) to predict the HCN J=1-0 line luminosity, since this line was not observed. For galaxies in the local Universe, generally only the HCN J=1-0 line has been observed; the higher frequency HCN J=5-4 line is not accessible to ground based observations due to a strong water absorption feature in the Earth's atmosphere.

Observed values of L_{FIR}/L'_{HCN} for star forming galaxies are typically less than 2000 $L_\odot$ (K km s^{-1} $pc^2)^{-1}$. The high redshift objects with secure HCN J=1-0 detections are H1413+117, F10214+4724 and J1409+5628, and show L_{FIR}/L'_{HCN} of 1700, 3000 and 5000, respectively (Carilli et al. 2005). For APM08279+5255, the spectrum has been decomposed into starburst and AGN components by Rowan-Robinson (2000) who concludes $L_{FIR} = 9.9 \times 10^{13}$ $L_\odot$ (under our assumed cosmology) from the starburst. Adopting this value, $L_{FIR}/L'_{HCN} = 2300$, similar to the ratios observed in the other high redshift objects and at the high end of the ratios observed in local galaxies. This ratio is sensitive to the detailed decomposition of the spectrum and would be higher if a higher fraction of L_{FIR} were due to star formation rather than AGN activity. This calculation also does not account for the possible effects of differential lensing, and it is plausible that differential lensing results in a higher magnification factor for the far-infrared emission than for the HCN emission, since the molecular gas may have a larger spatial extent (D99), and that could lead to an enhanced apparent value.

Perhaps the nearest analog to APM08279+5255 in the local Universe is Mrk231, an ultraluminous infrared galaxy (ULIRG) with an AGN, whose bolometric luminosity is dominated by a starburst (Solomon, Downes & Radford 1992a, Davies, Tacconi & Genzel 2004). In Mrk231, $L'_{HCN}/L'_{CO} \sim 0.25$, the highest in the Gao & Solomon (2004a) sample. In APM08279+5255, $L'_{HCN}/L'_{CO} = 0.34 \pm 0.09$, using the (inferred) HCN J=1-0 luminosity and the (observed) nuclear CO J=1-0 luminosity (Papadopoulos et al. 2001). This is at the high end of the range 0.10 - 0.25 found for local galaxies (Gao & Solomon 2004a, 2004b) as shown in Figure 4.7. The fact that both Mrk231

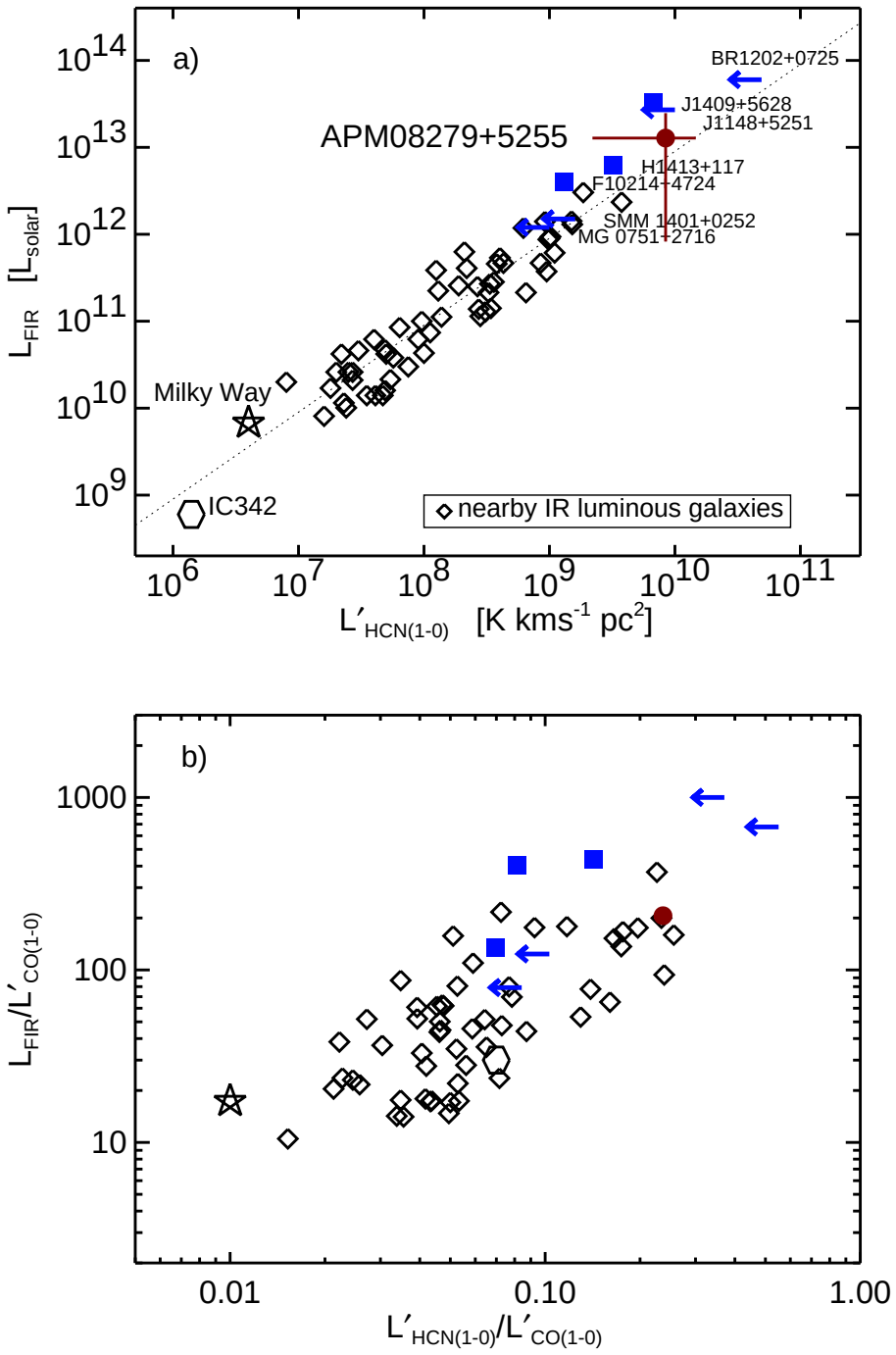

Figure 4.7: The same as Figure 4.3, but now including the new data on APM 08279+5255 (*filled circle*). The HCN J=1-0 line luminosity for APM 08279+5255 has been estimated from an extrapolation of the HCN J=5-4 line luminosity (Wagg et al. 2005) assuming the physical conditions derived from the CO line luminosity ratios (Weiss et al. 2006, in preparation)

and APM08279+5255 exhibit high L'_{HCN}/L'_{CO} values suggests a possible connection between the presence of an AGN and a high dense gas mass fraction. A physical mechanism to explain this connection might be that radiation pressure leads to an increased gas density in the vicinity of the AGN, as has been suggested for H1413+117 (Barvainis et al. 1997).

4.3 Atomic Carbon in APM 08279+5255 at z = 3.9

Given the wealth of molecular lines detected in APM 08279+5255, observations of additional diagnostic lines can provide further constraints on the physical conditions in this high-redshift object. One important tracer of the dense neutral gas within a galaxy's interstellar medium is atomic carbon, in particular the [CI] $^3P_1-^3P_0$ line with rest frequency 492.161 GHz (Gérin & Phillips 1998, 2000). This line has not been observed widely in local galaxies due to poor atmospheric transmission near this frequency; however, this line is redshifted into better atmospheric windows for objects at redshifts, $z \gtrsim 1$. The [CI] $^3P_1-^3P_0$ line provides a complimentary probe of the physical conditions of dense, neutral gas, and the [CI]/CO ratio may also provide information on the role of X-rays in the molecular excitation (Maloney et al. 1996). In addition, Papadopoulos et al. (2004a, b) argue that this line can provide a measure of the total molecular hydrogen (H_2) gas mass, independent of CO line emission.

To date, [CI] emission has been detected in four objects at $z > 2$, most of which are thought to be gravitationally lensed. The $^3P_1-^3P_0$ line was first detected in H1413+117 at z=2.6 (the "Cloverleaf"; Barvainis et al. 1997), and more recently the higher excitation $^3P_2-^3P_1$ line was also detected in this object (Weiss et al. 2003). Other high-redshift objects with [CI] $^3P_1-^3P_0$ line detections include IRAS F10214 at z=2.3 (and an upper-limit on the [CI] $^3P_2-^3P_1$ line intensity is reported by Papadopoulos 2005), SMM J14011+0252 at z=2.6 (Weiss et al. 2005), and PSS 2322+1944 at z=4.1 (Pety et al. 2005).

Another important species that acts as a major coolant of dense gas is water. In general, H_2O lines at local velocites are not accessible from the ground, but they have been observed from space and are ubiquitous in dense molecular cloud cores in the Galaxy (Ashby et al. 2000; Snell et

al. 2000). At high-redshift, a tentative detection of the H_2O $2_{11}-2_{02}$ line, with rest frequency 752.033 GHz, was reported in IRAS F10214 at z=2.3 (Encrenaz et al. 1993; Casoli et al. 1994). At more modest redshifts, the fundamental transition of ortho-water, H_2O $1_{10}-1_{01}$ has been detected in absorption towards B0218+357 at z=0.685 (Combes & Wiklind 1997). For APM 08279+5255, the lower excitation H_2O $1_{10}-1_{01}$ line with rest frequency 556.936 GHz is redshifted into the 3 millimeter atmospheric window.

Here we report a detection of [CI] $^3P_1-^3P_0$ line emission in APM 08279+5255 at z=3.91, and an upper-limit on H_2O $1_{10}-1_{01}$ line emission, obtained with the IRAM Plateau de Bure Interferometer (PdBI). Throughout this paper we adopt a Λ-dominated cosmology: $H_0 = 70$ km s^{-1} Mpc^{-1}, $\Omega_\Lambda = 0.7$, and $\Omega_m = 0.3$ (Spergel et al. 2006).

4.3.1 [CI] Observations

We used the IRAM PdBI to search for the [CI] $^3P_1-^3P_0$ and H_2O $1_{10}-1_{01}$ lines in APM 08279+5255, redshifted to the 3-millimeter band, on six dates in 1999 and 2001. As per the HCN data, the observations are carried out by the telescope operators. All of the observations were made in compact configurations of the four or five available antennas. The receivers were tuned to 100.216 GHz for the [CI] line, and 113.406 GHz for the H_2O line. Spectral correlators covered a velocity range of $\sim$1500 km s^{-1} for [CI], and $\sim$1300 km s^{-1} for H_2O. The phase center was offset by 1.25″ from the CO peak position in D99. Baseline lengths ranged from 17 to 81 meters, and the synthesized beam sizes were 7″.2×6″.0 (position angle 89^o) for the [CI] image, and 5″.9 × 4″.4 (position angle 82^o) for the H_2O image. The nearby quasar 0749+540 was used for complex gain calibration. The flux scale was set using standard sources including MWC349, CRL618, 3c345.3 and 0923+392, and should be accurate to better than 20%. The on-source integration time for the [CI] and H_2O images were equivalent to 7.3 hours and 3.1 hours, respectively, with the full six antenna array. The resulting [CI] image has an rms noise of 0.36 mJy beam^{-1} in a 150 km s^{-1} channel, and the H_2O image has a higher rms noise of 0.96 mJy beam^{-1} in a 130 km s^{-1} channel, reflecting lower atmospheric transmission near the edge of the 3-millimeter window.

[CI] $^3P_1$–$^3P_0$ peak:	2.20 ± 0.51 mJy
[CI] $^3P_1$–$^3P_0$ $\Delta V_{\rm FWHM}$:	386 ± 67 km s^{-1}
[CI] $^3P_1$–$^3P_0$ v_0:	117 ± 28 km s^{-1}
$S_{[CI]}$:	0.93 ± 0.13 Jy km s^{-1}
$L'_{[CI]}$:	$3.1 \pm 0.4 \times 10^{10}$ K km s^{-1} pc^2
100.2 GHz continuum:	1.18 ± 0.18 mJy

Table 4.2: [CI] $^3P_1$–$^3P_0$ line parameters for APM 08279+5255. The line velocity is given with respect to z=3.911, as determined from the CO lines. The [CI] $^3P_1$–$^3P_0$ line luminosity is uncorrected for lensing.

4.3.2 Results

Figure 4.8 shows images of the [CI] line and continuum emission over the full velocity range observed. The line emission is clearly detected in several velocity bins and appears spatially unresolved. The position of peak emission is consistent with that found previously for the dust continuum, CO lines, and HCN line. Figure 4.9 shows the spectra of the [CI] and H_2O lines at this position. There is no evidence for significant H_2O line emission. For the [CI] spectrum, we estimate the continuum level at 100.2 GHz using the "line-free" channels to be $S_{100\rm GHz} = 1.18 \pm 0.18$ mJy. For the H_2O spectrum, we estimate the continuum level at 113.4 GHz using all of the channels to be $S_{113\rm GHz} = 2.43 \pm 0.48$ mJy. These values are consistent with the 93.9 GHz continuum flux of 1.20 ± 0.30 mJy measured by D99 and a thermal spectrum. A Gaussian fit to the continuum subtracted [CI] $^3P_1$–$^3P_0$ spectrum yields a peak of 2.20 ± 0.51 mJy, central velocity $v_0 = 117 \pm 28$ km s^{-1} (z=3.9130 $\pm$ 0.0005), and $\Delta V_{\rm FWHM} = 386 \pm 67$ km s^{-1}. The integrated intensity of the [CI] $^3P_1$–$^3P_0$ line is 0.93 ± 0.13 Jy km s^{-1}, which implies a line luminosity $L'_{\rm CI} = (3.1 \pm 0.4) \times 10^{10}$ K km s^{-1} pc^2, following Solomon et al. (1992). Table 4.2 lists the fitted and derived [CI] $^3P_1$–$^3P_0$ line parameters.

We place an upper limit on the H_2O 1_{10}–1_{01} line emission from the noise around the mean in the spectrum, assuming $\Delta V_{\rm FWHM} = 450$ km s^{-1} like the CO, HCN, and [CI] lines. The 3-σ upper limit to the integrated intensity is $3 \cdot (\Delta V_{\rm FWHM}/\Delta V_{\rm chan})^{1/2} \cdot \sigma_{chan} = 0.70$ Jy km s^{-1}, which implies an upper limit to the H_2O line luminosity $L'_{\rm H_2O} < 1.8 \times 10^{10}$ K km s^{-1} pc^2.

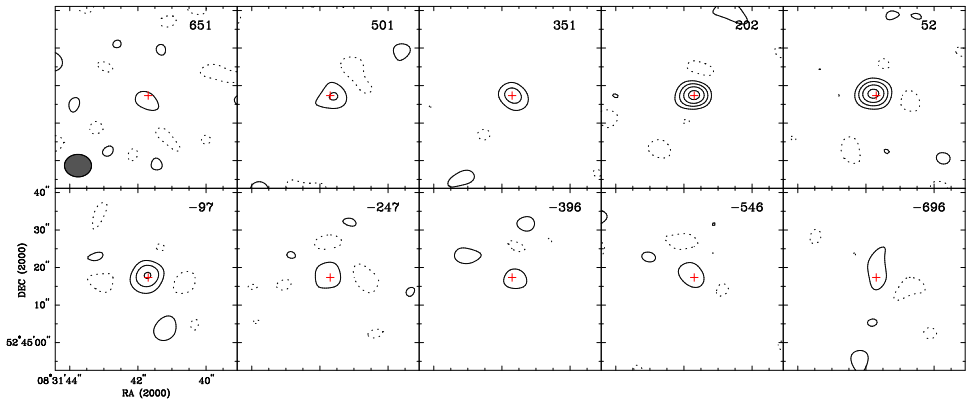

Figure 4.8: Channel maps of the [CI] $^3P_1-^3P_0$ and 100.2 GHz continuum emission in APM 08279+5255. The contour intervals are -2, 2, 4, 6 and $8\times\sigma$ (0.36 mJy beam^{-1}). The cross marks the position of the CO peak position from D99, which is offset ($1''.19$, $-0''.36$) from the phase center ($08^h31^m41^s.57$, $52^o45^m17^s.7$). The filled ellipse shows the $7''.2 \times 6''.0$ PA 89.0° synthesized beam. The velocities in each panel are relative to z=3.911.
.

4.3.3 Discussion

4.3.3.1 Emission Region and [CI]/CO Luminosity Ratio

The [CI] $^3P_1-^3P_0$ line center and width are compatible with previous observations of high-J CO lines (D99) and the HCN J=5-4 line (Wagg et al. 2005), and for analysis we assume that all of these gas tracers arise from the same region. The gas in this region is warm and dense, and is likely to be a circumnuclear disk of sub-kiloparsec size. The CO emission clearly has been magnified by gravitational lensing, and models suggest a magnification factor in the range 3 to 20 (D99, Lewis et al. 2002), or even higher in the models by Egami et al. (2000). The exact magnification factor depends critically on the intrinsic size of the emitting region. If the [CI], CO, and HCN emission are truly co-spatial, however, then the magnification factors are the same, and line luminosity ratios will not suffer any biases due to differential lensing effects.

The luminosity ratio between the [CI] and CO lines is potentially diagnostic of the gas excitation and carbon chemistry. To compare the luminosities of [CI] and CO in APM 08279+5255, we use the nuclear component of the CO

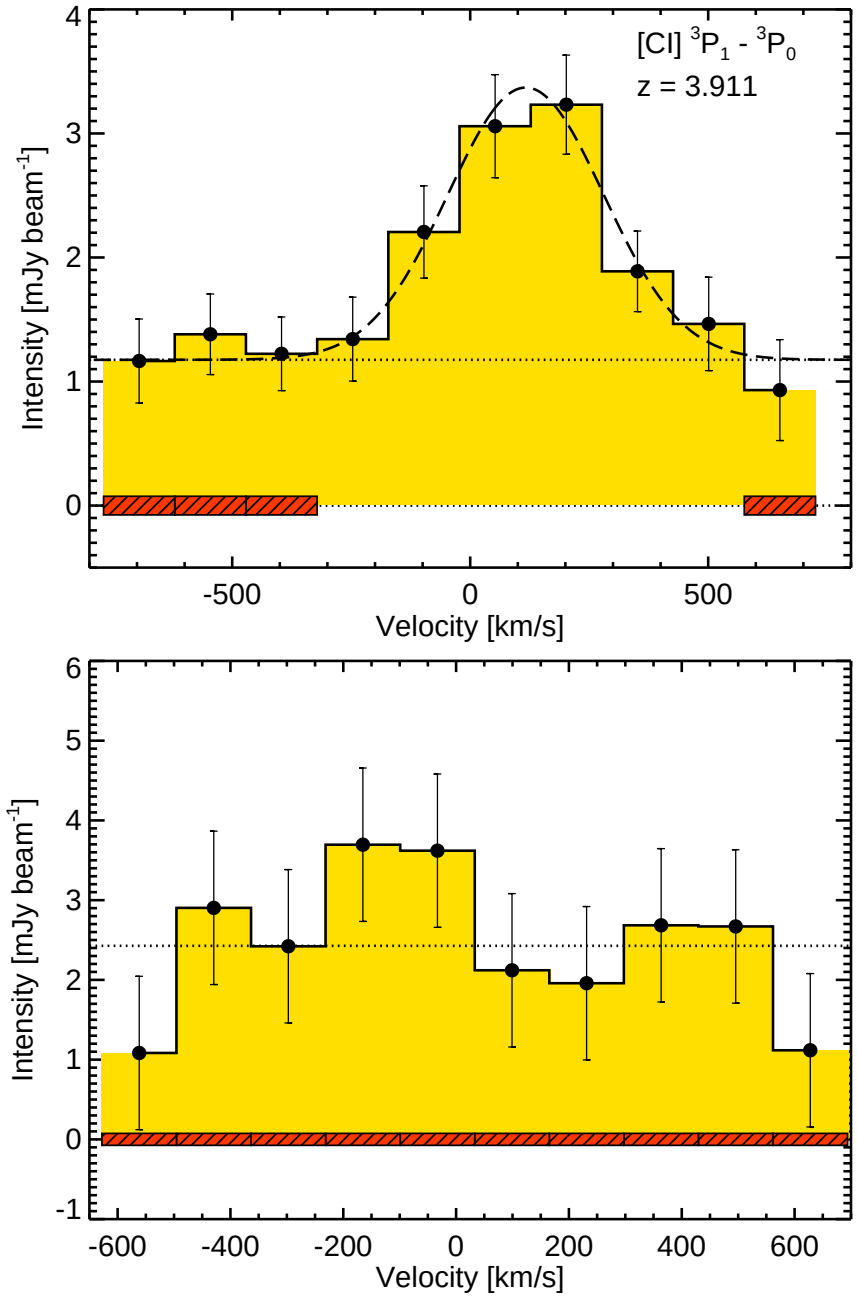

Figure 4.9: Spectra of [CI] $^3P_1$–$^3P_0$ (*top*) and H_2O 1_{10}–1_{01} (*bottom*). Dotted lines show the fitted continuum levels, calculated from the intensity in the channels marked by the hatched regions. The dashed line shows a Gaussian fit to the [CI] $^3P_1$–$^3P_0$ emission.

J=1-0 emission (Lewis et al. 2002), which gives $L'_{[CI]}/L'_{CO(1-0)} = 0.23 \pm 0.06$. This value falls within the range 0.2 ± 0.2 found for local galaxies (Gérin & Phillips 2000), and also the range $\sim$ 0.15 - 0.32 for the other four high-redshift objects that have been detected in both [CI] and CO emission. This ratio does not appear to have any strong dependence on environment, either in the local galaxy sample, or at high-redshifts. Given the significant uncertainties in the [CI]/CO luminosity ratio for any individual object, it is not possible to place strong constraints on the contribution of X-ray irradiation to the molecular gas excitation.

We can estimate the [CI/CO] abundance ratio from the observations, adopting the physical conditions derived from multi-transition CO observations (Wagg et al. 2005; A. Weiss et al. in preparation) and a simple radiative transfer model. Using an LVG code (Schöier et al. 2005), we find that an abundance ratio, [CI/CO] $\sim$ 0.6, reproduces the observed [CI] $^3P_1-^3P_0$ to CO J=1-0 line luminosity ratio. This ratio is similar to that found in the nearby starburst galaxy M82 ([CI/CO] $\sim$ 0.5; Schilke et al. 1993, White et al. 1994).

4.3.3.2 Neutral Carbon Mass

The luminosity of the [CI] $^3P_1-^3P_0$ line can be derived from the neutral carbon mass (Weiss et al. 2005), as

$$M_{[CI]} = 5.706 \times 10^{-4} \frac{Q(T_{ex})}{3} e^{23.6/T_{ex}} L'_{[CI]}\ [M_\odot], \tag{4.3}$$

where $Q(T_{ex}) = 1+3e^{-T_1/T_{ex}}+5e^{-T_2/T_{ex}}$ ($T_1 = 23.6$ K and $T_2 = 62.5$ K are the energies of the lower and upper transitions above the ground state). The only high-redshift object for which both the [CI] $^3P_1-^3P_0$ and [CI] $^3P_2-^3P_1$ lines have been measured is the "Cloverleaf" quasar, where $T_{ex} = 30$ K (Weiss et al. 2003, 2005). Without a measurement of the higher [CI] $^3P_2-^3P_1$ line in APM 09279+5255, the value of T_{ex} is uncertain. However, Weiss et al. (2005) show that for $T_{ex} > 20$ K and LTE, the estimated neutral carbon mass is insensitive to the assumed excitation temperature. Adopting a nominal value of $T_{ex} = 80$ K for the [CI] $^3P_1-^3P_0$ line in APM 08279+5255 (from the derived molecular gas and dust temperatures), the neutral carbon mass within the nuclear region of APM 08279+5255 is $M_{CI} = (4.4 \pm 0.6) m^{-1} \times 10^7$ $M_\odot$, where m is the lensing magnification factor. If T_{ex} were 20 K, then the estimated [CI] mass would be $\sim$30% lower.

Object	z_{CO}	$M_{[CI]}$ [$M_\odot/10^7$]	M_{H_2}(CO) [$M_\odot/10^{10}$]	M_{H_2}([CI]) [$M_\odot/10^{10}$]
IRAS F10214	2.29	$(2.7\pm0.3)m^{-1}$	$(11.3\pm2.5)m^{-1}$	$(18.8\pm2.4)m^{-1}$
H1413+117	2.56	$(8.1\pm1.2)m^{-1}$	$(44.3\pm0.7)m^{-1}$	$(55.8\pm8.6)m^{-1}$
SMM J14011+0252	2.57	$(3.7\pm0.6)m^{-1}$	$(9.5\pm1.0)m^{-1}$	$(25.9\pm4.3)m^{-1}$
APM 08279+5255	3.91	$(4.4\pm0.6)m^{-1}$	$(13.4\pm3.0)m^{-1}$	$(26.7\pm3.7)m^{-1}$
PSS 2322+1944	4.12	$(3.8\pm0.6)m^{-1}$	$(12.5\pm5.3)m^{-1}$	$(25.2\pm3.7)m^{-1}$

Table 4.3: Masses of neutral carbon and H_2 in high-redshift objects. The redshifts are those determined from CO line observations. m is the gravitational lensing magnification factor for a particular object, under the assumption of co-spation [CI] and CO line emission.

4.3.3.3 Molecular Gas Mass

The luminosity in the CO J=1-0 line is the traditional tracer of molecular gas (= H_2) mass in the Galaxy and in a variety of extragalactic environments. Following Papadopoulos et al. (2004a), the small scatter in the observed [CI]/CO luminosity ratio suggests that [CI] $^3P_1-^3P_0$ emission may provide an independent estimate of molecular gas mass. For nearby ultraluminous infrared galaxies (ULIRGs; Sanders & Mirabel 1996; Sanders et al. 1988), which are believed to be analogues to the currently detectable luminous high-redshift galaxies, the empirical scaling factor between CO J=1-0 luminosity and H_2 gas mass is $\sim$1 $M_\odot$ (K km s^{-1} pc^2)$^{-1}$ (Downes & Solomon 1998). If we apply this factor to the nuclear CO J=1-0 line emission in APM 08279+5255 (Papadopoulos et al. 2001; Lewis et al. 2002), then the molecular gas mass implied is $\sim 1.5m^{-1} \times 10^{11}$ $M_\odot$.

Papadopoulos et al. (2004a) relate the integrated [CI] line intensity, $S_{[CI]}$, to molecular (= H_2) gas mass, as

$$M_{\mathrm{H_2-[CI]}} = 1375.8 \frac{D_l^2}{1+z} \left(\frac{X_{\mathrm{[CI]}}}{10^{-5}}\right)^{-1} \left(\frac{A_{10}}{10^{-7}s^{-1}}\right)^{-1} Q_{10}^{-1} \frac{S_{\mathrm{[CI]}}}{[\mathrm{Jy\ km\ s^{-1}}]}\ [M_\odot], \tag{4.4}$$

where X_{CI} is the [CI]-to-H_2 abundance ratio (we assume $X_{\mathrm{CI}} = 3\times10^{-5}$), A_{10} is the Einstein A-coefficient ($A_{10} = 7.93\times10^{-8}$ s^{-1}), and Q_{10} is the excitation factor which depends on the kinetic temperature, and density of the gas. The cosmology dependence is included through the luminosity distance, D_l, and $Q_{10} = 0.5$ in the cosmology adopted here. Using the observed integrated intensity of the [CI] $^3P_1-^3P_0$ line in APM 08279+5255 gives $M_{\mathrm{H_2-[CI]}} = (2.7 \pm 0.4)m^{-1} \times 10^{11}$ $M_\odot$, in good agreement with the molecular gas mass estimated from the CO J=1-0 line.

Table 4.3 presents the molecular gas mass estimates derived from [CI] and from CO for the five high-redshift objects where both lines are detected, adjusted to a common cosmology. The [CI] $^3P_1-^3P_0$ line integrated intensities for IRAS F10214, SMM J14011+0252, and H1413+117 are taken from Weiss et al. (2005), and for PSS 2322+1944 from Pety et al. (2005). The CO J=1-0 line has been detected only in APM 08279+5255 and PSS 2322+1944 (Carilli et al. 2002). For the other objects, which are not detected in the CO J=1-0 line, we use observations of the CO J=3-2 line (IRAS F10214; Solomon et al. 1992, H1413+117; Weiss et al. 2003, SMM J14011+0252; Downes & Solomon 2003), which is approximately equal to the luminosity in the CO J=1-0 line

at high-redshifts for warm, dense gas (Solomon et al. 1992) Though the uncertainties are large, there is very good agreement between the molecular gas mass estimates from the two tracers.

4.3.3.4 H_2O

We did not detect any significant H_2O $1_{10}-1_{01}$ line emission in APM08279+5255. We can estimate the H_2O line luminosity expected for the circumnuclear region for a nominal water abundance, again adopting the previously derived physical conditions for the region. In Galactic molecular clouds, a typical ortho-H_2O abundance is 4.5×10^{-9} relative to H_2 (Snell et al. 2000; Ashby et al. 2000). For $T_{kin} = 80$ K, $n_{H_2} \sim 40,000$ cm^{-3}, an LVG calculation gives $N(H_2O)/\triangle v = 8.0 \times 10^{12}$ cm^{-2}(km s^{-1})$^{-1}$, $L'_{H_2O} = 1.1 \times 10^7$ K km s^{-1} pc^2, more than two orders of magnitude below the upper limit. In strongly shocked regions, the H_2O abundance has been observed to be enhanced by more than an order of magnitude, but even if that were the case, calculations show that the H_2O $1_{10}-1_{01}$ line emission would remain well below the achieved detection threshold.

4.4 Summary and Future Work

We have detected HCN J=5-4 emission from the ultraluminous quasar APM08279+5255 at z=3.91. The similarity of the HCN J=5-4 line profile to the CO J=4-3 and J=9-8 lines suggests the emission from these species is co-spatial. We have used a simple radiative transfer model to constrain the physical conditions in the molecular gas. The warm (T_{kin} ~80 K), dense ($n_{H_2} \sim 40,000$ cm^{-3}) gas is presumably located in a circumnuclear disk. However, the [HCN/CO] abundance ratio appears to be enhanced.

This is the first clear detection of high-J HCN emission redshifted into the 3-millimeter atmospheric window. Such observations of high-J transitions of dense gas tracers are expected to become routine with the Atacama Large Millimeter Array, which will provide an improvement in sensitivity by more than an order of magnitude. Observations of dense gas tracers in large samples of high redshift ultraluminous galaxies will help to probe their power sources, and star formation/AGN activity.

We have also detected [CI] $^3P_1-^3P_0$ line emission in APM 08279+5255. The [CI] $^3P_1-^3P_0$ line width and center are similar to those of previously

detected millimeter CO and HCN lines. Estimates of the molecular gas mass based on the [CI] $^3P_1-^3P_0$ line and based on CO lines yield similar results, and there is no evidence for any substantial contribution from a primarily atomic medium. Though the observational uncertainties remain large, this seems to be the case for the five high-redshift sources with reported detections of both CO and [CI] emission lines. The [CI] $^3P_1-^3P_0$ line may be a valuable alternative probe of molecular gas mass in systems lacking high excitation CO line emission, where the molecular medium is more diffuse and cooler ($T_{kin} \lesssim 20$ K,and $n_{H_2} \lesssim 10^4$ cm^{-3}; Papadopoulos et al. 2004a). The Atacama Large Millimeter Array will greatly expand the number of high-redshift sources accessible in [CI] and CO emission, and will have the capability to spatially resolve the emission to show directly the extent of the gas.

It is important to emphasize that the detections of the (rest-frame) submm/mm-wavelength emission lines presented in this chapter, were mainly possible due to the extreme nature of APM 08279+5255, ie. a large bolometric luminosity that is further amplified by gravitational lensing. Of the ∼35 high-redshift objects so far detected in CO line emission (termed Early Universe Molecular Emission Line Galaxies, or EMGs, by Solomon & Vanden Bout 2005), almost all would be classified as ultraluminous infrared galaxies (ULIRGs) based on their apparent far-infared luminosities ($L_{FIR} > 10^{12}$ L$_\odot$), implying star formation rates of ∼500 - 5000 M$_\odot$yr^{-1}. The majority of these objects lie in the redshift range, $2 < z < 4$, an epoch when most of the star formation in the Universe is thought to occur. Except for the single Lyman Break Galaxy (LBG; MS1512 cB58 at z=2.7) and Extremely Red Object (ERO; HR10 at z=1.4) in the sample, all of the EMGs have been selected because of intense AGN activity (e.g. radio galaxies and QSOs), or strong submm-wavelength emission (e.g. the submm galaxies described in Chapter 2). These selection effects likely introduce a bias in the EMG sample, meaning that we are not able to derive the true globally averaged properties (e.g. gas-to-dust ratio or dense gas fraction) for less luminous members of the high-redshift submillimetre galaxy population discussed in Chapter 2 (L$_{FIR} \leq 10^{12}$ L$_\odot$), which likely contribute 50% of the 850 μm background radiation.

In order to exploit the power of redshifted submm/mm-wavelength line emission for determining the physical conditions within large numbers of less-luminous high-redshift galaxies, we require larger, more sensitive facilities operating at submm-to-mm wavelengths. I am fortunate to be writing this thesis at a time when a number of new submm-to-mm facilities will be coming

online within the next few years. The two facilities expected to make the greatest impact on this field, are the LMT and ALMA.

The strength of the LMT for increasing (significantly) the number of EMGs is two-fold. First, the unprecedented mapping speed obtainable using large-format bolometer array cameras on the LMT ($\sim$0.36 square degrees per hour to a 1-σ rms of 1 mJy using the AzTEC camera; Wilson et al. 2004) means that wide-area extragalactic surveys at 1.1 mm should detect hundreds of thousands of new objects over the next five years (there are currently $\sim$500 high-redshift objects with observed $S_{850} \gtrsim 5$ identified in blank-field surveys). For example, in order to discover $\sim$100 *extreme* objects such as APM 08279+5255 in a very shallow (1-σ depth of 4 mJy at 1.1 mm) 50 sq. degree, would only require a 9 hour survey[11]. Such an enormous increase in the number of known far-infrared luminous objects at high-redshift will also lead to a rapid increase in the number of EMGs, owing to the second major strength of the LMT in this field. The first generation of instruments for the LMT includes a "redshift receiver" (PI - Neal Erickson), operating at $\sim$90 GHz with an instantaneous bandwidth of $\triangle\nu \sim 35$ GHz (see Figure 3.8). It is expected that this instrument can be used to obtain CO line redshifts for an object within specific redshift windows in less than an hour of LMT integration time. Detection of two, or more CO line transitions (separated by $\triangle\nu \sim 115/(1+z)$ GHz) reveals not only a redshift, but also the relative line strengths have the potential to provide an initial estimate of the physical conditions within the gas of the emission line region. Deeper integrations with the "redshift receiver" on the LMT may also detect the fainter emission lines from molecules such as HCN, HCO^+ and [CI], which generally exhibit line intensities which are a factor of 10 fainter than CO.

ALMA is one of the largest scientific projects ever collectively undertaken by members of the global community. Under construction in the Chilean Atacama Desert (elevation $\sim$5700 m), this 50 - 64 element array of 12 m diameter antennas will operate over the frequency range, $\sim$90 - 690 GHz. This instrument should provide an order of magnitude increase in line sensitivity over current submm/mm wavelength facilities. Given the wide spectral bandwidth capabilities of the LMT, and the high-angular resolution provided by ALMA, a great potential exists for coordinated studies of high-redshift emission line galaxies with these two facilities.

[11]The flux density of APM 08279+5255 is $\sim$20 mJy at 1.1 mm, and the 1.2 mm number counts (Greve et al. 2004) would predict 2 such objects per square degree.

Chapter 5

The impact of extreme high-redshift objects on the intergalactic medium

5.1 Introduction

In Chapters 2, 3 and 4, I have discussed submm-to-cm wavelength observations of continuum and line-emission in dusty objects with extreme infrared luminosities ($>10^{12}$ $L_{\odot}$), likely powered by some combination of AGN and star formation activity. These objects have typical redshifts, $2 < z < 4$, coincident with the epoch at which the global rates of UV derived star formation (Lilly et al. 1996) and AGN activity were likely at their peak (Madau et al. 1996). By virtue of the fact that these objects have mainly been selected for having large far-infrared luminosities which implies the presence of significant quantities of dust ($\gtrsim 10^9$ $M_{\odot}$), they are generally faint or non-detected at optical wavelengths[1]. Star forming galaxies and AGN have traditionally been identified through optical wavelength surveys, such as the Lyman Break Galaxy (LBG) surveys (Steidel et al. 1996) which utilize the Lyman (limit)

[1]The typical R_{AB} band magnitudes of the proposed IDs to the submm galaxies presented by Chapman et al. (2005) range from $R_{AB} = 18.3$ to $R_{AB} > 27.0$

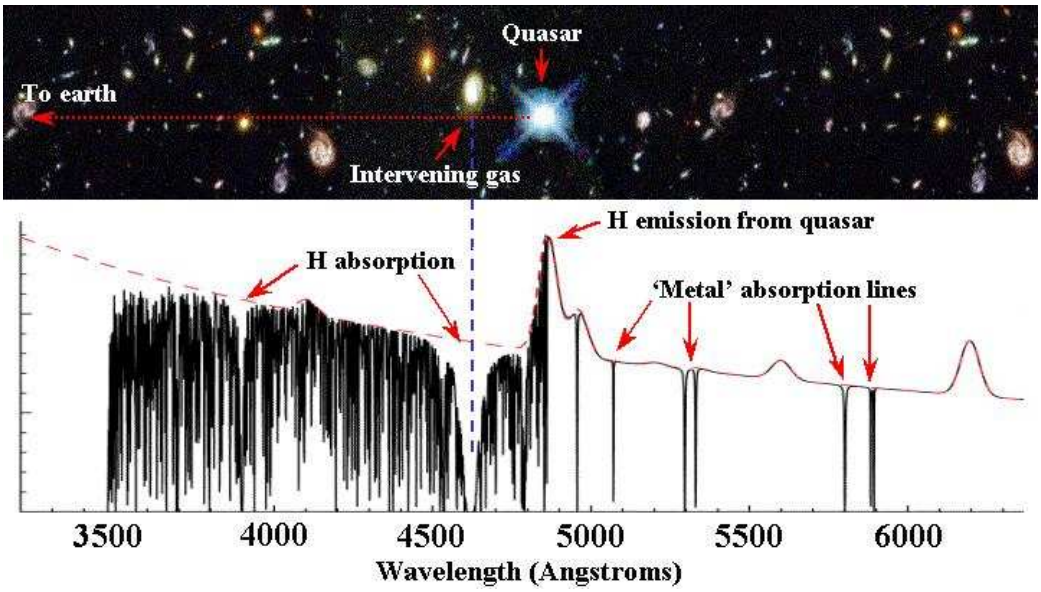

Figure 5.1: The optical spectra of a z∼3 QSO showing the menagerie of HI absorption lines blueward of the QSO Lyα emission, along with the absorption by suspected metal lines such as CIV at longer wavelengths. For illustrative purposes, the top image shows how galaxies along the line-of-sight to the QSO likely give rise to the highest column density ($N_{HI} \gtrsim 2{\times}10^{20}$ cm^{-2}) absorbers (taken from the homepage of Jochen Liske, ESO).

continuum absorption shortward of rest-frame 912 Å and Lyα line absorption at rest-frame 1216 Å (as well as Lyβ, Lyγ, etc.) due to neutral Hydrogen in the interstellar medium of gas rich objects, and in the intervening intergalactic medium (IGM), respectively. In this Chapter I examine how these extreme high-redshift objects, both obscured and un-obscured, collectively impact the physical state of the surrounding gas in the IGM. This reservoir of gas is destined to fuel not only the formation of new galaxies, but also the ongoing activity in those already in place at z $\gtrsim$ 2, so it is essential to study the IGM using independent methods. Nature has provided us with a tool for studying the physical state of the high-redshift IGM in the Lyα forest of HI absorption lines.

5.1.1 The Lyα forest as a Probe of Large-scale Structure and the Ionizing Background at High-redshift

First discovered by Lynds (1971), the serried nature of QSO spectra blueward of the Lyα emission (Figure 5.1) has proven to be an invaluable probe of both the large-scale distribution of baryonic matter in the Universe and of the cosmic ionizing background at z $>$ 2 (see Rauch 1998 and Weinberg et al. 1999 for great reviews). Originally believed to be due to absorption by neutral Hydrogen gravitationally confined in discrete cold dark matter minihalos (Rees 1986, Ikeuchi 1986), it is now generally accepted that most of the low column density absorption features are due to the spatial and temporal variation of HI density in the IGM associated with the emergence and evolution of the "Cosmic Web" (Bond & Wadsley 1997; see Figure 1.7). In keeping with this relatively new picture, many recent analyses of QSO spectra have focused on studies of the flux decrement distribution function (FDDF) and flux/transmission power spectrum. Pioneered by Croft et al. (1998), these measures are especially suited for analyses of continuously varying fields.

Historically, the Lyα forest has been analyzed using line statistics whereby the spectral features are decomposed into Voigt profiles characterized by their redshifts, HI column densities (N_{HI}), and line widths (b). In spite of having been conceived under the assumption that the absorption lines originate in discrete clouds, line-based approaches continue to provide fresh insights into the nature of the IGM, and in this sense offer alternative windows which nicely complement the flux-based schemes. Two examples stand out prominently. First, the distribution of doppler parameters at a given redshift offers a means of probing the IGM temperature at that epoch (Hui & Gnedin 1997; Schaye et al. 1999; McDonald et al. 2000; Theuns, Schaye & Haehnelt 2000). Second, it has long been known that the redshift evolution of the number density of Lyα absorbers ($n(z) \equiv dN/dz$) is the product of the joint evolution of the "Cosmic Web" and of the UV background. Using numerical simulations to isolate the effects of structure formation, Theuns et al. (1998) and Davé et al. (1999, hereafter DHKW) demonstrated that the abrupt transition in $n(z)$ observed at z $\sim$ 1.6 (Weymann et al. 1998) is explained by a decline in the quasar population at these epochs. Both of these studies focused on the period of abrupt transition from rapid evolution in the number density, rather than the statistical behaviour of absorbers at earlier times.

At high redshift, the greater density of Lyα forest lines leads to more biases when comparing simulated and observed line characteristics, as line-

blending has more of an impact than at low redshift. For example, Davé & Tripp (2001, hereafter DT01) perform a combined analysis of spectra from z < 0.3 QSO obtained with STIS (*HST*), in conjunction with artificial spectra generated from a Λ cold dark matter (ΛCDM) simulation, in constraining the amplitude of the Hydrogen ionizing background flux, $\Gamma_{\rm HI}$. At high redshift, the ability to constrain $\Gamma_{\rm HI}$ depends on knowing the value of Ω_b, as the IGM should have acted as cosmic gas reservoir, containing most of the baryonic matter at these early times. Rauch et al. (1997) use this insight to constrain Ω_b, adopting lower-limits for $\Gamma_{\rm HI}$ at z ∼1.5–4.5 and then comparing the FDDFs of high-resolution Keck spectra with the predictions of cosmological hydrodynamic simulations. Since their pioneering study, stronger constraints now exist for Ω_b, owing to the detection of the second acoustic peak in the power spectrum of cosmic microwave background (CMB) temperature fluctuations (Spergel et al. 2003). As the CMB analyses provide an independent measure of Ω_b (suggesting values of 0.04 – 0.05) it should now be possible to put constraints on the high redshift evolution of $\Gamma_{\rm HI}$ with the value of Ω_b as a prior.

In this work, I adopt an approach similar to that of Rauch et al. (1997) and DT01, in order to probe the prevailing conditions in the IGM at redshifts z ∼ 2.5 - 3.7. Specifically, I present results of a pilot program to study the properties of the Lyα forest in six high resolution QSO spectra, comparing their properties with those of the Lyα forest lines in a suite of simulated spectra constructed from realistic hydrodynamic simulations. Much of this work is also presented in Wagg et al. (2006c).

5.2 Simulation and Observations

5.2.1 Keck Spectra

Lyα forest studies have benefited immensely from the advent of high-resolution spectrographs on 8 to 10 meter class telescopes. For this particular study, this study utilizes high resolution QSO spectra obtained by Sara Ellison, Esther Hu and Antoinette Songaila with HIRES (Vogt et al. 1994) on the 10 meter Keck telescope, in analysing Lyα absorption features over the redshift range z∼2.5 - 3.7 (Table 5.1). Spectral resolutions vary from ∼6 kms^{-1} in the case of the APM 08279+5255 spectra, to ∼8 kms^{-1} for the four spectra of Hu et al. (1995, hereafter H95). A complete description of the data reduc-

QSO	z_{em}	<z>	$\triangle$z	Reference
0636+680	3.174	2.79	0.48	Hu et al. 1995
0302-003	3.286	2.87	0.48	Hu et al. 1995
0956+122	3.301	2.86	0.46	Hu et al. 1995
0014+813	3.384	2.95	0.48	Hu et al. 1995
1422+231	3.625	3.22	0.64	Ellison et al. 2000
08279+5255	3.911	3.43	0.55	Ellison et al. 1999

Table 5.1: The sample of QSO spectra used in this analysis. The mean redshifts for each line of sight, <z>, correspond to that of the Lyα forest lines included in the analysis sample which cover a redshift interval, $\triangle$z.

tion procedure leading to the continuum normalized spectra can be found in Songaila (1998) and Ellison et al. (1999, 2000). Although the continuum shape adopted for a spectra depends on the individual analyst, each series of absorption features is characterized in a consistent fashion.

The characterization of absorbers in the low column density Lyα forest suffers due to a degeneracy between the fit parameters. This degeneracy can lead to inconsistent line samples being produced using different algorithms applied to the same spectra. For this study, I adopt the use of AutoVP (Davé et al. 1997) to characterize the continuum normalized spectra, as this is also the software used to analyze the simulated spectra. It is important that both observed and simulated spectra be characterized in the same manner so as to avoid the introduction of biases in these results. For example, I compare the linelists generated from the spectra of Q1422+231 using both AutoVP and VPFIT (Webb 1987), and find that AutoVP identifies a greater number of narrow absorbers than VPFIT. As in the case of the simulated spectra, AutoVP is applied to the observed spectra with a 4.5-σ threshold for Lyα.

5.2.2 Simulated Spectra

To compare with the observed sample, Romeel Davé (U. Arizona) has generated simulated spectra from a cosmological simulation of a flat Λ-dominated Universe, adopting H_0=65 km s^{-1} Mpc^{-1}, Ω_m=0.4, Ω_Λ=0.6, Ω_b=0.0473, inflationary spectral index, n=0.95, and σ_8=0.8. The Parallel TreeSPH simulation (Davé, Dubinski & Hernquist 1997) employs smoothed particle hydrodynamics (SPH) and contains 128^3 gas particles and 128^3 dark matter

particles within a periodic cube of length 11.11 h^{-1} Mpc. Particle masses are $m_{gas} = 1.3 \times 10^7$ M$_\odot$ and $m_{dark} = 9.9 \times 10^7$ M$_\odot$, respectively. A gravitational softening length of 2.5 h^{-1} kpc comoving kernal spline is applied. Hereafter, I will refer to this simulation as model L1.

The boxsize of the L1 simulation is not sufficient to sample the largest fluctuations in the cosmic matter distribution. In cosmological simulations, long-wavelength perturbations are important for generating filamentary structures in the IGM gas distribution (Miralda-Escudé et al. 1996, Bond & Wadsley 1997). In an attempt to account for this, I also consider simulated spectra drawn from a second cosmological simulation with a boxsize of 22.2 h^{-1} Mpc. This simulation adopts the currently favoured ΛCDM model, with H_0=70 km s^{-1} Mpc^{-1}, Ω_m=0.3, Ω_Λ=0.7 and Ω_b=0.02 h^{-2}=0.0408 (Spergel et al. 2003). The resolution of this simulation is lower than that of the L1 model, containing 128^3 gas particles and 128^3 dark matter particles within a periodic cube of length $22.2h^{-1}$ Mpc. Particle masses are $m_{gas} = 7.5 \times 10^7$ M$_\odot$ and $m_{dark} = 5.5 \times 10^8$ M$_\odot$ respectively, while the softening length is $5.0h^{-1}$ kpc. This second simulation is presented here as model L2, and is included to assess the impact of simulated boxsize and resolution on the results. Although the larger L2 simulation is better suited to account for cosmic variance, the particle mass resolution in this model is not sufficient to resolve the Jeans mass over the HI column density range of interest (see Schaye 2001).

Although the focus of this comparison is on model L1, this simulation may also lack sufficient resolution to resolve density fluctuations on the smallest scales probed by the observed Lyα forest. Using a suite of cosmological simulations, Theuns et al. (1998) find that the line width distribution of absorbers only marginally converges in their highest resolution run ($m_{gas} = 2.1 \times 10^5$ M$_\odot$). Despite this, the L1 model should be able to resolve the gaseous Jeans mass for HI absorption systems with HI column densities, $N_{HI} \leq 4 \times 10^{14}$ cm^{-2}, over the redshift range of this study (Schaye 2001).

Both simulations include a redshift-dependant, HI ionizing radiation field as calculated by Haardt & Madau (1996, hereafter HM96), which assumes that QSOs are responsible for all of the radiation. The inclusion of this particular ionizing background would result in the reionization of Hydrogen at z $\sim$ 6 and HeII at z $\sim$ 4.5.

To match the redshift range of the observed Lyα forest line sample, spectra from 1000 lines of sight are generated at multiple time-steps from each of the two simulations. From model L1, 3 redshift steps are chosen centered

at z = 2.50, 3.00 and 3.50, where the co-moving size of the simulated box defines redshift intervals, $\triangle z$ = 0.016, 0.019 and 0.023, respectively. In the case of model L2, the spectra are extracted at z = 2.50, 3.00, 3.25, 3.50 and 3.75, with redshift intervals, $\triangle z$ = 0.027, 0.033, 0.036, 0.039 and 0.042.

It is important to account for any biases introduced by differences in the cosmological parameters adopted for models L1 and L2, in order to isolate the effects of volume or mass resolution on the predicted number density evolution. As shown by Rauch et al. (1997), $\Gamma_{\rm HI}$ should be proportional to $\Omega_b^2\ h^3\ \Omega_m^{-0.5}\ T^{-0.7}$. Ignoring the temperature dependance in this relation (which is taken to be equvalent for models L1 and L2), the difference in model parameters leads to $\Gamma_{\rm HI}({\rm L1})/\Gamma_{\rm HI}({\rm L2}) = 0.93$. Assuming that the parameters adopted by model L2 represent the most realistic description of our Universe, I apply the appropriate correction to the HI opacities (or in this case HI column densities) of absorption lines in the L1 simulation. In the standard picture of the high redshift IGM where all Lyα absorbers are optically thin, the Hydrogen opacity is inversely proportional to the ionization rate. This leads to a value which is 1.07 times larger than the original HM96 rates used in the L1 simulation.

The mean flux decrement in each spectra is normalized to that of the composite spectra of Press, Rybicki & Schneider (1993, hereafter PRS). This is accomplished by varying the HI ionization rate, Γ_{HI}, in the processing stage relative to that of the input HM96 (eg. Kollmeier et al. 2003). Post-simulation corrections to the ionization rates assume that the gas dynamics would remain unaffected, owing to only a weak dependance of gas temperature on Γ_{HI} (Weinberg et al. 1999). The ionization rate is found to be 1.5 times higher than that predicted by HM96 in order to match the PRS normalization. This issue is further discussed in §5.3.4.

Absorption features in simulated spectra are characterized using the AutoVP package, where a 4.5σ detection threshold for Lyα lines (Lanzetta, Turnshek & Wolfe 1987) has been imposed. Under the assumption of zero metallicity, the extracted absorption lines are all classified as Lyα (1216Å). Although this assumption is valid for simulated spectra, it is not valid when characterizing observed spectra. I address this issue in the following section.

5.2.3 Sample Definition

When defining the analysis sample of observed Lyα lines, I impose an upper limit on the redshift for each line of sight. This limit is determined

by the extent of the proximity effect, a decrement in the number of lines due to the ionizing radiation from the background QSO (Weymann, Carswell & Smith 1981; Carswell et al. 1987; BDO). For absorption lines in the APM 08279+5255 spectra, the upper redshift limit is the redshift at which the spectra is contaminated by material ejected away from the QSO at ∼13,100 km s^{-1} (Ellison et al. 1999). Lower limits to the redshifts of Lyα lines included in the analysis sample are also imposed so as to avoid including Lyβ lines in the sample.

Metal absorption by ionized species such as MgII and CII can be found intermingled with the Lyα absorption lines, and are thought to trace regions with a large number density of galaxies. These metal lines are usually identified through association with high column density Lyα lines ($N_{HI} > 10^{14}$ cm^{-2}) at equivalent redshifts. Included in the analysis sample, these metal lines are likely to be mistaken for narrow Lyα lines. To avoid the possibility of contaminating the analysis sample with metal lines, I impose a lower limit on the line widths (b-values) of absorption lines included.

To define a physically motivated lower limit on b, I first consider the argument that high column density Lyα lines arise in denser, and therefore higher temperature environments. This argument would lead to a natural relationship between b and N_{HI} (e.g. Figure 5.2). Although the width of a Lyα absorption line has a contribution from the bulk motion of the gas,

$$b = \sqrt{b_{\rm thermal}^2 + b_{\rm bulk}^2}, \tag{5.1}$$

the widths of the narrowest lines will be mainly determined by thermal motion. Within this context, the b-N_{HI} relation can be used to measure an effective 'equation of state' of the IGM (Schaye et al. 1999; McDonald et al. 2001a), and also the redshift dependance of the minimum IGM gas temperature.

Using a subset of the QSO sample (0636+680, 0014+813, 0956+122 and 0302-003), H95 examine the observed relationship between b and N_{HI}, finding a sharp cutoff in the distribution at low b-values. They calculate a lower envelope at $b = 16 + 4(N_{HI}\ /10^{14}\ {\rm cm}^{-2})$ km s^{-1} over the column density range, $2 \times 10^{12}\ {\rm cm}^{-2} \leq N_{HI} \leq 3 \times 10^{14}\ {\rm cm}^{-2}$, displayed as the *dot-dashed line* in Figure 5.2. Their results imply that all lines below this cutoff are probably metal lines not identified during line-fitting, an assumption

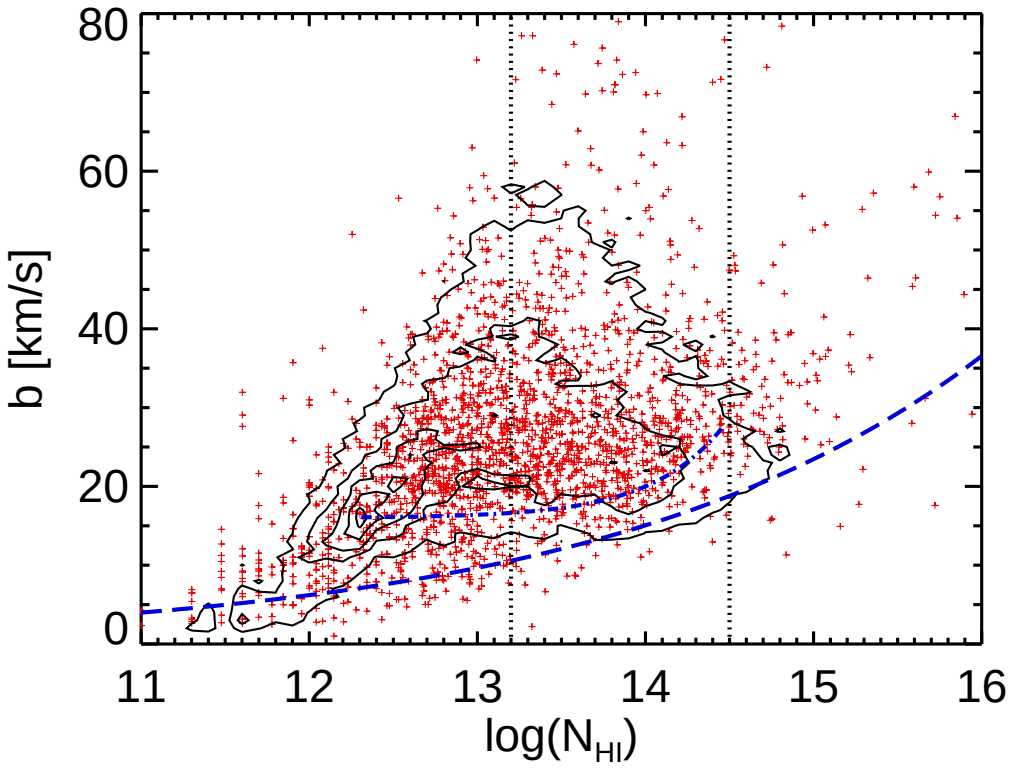

Figure 5.2: The b-N_{HI} relation for Lyα lines extracted from the observed spectra (*crosses*). *Contour intervals* define regions where the density of simulated absorbers (model L1) in the b-N_{HI} plane is equal to 10, 30, 50, 70 and 90% of the maximum density. The entire L1 sample has a total of 44501 Lyα absorption lines extracted from 1000 spectra at 3 redshifts. The vertical *dotted lines* mark the N_{HI} range, 1.6×10^{13} cm$^{-2} \leq N_{HI} \leq 3.2 \times 10^{14}$ cm^{-2}, which defines the analysis sample, while the *dashed line* shows the model for the minimum thermal doppler width (DT01) calculated at z = 3. Finally, the *dot-dashed line* defines the observational limit measured by H95.

confirmed upon follow-up inspection of the data.

Theoretical predictions for the thermal contribution to the line widths of Lyα forest lines have been made using cosmological hydrodynamic simulations. It has been shown that in the lower density IGM, the 'equation of state' of the gas follows a power-law of the form:

$$T = T_0(\rho/\bar{\rho})^{\alpha-1}K, \tag{5.2}$$

where T and ρ are the temperature and local baryon density respectively (Hui & Gnedin 1997). Observational and theoretical analyses suggest values for T_0 in the range, $10^{3.0} < T_0 < 10^{4.3}$ K (Croft et al. 1998, Schaye et al. 1999; McDonald et al. 2001a). In this work, I adopt a nominal value of $T_0 = 16{,}000$ K, and also $\alpha = 1.55$, as predicted by simulations of the high redshift IGM.

DHKW and DT01 express the redshift dependance of the relationship between physical overdensity and HI column density as:

$$\frac{\rho}{\bar{\rho}} \approx 12 \left(\frac{N_{HI}}{10^{14} cm^{-2}} \right)^{0.7} 10^{-0.4z}. \tag{5.3}$$

Following DT01, one can combine the expression for thermal broadening, $b_{therm} = (2k_bT/m_p)^{1/2}$, with equations 5.2 and 5.3 to derive a lower limit on b, which may then be applied to both the simulated and observed line samples:

$$b_{therm} = 32.2 \left(\frac{N_{HI}}{10^{14} cm^{-2}} \right)^{.1925} 10^{-0.11z} kms^{-1}. \tag{5.4}$$

This function is calculated at z = 3 (*dashed line* in Figure 5.2), and exhibits good agreement with the lower b-envelope apparent for simulated and real absorption lines. Interestingly, very few absorbers have widths below this curve, even though I am using a larger value of T_0 than that favoured by simulations. This implies that at these redshifts, the doppler broadening of Lyα forest absorbers is governed primarily by Hubble flow, rather than the kinetic temperature of the gas.

I impose further selection criteria based on HI column density. The spectral resolution and signal to noise of the observed spectra define a completeness limit of $N_{HI} \sim 10^{12.9}$ cm^{-2} (H95). Although this lower limit is appropriate for lines in the observed line sample, I find that at this HI column density there is incompleteness in the simulated line sample due to the spatial resolution of the L1 and L2 box sizes. I therefore adopt $N_{HI} \geq 10^{13.2}$ cm^{-2}

as the lower limit to N_{HI} for lines in the analysis sample, but for completeness present results based on the previous limit of $N_{HI} \geq 10^{12.9}$ cm^{-2}. I also impose an upper limit on the HI column density by excluding lines with $N_{HI} > 10^{14.5}$ cm^{-2}, as Voigt profile fitting (without the use of Lyβ absorbers) is generally more ambiguous at these high HI column densities due to saturation of absorption features.

Limiting the analysis sample to Lyα absorbers with HI column densities, 1.6×10^{13} cm^{-2} $\leq N_{HI} \leq 1.2 \times 10^{14}$ cm^{-2}, leaves 47% of the raw model L1 line sample, and 45% of the raw observed line sample. By imposing both the N_{HI} selection criteria and the lower b-limit defined by Equation 5.4, 46% of the raw model L1 sample, and 44% of the raw observed line sample remain. Application of the H95 lower b-limit leaves 41% of the raw model L1 line sample, and 40% of the raw observed line sample. Although the H95 limit eliminates a greater fraction of observed lines from the analysis sample, the fraction is not significantly greater than that removed after applying Equation 5.4. As such, I adopt the theoretical b_{therm} limit of Equation 5.4 in defining the analysis sample, as one may be confident that it holds over a large range in HI column density, and that it is physically motivated. This lower-limit on the line widths of Lyα absorbers in the analysis sample ensures that the sample is not contaminated by narrow metal line absorbers.

Finally, to measure the column density dependance of the redshift evolution of HI absorber number density, I consider intervals $N_{HI} \geq 10^{13.2}$, $10^{13.4}$, $10^{13.6}$ and $10^{13.8}$ cm^{-2}.

5.3 The z ∼ 3 Lyα Forest

5.3.1 Line Widths

After defining the analysis sample, I calculate the dependence of line width on HI column density for observed lines, comparing this with the predictions of the two simulations. I focus on model L1 for this comparison, as it appears that insufficient numerical resolution in model L2 leads to artificial broadening of absorbers. Figure 5.2 displays the b-N_{HI} relations, along with the bounds on the sample defined in the previous section. The *crosses* represent the complete sample of lines extracted from the observed spectra, while the *contour levels* define regions with a density of L1 simulated lines equal to 10,

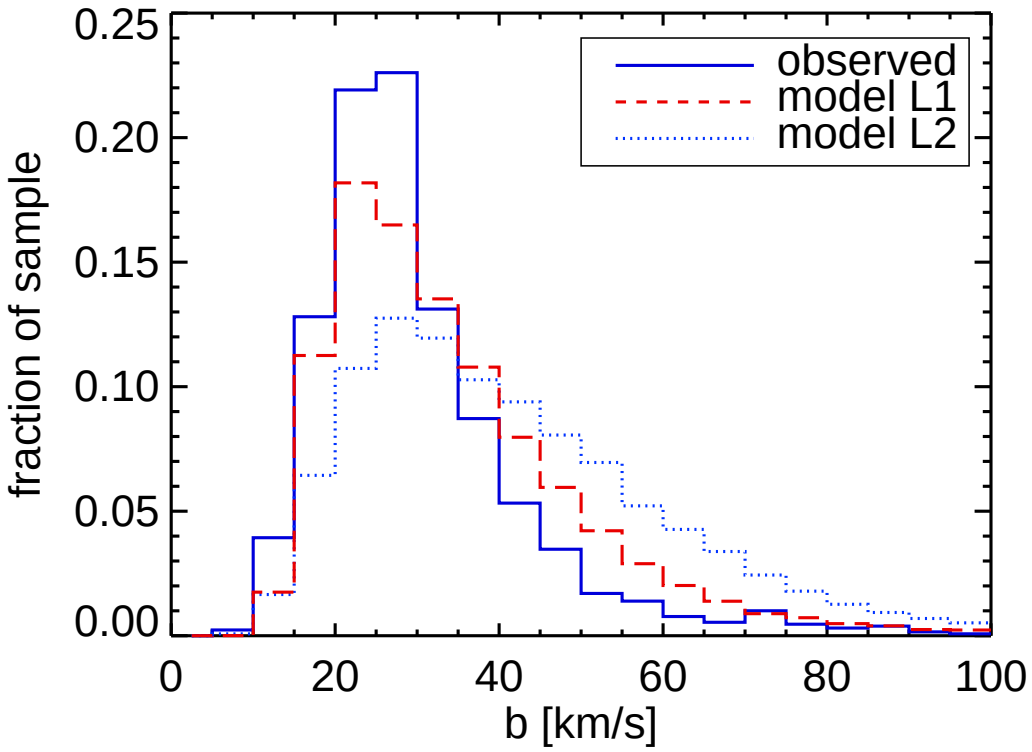

Figure 5.3: Distribution of line widths for absorbers in the observed sample (*solid line*), compared to those identified in the L2 simulated spectra (*dotted line*). The impact of particle mass resolution on the predicted b-distribution is demonstrated by the distribution of simulated absorbers in the L1 model (*dashed line*), shown to be in better agreement with the observed distribution than that predicted by model L2. The three samples have been defined according to the selection criteria, with $N_{HI} \geq 10^{13.2}$ cm^{-2}.

30, 50, 70 and 90% of the maximum density.

Figure 5.3 shows the normalized b-distribution of lines after application of the selection criteria described in the previous section (with $N_{HI} \geq 10^{13.2}$ cm^{-2}). Strong skewness in the distribution of L2 absorber line widths results in a median b-value of 38.1 km s^{-1}, while the distribution of observed line widths has a lower median of 27.3 km s^{-1}. The median line width of the absorption lines in the higher resolution L1 model is 30.8 km s^{-1}, in better agreement with that of the observed absorbers. This difference implies that the higher mass resolution of the L1 simulation is required to conduct an unbiased comparison between the widths of observed and simulated Lyα forest lines. However, it is apparent that even the higher resolution afforded by the L1 model has not resulted in perfect agreement between the line width distributions of simulated and observed absorption lines.

Theuns et al. (1998) compare the predicted properties of Lyα forest absorbers in simulations with different particle masses and simulated box sizes. Their analysis demonstrates the impact of mass resolution on the mean line widths of HI absorbers extracted from artificial spectra. Insufficient mass resolution results in a distribution of line widths which is skewed towards broader lines, so that there is an excess of wide lines over that in observed spectra. The study of Theuns et al. (1998) shows that this numerical effect is present when the particle gas mass is equal to that of the higher resolution L1 model. Even in their highest resolution simulation ($m_{gas} = 2.1 \times 10^5$ M$_\odot$) the line width distribution has not coverged.

Figure 5.4 illustrates the impact of mass resolution on the simulated line width distributions. After applying the selection criteria described in § 5.2.3, the samples are divided by both redshift and HI column density. In the *top* panels I plot the absorption line width distributions for lines above, and below, the column density threshold, $\log(N_{HI}) \leq 13.6$. From the comparison of the model L1 line width distribution with the observed line width distribution, there is better agreement between the distribution of lines widths for high column density absorbers, implying that low density regions (traced by low HI column density absorption lines) in the simulation are not fully resolved. A similar level of bias is seen when the observed line width distribution is compared with the line width distributions predicted by the models when the samples are divided by redshift. At redshifts z $\gtrsim$ 3, absorption lines are artificially broadened due to Hubble flow, an effect which manifests itself

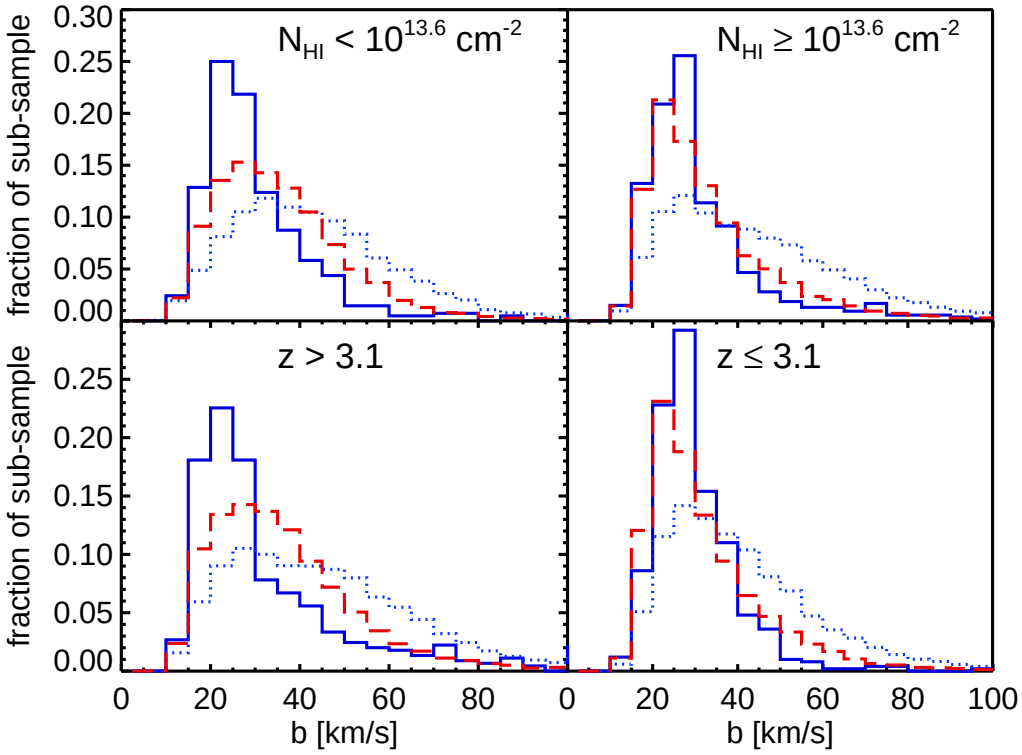

Figure 5.4: Line width distribution of HI absorbers in the observed sample (*solid line*), L1 model sample (*dashed line*) and L2 model sample (*dotted line*). The distributions have been plotted for four scenarios which highlight the impact of mass resolution on the widths of simulated absorption lines. The *top* two panels show typical widths of absorbers with low (*left*) and high column densities (*right*), independant of redshift. The *bottom* two panels display the effect of absorber redshift on the distributions. In all cases, only those absorption lines allowed by the selection criteria described in § 5.2.3 are included.

as a skewness in the distribution of simulated line widths.

5.3.2 Column Density Distribution

Following the comparison of HI line widths, I now compare the distributions of absorber HI column density. The column density distribution of Lyα forest lines is defined as:

$$\frac{dN^2}{dN_{HI}dz} \propto N_{HI}^{-\beta} \tag{5.5}$$

(Tytler 1987). Measurements of the power-law index at z ≥ 2.5, find $\beta \sim 1.5$ across nearly three decades in HI column density (H95; Lu et al. 1996; Kim et al. 1997; Kirkman & Tytler 1997).

Figure 5.5 shows the HI column density distributions of observed and simulated (model L1) lines in the analysis sample, having been refined according to Equation 5.4. Theuns et al. (1998) show that insufficient mass resolution will have an impact on the predicted column density distribution of absorbers. However, their analysis shows that simulations with the same mass resolution as the L1 model will be incomplete for column densities, $\log(N_{HI}) \lesssim 12.5$, so this comparison should not suffer any biases over the chosen column density range.

Calculating the power-law index of Equation 5.5 over the range $13.2 \leq \log(N_{HI}) \leq 14.5$ results in $\beta = 1.42 \pm 0.10$ for the observed distribution and $\beta = 1.40 \pm 0.02$ for lines in the L1 model. This level of agreement with the observed column densities is not achieved when comparing to the column densities predicted by the lower resolution L2 model. The column density distribution calculated from the L2 absorbers begins to show signs of incompleteness at column densities as large as, $\log(N_{HI}) \lesssim 14$, leading to a shallower power-law slope ($\beta = 1.17 \pm 0.01$ for L2). This result reflects the lower resolution models' inability to adequately resolve the lowest density regions.

Although I do not attempt to account for incompleteness in the observed sample when fitting the column density distribution, the reader is referred to H95 where the impact of incompleteness is accounted for in their calculation of β. Using simulated spectra, they estimate their sample to be 82% complete for absorption lines with $12.9 \leq \log(N_{HI}) \leq 13.2$.

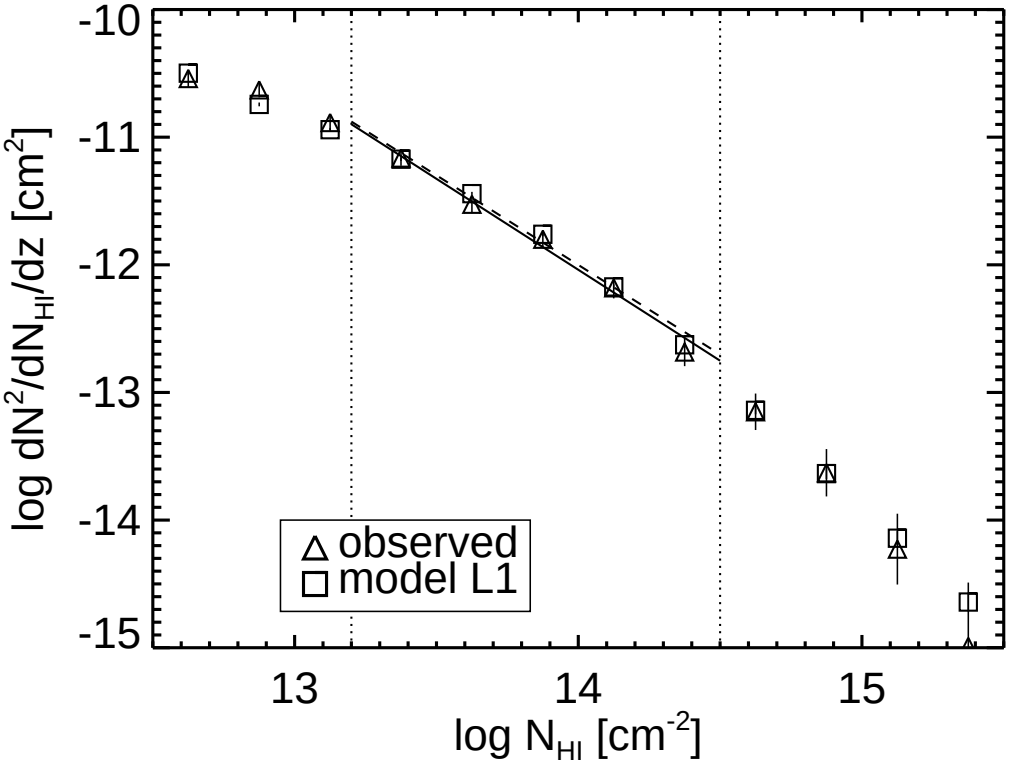

Figure 5.5: HI column density distribution of simulated lines in the L1 model (*squares*) compared with the distribution for those in the observed sample (*triangles*), where all absorption lines have widths greater than b_{therm} (§ 5.2.3). The *solid line* is the best fit power-law to the data between $13.2 \leq \log(N_{HI}) \leq 14.5$ which yields $\beta = 1.42 \pm 0.10$. A fit to the L1 simulated HI absorber column density distribution (*dashed line*) results in $\beta = 1.40 \pm 0.02$.

5.3.3 Number Density Evolution

The redshift evolution in the HI absorber number density has previously been used to measure the general trend in the UV background intensity (Theuns et al. 1998, DHKW), although it has not been as successful at constraining the overall amplitude of the intensity due to limitations imposed by insufficient mass resolution in the simulations. As an alternative approach, comparison of the FDDFs in simulated and observed spectra does not suffer the same degree of bias, as one measures the total HI opacity over a redshift interval significantly greater than that of a single absorber. Over the past few years, a great deal of effort has been spent quantifying the impact of varying simulation parameters, on the measured values of $\Gamma_{\rm HI}$ (Tytler et al. 2004, Bolton et al. 2005, Jena et al. 2005). These studies rely on measuring the mean HI opacity rather than the number density evolution of individual HI absorbers. In this work, I invoke the latter of these two approaches.

To conduct a fair comparison between simulated and observed absorber redshift evolution, one must first account for the small size of the observed sample. The effect of such a small sample can be quantified using the simulated spectra, from which I calculate the statistical cosmic variance due to a finite redshift interval. The total redshift path for the six observed spectra is 3.09, so I therefore calculate $n(z)$ from a randomly selected sub-sample of simulated spectra covering an equal redshift interval. This exercise is repeated 100 times for different random sub-samples, and the standard deviation in $n(z)$ at each redshift is then a measure of statistical cosmic variance. The uncertainties derived in this way are greater for model L2, reflecting the larger simulation volume. Cosmic variance due to finite simulation volume is also taken into consideration when making predictions for the absorber redshift evolution, as there is a suppression of power in fluctuations above a certain scale. The final conclusion is that the larger volume L2 model is the more appropriate to use when assessing the impact of cosmic variance. Uncertainties in the density evolution derived from model L2 are also adopted for that predicted by L1.

The number density evolution is shown in Figure 5.6 for both models (*open symbols*), plotted in comparison with that calculated from the observed line sample (*closed symbols*). The analysis sample selection criteria described in §5.2.3 has been applied in each case. From the evolution of lines exhibiting $N_{HI} \geq 10^{12.9}$ cm^{-2}, it is evident that the L2 simulation tends to under-

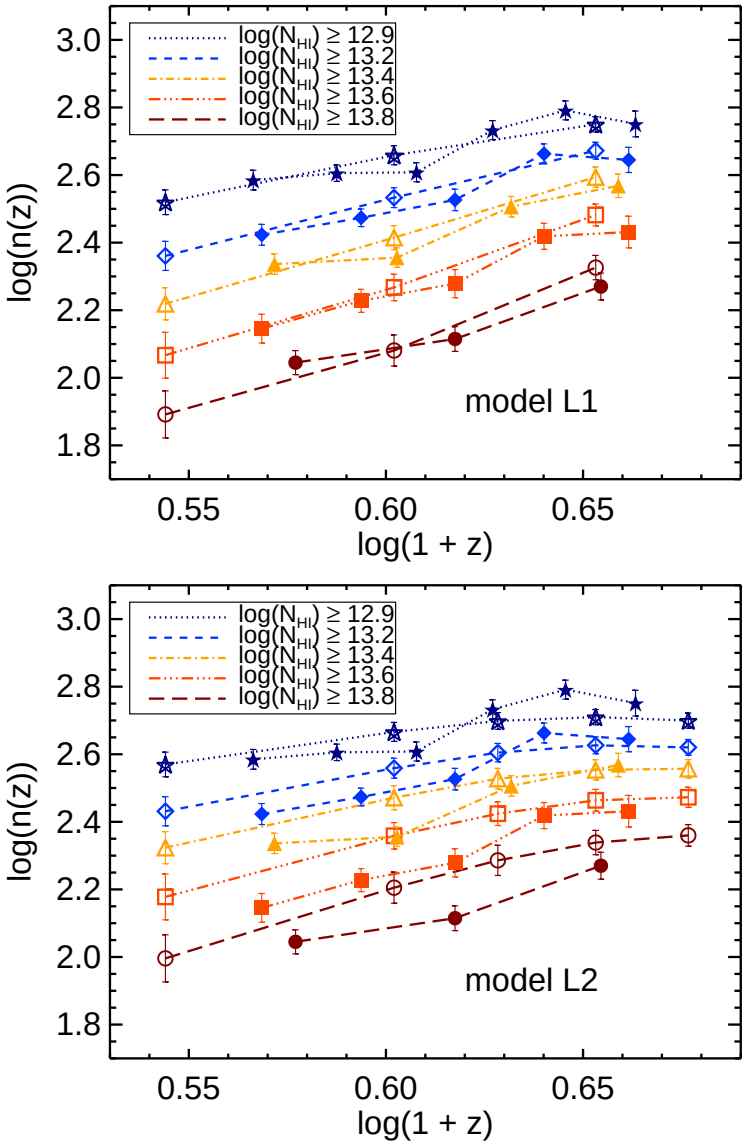

Figure 5.6: The redshift evolution of Lyα lines in simulated (*open symbols*) and observed spectra (*filled symbols*). Errors are derived for the observed data assuming Poisson statistics, while those on simulated data have been calculated from cosmic variance considerations (as described in the text). The top panel shows the comparison, and apparent agreement between the data and the L1 model, while the bottom panel displays the predictions of the lower resolution L2 simulation. Samples have been filtered according to the minimum b_{therm} and also exclude absorbers with $\log(N_{HI}) > 14.5$.

predict the number density of absorbers at high redshift. I suggest that the descrepancy is likely the result of limited spatial resolution in the simulation. Weaker HI absorbers preferentially trace less dense regions where the spatial resolution of the simulation is lower. The effect is more pronounced at high redshift where the greater density of the Universe leads to these regions becoming increasingly more difficult to resolve. This idea is strengthened by the observation that the 'turnover' in the evolution at z ∼ 3.5 is not as pronounced in the evolution of the highest column density absorbers, which should trace denser regions of the Universe. Based on this, I shall hereafter focus the comparison on those absorbers exhibiting $N_{HI} \geq 10^{13.2}$ cm^{-2}.

There is a striking difference between the number density evolution of absorbers predicted by the L1 model and that predicted by L2. Model L2 tends to over-predict the evolution at all column density intervals, and at all redshifts (with the exception of the $N_{HI} \geq 10^{12.9}$ cm^{-2} interval for the highest redshift bin, as discussed above). Taken by itself, the number density evolution in L2 absorbers would imply that these lines exhibit stronger clustering, are more heavily blended, or both (Babul 1991). On the other hand, model L1 is in excellent agreement with the observed evolution across all HI column densities and redshifts. Given that I have already shown that model L2 lacks the necessary resolution to adequately reproduce the observed distribution of line widths, it is evident that this model also lacks the resolution required to accurately reproduce the number density evolution. The implication is that the mass resolution of model L1 represents a minimum in that required when attempting to fully reproduce the evolution in Lyα forest absorption lines.

Focusing on the comparison of the evolution of model L1 absorbers with those in the observed data, I find excellent agreement down to the completeness limit of $N_{HI} \geq 10^{12.9}$ cm^{-2}. Taking into account that model L1 may not contain sufficient mass resolution to reproduce the observed line widths of low column density absorbers at z $\gtrsim$ 3 (Figure 5.4), the level of agreement observed at lower redshifts is evidence that the L1 model, with the modified HM96 ionization is suitable for describing the density evolution at these epochs.

5.3.4 HI Ionization Rate

Provided that absorbers are unsaturated (ie. $N_{HI} \lesssim 10^{14}$ cm^{-2}), a change in the ionization rate is roughly equivalent to altering the HI opacity of

simulated absorbers at a particular redshift. This will be true in the sample presented here, as most of the absorbers satisfy the saturation condition. For optically thin Lyα absorbers, the HI opacity, τ, is proportional to the local baryon density and the rate of HI ionizing photons, $\Gamma_{\rm HI}$, through (Croft et al. 1998):

$$\tau \propto \rho^{1.6} {\Gamma_{\rm HI}}^{-1}. \tag{5.6}$$

The criteria that the mean flux decrement at each redshift be the same in both simulated and observed Lyα forest spectra, requires that the HI ionization rate in the simulation be the same as that in the observed Universe. In order to obtain agreement between the redshift evolution of Lyα absorbers predicted by model L1, and that measured from the observed Lyα line sample, I calculate the factors, $f(z)$, by which the HI column densities (proportional to the HI opacity) of simulated Lyα lines must change at each redshift. $f(z)$ is then the inverse of the factors which should be applied to the original $\Gamma_{\rm HI}$ in the simulation to agree with that in the observed Universe.

The degree of line-blending is less severe for high column density Lyα absorbers, and should therefore provide a less biased estimate of the true redshift evolution of absorbers. The observed number density of Lyα absorbers with, $N_{HI} \geq 10^{13.8}$ cm^{-2}, is not well constrained due to a small number of observed absorbers in this column density range so I use the second highest column density interval, $N_{HI} \geq 10^{13.6}$ cm^{-2}, to calculate $f(z)$. I find that in order to match the observed number density evolution of Lyα absorbers, the column densities of L1 simulated lines must change by $f(z) = (1.00^{+0.33}_{-0.23}, 0.95^{+0.21}_{-0.16}, 0.75^{+0.22}_{-0.11})$ at z = 2.5, 3.0 and 3.5, respectively. Recall that there is an additional factor of 0.93 which has been applied to the model L1 absorber column densities in order to correct for the value of Ω_b originally adopted for the L1 simulation (see §5.2.2). An estimate of the true HI ionization rate is then obtained by correcting the HM96 ionization rates by factors of, $(0.93 f(z))^{-1} = (1.07^{+0.35}_{-0.28}, 1.13^{+0.24}_{-0.21}, 1.43^{+0.26}_{-0.34})$ at z = 2.5, 3.0 and 3.5.

Revised values of $\Gamma_{\rm HI}$ are shown in Figure 5.7 along with the predictions of the HM96 QSO-only rates. At redshifts, z = (2.5, 3.0, 3.5), the rates required to reproduce the observed number density evolution are, $\Gamma_{\rm HI} = (1.06^{+0.35}_{-0.27}$, $0.94^{+0.20}_{-0.18}$, $0.79^{+0.15}_{-0.19})$, in units of 10^{-12} s^{-1}. Larger HI photoionization rates are predicted by model Q2 of Fardal, Giroux & Shull (1998, hereafter FGS),

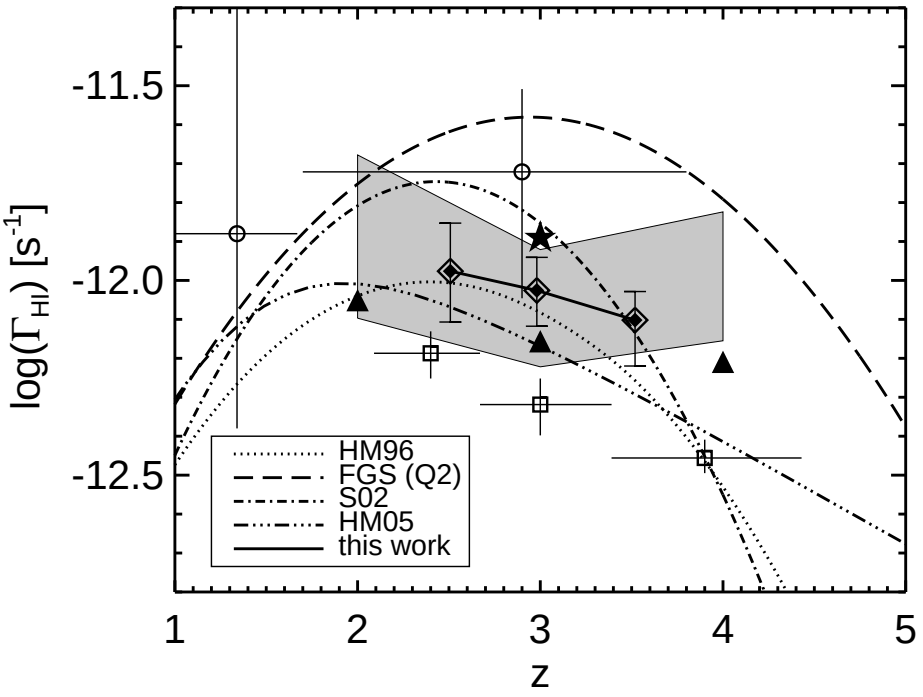

Figure 5.7: Evolution of the HI photoionization rate at high redshift. The model of HM96 used in the simulation is shown as the *dotted line*, along with the revised estimates, based on matching the evolution of simulated L1 lines with those in the observed sample (*diamonds*, *solid line*). For comparison, the *dashed line* is model Q2 of FGS which assumes a greater number of quasars at earlier cosmic epochs than the HM96 model, while the *dot-dot-dot-dashed line* is a revised prediction based on the QSO-only model of HM96 (HM05; Francesco Haardt, private communication). The *shaded region* defines the 1-σ bounds determined by Bolton et al. (2005), who take into account the uncertainties in physical parameters as well as those resulting from numerical effects in cosmological simulations. *Circles* show the proximity effect measurements of S02, while the *dot-dashed line* is their best-fit to the parameterization of the HM96 model assuming $\beta = 1.7$. The *squares* are from McDonald et al. (2001a, b) while the *triangles* are the estimates of Rauch et al. (1997). Finally, the HI ionization rate at z=3 determined by Kirkman et al. (2005) is included as a *star*.

hypothesizing the contribution from a greater number of quasars at high redshift (*dashed line*). These high rates are contrasted by the most recent QSO-only model of Haardt & Madau (HM05) provided by Francesco Haardt (private communication).

The model predictions are compared with values measured from observed properties of the Lyα forest. Scott et al. (2000, 2002, hereafter S02) compile a sample of nearly 100 moderate resolution high redshift QSO spectra, along with 170 spectra of low redshift QSO. Their large sample is used to calculate $\Gamma_{\rm HI}$ from the proximity effect (*circles*). Adopting the HM96 parametrization for the ionization rate, and assuming $\beta = 1.7$, the model parameters which best fit their data are, (A_{HM}, B_{HM}, z_c, S) = (3.2×10^{-13}, 1.45, 2.13, 1.42), shown as the *dot-dashed line* in Figure 5.7. McDonald et al. (2001a, b) measure the observed evolution in the mean transmitted flux, and compare this with that predicted by simulated spectra to derive values for $\Gamma_{\rm HI}$ (*squares*) which are $\sim$0.6 dex lower than the proximity effect measurements of S02.

The new $\Gamma_{\rm HI}$ estimates are in very good agreement with the estimates of Bolton et al. (2005), but are higher than the estimates of McDonald et al. (2001a, b). These results also rule out higher ionization rates, such as those predicted by FGS, or presented in S02. High values of $\Gamma_{\rm HI}$ would support the idea that star-forming galaxies make a significant contribution to the ionizing background at these redshifts (e.g. Steidel et al. 2001, Bolton et al. 2005). Adopting the HM05 prediction for the contribution from QSOs, these revised $\Gamma_{\rm HI}$ estimates imply that star-forming galaxies are required to account for 19%, 27% and 35% of the total ionizing background at z = 2.5, 3.0 and 3.5. This indicates that, while QSOs are potentially responsible for most of the HI ionizing background at, $z \lesssim 3.5$, at earlier epochs the intense UV radiation emitted by star-forming galaxies may become the dominant source of ionizing photons. The bulk of the star-forming galaxies responsible for the ionizing background are likely to also be detected as LBGs (Steidel et al. 2001), however there may also be a contribution from the dusty SMGs discussed in Chapters 2 and 3, whose abundance has recently been shown to peak at, $z > 2$ (Chapman et al. 2003, 2005; Aretxaga et al. 2003, 2006). This possibility will be discussed further in Section 5.5.

5.4 The Spatial Distribution of Lyα Forest Absorbers

The weak clustering strength of Lyα forest absorbers, relative to that measured for galaxies, provided the first evidence for the intergalactic origin of these absorption lines (Sargent et al. 1980). A major obstacle for clustering studies of the Lyα forest is the impact of line-blending. Typical line widths of 20 to 30 km/s serve to dilute any clustering signal owing to overlap between adjacent absorbers. As a result, marginal detections of weak signals have solely been measured on scales of $\sim$100 km/s (Rauch et al. 1992; H95; Cristiani et al. 1995; Lu et al. 1996; Kirkman & Tytler 1997). A more successful technique has been to use the narrower CIV absorbers found associated with high column density HI lines (Fernandez-Soto et al. 1996). This approach has the caveat that it is probing the most overdense structures, as CIV line samples are normally complete for $\log(N_{HI}) \geq 14$, or $\log(N_{CIV}) \geq 12.75$ (Ellison et al. 2000), although this limit may be extended through the analysis of pixel statistics (Aguirre et al. 2002, Schaye et al. 2003).

In this section, I use the simulated and observed HI linelists described in Section 5.2, to quantify the spatial distribution of individual Lyα forest absorbers. In order to quantify the effects of blending and thereby extract any underlying clustering signal in the data, I adopt the approach originally developed by OBD. This technique is based on the assumption that the LOS spatial distribution of absorbers is governed by both line-blending and the intrinsic clustering strength. This is the first time this technique is applied to high-resolution spectra and those predicted by ΛCDM, hydrodynamic simulations.

5.4.1 Fitting the Blending Model

Following Duncan, Ostriker & Bajtlik (1989, hereafter DOB), I begin by assuming that the 'true' number density of HI lines is described by a power law,

$$n\,(z) \equiv \frac{dN}{dz} = A(1+z)^{\gamma}, \tag{5.7}$$

and that the observed evolution is a result of line-blending. By calculating this underlying distribution I am able to compute the separation between adjacent absorbers in a redshift independant manner. The redshift interval,

δz, between two lines satisfying the selection criteria, can be converted to a scaled separation:

$$y \equiv n(z)\delta z, \tag{5.8}$$

assuming that the change in $n(z)$ is negligible across δz as is the case here.

Once line-blending is accounted for, the probability distribution of line intervals, $P(y)$, gives a measure of the clustering amplitude. Following DOB, I assume that blending results in a decrement to the number of small separations, quantified by a Gaussian filter:

$$B(y;z) = 1 - e^{-(y/y_0)^2}. \tag{5.9}$$

The blending scale is then defined as:

$$y_0 = \zeta n(z)(1+z), \tag{5.10}$$

as per Babul (1991), where the redshift dependance takes account of the higher blending probability induced by a greater density of lines.

When describing the distribution of local line-spacings, one chooses a particular clustering model, $P(y;z)$, satisfying the condition $\int_0^\infty P(y;z)dy = 1$. As a first approximation, I assume that Lyα lines arise at random intervals along the LOS so that the probability distribution can be described by a Poisson function, $P(y;z) = e^{-y}$.

To compare this model with the data, I calculate the prediction for the observed number density evolution, under the assumption of a 'true' evolution:

$$n_0(z) \equiv \frac{dN_0}{dz} = n(z)\int_0^\infty B(y;z)P(y;z)dy. \tag{5.11}$$

It follows that the measured distribution of line intervals may be compared with the 'z-integrated' probability distribution of the model:

$$P_0(y) = \frac{\int_{z_L}^{z_H} dz B(y;z)P(y;z)n(z)}{\int_0^\infty dy \int_{z_L}^{z_H} dz B(y;z)P(y;z)n(z)}. \tag{5.12}$$

The bounds, z_L and z_H, denote the lowest and highest redshifts of absorbers along a single LOS. Accounting for multiple QSO spectra, each with a unique redshift range for Lyα, I generalize Equation 5.12 to:

$$P_0(y) = \frac{\sum_i \int_{z_L(i)}^{z_H(i)} dz B(y;z)P(y;z)n(z)}{\sum_i \int_0^\infty dy \int_{z_L(i)}^{z_H(i)} dz B(y;z)P(y;z)n(z)}, \tag{5.13}$$

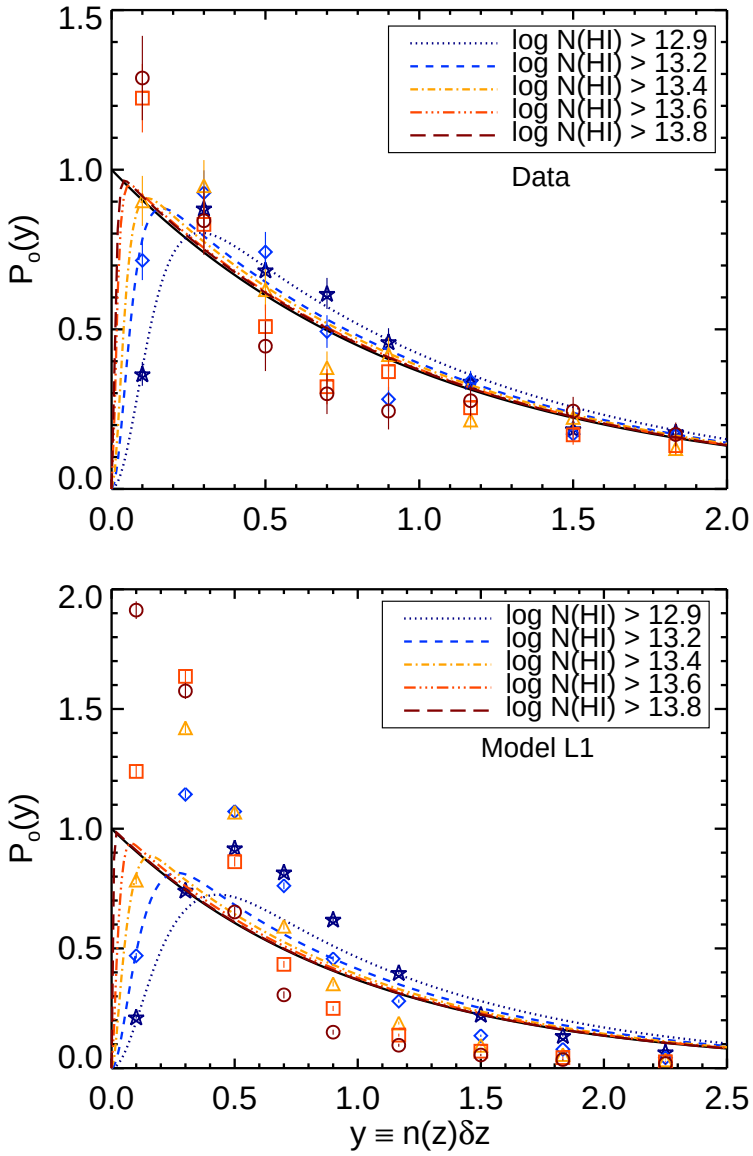

Figure 5.8: Probability distribution of scaled line intervals calculated for the Keck spectra (top) and those of the L1 model spectra (bottom). Symbols show the observed distributions for HI lines with $\log(N_{HI}) \geq 12.9$ (*stars*), 13.2 (*diamonds*), 13.4 (*triangles*), 13.6 (*squares*) and 13.8 (*circles*). A decrement at short spacings results due to blending of lines, an effect which becomes more pronounced when lower column density lines are included. The best-fit, blended Poisson models are plotted for comparison.

where i is the index of a single LOS (Figure 5.8).

When fitting the model to the observed and simulated samples there are 3 free parameters: γ, A and ζ. The blending parameter, ζ, is calculated from the probability distribution of short line intervals for those y-values where incompleteness is presumed to have an impact. The model then predicts an observed number density evolution (5.11), from which A is determined. Finally, the best-fit model is the one for which γ produces a minimum χ^2 value, as calculated from the redshift evolution of lines in that particular sample.

The level of agreement between the fitted model and the sample is determined by calculating the cumulative probability distribution,

$$S_o(y) = \int_0^y P_0(y')dy'. \tag{5.14}$$

Using this equation, the Kolmogorov-Smirnoff (KS) test measures the probability, Q_{KS}, that the model and the sample are drawn from the same distribution.

This model is fit to the observed data and to simulated lines from the simulations L1 and L2 (before and after modifying $\Gamma_{\rm HI}$), for the five column density ranges, and present the results in Table 5.2. As expected, the rate of evolution is greater for observed lines than that predicted by simulation L2, with values of γ higher by at least 1 in most cases. However, the level of agreement is much better when the observations are compared to the L1 model with the exception of the range, $\log(N_{HI}) \geq 13.8$, where observed absorption lines show $\gamma < 3$. Unfortunately, this is most-likely due to the small number of observed lines with $\log(N_{HI}) \geq 13.8$ (374 out of 1886 in the complete sample), leading to only 3 redshift bins and a γ which is most likely under-estimated here.

Another important feature revealed by the model parameters, is the degree of line-blending predicted by L1 versus that predicted by the L2 model. It is clear that the higher mass resolution L1 simulated spectra exhibit a completeness level closer to that of the data than those of L2. Across each column density range, the blending parameter (ζ) calculated from the L2 sample (before and after the correction to $\Gamma_{\rm HI}$) is more than twice that of the observations. When considering the best-fit values of ζ from L1 the agreements is much better, however there remains a slightly heavier degree of blending between adjacent absorbers than that in the observed sample.

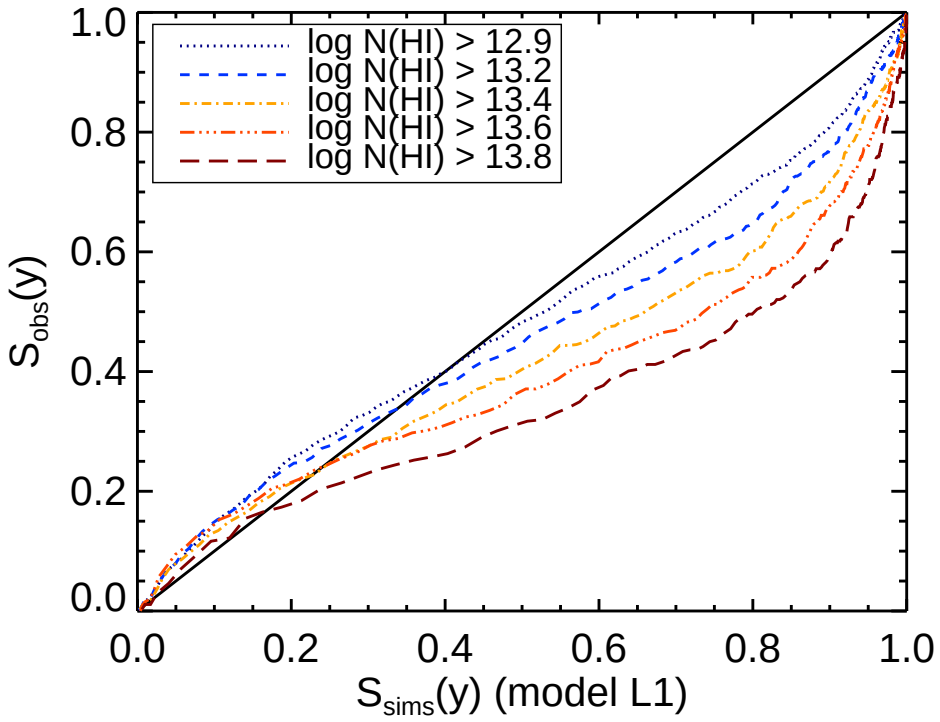

Figure 5.9: The cumulative distribution of line intervals in the observed sample compared to simulated lines from model L1. A slight initial rise in in each curves is due to the simulated lines being more strongly blended, a trend which reverses at longer spacings, indicating a larger clustering amplitude predicted by the model.

Sample	$\log(N_{HI})$	γ	A	ζ	D_{ks}	y_{max}	Q_{KS}
Observations....	≥ 12.9	2.89±0.44	8.81	7.0×10^{-5}	0.03	0.87	0.7243
	≥ 13.2	3.13±0.47	5.23	5.0×10^{-5}	0.07	0.62	0.0365
	≥ 13.4	3.31±0.51	3.59	4.2×10^{-5}	0.08	0.48	0.0044
	≥ 13.6	3.51±0.58	3.14	2.5×10^{-5}	0.10	0.42	0.0007
	≥ 13.8	2.98±0.70	2.03	2.6×10^{-5}	0.12	0.32	9.9×10^{-6}
Simulation L1...	≥ 12.9	2.60±0.02	14.91	1.0×10^{-4}	0.13	1.13	4.3×10^{-5}
	≥ 13.2	3.13±0.04	5.14	7.0×10^{-5}	0.20	0.90	8.7×10^{-11}
	≥ 13.4	3.57±0.05	2.01	4.5×10^{-5}	0.25	0.72	5.6×10^{-17}
	≥ 13.6	3.94±0.05	0.84	2.7×10^{-5}	0.31	0.65	3.3×10^{-26}
	≥ 13.8	4.17±0.06	0.41	8.0×10^{-6}	0.38	0.50	3.8×10^{-40}
Simulation L2...	≥ 12.9	2.00±0.03	39.29	1.5×10^{-4}	0.07	0.96	0.1033
	≥ 13.2	2.00±0.03	30.41	1.1×10^{-4}	0.15	0.99	2.1×10^{-6}
	≥ 13.4	2.08±0.03	18.54	1.0×10^{-4}	0.20	0.82	1.2×10^{-11}
	≥ 13.6	2.43±0.03	8.95	8.0×10^{-5}	0.26	0.66	7.1×10^{-19}
	≥ 13.8	2.83±0.03	3.62	6.0×10^{-5}	0.32	0.51	1.0×10^{-28}
Simulation L2...	≥ 12.9	2.49±0.03	19.34	1.3×10^{-4}	0.09	1.07	0.0147
(modified)	≥ 13.2	2.64±0.03	9.99	1.0×10^{-4}	0.17	0.89	1.0×10^{-7}
	≥ 13.4	2.99±0.03	4.68	8.0×10^{-5}	0.22	0.77	6.3×10^{-13}
	≥ 13.6	3.48±0.03	1.65	6.0×10^{-5}	0.27	0.66	4.1×10^{-20}
	≥ 13.8	4.02±0.03	0.48	5.0×10^{-5}	0.33	0.51	6.9×10^{-30}

Table 5.2: Best-fitting blended Poisson model parameters to describe the scaled line intervals of simulated and observed Lyα forest lines. D_{KS} is the maximum seperation between the blended model and the observed or simulated distribution, while y_{max} is the scaled interval at the maximum separation.

This descrepency between the values of ζ measured from model L1 and the observations is most likely due to a larger clustering amplitude between simulated lines. This becomes clear when considering the maximum deviation between the blended Poisson model and the cumulative probability distributions, D_{max}. The values of Q_{KS} then imply that for all HI column density intervals, the simulated lines are more strongly clustered than those observed.

There are a number of possible reasons why the simulated lines may appear to be more clustered than those in real QSO spectra, including:

1. Insufficient mass resolution in the L1 simulation (as discussed in Section 5.3.1) may cause a greater level of incompleteness, or stronger degree of line-blending between simulated absorbers when compared to those in observed spectra. Such an effect could lead to an apparent increase in the clustering strength between adjacent absorption lines in the simulated spectra. This potential bias to clustering analyses using individual absorption lines is part of the reason that most studies now focus on measuring the mean opacity in simulated and observed spectra, which should be proportional to the underlying mass density (e.g. Croft et al. 1998).

2. Structure grows more rapidly in the simulations than in the real Universe due to some physical mechanism that is yet unknown, or unaccounted for in the models. Although for this thesis I have assumed that the ΛCDM model provides the best description of the Universe, structure would grow less rapidly in the models if Ω_m were lower or Ω_Λ were higher. There is also evidence that lower mass structures would grow more slowly in a Warm Dark Matter Universe.

3. Feedback from galactic winds in the early AGN and star forming galaxies discussed in Chapters 2, 3 and 4, not properly accounted for in the simulations, may produce significant regions devoid of HI gas in the real Universe. This effect would result in an excess of wide line separations in the observed spectra over that measured in the simulated spectra.

From the line width distribution shown in Figure 5.3, it is apparent that even the L1 model lacks the mass resolution required for convergence, which is consistent with the findings of Theuns et al. (1998). This leads me to

suspect that item (1) above is the correct explanation (though the least exciting) for the simulated Lyα lines exhibiting a stronger clustering signal than those in the observed spectra. However, confirming this hypothesis requires further analysis using higher mass resolution cosmological simulations, with comparable volume to that of the L1 box, or preferably that of the L2 box, so that the cosmic variance uncertainties are properly accounted for.

5.5 Summary and Future Work

This Chapter compares the statistics of high redshift HI absorbers in the Lyα forest with predictions by modern SPH simulations of a ΛCDM Universe. The high spectral resolution and signal to noise of the data allow us to study HI absorbers in the low column density IGM with, $\log(N_{HI}) \gtrsim 12.9$. The main findings can be summarized as follows:

1. After applying the selection criteria to the sample, the lower resolution L2 model predicts a greater number of wide absorption lines, over that observed. Although the L1 model does a better job of reproducing the b-distribution of observed lines, a small excess of wide absorbers implies that this simulation also lacks necessary mass resolution required for convergence. Given the better agreement between model L1 over L2 with the observed spectra, differences between simulated and observed line widths is most likely due to insufficient mass resolution, which introduces a bias that increases when comparing higher redshift and lower HI column density lines.

2. Considering only the predictions of the higher mass resolution L1 simulation, there is good agreement between the observed and simulated number density of lines. This agreement is achieved by adopting HI photoionization rates, $\Gamma_{\rm HI} = (1.06^{+0.35}_{-0.27}, 0.94^{+0.20}_{-0.18}, 0.79^{+0.15}_{-0.19}) \times 10^{-12}$ s^{-1}, at redshifts, z = 2.5, 3.0 and 3.5. It is possible that these estimates are biased due to insufficient mass resolution in the L1 simulation.

3. Accounting for the impact of line blending with a model for the spatial distribution of absorption lines, the L1 simulated lines appear to be more strongly clustered than those in the observed spectra. Although the most likely explanation for this is, again, insufficient mass resolution, there is also the possibility that outflows from high-redshift

objects have created an excess in the observed number of "voids", or more speculative is the possibility that the growth of structure is proceeding less rapidly than predicted by the models.

Assessing the impact of statistical cosmic variance using simulated spectra implies that the small sample size of only six QSO is not biasing the results. However, the findings presented here could be strengthened by the analysis of a much larger sample of high signal-to-noise spectra with resolutions comparable to that of the KECK/HIRES spectra. Even if a larger sample of QSO spectra are included, the results of this analysis suggest that the most significant advances could be made using higher particle mass resolution cosmological, hydrodynamic simulations.

5.5.1 Dusty starburst galaxies and the Lyα forest

Although optically luminous QSOs and star-forming galaxies are the most likely candidates contributing to the UV background radiation and the observed physical state of the Lyα forest (e.g. temperatures $\sim 10^4$ K and HI ionization fraction $\gtrsim$90%), there have been no studies on the impact of the optically faint, but extreme submm-selected starburst galaxies at z$\sim$2-4 (SMGs; see Chapters 2 and 3). Nearby far-infrared luminous starburst galaxies such as M82 and Arp220 (believed to be local analogues to the high-redshift SMGs), exhibit large-scale outflows from their nuclear regions with velocities $\gtrsim$100 km s^{-1}. An important outstanding question is whether or not the high-redshift SMGs also exhibit outflows which cannot be observed directly given the limited sensitivity aned angular resolution of current submm/mm facilities.

One method of indirectly testing for the presence of outflows from SMGs, would be to observe their impact on the spatial distribution and temperature of the gas in the surrounding IGM. In practice, the large beamsizes of single-dish submm/mm instruments ($\sim$10-15″), means that we may only identify z=3 SMGs separated by $75-100$ kpc from the line-of-sight to a distant QSO (used to obtain spectra of the Lyα forest), and are limited in sensitivity by the confusion noise due to fainter background SMGs on the scale of the beam. With the advent of large, high angular resolution submm/mm interferometers such as the SMA, PdBI and ALMA (see Chapter 4), it will be possible to detect SMGs which are separated by $\lesssim$10 kpc from the IGM gas probed by current Lyα forest observations. Over such small scales, the impact of

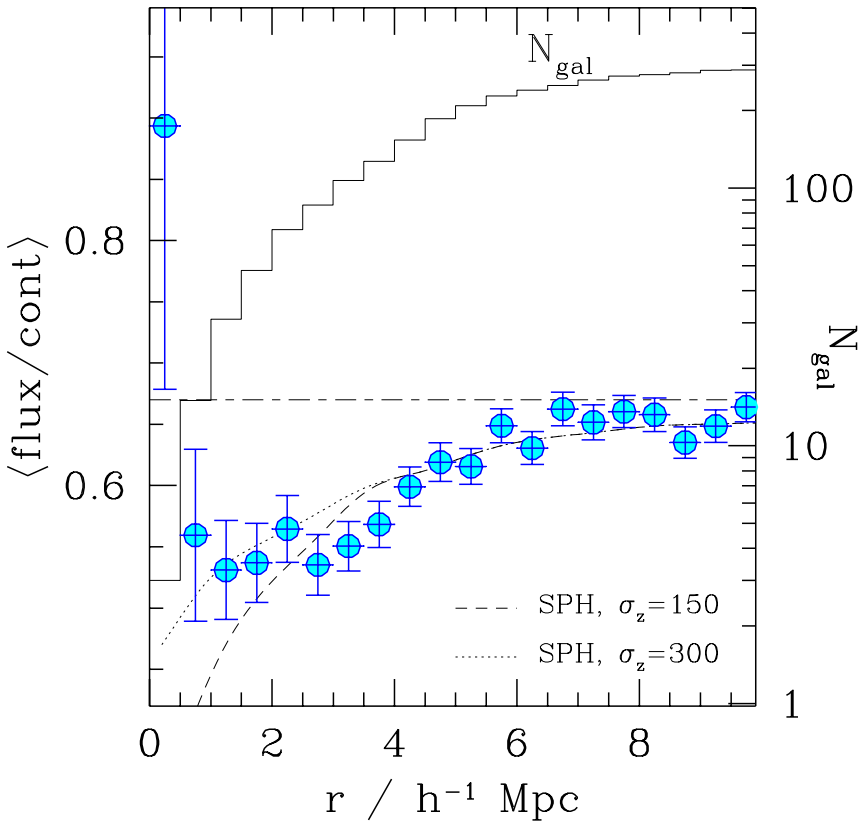

Figure 5.10: The mean Lyα forest flux decrement (proportional to the mean HI opacity) as a function of comoving separation between individual LBGs and the QSO line of sight (Adelberger et al. 2003). The filled circles show the observed data (where the number of LBGs in each bin is indicated by the histogram corresponding to the y-axis on the right), while the dotted and dashed lines are the predictions of a ΛCDM simulation, which does not include a prescription for the physical impact of galaxies on the IGM. σ_z is the uncertainty on the LBG redshift [km s^{-1}] assumed for the LBGs in the simulation.

galactic outflows from SMGs on the surrounding HI gas can be studied using a similar technique to that employed by Adelberger et al. (2003) to study outflows from Lyman break galaxies (LBGs).

Adelberger et al. (2003) perform a cross-correlation analysis of the HI opacity in the Lyα forest of 8 QSO spectra, and the physical distance to 431 z$\sim$3 LBGs identified in these 8 fields. In their study, they measure the mean transmissivity in a $\triangle$z=0.02 section of the Lyα forest at the corrected redshift[2] of each LBG in their sample. The angular separation between the LBG and the QSO can then be converted to a co-moving physical separation [Mpc h^{-1}] between the LBG and the associated IGM at the LBG redshift. The results of calculating the mean transmissivity in the Lyα forest associated with LBGs at various distances is shown in Figure 5.10.

There are two important physical concepts illustrated in Figure 5.10. The first is that there is a statistically significant decrement in the transmitted Lyα forest flux for LBGs within $\lesssim$5 Mpc h^{-1} of the QSO line of sight. As the transmitted flux is inversely proportional to the HI opacity (or equivalently gas density where the gas density should reflect the underlying density of dark matter), the increase in the flux decrement with decreasing LBG separation would imply that LBGs trace physically dense regions of the matter (visible and dark) distribution. The second important result illustrated by Figure 5.10 is that on the smallest angular separations between the LBGs and the HI Lyα forest ($\lesssim$0.5 Mpc h^{-1}), there is a sharp increase in the transmitted flux, which corresponds to an apparent decrease in the density of neutral Hydrogen close to these LBGs. This result can be explained either by *i)* UV photons from the starburst in the LBG ionizing the nearby Hydrogen gas, or *ii)* galactic outflows creating regions physically devoid of gas around the LBGs.

In a similar fashion, a complementary approach to studying the interplay between high-redshift starburst galaxies and the IGM, would be to obtain deep ALMA imaging of dusty SMGs in the fields of the QSOs used to probe the Lyα forest. Under the assumed cosmology, an angular separation of 0.5 Mpc h^{-1} at z=3 corresponds to $\sim$1.5$'$, so we would need to survey a $\sim 3' \times 3'$ region centered on the QSO in order to sample the physical scales of interest. As such, deep 290 GHz (1 mm) ALMA imaging in intermediate

[2]In their follow-up Keck spectroscopy of z$\sim$3 LBG candidates, the typical velocity difference between the Lyα emission line redshift and the mean redshift determined from interstellar absorption lines in the LBG spectra is $\langle \triangle \mathrm{v} \rangle = 614 \pm 316$ km s^{-1}.

resolution configurations (synthesized beamsize $\sim 1-2''$) would be sufficient to identify luminous SMGs in these fields. An extrapolation of the most recent 1100 μm source counts from Laurent et al. (2006) suggest that a deep ($\sigma_{1mm} = 20$ μJy) survey would detect $\sim$25–250 sources at the 5-σ significance level[3] in a 9 square arcmin field. Such a survey would require $\sim$34 hours of integration time with ALMA under the assumption of a 50-element array of 12 m diameter antennas.

Once SMGs have been identified in the QSO fields, the challenging (but essential) task of obtaining redshifts for these objects begins. The single-dish, wide bandwidth mm-to-cm wavelength CO line spectroscopy discussed in Chapter 3, lacks the angular resolution required to obtain redshifts for individual objects in these proposed mm-wavelength interferometer surveys. Unless either the ALMA or PdBI instruments are equipped with large correlators that have the ability to correlate signals from wide bandwidth receivers between as many as 50 antennas (or 6 in the case of PdBI), then high angular resolution CO spectroscopy to determine redshifts will not be practical. Therefore, the optimal means of obtaining redshifts for these SMGs would be through the use of multi-object spectroscopy of their optical/IR counterparts with 8-10 m class optical telescopes such as Keck or Gemini. Given that the SMGs would be initially detected at an angular resolution of $\sim$1-2$''$, identification of optical/IR counterparts should be relatively straightforward (e.g. Dunlop et al. 2004).

There is a distinct difference between the potential outcome of this proposed SMG study and that of the Adelberger et al. (2003) study of the impact that LBGs have on their local environments. Given that the SMGs are optically faint due to both obscuration by dust and cosmological dimming, only a small fraction of the HI ionizing UV photons produced through star-formation and AGN activity are likely to escape and alter the ionization state of the surrounding IGM gas. As such, detection of an increase in the transmitted Lyα forest flux density (corresponding to a decrease in the HI gas density) at the smallest SMG separations (such as that shown in Figure 5.10), could only be interpreted as the signature of outflows from these high-redshift SMGs. Tacconi et al. (2006) suggest that the gravitational potentials of the high-redshift SMGs would be too great so as to suppress the

[3]Adopting the conversion factor, $L_{FIR} = S_{850} \cdot 1.9 \times 10^{12}$ L$_\odot$, a ν^3 greybody spectrum and $SFR = L_{FIR} \cdot 1.2 \times 10^{-10}$ M$_\odot$ yr^{-1}, an $S_{850} = 0.15$ mJy source would have a $SFR \sim 150$ M$_\odot$ yr^{-1}.

wide scale distribution of gas from outflows. On the other hand, outflows, or winds are generally associated with nuclear starburst activity (as in the case of M82) so the inferred physical scales and velocities over which these outflows have an impact may be used to estimate the level of star-formation activity and gravitational potentials (mass) of this exciting new class of objects. Such observations would nicely complement the mm/cm wavelength spectroscopy of molecular diagnostic lines such as HCN and [CI], as discussed in Chapter 4.

Chapter 6

Thesis summary and future prospects

Given the wealth of new multi-wavelength facilities, including ground-based single-dish and interferometric facilities, along with satellite-borne telescopes coming on line during the next decade (particularly at (sub)mm wavelengths), it is an exciting time to be working in this area of observational cosmology. The analyses presented in this thesis have been stimulated by the opportunity to explore the complentarity that *currently* exists for studying massive galaxy and structure formation at high-redshift, through observations of various phenomena between optical and radio wavelengths. In particular, this work uses existing (sub)mm wavelength facilities to address some of the many outstanding problems in the field of dust-enshrouded star formation at high-redshift, in order to motivate the need for sensitive, higher angular resolution (sub)mm surveys and the detailed studies of individual objects with near future facilities such as the LMT and ALMA.

It has been less than 10 years since the cosmic infrared background (CIB) was first resolved into discrete point sources by deep surveys at (sub)mm wavelengths (Smail, Ivison & Blain 1997; Hughes et al. 1998, Barger et al. 1998; Bertoldi et al. 2000). The implication of the faintness (or non-detection) of these sources at shorter (e.g. 450 μm) and longer (e.g. 20 cm) wavelengths is that they are likely to be dusty starburst galaxies at z$\sim$2–

4 with infrared luminosities $L_{IR} \geq 10^{12}\ L_{\odot}$ and star formation rates 100–1000 $M_{\odot}\ yr^{-1}$. The discovery of this optically-obscured population of submm galaxies (SMGs) has motivated a slew of subsequent surveys of varying depths and areas (Scott et al. 2002; Borys et al. 2003; Greve et al. 2004; Laurent et al. 2005). Despite the great progress that these surveys have made, the sensitivities and mapping speeds of current instruments on existing facilities have not been sufficient to answer the fundamental question: *are the (sub)mm galaxies (SMGs) the progenitors of massive, present-day elliptical galaxies?* In order to answer this question, wider-area surveys are required to better constrain both the co-moving number density, and clustering strength of this population. Such a need has helped to motivate the SHADES survey, originally intended to cover 0.5 sq. degrees between two fields down to a 3-σ rms of $\sim$8 mJy at 850 μm.

The initial results of the SHADES survey, conducted with SCUBA at 850 and 450 μm are presented in chapter 2. This analysis is one of four independent analysis carried out separately by groups at the IfA, Kent, UBC and INAOE. The agreement in the 850 μm source candidates and source counts is generally good between all four groups, as presented in Coppin et al. (2006), however the comparison of three individual reductions of the 450 μm data finds that only two are found to be consistently correct. As such, Coppin et al. (2006) do not develop the 450 μm SHADES data beyond a short presentation of the 450 μm peak-pixel flux stacking analysis.

In this thesis, along with presenting the INAOE ('Group C') analysis of the 850 μm source counts and candidate list, I have further exlored the usefulness of the 450 μm SHADES dataset, which is currently the largest short wavelength submm dataset in existence. Although I find that the data do not allow for strong constraints on the 450 μm source counts, my version of the stacking analysis reveals that the population of 1.4 GHz radio-detected 850 μm consortium sources is securely detected at 450 μm, while the radio-undetected subsample is also marginally detected. A simple comparison of the 450-to-850 μm flux density ratios of each subsample with the expected evolution in an Arp220 spectral energy distribution (Figure 2.28), implies that the radio-undetected subsample is likely at a higher redshift than the radio-detected subsample (mean redshift of $z \sim 3.7$ compared to $\sim$2.5, respectively). Although such a result should be confirmed with follow-up redshift studies of the radio-undetected submm galaxies, the implication for the existence of a high-redshift tail of submm galaxies is tantalizing, and will be further discussed in an upcoming SHADES publication (Wagg et al. in prepa-

ration).

In order to robustly determine the FIR luminosity (proportional to the obscured star formation rate) of a SMG we first require the measurement of its redshift. The course angular resolution of the antennas used to discover these SMGs (typically 10–18″), means that the optical/infrared galaxy counterpart responsible for the intense (sub)mm emission cannot be immediately or unambiguously identified, and so optical spectroscopy to measure a redshift is not possible. As such, the method adopted by most groups for measuring SMG redshifts, is to use deep radio interferometry imaging (e.g. the VLA at 1.4 GHz) to identify the most likely galaxy counterparts, for which optical spectra are subsequently obtained (e.g. Smail et al. 2002; Chapman et al. 2003, 2005). This method may lead to biases in the measured redshift distribution of the global population, as the positive K-correction to the radio flux means that the highest redshift SMGs ($z \gg 3$) will not be detected in the deep radio imaging. Ivison et al. (2005) find that only $\sim$10% of the bright ($\sim$8 mJy) population is undetected at 1.4 GHz down to a 1-σ rms of 4.6 μJy beam^{-1}, and so conclude that a significant population of $z \gg 3$ SMGs is not excluded by the optical redshift surveys. Confirming (or disproving) this result ultimately requires redshifts to be measured for the radio-undetected sources using alternative methods. The results of the 450 μm stacking analysis of SHADES 850 μm catalogue sources, both detected and undetected at 1.4 GHz, implies that a significant fraction of the SHADES sources are likely to lie at $z \gg 3$.

In chapter 3, I have presented the first attempt at implementing a potentially powerful method of measuring unambiguous redshifts for the far-infrared (FIR) luminous SMGs discussed in chapter 2. The method uses broadband mm-to-cm wavelength spectroscopy of these objects to search for molecular emission lines such as CO, whose luminosity correlates roughly with the FIR luminosity. The success of such methods relies on the assumption that the locally observed relation between the FIR and CO line luminosities (Young & Scoville 1991) holds for these high-redshift objects (see discussion in Riechers et al. 2006a). In this pilot study, a 'guided' search for CO J=1-0 and CO J=2-1 line emission in HDF850.1 over the redshift interval $3.3 \lesssim z \lesssim 5.4$ was conducted with the 100 m GBT. The redshift of HDF850.1 (the first SMG discovered in a blank-field, extragalactic 850 μm survey; Hughes et al. 1998) has remained elusive, despite the fact that the *Hubble Deep Field* North field has some of the most sensitive observations

that currently exist at X-ray to radio wavelengths. The lensed galaxy counterpart to HDF850.1 has only recently been discovered in deep K' band imaging with the Subaru telescope (Dunlop et al. 2004), but is too faint for optical spectroscopy.

Our search for CO line emission over the aforementioned redshift interval was motivated by the predictions of a FIR to radio photometric redshift technique (Hughes et al. 2002; Aretxaga et al. 2003, 2005; Chapin 2004). Despite 70 hours of GBT observing time, spectral baseline irregularities limit the sensitivity of the final spectra, and we do not detect low-J CO line emission in this object (Wagg et al. 2006b). The limits obtained on the CO line luminosity are not sufficient to assess the validity of the photometric redshift technique within the context of the FIR-to-CO luminosity relation. As spectral baselines are generally more stable when observing with an interferometer than with a single dish antenna, obtaining SMG redshifts from low-J CO lines will be more effectively accomplished with the EVLA. Alternatively, future searches for high-J CO line emission at mm-wavelengths using instruments such as the 'redshift receiver' on the LMT (Figure 3.8), may be more successful than cm-wavelength searches as the molecular emission-line regions in these high-redshift SMGs are expected to be warm and dense (Weiss et al. 2005), with the result that the high-J CO line intensities should be 10–20$\times$ greater than that in the low-J CO lines.

Once redshifts have been obtained for high redshift FIR luminous AGN and starburst galaxies, one can begin to study the physical conditions responsible for their extreme nature by observing additional molecular emission lines redshifted into the submm-to-cm windows. To date, only 36 objects at $1.0 \lesssim z \lesssim 6.4$ have been detected in CO line emission, while only 5 of the brightest members of this sample have also been detected in other species such as HCN and [CI]. The reason that so few detections of emission lines other than CO have been made, is that their intensities are typically $\geq$10$\times$ fainter than CO. The spectral line sensitivities and receiver bandwidths of current facilities such as the VLA and the PdBI, limit us to searching for faint molecular emission-lines in only the most apparently luminous high-redshift objects, where many have had their fluxes amplified by gravitational lensing.

In chapter 4, I present detections of HCN J=5-4 and [CI] $^3P_1$–$^3P_0$ in the ultraluminous quasar APM 08279+5255 at z=3.91 using the PdBI (Wagg et al. 2005; 2006a). This object has an apparent FIR luminosity of 10^{15} $L_\odot$ (Lewis et al. 1998), though it is believed to be gravitationally lensed by a

factor of 10–100 (Ledoux et al. 1998; Ibata et al. 1999; Egami et al. 2000). Although the lensed nature of this object alone makes it an ideal candidate for studies of faint molecular emission lines, PdBI detections of intense CO J=4-3 and J=9-8 emission imply that it also contains a warm and dense circumnuclear disk (Downes et al. 1999). The conclusion that the gas is dense can be confirmed through observations of dense-gas tracers such as HCN and HCO^+ ($n_{H_2} > 10^4$ cm^{-2}), which have higher dipole moments than CO, and generally arise within star forming cores in the Milky Way. The HCN J=1-0 line luminosity in both nearby galaxies and Milky Way giant molecular clouds has been found to correlate strongly with IR luminosity over the range $4.5 \lesssim \log L_{IR}/L_{\odot} \lesssim 12.5$ (Gao & Solomon 2004a, 2004b; Wu et al. 2006), implying that the HCN line luminosity in high-redshift objects may be used to estimate their star formation rates (Solomon et al. 2003). The intensities in the high-J CO lines also implies a large mass of molecular gas ($\gtrsim 10^{10}$ M$_{\odot}$) within the nuclear region of APM 08279+5255, which is confirmed by the detections of CO J=1-0 and CO J=2-1 (Papadopoulos et al. 2001; Lewis et al. 2002; Riechers et al. 2006). An independent means of confirming such a large gas mass is through observations of redshifted [CI] line emission (Papadopoulos et al. 2005; Papadopoulos & Greve 2004).

The new data which I present on APM 08279+5255 confirms the results of previous studies, while also revealing unexpected surprises. By using the [CI] $^3P_1 - ^3P_0$ line luminosity to infer the total molecular gas mass in APM 08279+5255, I calculate a mass which agrees with that calculated from the CO J=1-0 line luminosity to within a factor of 2. This same level of agreement is also found for the other four high-redshift objects previously detected in both CO and [CI], implying that [CI] line emission may indeed be used as an alternative estimator for the gas mass in high-redshift objects when CO is not observable. This is particularly important when considering that the sensitive ALMA interferometer will be able to observe the [CI] line transitions out to $z > 10$, redshifts where only the very high-J CO lines ($J_{\rm upper} \geq 9$) will be observable with the currently funded ALMA receivers.

Although the [CI] $^3P_1 - ^3P_0$ line luminosity in APM 08279+5255 is not unusual, the luminosity in the HCN J=5-4 line is approximately an order of magnitude larger than expected based on typical [HCN/CO] abundance ratios and physical conditions derived from the relative CO line intensities (where the CO line emission is assumed to be cospatial with the HCN J=5-4 line emission). I have proposed a number of plausible explanations for such an anomaly, including the most likely scenario where the HCN J=5-4 line

is radiatively excited by infrared radiation emitted from the central AGN. Distinguishing between the various scenarios, which might explain the enhanced excitation of HCN J=5-4, requires observations of additional HCN line transitions. As such, I have recently proposed to observe both HCN J=6-5 with the PdBI and HCN J=2-1 with the GBT for the upcoming observing semester. Observations of an additional high-J HCN line will help constrain the turnover transition of the HCN spectral energy distribution, while the luminosity in the low-J HCN lines is expected to provide a better estimate of the dense gas mass.

Outflows from luminous high-redshift objects such as APM 08279+5255[1] should have an impact on the gas in the surrounding intergalactic medium (IGM) where most of the baryons in the Universe are expected to be found prior to $z \gtrsim 2$. The observed manifestation of the high-redshift IGM comes in the form of the Lyα forest of HI absorption lines in the spectra of distant QSOs. Numerical simulations have shown that absorption at different redshifts by the 1215.67 Å transition of HI along the QSO line of sight, can be used to estimate the amplitude of the density fluctuations in the underlying dark matter distribution (e.g. Croft et al. 1998). The currently favoured model for the Lyα forest is one in which the high ionization fraction of the Hydrogen gas ($\geq$90 %) is likely maintained by energetic UV photons emitted by the same extreme AGN and star-forming galaxies discussed in chapters 2, 3 and 4.

In chapter 5, I have presented an analysis of the number density evolution of Lyα forest lines in a sample of 6 high-resolution QSO spectra. I compare the results to those obtained from artificial spectra predicted by a pair of cosmological hydrodynamic simulations of a ΛCDM Universe. The redshift evolution of the number density of absorbers is related to the neutral Hydrogen opacity, which is inversely proportional to the photoionization rate for a fixed cosmological model. Under the assumption of the year-1 *WMAP* cosmological parameters (Spergel et al. 2003), the artificial spectra are used to calibrate the ionization rate required to reproduce the observed number density of absorbers at z=2.5–3.5. QSO-only models of Haardt & Madau (2005; private communication) predict ionization rates which are 19%, 27%

[1]Outflowing material from this broad absorption line quasar has been observed to exhibit velocities $\simeq$13,100 km s^{-1} with respect to the systematic redshift of z=3.91 (Ellison et al. 1999).

and 35% lower at z=2.5, 3.0 and 3.5 than those found here, and I suggest that star forming galaxies should be responsible for this discrepancy (e.g. Bolton et al. 2005). Though the gas-rich Lyman Break Galaxies (LBGs; Steidel et al. 1996), with estimated star formation rates in the range 1–10 $M_{\odot}$ yr^{-1}, are likely responsible for much of the excess ionizing radiation, the escape fraction of UV photons from these objects is uncertain. Another possibility is the population of SMGs, although their large dust masses and subsequent opacity to UV/optical photons should make these objects insignificant contributors to the HI ionizing background (despite estimated star formation rates of 100–1000 $M_{\odot}$ yr^{-1}). Future UV/optical spectroscopy of large samples of SMG galaxy counterparts are required to measure the escape fraction of HI ionizing photons.

In chapter 5, I also present an analysis of the line-of-sight spatial clustering of HI absorption lines in the Lyα forest of both observed and artificial spectra. Most present-day studies of large-scale structure using the Lyα forest focus on the smooth variations in the flux decrement, or mean HI opacity in individual spectra, believed to trace the physical overdensities in the underlying dark matter density distribution (e.g. Cen & Ostriker 1993). However, the particle mass-resolution in modern cosmological hydrodynamic simulations is now becoming high enough that we may begin to compare the clustering properties of individual absorption lines in both observed and artificial spectra, as I have done here in this thesis. This is important as it is then possible to simultaneously constrain the IGM gas temperature, estimated from the HI absorption line widths. My preliminary results show that HI absorbers in the artificial spectra are more strongly clustered than those observed, which may be due to insufficient particle mass-resolution in the simulations. A higher mass-resolution simulation has recently become available (Romeel Davé, private communication), and so I expect to analyze artificial spectra from this new simulation and present these results for publication in the near future.

High-resolution spectrographs on existing facilities such as Keck and the Very Large Telescope (VLT) have already been used to compile large samples of QSO Lyα forest spectra of similar quality to those used in this thesis. As this analysis has been intended as a pilot study, the ultimate aim is to use large samples of existing QSO spectra (10–100), in conjunction with artificial spectra derived from higher mass-resolution simulations, to place strong constraints on the HI photoionization rate over the redshift interval z$\sim$2–6. The current uncertainty in both the redshift, and duration of reionization

has led to a great deal of effort in trying to reconcile the presence of a Gunn-Peterson absorption trough in z > 6 QSO spectra, implying that reionization may have ended as late as z ∼ 6.2 (Becker et al. 2001; White et al. 2003; Fan et al. 2002, 2006), with the CMB temperature-polarization cross correlation signal measured in *WMAP*, which suggests an instantaneous reionization at $z = 10.9^{+2.7}_{-2.3}$ (Page et al. 2006). By accurately measuring the evolution of the HI photoionization rate out to z ≲ 6, it should be possible to constrain the mean redshift and duration of the reionization epoch by extrapolating to higher redshifts.

To conclude, the analyses presented in this thesis have used facilities operating over a broad range of observed wavelengths (∼4200 Å to 2 cm), to study distinct, but related phenomena in the high redshift Universe. Although optical studies of the Lyα forest, such as those presented in chapter 5, have become a powerful tool for studying large scale structure in the Universe, it is important to point out that the Lyα forest was first discovered 30 years ago, while extragalactic astronomy at optical wavelengths has been developing since Edwin Hubble first discovered that the Universe was expanding almost 80 years ago. In comparison, the observational window recently opened at (sub)mm wavelengths by the invention of single, and multi-pixel bolometer cameras (chapter 2) has only existed for the past 3 decades and (sub)mm observations beyond the relatively local Universe ($z \gtrsim 0.1$) have only been possible for the last 15 years. Given that the cosmic infrared background exhibits an energy density comparable to that of the optical background (e.g. Franceschini et al. 2001), it may be said that we have only recently begun to study the second half of the Universe, with new and existing facilities such as Akari, Spitzer, BLAST, JCMT, APEX, IRAM 30-m, PdBI, and in the near future with Hershel, LMT and ALMA.

Bibliography

[1] Adelberger et al. 2003, ApJ, 584, 45

[2] Archibald E. N., Wagg J. W., Jenness T., 2000, SCD System Note 2.2 (http://www.jach.hawaii.edu/JACdocs/JCMT/SCD/SN/002.2)

[3] Archibald, E.N., et al. 2001, MNRAS, 323, 417

[4] Archibald E. N., et al., 2002, MNRAS, 336, 1

[5] Aretxaga, I., Hughes, D. H., Chapin, E. L., Gaztañaga, E., Dunlop, J. S., & Ivison, R. J. 2003, MNRAS, 342, 759

[6] Aretxaga, I., Hughes, D. H., & Dunlop, J. S. 2005, MNRAS, 358, 1240

[7] Avila-Reese et al. 2003, ApJ, 598, 36

[8] Babul, A., 1991, MNRAS, 248, 177

[9] Bajtlik, S., Duncan, R.C. & Ostriker, J. P. 1988. ApJ, 327, 570

[10] Barger A.J., Cowie L.L., Sanders D.B., Fulton E., Tanigushi Y., Sato Y., Kawara K., Okuda H., 1998, Nat, 394, 248

[11] Barger, A.J., Cowie, L.L., & Sanders, D.B. 1999, ApJ, 518, L5

[12] Bartolo, N., Komatsu, E., Matarrese, S., Riotto, A. 2004, Physics Report 402, 103

[13] Barvainis, R., Maloney, P., Antonucci, R., and Alloin, D., 1997, ApJ, 484, 695

[14] Basilakos, S., Plionis, M., Georgakakis, A., and Georgantopoulos, I. 2005, MNRAS, 356, 183

[15] Baugh C. M., Efstathiou G., 1993, MNRAS, 265, 145

[16] Baugh, C.M., et al. 2003, in *The Masses of Galaxies at Low and High Redshift*, ed. R. Bender, A. Renzini. p.91-96, Berlin, Springer Verlag

[17] Becker R. H., et al., 2001, AJ, 122, 2850

[18] Bennett C. L., et al., 1996, ApJ, 464, L1

[19] Bennett, C.L., et al. 2003, ApJS, 148, 1

[20] Bertoldi F., et al., 2000, A&A, 360, 92

[21] Bolatto A. D., Di Francesco J., Willott C. J., 2004, ApJ, 606, L101

[22] Bolton, J.S., Haenhelt, M.G., Viel, M. & Springel, V., 2005, MNRAS, 257, 1178

[23] Bond, J.R., Wadsley, J.W., 1997, *Computational Astrophys. Proc. 12th Kingston Conf., Halifax, October 1996, ed.* D. Clarke, M. West, *ASP Conf. Ser.,* p. 323. San Francisco: Astron. Soc. Pac.

[24] Borys, C., Chapman, S.C., Halpern, M., Scott, D., 2002 MNRAS, 330, L63

[25] Blain, A. W., Smail, I., Ivison, R. J., Kneib, J.-P., & Frayer, D.T. 2002, Phys. Rep., 369, 111

[26] Blain A. W., Chapman S. C., Smail I., Ivison R., 2004, ApJ, 611, 725

[27] Bryan, G.L., Machacek, M., Anninos, P., Norman, M.L., 1999, ApJ, 517, 13

[28] Carilli C. L., Yun M. S., 1999, ApJ, 513, L13

[29] Carilli C. L., Yun M. S., 2000, ApJ, 530, 618

[30] Carilli C. L., Blain A. W., 2002, ApJ, 569, 605

[31] Carilli, C. L., *et al.* , 2005, ApJ, 618, 586

[32] Carlberg et al. 2000, ApJ, 542, 57

[33] Carswell, R. F., Webb, J. K., Baldwin, J. A., & Atwood, B. 1987, ApJ, 319, 709

[34] Casoli F., Dickey J., Kazës I., Boselli A., Gavazzi G., Jore K., 1996, A&AS, 116, 193

[35] Cen, R. & Ostriker, J. P. 1993, 417, 404

[36] Cen R., Miralda-Escude, J., Ostriker, J. P., Rauch, M. 1994, ApJL, 437, 9

[37] Cen R., 2003, ApJ, 591, L5

[38] Chapin, E. L., 2004, PhD thesis, INAOE

[39] Chapman S.C., et al. , 2003a, Nature, 422, 695

[40] Chapman, S.C. et al. 2003b, ApJ, 585, 57

[41] Chapman S.C., et al. , 2005, ApJ, 622, 772

[42] Chini R., Krügel E., Lemke R., 1996, A&AS, 118, 47

[43] Cole, S. et al. 2001, MNRAS, 326, 255

[44] Colless M.M., 1999, Phil.Trans.Roy.Soc.Lond.A, 357, 105

[45] Coppin K., et al., 2006, MNRAS, 372, 1621

[46] Cowie, L.L., Barger, A.J., & Kneib, J.-P. 2002, AJ, 123, 2197

[47] Croft R. A. C., Weinberg D. H., Katz N., Hernquist L., 1998, ApJ, 495, 44

[48] Croom S. M., Shanks T., Boyle B. J., Smith R. J., Miller L., Loaring N. S., Hoyle F., 2001, MNRAS, 325, 483

[49] Davé, R., Dubinksi, J., & Hernquist, L. 1997, NewAst, 2, 277

[50] Daveé, R., Hernquist, L., Katz, N., & Weinberg, D. H. 1999, ApJ, 511, 521

[51] Davé, R., & Tripp, T. M., 2001, ApJ, 553, 528

[52] Davies R. I., Tacconi L. J., Genzel R., 2004, ApJ, 613, 781

[53] de Bernardis, P. et al. 1999, *New Astronomy Review*, 43, 289

[54] De Troia, G. et al. 2003, MNRAS, 343, 284

[55] Devlin, M. et al. 1998, ApJL, 509, L69

[56] Devlin M. J., et al., 2004, SPIE, 5498, 42

[57] Dey, A., et al. 1999, ApJ, 519, 610

[58] Downes D., Neri R., Wiklind T., Wilner D. J., Shaver P. A., 1999, ApJ, 513, L1 (D99)

[59] Downes, D. & Solomon, P.M. 1998, ApJ, 507, 615

[60] Dunlop et al. 1994. Nature, 370, 347

[61] Dunlop J., et al. , 2004, MNRAS, 350, 769

[62] Dunne L., Clements D.L., Eales S.A., 2000a, MNRAS, 319, 813

[63] Dunne L., Eales S.A., Edmunds M., Ivison R.J., Alexander P., Clements D.L., 2000b, MNRAS, 315, 115

[64] Egami E., Neugebauer G., Soifer B. T., Matthews K., Ressler M., Becklin E. E., Murphy T. W., Dale D. A., 2000, ApJ, 535, 561

[65] Eisenstein D. J., Blanton M., Zehavi I., Bahcall N., Brinkmann J., Loveday J., Meiksin A., Schneider D., 2005, ApJ, 619, 178

[66] Ellison S. L., Lewis G. F., Pettini M., Sargent W. L. W., Chaffee F. H., Foltz C. B., Rauch M., Irwin M. J., 1999, PASP, 111, 946

[67] Ellison S. L., Songaila A., Schaye J., Pettini M., 2000, AJ, 120, 1175

[68] Fan, X. et al. 2003, AJ, 125, 1649

[69] Fardal, M., Giroux, M. L., & Shull, J. M. 1998, AJ, 115, 2206 (FGS)

[70] Fernandez-Soto, A., et al. 1996, ApJL, 460, L85

[71] Fixsen, D. J., Dwek, E., Mather, J. C., Bennett, C. L., & Shafer, R. A. 1998, ApJ, 508, 123

[72] Fosalba P., Gaztañaga E., 2004, MNRAS, 350, L37

[73] Fox, M.J. et al. 2002, MNRAS, 331, 839

[74] Frayer et al. 1999, ApJ, 514, L13

[75] Freedman, W.L., et al. 2001, ApJ, 663, 47

[76] Garcia-Burillo, J., et al. 2006, *astroph/0605656*

[77] Gallagher S. C., Brandt W. N., Chartas G., Garmire G. P., 2002, ApJ, 567, 37

[78] Gao, Y. & Solomon, P. M. 2004a, ApJS, 152, 63

[79] Gao, Y. & Solomon, P. M. 2004b, ApJ, 606, 271

[80] Gaztañaga E., Wagg J., Multamäki T., Montaña A., Hughes D. H., 2003, MNRAS, 346, 47

[81] Gaztañaga E., Wagg J., 2003, PhRvD, 68, 021302

[82] Genzel, R. et al. 2003, ApJ, 584, 633

[83] Genzel R., et al., 2005, in "Multiwavelength mapping of galaxy formation and evolution,"

[84] Goldreich P. & Kwan J. 1974, ApJ, 537, 53

[85] Gonzalez A. H., Tran K.-V. H., Conbere M. N., Zaritsky D., 2005, ApJ, 624, L73

[86] Governato, et al. 1998, Nature, 329, 359

[87] Graciá-Carpio J., García-Burillo S., Planesas P., Colina L., 2006, ApJ, 640, L135

[88] Greve, T.R., Ivison, R.J., & Papadopoulos, P.P. 2004, A&A, 419, 99

[89] Greve T.R., Ivison R.J., Bertoldi F., Stevens J.A., Dunlop J.S., Lutz D., Carilli C.L., 2004, MNRAS, 354, 779

[90] Greve T.R. et al. 2005, MNRAS, 359, 1165

[91] Haardt F., Madau P. 1996, ApJ, 461, 20 (HM96)

[92] Hainline L. J., Blain A. W., Greve T. R., Chapman S. C., Smail I., Ivison R. J., 2006, ApJ, 650, 614

[93] Hanany, S., et al. 2000, ApL, 545, L5

[94] Hinshaw, G., et al. 1996a, ApJ, 464, L17

[95] Hinshaw, G., et al. 1996b, ApJ, 464, L25

[96] Hasinger G., Schartel N., Komossa S., 2002, ApJ, 573, L77

[97] Helfer, T. & Blitz L., 1997, ApJ 478, 233

[98] Helou, G., et al., 1985, ApJ, 298, L7

[99] Hinshaw G., et al., 2003, ApJS, 148, 135

[100] Hinshaw et al. 2006, *astro-ph/0603451*

[101] Holland W. S., et al., 1999, MNRAS, 303, 659

[102] Holland W., et al., 2006, SPIE, 6275,

[103] Hu, E. M., Kim, T.-S., Cowie, L. L. & Songaila, A. 1995, AJ, 110, 4 (H95)

[104] Hubble, E., "A Relation Between Distance and Radial Velocity Among Extra-Galactic Nebulae", 1929, *The Proceedings of the National Academy of Sciences*, 15, 168

[105] Hughes, D.H., et al. 1997, MNRAS, 289, 766

[106] Hughes D. H., et al., 1998, Natur, 394, 241

[107] Hughes D. H., et al., 2002, MNRAS, 335, 871

[108] Hui L., Gnedin N. Y., 1997, MNRAS, 292, 27

[109] Ibata R. A., Lewis G. F., Irwin M. J., Lehár J., Totten E. J., 1999, AJ, 118, 1922

[110] Ikeuchi, 1986, Ap&SS, 118, 509

[111] Imanishi M., Nakanishi K., Kohno K., 2006, AJ, 131, 2888

[112] Iono, D. et al. 2006, *astro-ph/0606043*

[113] Irwin M. J., Ibata R. A., Lewis G. F., Totten E. J., 1998, ApJ, 505, 529

[114] Isaak, K., Chandler, C., & Carilli, C. 2004, MNRAS, 348, 1035

[115] Ivison, R.J. et al. 1998, MNRAS, 298, 583

[116] Ivison, R.J. et al. 2000, ApJ, 542, 27

[117] Ivison, R.J. et al. 2002, MNRAS, 337, 1

[118] Jena T., et al., 2005, MNRAS, 361, 70

[119] Jenness T., Lightfoot J.F., 1998, ADASS, 145, 216

[120] Jewell, P.R., & Prestage, R.M. 2004, Proc. SPIE, 5489, 312

[121] Laurent G. T., et al., 2005, ApJ, 623, 742

[122] Lavezzi T. E., Dickey J. M., 1998, AJ, 115, 405

[123] Kauffmann, G., et al. 1999, MNRAS, 303, 188

[124] Kennicutt, R.C., 1998, ARA&A, 36, 189

[125] Kim, T.-S., Hu, E. M., Cowie, L. L., Songaila, A. 1997, AJ, 114, 1

[126] Kirkman, D. & Tytler, D. 1997, ApJ, 484, 672

[127] Kirkman D., et al., 2005, MNRAS, 360, 1373

[128] Klamer, I.J., Ekers, R.D., Sadler, E.M., et al. 2005, ApJ, 621, L1

[129] Kogut, A. et al. 1996, ApJ, 464, L5

[130] Kohno K., Matsushita S., Vila-Vilaró B., Okumura S. K., Shibatsuka T., Okiura M., Ishizuki S., Kawabe R., 2001, ASPC, 249, 672

[131] Kohno K., 2005, AIPC, 783, 203

[132] Komatsu, E., et al. 2003, ApJS, 148, 119

[133] Koopmans, L.V.E., Treu, T., Fassnacht, C.D., Blandford, R.D., & Surpi, G., 2003, ApJ, 599, 70

[134] Kreysa, E., et al. 1998, Proc. SPIE, 3357, 319

[135] Kuo, C. L., et al. 2004, ApJ, 600, 32

[136] Lanzetta, K. M., Turnshek, D. A., & Wolfe, A. M. 1987, ApJ, 322, 739

[137] Ledoux C., Theodore B., Petitjean P., Bremer M. N., Lewis G. F., Ibata R. A., Irwin M. J., Totten E. J., 1998, A&A, 339, L77

[138] Lepp, S., & Dalgarno, A. 1996, A&A, 306, L21

[139] Lewis, G.F., Chapman, S.C., Ibata, R.A., Irwin, M.J., & Totten, E.J. 1998, ApJ, 505, L1

[140] Lewis, G.F., Carilli, C., Papadopoulos, P., Ivison, R.J., 2002, MNRAS, 330, L15

[141] Lilly S. J., Le Fevre O., Hammer F., Crampton D., 1996, ApJ, 460, L1

[142] Lilly, S.J., et al. 1999, ApJ, 518, 641

[143] Lu, L., Wolfe, A. M. & Turnshek, D. A. 1991, ApJ, 367, 19

[144] Lu L., Sargent W. L. W., Womble D. S., Takada-Hidai M., 1996, ApJ, 472, 509

[145] Lynds, R. 1971, ApJ, 164, L73

[146] Madau P., Ferguson H. C., Dickinson M. E., Giavalisco M., Steidel C. C., Fruchter A., 1996, MNRAS, 283, 1388

[147] Maiolino R., Ruiz M., Rieke G. H., Papadopoulos P., 1997, ApJ, 485, 552

[148] Maiolino R., et al. 2005, A&A, 440, L51

[149] Marsden G., Borys C., Chapman S. C., Halpern M., Scott D., 2005, MNRAS, 359, 43

[150] Mathis H., Diego J. M., Silk J., 2004, MNRAS, 353, 681

[151] McDonald P., Miralda-Escudé J., Rauch M., Sargent W. L. W., Barlow T. A., Cen R., Ostriker J. P., 2000, ApJ, 543, 1

[152] McDonald P., Miralda-Escudé J., Rauch M., Sargent W. L. W., Barlow T. A., Cen R. 2001a, ApJ, 562, 52

[153] McDonald P. & Miralda-Escudé J. 2001b, ApJ, 549, L11

[154] Miralda-Escudé, J., Cen, R., Ostriker, J.P., Rauch, M., 1996, ApJ, 471, 582

[155] Mortier A.M.J., 2005, MNRAS, 363, 563

[156] Neri R. et al. 2003, ApJ, 597, L113

[157] Nolta M. R., et al., 2004, ApJ, 608, 10

[158] Norberg P., et al., 2002, MNRAS, 332, 827

[159] Overzier R. A., Röttgering H. J. A., Rengelink R. B., Wilman R. J., 2003, A&A, 405, 53

[160] Padin S., et al., 2002, PASP, 114, 83

[161] Page, L. et al. 2006, *astro-ph/0603450*

[162] Papadopoulos, P., Ivison, R.J., Carilli, C., Lewis., G. 2001, Nature, 409, 58

[163] Peebles, P.J.E., 2001 *astroph/0103040*

[164] Pelló R., Schaerer D., Richard J., Le Borgne J.-F., Kneib J.-P., 2004, A&A, 416, L35

[165] Porciani C., Giavalisco M., 2002, ApJ, 565, 24

[166] Rauch, M., et al. 1997, ApJ, 489, 7.

[167] Rauch, M. 1998, ARA&A, 36, 267

[168] Rees M. J., 1986, MNRAS, 218, 25P

[169] Rengarajan T.N. & Takeuchi T.T., 2001, PASJ, 53, 433

[170] Riechers D. A., et al., 2006a, ApJ, 650, 604

[171] Riechers D. A., Walter F., Carilli C. L., Weiss A., Bertoldi F., Menten K. M., Knudsen K. K., Cox P., 2006b, ApJ, 645, L13

[172] Riess, A.G. et al. 2005, ApJ, 627, 579

[173] Rowan-Robinson M., 2000, MNRAS, 316, 885

[174] Sachs R. K., Wolfe A. M., 1967, ApJ, 147, 73

[175] Sánchez A. G., Baugh C. M., Percival W. J., Peacock J. A., Padilla N. D., Cole S., Frenk C. S., Norberg P., 2006, MNRAS, 366, 189

[176] Sanders D. B., Mirabel I. F., 1985, ApJ, 298, L31

[177] Sanders D. B., Young J. S., Soifer B. T., Schloerb F. P., Rice W. L., 1986, ApJ, 305, L45

[178] Sanders D. B., Scoville N. Z., Soifer B. T., 1991, ApJ, 370 158

[179] Sargent, W. L. W., *et al.* 1980, AJS, 42, 41

[180] Saunders W., Rowan-Robinson M., Lawrence A., Efstathiou G., Kaiser N., Ellis R. S., Frenk C. S., 1990, MNRAS, 242, 318

[181] Schaye J., Theuns T., Leonard A., Efstathiou G., 1999, MNRAS, 310, 57

[182] Scott J., Bechtold J., Dobrzycki A., Kulkarni V. P., 2000, ApJS, 130, 67

[183] Scott J., Bechtold J., Morita, M., Dobrzycki A., Kulkarni V. P. 2002, ApJ, 571, 665

[184] Schöier, F.L., van der Tak, F.F.S., van Dishoek, E.F., Black, J.H., 2005, A&A, 432, 369

[185] Scott J., Bechtold J., Morita, M., Dobrzycki A., Kulkarni V. P. 2002, ApJ, 571, 665

[186] Scott, S.E., et al. 2002, MNRAS, 331, 817

[187] Scoville, N. & Solomon, P.M. 1974, ApJ 187, L67

[188] Scranton R., et al., 2002, ApJ, 579, 48

[189] Seljak U., Zaldarriaga M., 1996, ApJ, 469, 437

[190] Serjeant S., et al., 2003, MNRAS, 344, 887

[191] Serrano, A., Schloerb, P., Hughes, D.H., and Yun, M. 2006, SPIE, 6267, 1

[192] Shalabiea, O.M., & Greenberg, J.M. 1996, A&A, 307, 52

[193] Smail I., Ivison R.J., Blain A.W. & Kneib, J.-P. 1998, ApJ, 507, L21

[194] Soifer B. T., et al., 2004, ApJS, 154, 151

[195] Solomon, P.M., Downes, D., Radford, S.J.E., 1992a, ApJ, 387, L55

[196] Solomon, P.M., Downes, D., Radford, S.J.E., 1992b, ApJ, 398, L29

[197] Solomon, P.M., Vanden Bout, P., Carilli, C., Guelin, M. 2003, Nature, 426, 636

[198] Solomon P. M., & Vanden Bout P. A., 2005, ARA&A, 43, 677

[199] Spergel D. N., et al., 2003, ApJS, 148, 175

[200] Spergel D. N., et al., 2006, *astro-ph/0603449*

[201] Steidel C. C., Giavalisco M., Pettini M., Dickinson M., Adelberger K. L., 1996, ApJ, 462, L17

[202] Steidel C. C., Pettini M., Adelberger K. L., 2001, ApJ, 546, 665

[203] Sternberg, A., Genzel, R., & Tacconi, L.J. 1994, ApJ, 436, L131

[204] Stevens, J.A., et al. 2003, Nature, 425, 264

[205] Theuns, T., Leonard, A., & Efstathiou, G. 1998, MNRAS, 297, L49

[206] Theuns T., Schaye J., Haehnelt M. G., 2000, MNRAS, 315, 600

[207] Tytler D., 1987, ApJ, 321, 69

[208] Tytler, D., et al. 2004, ApJ, 617, 1

[209] Usero, A., García-Burillo, S., Fuente, A., Martín-Pintado, J., & Rodríguez-Fernández, N.J. 2004, A&A, 419, 897

[210] Vanden Bout, P.A., Solomon, P.M., & Maddalena, R. 2004, ApJ, 614, L97

[211] van Kampen E., et al., 2005, MNRAS, 359, 469

[212] Vogt, S. S., *et al.* 1994, S.P.I.E., 2198, 362

[213] Wagg J., Wilner D. J., Neri R., Downes D., Wiklind T., 2005, ApJ, 634, L13

[214] Wagg J., Wilner D. J., Neri R., Downes D., Wiklind T., 2006a, ApJ, 651, 46

[215] Walter F., et al., 2003, Natur, 424, 406

[216] Webb, J. K. 1987, PhD thesis, University of Cambridge

[217] Weinberg S., 1972, gcpa.book,

[218] Weinberg D. H., Hernquist L., Katz N., Croft R., Miralda-Escudé J., 1998, semi.conf, 133

[219] Weinberg D., et al., 1999, elss.conf, 346

[220] Weymann, R. J., et al. 1998, ApJ, 506, 1

[221] West, M.J., 1994, MNRAS 268, 79

[222] Wiklind T., 2003, ApJ, 588, 736

[223] Wilson G. W., Austermann J., Logan D. W., Yun M., 2004, SPIE, 5498, 246

[224] Wu, J.H.P., et al. 2001. PhRvL, 87, 1303

[225] Yao, L., Seaquist, E.R., Kuno, N., & Dunne, L., 2003, ApJ, 588, 771

[226] York D. G., et al., 2000, AJ, 120, 1579

[227] Young J. S., Scoville N. Z., 1991, ARA&A, 29, 581

[228] Yun M.S. & Carilli C.L., 2002, ApJ, 568, 88

Appendix A

SHADES sourcelists

CONS ID	RA (J2000)	Dec (J2000)	S_{850} (deb.) [mJy]	INAOE S_{450} (or 3-σ) [mJy]
LH850.1	$10^h52^m01^s42$	57°24′43″0	8.85 ($\pm^{1.0}_{1.0}$)	55.8 ± 9.9
LH850.2	$10^h52^m57^s32$	57°21′05″8	13.45 ($\pm^{2.1}_{2.1}$)	< 78.4
LH850.3	$10^h52^m38^s25$	57°24′36″5	10.95 ($\pm^{1.8}_{1.9}$)	< 31.7
LH850.4	$10^h52^m04^s17$	57°26′58″9	10.65 ($\pm^{1.7}_{1.8}$)	108.0 ± 23.0
LH850.5	$10^h53^m02^s62$	57°18′27″0	8.15 ($\pm^{2.0}_{2.1}$)	< 69.5
LH850.6	$10^h52^m04^s13$	57°25′26″3	6.85 ($\pm^{1.3}_{1.3}$)	< 53.9
LH850.7	$10^h53^m01^s40$	57°25′54″2	8.55 ($\pm^{1.8}_{1.9}$)	< 60.1
LH850.8	$10^h51^m53^s86$	57°18′39″8	5.45 ($\pm^{1.1}_{1.2}$)	< 31.6
LH850.9	$10^h52^m16^s09$	57°25′04″1	5.95 ($\pm^{1.6}_{1.6}$)	< 44.6
LH850.10	$10^h52^m48^s61$	57°32′58″6	9.15 ($\pm^{2.7}_{2.9}$)	254.4 ± 69.8
LH850.11	$10^h51^m29^s53$	57°24′05″2	6.25 ($\pm^{1.7}_{1.8}$)	< 74.2
LH850.12	$10^h52^m27^s61$	57°25′13″1	6.15 ($\pm^{1.7}_{1.7}$)	< 24.4
LH850.13	$10^h51^m32^s33$	57°31′34″8	5.65 ($\pm^{2.3}_{2.9}$)	< 110.3
LH850.14	$10^h52^m30^s11$	57°22′15″6	7.25 ($\pm^{1.8}_{1.9}$)	< 77.8
LH850.15	$10^h53^m19^s20$	57°21′10″6	13.25 ($\pm^{4.3}_{5.0}$)	< 261.3
LH850.16	$10^h51^m51^s45$	57°26′37″0	5.85 ($\pm^{1.8}_{1.9}$)	< 36.9
LH850.17	$10^h51^m58^s25$	57°18′00″8	4.75 ($\pm^{1.3}_{1.3}$)	< 36.6
LH850.18	$10^h52^m27^s69$	57°22′17″8	6.05 ($\pm^{1.9}_{2.1}$)	< 65.6
LH850.19	$10^h52^m35^s71$	57°31′19″1	5.15 ($\pm^{2.0}_{2.4}$)	< 87.7
LH850.21	$10^h52^m56^s86$	57°30′38″1	4.15 ($\pm^{2.0}_{2.5}$)	< 62.0
LH850.22	$10^h51^m37^s55$	57°33′23″3	7.55 ($\pm^{3.2}_{4.2}$)	< 239.0
LH850.23	$10^h52^m13^s74$	57°31′54″1	4.35 ($\pm^{1.9}_{2.4}$)	< 83.6
LH850.24	$10^h52^m00^s23$	57°20′38″1	2.75 ($\pm^{1.2}_{1.2}$)	< 27.5
LH850.26	$10^h52^m40^s95$	57°23′12″0	5.85 ($\pm^{2.4}_{2.9}$)	< 78.5
LH850.27	$10^h52^m03^s57$	57°18′13″5	5.05 ($\pm^{1.3}_{1.3}$)	< 37.5
LH850.28	$10^h52^m57^s00$	57°31′07″1	6.45 ($\pm^{1.7}_{1.8}$)	< 57.4
LH850.29	$10^h52^m30^s92$	57°20′36″0	6.75 ($\pm^{2.0}_{2.2}$)	< 58.3
LH850.30	$10^h52^m07^s79$	57°19′06″6	4.75 ($\pm^{1.5}_{1.6}$)	< 64.3
LH850.31	$10^h52^m16^s06$	57°16′21″1	6.05 ($\pm^{1.8}_{2.0}$)	< 55.2
LH850.33	$10^h51^m55^s98$	57°23′11″8	3.85 ($\pm^{1.0}_{1.1}$)	< 29.2
LH850.34	$10^h52^m13^s50$	57°33′28″1	14.05 ($\pm^{3.1}_{3.2}$)	< 109.4
LH850.35	$10^h52^m46^s92$	57°20′56″3	6.15 ($\pm^{2.2}_{2.4}$)	< 57.3
LH850.36	$10^h52^m09^s34$	57°18′06″8	6.35 ($\pm^{1.7}_{1.8}$)	< 86.1
LH850.37	$10^h51^m24^s13$	57°23′34″9	7.55 ($\pm^{2.9}_{3.5}$)	< 102.9

Continued on Next Page...

LH850.38	$10^h53^m07^s10$	$57°24'31''4$	4.35 ($\pm^{2.2}_{2.7}$)	< 64.7
LH850.39	$10^h52^m24^s85$	$57°16'09''8$	6.55 ($\pm^{2.2}_{2.7}$)	< 55.5
LH850.40	$10^h52^m02^s01$	$57°19'15''8$	3.05 ($\pm^{1.1}_{1.2}$)	< 27.9
LH850.41	$10^h51^m59^s86$	$57°24'23''6$	3.85 ($\pm^{0.9}_{1.0}$)	< 25.7
LH850.43	$10^h52^m57^s17$	$57°23'51''8$	4.95 ($\pm^{2.1}_{2.6}$)	< 85.2
LH850.47	$10^h52^m35^s63$	$57°25'14''0$	3.55 ($\pm^{1.7}_{2.1}$)	< 24.5
LH850.48	$10^h52^m56^s24$	$57°32'45''8$	5.45 ($\pm^{2.1}_{2.5}$)	< 79.7
LH850.52	$10^h52^m45^s53$	$57°31'21''9$	3.95 ($\pm^{2.2}_{2.7}$)	< 86.0
LH850.53	$10^h52^m40^s49$	$57°19'28''4$	4.45 ($\pm^{2.3}_{2.9}$)	< 68.4
LH850.60	$10^h51^m43^s58$	$57°24'46''0$	3.15 ($\pm^{1.7}_{2.0}$)	< 51.5
LH850.63	$10^h51^m53^s91$	$57°25'05''1$	3.65 ($\pm^{1.2}_{1.3}$)	< 33.3
LH850.64	$10^h52^m51^s81$	$57°32'42''2$	5.85 ($\pm^{2.5}_{3.2}$)	< 86.4
LH850.66	$10^h51^m38^s69$	$57°20'17''2$	4.25 ($\pm^{1.9}_{2.2}$)	< 54.5
LH850.67	$10^h52^m09^s00$	$57°23'55''1$	2.55 ($\pm^{1.5}_{1.5}$)	< 69.5
LH850.70	$10^h51^m48^s52$	$57°30'46''7$	3.85 ($\pm^{2.2}_{2.5}$)	< 88.0
LH850.71	$10^h52^m18^s62$	$57°19'03''8$	3.95 ($\pm^{1.8}_{2.0}$)	< 100.4
LH850.73	$10^h51^m41^s66$	$57°22'17''6$	3.55 ($\pm^{1.9}_{2.3}$)	< 57.0
LH850.75	$10^h53^m15^s93$	$57°26'45''5$	4.45 ($\pm^{2.2}_{2.6}$)	< 101.1
LH850.76	$10^h51^m48^s52$	$57°28'38''7$	4.75 ($\pm^{2.5}_{3.1}$)	< 82.9
LH850.77	$10^h51^m57^s00$	$57°22'10''1$	3.25 ($\pm^{1.2}_{1.3}$)	< 30.6
LH850.78	$10^h51^m45^s33$	$57°17'38''7$	4.55 ($\pm^{2.2}_{2.7}$)	< 75.8
LH850.79	$10^h51^m52^s10$	$57°21'27''4$	3.15 ($\pm^{1.3}_{1.5}$)	< 34.2
LH850.81	$10^h52^m31^s99$	$57°18'00''4$	5.35 ($\pm^{1.9}_{2.3}$)	< 85.5
LH850.83	$10^h53^m07^s94$	$57°28'39''1$	3.15 ($\pm^{2.0}_{2.1}$)	< 55.7
LH850.87	$10^h51^m53^s30$	$57°17'33''4$	3.45 ($\pm^{1.5}_{1.7}$)	< 55.5
LH850.100	$10^h51^m39^s06$	$57°15'09''8$	11.25 ($\pm^{4.2}_{5.3}$)	< 69.3

Table A.1: The consortium 850 μm source list for the SHADES coverage of the LH region. Positional accuracy for these 60 sources is $\lesssim 3$ arcsec. Our estimate of the true unbiased flux of each source is given, with accompanying error bars representing the 68% confidence bounds of the (non-Gaussian) deboosted flux distribution. 450 μm fluxes (or 3-σ limits) are from the INAOE reduction, whereby I have defined any 3.5-σ peak within 7.5 arcsecs of the consortium position to be a detection.

CONS ID	RA (J2000)	Dec (J2000)	S_{850} (deb.) [mJy]	INAOE S_{450} (or 3-σ) [mJy]
SXDF850.1	$02^h17^m30^s53$	$-04°59'37''0$	10.45 $(\pm^{1.5}_{1.4})$	< 47.5
SXDF850.2	$02^h18^m03^s51$	$-04°55'27''2$	10.15 $(\pm^{1.6}_{1.6})$	< 57.7
SXDF850.3	$02^h17^m42^s14$	$-04°56'28''2$	8.75 $(\pm^{1.5}_{1.6})$	< 45.6
SXDF850.4	$02^h17^m38^s62$	$-05°03'37''5$	4.45 $(\pm^{1.7}_{2.0})$	58.7 ± 16.6
SXDF850.5	$02^h18^m02^s88$	$-05°00'32''8$	8.45 $(\pm^{1.7}_{1.9})$	66.7 ± 15.2
SXDF850.6	$02^h17^m29^s80$	$-05°03'29''7$	7.15 $(\pm^{2.1}_{2.4})$	< 50.5
SXDF850.7	$02^h17^m38^s92$	$-05°05'23''7$	7.15 $(\pm^{1.5}_{1.6})$	< 39.8
SXDF850.8	$02^h17^m44^s43$	$-04°55'54''7$	6.05 $(\pm^{1.8}_{1.9})$	< 41.8
SXDF850.9	$02^h17^m56^s42$	$-04°58'06''7$	6.45 $(\pm^{2.0}_{2.1})$	< 58.6
SXDF850.10	$02^h18^m25^s25$	$-04°55'57''2$	7.75 $(\pm^{2.6}_{3.1})$	< 107.4
SXDF850.11	$02^h17^m25^s12$	$-04°59'37''4$	4.55 $(\pm^{1.9}_{2.2})$	< 59.2
SXDF850.12	$02^h17^m59^s37$	$-05°05'03''7$	5.75 $(\pm^{1.7}_{1.8})$	< 87.0
SXDF850.14	$02^h18^m19^s26$	$-05°02'44''2$	4.85 $(\pm^{1.9}_{2.1})$	< 77.9
SXDF850.15	$02^h18^m15^s70$	$-04°54'05''2$	6.25 $(\pm^{1.6}_{1.6})$	< 57.7
SXDF850.16	$02^h18^m13^s89$	$-04°57'41''7$	4.85 $(\pm^{1.7}_{1.8})$	< 49.9
SXDF850.17	$02^h17^m54^s98$	$-04°53'02''8$	7.65 $(\pm^{1.7}_{1.7})$	< 60.4
SXDF850.18	$02^h17^m57^s79$	$-05°00'29''8$	6.45 $(\pm^{2.0}_{2.2})$	< 54.9
SXDF850.19	$02^h18^m28^s15$	$-04°58'39''2$	4.35 $(\pm^{1.8}_{2.1})$	< 45.7
SXDF850.20	$02^h17^m44^s18$	$-05°02'16''0$	4.45 $(\pm^{2.0}_{2.2})$	< 61.2
SXDF850.21	$02^h17^m42^s80$	$-05°04'27''7$	5.25 $(\pm^{2.0}_{2.2})$	< 54.7
SXDF850.22	$02^h18^m00^s38$	$-05°07'41''5$	6.25 $(\pm^{2.3}_{2.6})$	< 161.8
SXDF850.23	$02^h17^m42^s53$	$-05°05'45''5$	5.25 $(\pm^{1.7}_{2.0})$	< 51.3
SXDF850.24	$02^h17^m34^s58$	$-05°04'37''7$	5.15 $(\pm^{2.0}_{2.3})$	< 44.9
SXDF850.25	$02^h18^m12^s12$	$-05°05'55''7$	4.05 $(\pm^{2.1}_{2.5})$	< 81.3
SXDF850.27	$02^h18^m07^s86$	$-05°01'48''5$	5.65 $(\pm^{2.0}_{2.3})$	< 36.7
SXDF850.28	$02^h18^m07^s04$	$-04°59'15''5$	4.85 $(\pm^{2.2}_{2.7})$	< 53.9
SXDF850.29	$02^h18^m16^s47$	$-04°55'11''8$	5.35 $(\pm^{1.8}_{1.9})$	82.4 ± 21.5
SXDF850.30	$02^h17^m40^s31$	$-05°01'16''2$	5.75 $(\pm^{2.0}_{2.2})$	< 61.3
SXDF850.31	$02^h17^m36^s30$	$-04°55'57''5$	6.05 $(\pm^{1.7}_{2.0})$	< 50.7
SXDF850.32	$02^h17^m22^s89$	$-05°00'38''1$	6.05 $(\pm^{2.4}_{3.0})$	< 79.4
SXDF850.35	$02^h18^m00^s89$	$-04°53'11''2$	5.35 $(\pm^{1.8}_{2.1})$	< 63.1
SXDF850.36	$02^h18^m32^s27$	$-04°59'47''2$	5.45 $(\pm^{1.8}_{1.9})$	< 49.9
SXDF850.37	$02^h17^m24^s45$	$-04°58'39''9$	4.55 $(\pm^{2.2}_{2.6})$	< 64.4
SXDF850.38	$02^h18^m25^s43$	$-04°57'14''7$	3.85 $(\pm^{2.3}_{2.7})$	< 89.9

Continued on Next Page...

SXDF850.39	$02^h17^m50^s60$	$-04°55'40''2$	4.05 $(\pm^{1.7}_{2.1})$	< 51.4
SXDF850.40	$02^h17^m29^s67$	$-05°00'59''2$	3.65 $(\pm^{1.5}_{1.6})$	< 45.2
SXDF850.45	$02^h18^m29^s33$	$-05°05'40''7$	21.95 $(\pm^{6.2}_{6.8})$	< 317.3
SXDF850.47	$02^h17^m33^s89$	$-04°58'57''7$	3.05 $(\pm^{1.6}_{1.9})$	< 42.5
SXDF850.48	$02^h17^m24^s62$	$-04°57'17''7$	7.65 $(\pm^{2.5}_{2.9})$	< 76.7
SXDF850.49	$02^h18^m20^s26$	$-04°56'48''5$	3.35 $(\pm^{2.0}_{2.2})$	< 62.4
SXDF850.50	$02^h18^m02^s86$	$-04°56'45''5$	5.35 $(\pm^{2.0}_{2.5})$	< 60.2
SXDF850.52	$02^h18^m04^s90$	$-05°04'53''7$	3.25 $(\pm^{1.8}_{2.1})$	< 72.6
SXDF850.55	$02^h17^m52^s19$	$-05°04'46''5$	3.95 $(\pm^{2.2}_{2.7})$	< 55.8
SXDF850.56	$02^h17^m50^s68$	$-05°06'31''8$	3.65 $(\pm^{2.2}_{2.5})$	< 106.0
SXDF850.63	$02^h17^m45^s80$	$-04°57'50''5$	4.15 $(\pm^{1.7}_{2.1})$	< 43.1
SXDF850.65	$02^h18^m07^s94$	$-05°04'03''2$	4.35 $(\pm^{1.9}_{2.3})$	< 69.1
SXDF850.69	$02^h17^m51^s40$	$-05°02'50''8$	3.65 $(\pm^{2.1}_{2.4})$	< 55.2
SXDF850.70	$02^h18^m11^s20$	$-05°02'47''2$	4.05 $(\pm^{1.9}_{2.3})$	< 57.4
SXDF850.71	$02^h18^m21^s24$	$-04°59'03''2$	4.15 $(\pm^{1.9}_{2.4})$	< 51.7
SXDF850.74	$02^h17^m58^s73$	$-04°54'28''8$	3.35 $(\pm^{1.8}_{2.1})$	< 52.7
SXDF850.76	$02^h17^m55^s78$	$-05°06'21''8$	4.45 $(\pm^{2.0}_{2.4})$	< 97.1
SXDF850.77	$02^h17^m36^s43$	$-05°04'32''2$	3.05 $(\pm^{2.0}_{2.1})$	< 51.7
SXDF850.86	$02^h18^m17^s18$	$-05°04'04''7$	3.65 $(\pm^{1.9}_{2.2})$	< 85.0
SXDF850.88	$02^h18^m00^s99$	$-05°04'48''5$	4.55 $(\pm^{2.1}_{2.5})$	< 78.2
SXDF850.91	$02^h17^m34^s81$	$-04°57'23''9$	3.55 $(\pm^{2.1}_{2.5})$	< 47.4
SXDF850.93	$02^h17^m33^s08$	$-04°58'13''5$	3.15 $(\pm^{2.0}_{2.1})$	< 46.9
SXDF850.94	$02^h17^m40^s08$	$-04°58'17''7$	4.15 $(\pm^{1.8}_{2.1})$	< 41.8
SXDF850.95	$02^h17^m41^s72$	$-04°58'33''7$	3.45 $(\pm^{1.9}_{2.2})$	< 48.1
SXDF850.96	$02^h18^m00^s00$	$-05°02'12''8$	4.75 $(\pm^{2.1}_{2.5})$	< 56.9
SXDF850.119	$02^h17^m56^s35$	$-04°52'55''2$	4.55 $(\pm^{2.1}_{2.5})$	< 64.3

Table A.2: The consortium 850 μm source list for the SXDF. Positional accuracy for these 60 sources is $\lesssim 3$ arcsec. Our estimate of the true unbiased flux of each source is given in the penultimate column, with accompanying error bars representing the 68 per cent confidence bounds of the (non-Gaussian) deboosted flux distribution. 450 μm fluxes (or 3-σ limits) are from the INAOE reduction, whereby I have defined any 3.5-σ peak within 7.5 arcsecs of the consortium position to be a detection.

INAOE ID	RA (J2000)	Dec (J2000)	S_{850} [mJy]	INAOE S_{450} (or 3-σ) [mJy]
LH850.1	$10^h52^m01^s51$	$57^o24'42''8$	9.48±1.2	55.8 ± 10.0
LH850.2	$10^h52^m57^s29$	$57^o21'04''8$	15.05±2.4	< 77.7
LH850.3	$10^h52^m38^s28$	$57^o24'37''0$	12.75±2.1	< 31.7
LH850.4	$10^h52^m04^s09$	$57^o27'01''9$	12.80±2.2	108.0 ± 23.0
LH850.5	$10^h52^m04^s23$	$57^o25'25''9$	8.51±1.5	< 54.8
LH850.6	$10^h53^m01^s44$	$57^o25'54''7$	10.73±2.1	< 60.1
LH850.7	$10^h51^m54^s06$	$57^o18'37''7$	6.15±1.2	< 31.6
LH850.8	$10^h52^m27^s51$	$57^o25'15''0$	8.39±1.8	< 24.4
LH850.9	$10^h52^m03^s57$	$57^o18'13''9$	6.43±1.4	< 37.5
LH850.10	$10^h52^m15^s99$	$57^o25'05''0$	7.67±1.7	< 44.6
LH850.11	$10^h52^m09^s37$	$57^o18'06''9$	7.95±1.8	< 86.1
LH850.12	$10^h53^m02^s56$	$57^o18'26''7$	9.04±2.0	< 69.5
LH850.13	$10^h52^m30^s23$	$57^o22'15''0$	8.66±1.9	< 79.2
LH850.14	$10^h52^m57^s30$	$57^o31'05''8$	7.94±1.8	< 57.2
LH850.15	$10^h51^m51^s46$	$57^o26'37''7$	7.59±1.8	< 36.8
LH850.16	$10^h52^m56^s33$	$57^o32'47''8$	8.73±2.1	< 80.3
LH850.17	$10^h52^m47^s03$	$57^o20'55''9$	8.63±2.2	< 57.0
LH850.18	$10^h52^m28^s62$	$57^o22'16''0$	7.90±2.0	< 68.1
LH850.19	$10^h52^m56^s67$	$57^o30'34''8$	7.23±1.9	< 62.4
LH850.20	$10^h52^m07^s88$	$57^o19'06''9$	6.10±1.6	< 66.5
LH850.21	$10^h52^m16^s16$	$57^o16'21''0$	7.19±1.9	< 55.2
LH850.22	$10^h51^m58^s26$	$57^o18'02''8$	5.13±1.3	< 36.4
LH850.23	$10^h51^m55^s97$	$57^o23'12''8$	4.27±1.1	< 29.2
LH850.24	$10^h52^m18^s62$	$57^o19'02''0$	6.41±1.7	< 99.1
LH850.25	$10^h51^m48^s41$	$57^o30'45''6$	7.18±1.9	< 88.0
LH850.26	$10^h51^m38^s59$	$57^o20'19''4$	6.75±1.8	< 54.5
LH850.27	$10^h51^m37^s92$	$57^o33'26''4$	12.84±3.5	< 241.0
LH850.28	$10^h52^m35^s55$	$57^o25'15''0$	5.58±1.5	< 24.4
LH850.29	$10^h52^m32^s20$	$57^o18'01''0$	7.01±1.9	< 87.2
LH850.30	$10^h52^m35^s70$	$57^o31'17''0$	7.09±1.9	< 87.7
LH850.31	$10^h51^m53^s96$	$57^o25'05''7$	4.80±1.3	< 33.6
LH850.32	$10^h51^m22^s70$	$57^o18'44''0$	15.41±4.3	< 218.8
LH850.33	$10^h52^m59^s88$	$57^o29'13''8$	7.02±1.9	< 55.2
LH850.34	$10^h51^m29^s72$	$57^o24'05''2$	8.40±2.3	< 72.8

Continued on Next Page...

LH850.35	$10^h51^m57^s09$	$57^o22'09''8$	4.30±1.2	< 30.7
LH850.36	$10^h52^m48^s75$	$57^o32'58''9$	10.74±3.0	254.4±69.8
LH850.37	$10^h52^m49^s24$	$57^o32'02''9$	8.62±2.4	< 95.2
LH850.38	$10^h52^m27^s38$	$57^o26'27''0$	6.91±1.9	< 30.9
LH850.39	$10^h52^m26^s64$	$57^o16'22''0$	8.26±2.3	< 55.8
LH850.40	$10^h52^m13^s85$	$57^o31'56''0$	6.57±1.9	< 83.5
LH850.41	$10^h52^m45^s63$	$57^o31'21''9$	6.51±1.8	< 85.8
LH850.42	$10^h51^m43^s69$	$57^o24'45''5$	5.91±1.7	< 51.7
LH850.43	$10^h51^m53^s46$	$57^o17'32''7$	5.05±1.4	< 54.1
LH850.44	$10^h51^m31^s17$	$57^o20'36''2$	8.10±2.3	< 58.2
LH850.45	$10^h51^m52^s41$	$57^o21'25''7$	4.19±1.2	< 33.0
LH850.46	$10^h52^m00^s45$	$57^o20'38''8$	3.89±1.1	< 27.8
LH850.47	$10^h51^m41^s64$	$57^o22'17''5$	5.78±1.7	< 57.0
LH850.48	$10^h52^m34^s19$	$57^o25'27''0$	5.18±1.5	< 21.7
LH850.49	$10^h52^m41^s24$	$57^o23'11''0$	7.26±2.1	< 78.5
LH850.50	$10^h51^m45^s43$	$57^o17'38''6$	6.76±2.0	< 75.9
LH850.51	$10^h53^m23^s05$	$57^o23'25''3$	16.37±4.9	< 112.6
LH850.52	$10^h51^m37^s72$	$57^o31'28''4$	7.44±2.2	< 83.3
LH850.53	$10^h52^m00^s15$	$57^o24'40''8$	4.02±1.2	< 28.6
LH850.54	$10^h51^m56^s61$	$57^o21'20''8$	3.87±1.2	< 27.9
LH850.55	$10^h53^m12^s18$	$57^o18'06''5$	8.34±2.5	< 94.2
LH850.56	$10^h53^m04^s81$	$57^o20'13''7$	7.34±2.3	< 109.1
LH850.57	$10^h51^m39^s60$	$57^o30'25''4$	6.55±2.0	< 69.9
LH850.58	$10^h51^m24^s29$	$57^o23'35''0$	12.25±3.8	< 102.7
LH850.59	$10^h52^m32^s35$	$57^o32'10''0$	6.31±2.0	< 85.3
LH850.60	$10^h53^m22^s44$	$57^o23'31''3$	15.28±4.8	< 108.8
LH850.61	$10^h51^m34^s85$	$57^o26'40''3$	6.87±2.2	< 51.2
LH850.62	$10^h52^m02^s44$	$57^o19'15''8$	3.75±1.2	< 28.1
LH850.63	$10^h52^m30^s36$	$57^o26'14''0$	5.32±1.7	< 27.0
LH850.64	$10^h52^m08^s70$	$57^o23'51''9$	4.34±1.4	< 71.5
LH850.65	$10^h51^m54^s71$	$57^o24'14''7$	3.74±1.2	< 25.8
LH850.66	$10^h52^m59^s83$	$57^o17'34''8$	7.25±2.3	< 73.3
LH850.67	$10^h51^m48^s69$	$57^o28'37''6$	7.38±2.4	< 82.7
LH850.68	$10^h53^m15^s95$	$57^o26'45''4$	6.11±2.0	< 101.1
LH850.69	$10^h52^m55^s21$	$57^o32'46''8$	7.52±2.4	< 81.5
LH850.70	$10^h53^m19^s36$	$57^o19'02''4$	14.04±4.6	< 185.1

Continued on Next Page...

LH850.71	$10^h52^m46^s66$	$57^o21'03''9$	6.40±2.1	< 60.2
LH850.72	$10^h52^m51^s73$	$57^o32'40''9$	7.45±2.4	< 87.0
LH850.73	$10^h52^m48^s35$	$57^o30'06''9$	6.93±2.3	< 85.0
LH850.74	$10^h52^m25^s52$	$57^o32'53''0$	7.70±2.5	< 100.1
LH850.75	$10^h53^m11^s87$	$57^o20'46''5$	9.99±3.3	< 133.9
LH850.76	$10^h51^m35^s31$	$57^o33'23''3$	11.30±3.8	< 214.2

Table A.3: The INAOE 850 μm source list for the SHADES coverage of the LH region. Positional accuracy for the 76 sources is $\lesssim 3$ arcsec. 450 μm fluxes (or 3-σ limits) are from the INAOE reduction, whereby I have defined any 3.5-σ peak within 7.5 arcsecs of the consortium position to be a detection. The three INAOE 850 μm sources with tentative 450 μm counterparts are also present in the 850 μm consortium catalogue (Table A.1).

INAOE ID	RA (J2000)	Dec (J2000)	S_{850} [mJy]	INAOE S_{450} (or 3-σ) [mJy]
SXDF850.1	$02^h17^m30^s49$	$-04^o59'37''0$	12.15±1.7	< 47.5
SXDF850.2	$02^h18^m03^s48$	$-04^o55'27''0$	12.71±1.8	< 57.7
SXDF850.3	$02^h17^m54^s98$	$-04^o53'03''0$	10.01±1.8	< 60.4
SXDF850.4	$02^h17^m42^s13$	$-04^o56'28''0$	10.29±2.1	< 45.6
SXDF850.5	$02^h17^m38^s98$	$-05^o05'25''0$	8.37±1.7	< 40.0
SXDF850.6	$02^h18^m15^s72$	$-04^o54'05''0$	7.84±1.7	< 57.7
SXDF850.7	$02^h17^m44^s41$	$-04^o55'53''0$	8.56±1.9	< 42.6
SXDF850.8	$02^h18^m00^s87$	$-04^o53'13''0$	7.55±1.8	< 62.9
SXDF850.9	$02^h17^m42^s53$	$-05^o04'27''0$	8.18±2.0	< 55.4
SXDF850.10	$02^h17^m59^s20$	$-05^o05'03''0$	7.85±1.9	< 84.5
SXDF850.11	$02^h18^m00^s20$	$-05^o07'41''0$	9.27±2.3	< 161.1
SXDF850.12	$02^h17^m56^s05$	$-04^o52'57''0$	7.61±1.9	< 63.9
SXDF850.13	$02^h17^m42^s46$	$-05^o05'46''0$	6.89±1.8	< 51.3
SXDF850.14	$02^h17^m24^s33$	$-04^o57'11''9$	12.27±3.2	< 86.5
SXDF850.15	$02^h18^m07^s96$	$-05^o01'49''0$	8.84±2.3	< 37.2
SXDF850.16	$02^h17^m29^s75$	$-05^o03'27''0$	9.77±2.6	< 49.8
SXDF850.17	$02^h17^m25^s13$	$-04^o59'35''9$	6.69±1.8	< 59.1
SXDF850.18	$02^h18^m25^s16$	$-04^o55'59''0$	10.36±2.7	< 107.4
SXDF850.19	$02^h17^m57^s73$	$-05^o00'30''0$	9.13±2.4	< 54.9
SXDF850.20	$02^h18^m02^s74$	$-05^o00'38''0$	8.74±2.3	61.1±14.6
SXDF850.21	$02^h17^m22^s72$	$-05^o00'38''9$	10.41±2.8	< 80.5
SXDF850.22	$02^h18^m32^s12$	$-04^o59'50''0$	10.62±2.9	< 48.8
SXDF850.23	$02^h17^m24^s47$	$-04^o58'38''9$	7.16±1.9	< 64.4
SXDF850.24	$02^h18^m16^s53$	$-04^o55'11''0$	6.69±1.8	82.4±21.6
SXDF850.25	$02^h17^m41^s93$	$-04^o56'21''0$	7.11±1.9	< 49.4
SXDF850.26	$02^h17^m36^s38$	$-04^o56'02''0$	6.64±1.8	< 50.8
SXDF850.27	$02^h17^m40^s26$	$-05^o01'17''0$	6.94±1.9	< 61.0
SXDF850.28	$02^h18^m01^s00$	$-05^o04'48''0$	6.88±1.9	< 78.2
SXDF850.29	$02^h17^m30^s29$	$-04^o59'27''0$	6.51±1.8	< 45.5
SXDF850.30	$02^h18^m03^s61$	$-05^o04'11''0$	7.36±2.1	< 76.6
SXDF850.31	$02^h17^m29^s68$	$-05^o00'59''0$	5.36±1.5	< 45.2
SXDF850.32	$02^h17^m50^s63$	$-05^o06'31''0$	6.69±1.9	< 105.2
SXDF850.33	$02^h18^m13^s79$	$-04^o57'42''0$	6.13±1.8	< 50.3
SXDF850.34	$02^h17^m39^s12$	$-05^o05'17''0$	5.95±1.7	< 40.3

Continued on Next Page...

SXDF850.35	$02^h17^m32^s97$	$-04^o58'13''0$	5.98±1.7	< 47.6
SXDF850.36	$02^h17^m36^s18$	$-04^o55'45''0$	6.44±1.9	< 52.7
SXDF850.37	$02^h17^m38^s58$	$-05^o03'38''0$	5.46±1.6	58.7±16.5
SXDF850.38	$02^h18^m15^s26$	$-05^o01'51''0$	7.03±2.1	< 69.6
SXDF850.39	$02^h18^m05^s29$	$-05^o06'14''0$	7.89±2.3	< 83.1
SXDF850.40	$02^h17^m40^s26$	$-05^o05'20''0$	5.82±1.7	< 46.0
SXDF850.41	$02^h17^m58^s73$	$-04^o54'29''0$	5.55±1.6	< 52.7
SXDF850.42	$02^h18^m15^s93$	$-04^o53'56''0$	5.94±1.8	< 56.1
SXDF850.43	$02^h17^m44^s21$	$-05^o02'16''0$	6.27±1.9	< 61.2
SXDF850.44	$02^h18^m09^s57$	$-04^o52'26''0$	7.58±2.3	< 82.2
SXDF850.45	$02^h18^m25^s49$	$-04^o55'52''0$	11.14±3.4	< 110.2
SXDF850.46	$02^h17^m36^s31$	$-05^o04'32''0$	5.49±1.7	< 50.8
SXDF850.47	$02^h17^m45^s41$	$-04^o55'56''0$	6.32±1.9	< 43.1
SXDF850.48	$02^h18^m11^s18$	$-05^o02'46''0$	6.13±1.9	< 57.3
SXDF850.49	$02^h18^m07^s43$	$-04^o59'09''0$	7.74±2.4	< 56.5
SXDF850.50	$02^h17^m59^s67$	$-05^o04'59''0$	6.09±1.9	< 89.1
SXDF850.51	$02^h17^m32^s97$	$-04^o55'18''0$	6.31±2.0	< 57.1
SXDF850.52	$02^h17^m56^s72$	$-04^o52'40''0$	7.31±2.3	< 69.5
SXDF850.53	$02^h18^m28^s04$	$-04^o58'39''0$	5.71±1.8	< 45.7
SXDF850.54	$02^h17^m26^s54$	$-05^o01'44''9$	7.41±2.4	< 61.0
SXDF850.55	$02^h17^m50^s50$	$-04^o55'39''0$	5.50±1.8	< 51.1
SXDF850.56	$02^h18^m09^s30$	$-04^o59'28''0$	6.93±2.2	< 46.7
SXDF850.57	$02^h17^m40^s80$	$-04^o54'18''0$	5.24±1.7	< 55.0
SXDF850.58	$02^h18^m15^s19$	$-04^o54'03''0$	5.18±1.7	< 60.6
SXDF850.59	$02^h18^m02^s94$	$-04^o56'44''0$	7.32±2.4	< 61.2
SXDF850.60	$02^h17^m33^s03$	$-05^o01'57''0$	4.86±1.6	< 46.2
SXDF850.61	$02^h18^m30^s25$	$-04^o57'41''0$	11.17±3.7	< 96.6
SXDF850.62	$02^h18^m10^s11$	$-05^o04'43''0$	5.58±1.8	< 64.6
SXDF850.63	$02^h17^m37^s11$	$-05^o00'28''0$	5.15±1.7	< 55.8
SXDF850.64	$02^h17^m43^s54$	$-04^o59'00''0$	5.91±1.9	< 38.2
SXDF850.65	$02^h17^m38^s25$	$-05^o06'45''0$	7.45±2.5	< 55.5
SXDF850.66	$02^h18^m02^s28$	$-04^o59'07''0$	6.11±2.0	< 71.9

Continued on Next Page...

Table A.4: The INAOE 850 μm source list for the SHADES coverage of the SXDF region. Positional accuracy for the 66 sources is $\lesssim 3$ arcsec. 450 μm fluxes (or 3-σ limits) are from the INAOE reduction, whereby I have defined any 3.5-σ peak within 7.5 arcsecs of the consortium position to be a detection. The three INAOE 850 μm sources with tentative 450 μm counterparts are the same as those in the consortium 850 μm list in Table A.2.